Mitigation of tip leakage induced phenomena in a low Reynolds number centrifugal compressor via blade loading distribution

Thèse N° 9720

Présentée le 28 août 2019

à la Faculté des sciences et techniques de l'ingénieur
Laboratoire de conception mécanique appliquée
Programme doctoral en energie

pour l'obtention du grade de Docteur ès Sciences

par

Markus DIEHL

Acceptée sur proposition du jury

Dr J. Van Herle, président du jury
Prof. J. A. Schiffmann, directeur de thèse
Prof. N. Binder, rapporteur
Prof. B. Ribi, rapporteur
Prof. T. Schneider, rapporteur

2019

ÉCOLE POLYTECHNIQUE
FÉDÉRALE DE LAUSANNE

The future is a concept — it doesn't exist. There is no such thing as tomorrow. There never will be because time is always now. That's one of the things we discover when we stop talking to ourselves and stop thinking. We find there is only present, only an eternal now.

— Alan W. Watts

To my parents…

Acknowledgements

First of all, I would like to thank the Swiss National Science Foundation (SNF), grant PYAPP2_154278/1, for their financial support of my PhD.

I would like to thank my boss and supervisor Prof. Dr. Jürg Schiffmann. I appreciate a lot the possibilities and freedom in research he offered me during my PhD time.

Furthermore, I would like to thank the members of my PhD jury, namely Dr. Jan Van Herle, Prof. Dr. Nicolas Binder, Prof. Dr. Beat Ribi and Prof. Dr. Tobias Schneider for reading my thesis and being examiner at my oral exam. Especially the recommendations of Prof. Dr. Beat Ribi and Prof. Dr. Nicolas Binder helped me a lot for further improving my work.

A big thank goes to my PhD colleague Suresh Katuwal Chhetri. During my PhD time we became such good friends thus this friendship is one of my biggest achievements besides the PhD.

The test-rig design and assembly was a hard and also quite frustrating task. However, it is the first time in my life I feel like a mother who is taking care about her baby. I would like to thank Nicolas Hueguelet, who did the design of the compressor unit. With this system you build something, which can be used as instrument of torture for the next generations of PhD students. Nonetheless, without the help of the workshop ATME (especially Marc Jeanneret) as well as the Microcity workshop (Joël Currit) the test-rig would not be possible.

In addition, I would like to thank my PhD colleague and friend Philipp Bättig, who does not represent the classical PhD in terms of practical skills. Every time when the workshop was not able to follow my wishes he did the required modifications. I will never forget your four hours welding on the heat exchanger.

I would also like to give a special thank to Dr. Christoph Schreiber, who helped me a lot in defining and finishing my PhD. The first thing you showed me was Heilmeier's catechism and honestly I am still not able to answer you all the questions.

Furthermore, a special thank goes to Dr. Patrick Wagner, who was the first one, who build something like a lab structure. You helped me so much with your knowledge.

In addition, I would like to express my special thank to the centrifugal compressor experts Dr. Mick Casey and Dr. Daniel Rusch, who were my sparring partners during this PhD. Especially the last meeting at Mick's place was quite helpful for me, in order to get prepared for the oral exam.

I would like to give some special thanks to all of my team members, namely Ansgar, Kosi, Lili, Wanhui, Christoph, Julie, Thierry, Antonio, Christophe, Philipp, Tomohiro, Eliott, Cyril, Jürg, Kevin, Eric, Sajjad, Patrick and Suresh.

Another thank goes to my girlfriend Lia. I know it was not easy at the last time of my PhD, but you supported me and showed me that the world also offers other things than thermal turbomachinery.
A special thank goes to my family for their continuous support. Due to the profession of my grandfather and father, I wanted to become an engineer and without them this PhD-thesis would never take place. On the other hand, without the good food and the easy life I had during my childhood, which is mostly attributed to my mother, this thesis would not take place, too. Hence, this work is dedicated to them.

Neuchâtel, 12. August 2019 M. D.

Abstract

Reduced-scale refrigeration compressors supported on gas-lubricated bearings have been identified as a key technology for domestic heat pump applications, in order to improve both the system efficiency and the reliability. Unfortunately, reduced-scale machines suffer from increased aerodynamic losses compared to large-scale industrial machines, which are caused by the small feature size and manufacturing tolerances. Due to the small feature size, the machine Reynolds number is low and higher frictional losses occur. The manufacturing tolerances as well as form and positioning tolerances for assembly require larger relative clearances in reduced-scale machines compared to large-scale ones, leading to increased losses caused by tip leakage.

Centrifugal compressor design and performance prediction strongly depend on empirical guidelines and correlations, which are deduced experimentally and numerically from test data of large-scale machines. Hence, the question arises whether these empirical design implications and correlations are applicable for reduced-scale compressors.

This PhD-thesis presents results on the investigation of the impact of low Reynolds number flow and large relative tip clearances on the compressor performance and flow patterns. The investigation is performed both experimentally and numerically (CFD and one-dimensional compressor model) on two reduced-scale centrifugal compressor designs. An experimental test facility of an up-scaled refrigeration compressor has been realized and tests in terms of impact of clearance ratio alteration as well as performance improvements by impeller design have been performed. Large relative clearance ratios of up to 20 % have been investigated.

Empirical correlations accounting for the impact of geometrical scaling as well as altering the tip clearance gap are assessed and improved. These correlations are tested and validated at design and off-design conditions.

Design implications on how to design a centrifugal compressor with respect to large clearance ratios have been postulated. The hub and shroud end-wall distribution as well as the shroud blade angle distribution have been identified as main design parameters for mitigating the negative effect of large relative clearance ratios. Furthermore, it has been shown that compressor optimization in terms of tip leakage induced phenomena depend on tip leakage and even more on the guidance of main and splitter blade tip leakage vortices. A mid-loaded shroud blade loading distribution offers the best tradeoff between both. Superior efficiency of such a loading configuration has been verified both numerically and experimentally. The loading distribution is suggested to have a minor impact on compressor efficiency at low relative tip clearance ratios, however, at large relative clearance an efficiency difference of up to 2 %

occurs between the different loading distributions.

Keywords: Centrifugal compressors, Low Reynolds numbers, Large relative clearance ratios, CFD, Experimental investigation, 1D-Compressor-Model, Centrifugal compressor design, Refrigeration application, R134a

Résumé

Les compresseurs frigorifiques à échelle réduite montés sur paliers à gaz ont été identifiés comme une technologie clé dans les applications de pompes à chaleur domestiques, dans le but d’améliorer à la fois l’efficacité du système ainsi que la fiabilité. Cependant, les machines de taille réduite ont le désavantage du subir des pertes aérodynamiques plus importantes en comparaison aux machines industrielles de grande échelle, qui sont engendrées par leur taille réduite et les tolérances de fabrication. En raison de leur petite taille, le nombre de Reynolds de la machine est faible, ce qui engendre des pertes par frottement plus importantes. Les tolérances de fabrication ainsi que les tolérances de forme et de positionnement pour l’assemblage requirent de plus grands jeux relatifs pour les machines à échelle réduite en comparaison aux machines de grande échelle, ce qui entraine des pertes plus importantes par débit de fuite.

La conception de compresseurs centrifuges et la prédiction de leurs performances dépend fortement de lois empiriques et de corrélations qui sont déduites expérimentalement et numériquement des donnés de tests effectués sur des machines de grande échelle. Par conséquent, la question se pose sur l’applicabilité de ces lois empiriques et corrélations sur les compresseurs d’échelle réduite.

Cette thèse de doctorat présente les résultats de l’étude de l’impact d’un débit à faible nombre de Reynolds, du jeu d’extrémité relatif sur les performances du compresseur et sur les modèles écoulements. Les investigations sont réalisées de manières expérimentales et numériques (CFD et modèle de compresseur unidimensionnel) sur deux designs de compresseurs centrifuges à échelle réduite. Un équipement de test expérimental d’un compresseur frigorifique a été fabriqué et des essais en termes d’impact de la modification du jeu d’extrémité ainsi que l’amélioration des performances par design de la roue ont été réalisés. De grands ratios du jeu d’extrémité allant jusqu’ à 20 % ont été investigués.

Les corrélations empiriques tenant compte de l’impact d’une mise à l’échelle géométrique ainsi que la modification du jeu d’extrémité ont été validées et améliorées. Ces corrélations ont été testées et validées à des conditions de charge nominale, partielle et de surcharge.

Les suggestions sur comment concevoir un compresseur centrifuge en respectant d’importants ratios du jeu d’extrémité ont été identifiés. La distribution sur les contours du moyeu et du carter ainsi que l’angle des aubes côté carter ont été identifiés comme paramètres principaux pour minimiser les effets négatifs de la présence d’importants ratios du jeu d’extrémité. Par ailleurs, il a été démontré que l’optimisation du compresseur en termes de phénomènes induits par le jeu d’extrémité dépend de celui-ci et d’autant plus que de l’orientation des vortex générés par le débit de fuite des aubes principales et secondaires. Une répartition de la charge au milieu des aubes côté carter offre le meilleur compromis entre les deux. Une efficacité plus importante a été vérifiée numériquement et expérimentalement pour une telle configuration de distribution de la charge. Il est suggéré que la distribution de la charge ait un impact mineur sur l'efficacité du compresseur pour de faibles ratios du jeu d'extrémité. Cependant, avec un grand jeu d'extrémité une différence d'efficacité allant jusqu'à 2 % se produit entre les différents cas de distributions de la charge.

Mots clés : Compresseur centrifuge, Nombre de Reynolds faible, Grands ratios du jeu d'extrémité, CFD, Investigations expérimentales, Modèle unidimensionnel de compresseur, Conception de compresseurs centrifuges, Applications frigorifiques, R134a

Kurzfassung

Gasgelagerte Kältemittelverdichter von kleiner Abmessung wurden bedingt durch einen positiven Einfluss auf den Systemwirkungsgrad sowie auf die Systemzuverlässigkeit als Schlüsseltechnologie für heimische Wärmepumpenanwendungen identifiziert. Verglichen zu größeren Maschinen, sind Maschinen von kleiner Abmessung erhöhten aerodynamischen Verlusten ausgesetzt, was durch die Bauteilgröße sowie Fertigungstoleranzen begünstigt wird. Durch die geringe Bauteilgröße resultiert eine kleine Reynoldszahl, was erhöhte Reibungsverluste zur Folge hat. Fertigungs- sowie Form- und Lagetoleranzen erfordern einen vergrößerten relativen Gehäusespalt verglichen zu größeren Maschinen, sodass ein erhöhter Spaltverlust auftritt.

Die Auslegung und Nachrechnung von Radialverdichtern basiert sehr stark auf Erfahrungswerten, welche experimentell sowie numerisch von Radialverdichtern mit großer Abmessung gewonnen wurden. Es stellt sich deshalb die Frage, ob diese erfahrungsbasierten Auslegungsstrategien und Verlustkorrelationen für Radialverdichter von kleiner Abmessung anwendbar sind.

Ergebnisse über den Einfluss von kleinen Reynoldszahlen sowie von großen Radialspalten auf das Leistungsverhalten und die Strömung von Verdichtern werden in dieser Doktorarbeit präsentiert. Hierfür werden zwei verschiedene Radialverdichter von kleiner Abmessung experimentell sowie numerisch (CFD und 1D-Verdichtermodell) untersucht. Es wurde ein Prüfstand für einen hoch skalierten Kältemittelverdichter entwickelt und Tests bezüglich Variation der Spalthöhe sowie Verbesserung der Verdichterleistung durch eine entsprechende Laufradgestaltung durchgeführt. Hierbei wurden relative Gehäusespalte von bis zu 20 % untersucht.

Empirische Korrelationen, welche den Bauteilgrößeneinfluss sowie Änderungen der Spalthöhe berücksichtigen, werden validiert und wenn nötig verbessert. Die Validierung der Korrelationen wird sowohl am Auslegungspunkt als auch bei Teil -und Überlast durchgeführt.

Auslegungsvorschläge für Radialverdichter mit großen Spalthöhen werden vorgeschlagen. Dabei wurden die Wandkonturen von Nabe und Gehäuse sowie die gehäuseseitige Schaufelwinkelverteilung als Auslegungsmöglichkeiten identifiziert, um die negativen Aspekte von vergrößerten Gehäusespalten abzuschwächen. Des Weiteren wurde gezeigt, dass Auslegungsoptimierungen bezüglich Spaltleckage von der Spaltleckage an sich und viel mehr von der richtigen Führung von Haupt- und Zwischenschaufelspaltwirbeln abhängen. Eine gehäuseseitige Schaufelbelastungsverteilung, bei welcher der maximale Schaufelbelastungspunkt in der Mitte liegt, bietet einen Kompromiss zwischen beidem. Ein erhöhter Wirkungsgrad wurde für solch eine Schaufelbelastungsverteilung sowohl numerisch als auch experimentell nachgewiesen. Es wurde gezeigt, dass die Schaufelbelastungsverteilung bei kleinen relativen Gehäusespalten einen geringen Einfluss auf den Wirkungsgrad aufweist, diese jedoch bei großen Spaltweiten in einem Wirkungsgradunterschied von bis zu 2 % resultiert.

Stichwörter: Radialverdichter, Kleine Reynoldszahlen, Große relative Spaltweiten, CFD, Experimentelle Untersuchung, 1D-Verdichter-Modell, Auslegung von Radialverdichtern, Kältetechnikanwendung, R134a

Contents

Acknowledgements **v**

Abstract (English/Français/Deutsch) **vii**

Contents **xvi**

List of figures **xxiv**

List of tables **xxv**

List of Symbols **xxxi**

Introduction **1**

1 Introduction **1**

1.1 Compressor performance deterioration due to reduced feature size 2

1.1.1 Underlying phenomena in relative large tip gaps 2

1.1.2 Low Reynolds number centrifugal compressors 7

1.1.3 Diabatic compressor operation 11

1.2 Problem Statement 13

1.3 Objectives 14

1.4 Used Methodologies 14

1.5 Structure of the thesis 15

2 Methods **17**

2.1 Aero-thermal working principle of a centrifugal compressor stage 17

2.2 Dimensionless performance values in centrifugal compressor theory 20

2.3 Investigated compressor geometries 23

2.3.1 Compressor by Schiffmann 23

2.3.2 Compressor by Javed et al. 23

2.3.3 Scaled up version of compressor by Javed et al. (scaling factor 4.6) 24

2.4 Experimental procedure 24

2.4.1 Experimental approach by Schiffmann 25

2.4.2 Experimental compressor setup for testing the scaled up compressor by Javed et al. 25
2.5 One-dimensional centrifugal compressor model 31
2.5.1 Impeller modeling 32
2.5.2 Model of vaneless diffuser 33
2.5.3 Volute/scroll model 33
2.5.4 Performance map prediction 34
2.5.5 Validation of one-dimensional model 34
2.6 Computational Fluid Dynamics 36
2.6.1 Creating the computational grid 38
2.6.2 Boundary conditions and solver setup 39
2.6.3 Mesh sensitivity study and comparison of two turbulence models 41
2.6.4 Validation of the numerical setup 44

3 Scaling analysis of a centrifugal compressor **53**
3.1 Impact of low Reynolds numbers on compressor performance 53
3.1.1 Geometrical scaling of the reduced-scale centrifugal compressor by Schiffmann 53
3.1.2 Verification of scaling approach 54
3.1.3 Performance alteration caused by Reynolds number effect 55
3.1.4 Assessment of empirical correlations used for scaling 56
3.1.5 Quality of used modeling approach 61
3.1.6 The role of transition 63
3.2 Reynolds number independence of tip leakage loss 66
3.3 Plausibility check of one-dimensional centrifugal compressor model (see section 2.5) 68
3.4 Down-scaling a compressor under consideration of tip clearance alteration . . 69
3.5 Summary and implications for this thesis 75

4 Impact of tip clearance alteration on the compressor performance **77**
4.1 Performance deterioration due to alteration of tip clearance 77
4.1.1 Numerical results (CFD) of compressor by Schiffmann 78
4.1.2 Experimental results of compressor by Schiffmann 83
4.1.3 Numerical results of the up-scaled compressor by Javed et al. 84
4.1.4 Experimental results of scaled up compressor by Javed et al. 89
4.2 Assessment of empirical tip clearance loss correlations 92
4.3 Tip clearance sensitivity parameter 95
4.3.1 Sensitivity of compressor by changing its tip gap 95
4.3.2 Scaling tip clearance sensitivity 98
4.4 Interaction of tip leakage with blade loading and diffusion 101
4.5 Prediction of performance and leakage by reduced-order models 113
4.5.1 Tip clearance sensitivity by one-dimensional model (section 2.5) 113
4.5.2 Preliminary estimation of tip leakage mass flow 116

4.6 Chapter summary and implications . . . 117

5 End wall and blade loading investigation 119

5.1 Modifications of impeller geometry . . . 119

5.1.1 New end-wall distribution . . . 119

5.1.2 Different loading distributions . . . 120

5.1.3 Common impeller blade design . . . 122

5.2 Effect of changing the blade loading and end-wall distribution on compressor performance . . . 123

5.2.1 Impact on compressor performance (numerical and experimental approach) . . . 123

5.2.2 Impact on tip leakage, trajectory of tip leakage vortices and blade secondary flows . . . 129

5.2.3 Tip clearance sensitivity parameter . . . 141

5.3 Summary and design implications . . . 143

6 Conclusion and further steps 147

6.1 Summary and Conclusion . . . 147

6.2 Recommendations about empirical correlations . . . 150

6.3 Design implications for compressors operating at relative clearance ratios exceeding 5 % . . . 151

6.4 Further steps . . . 152

A Appendix A 155

A.1 Geometrical details about investigated centrifugal compressor geometries . . . 155

A.1.1 Centrifugal compressor by Schiffmann . . . 155

A.1.2 Centrifugal compressor by Javed et al. . . . 156

A.2 Details about experimental setup . . . 158

A.2.1 Compressor unit, drive and magnetic coupling . . . 158

A.2.2 Refrigeration loop . . . 158

A.2.3 Used measurement devices . . . 161

A.3 One-dimensional compressor model . . . 163

A.4 Computational grid . . . 167

A.5 Experimental data of up-scaled compressor by Javed et al. . . . 169

B Appendix B 171

B.1 Solver setup for scaling analysis . . . 171

B.2 Modified friction model for turbomachinery provided by Casey and Robinson . 173

B.3 Shift of flow coefficient due to scaling . . . 173

C Appendix C 175

C.1 Solver setup for tip gap analysis . . . 175

C.2 Experimental data of tip gap study . . . 176

C.3 Performance and error analysis of tip gap study . . . 178

D Appendix D **183**
D.1 Different loading distributions 183
D.2 Solver setup for loading study 184
D.3 Experimental data of loading study 186
D.4 Performance and error analyis of loading study 187
D.5 Isentropic Mach number distribution on blade surfaces 192

Bibliography **204**

Curriculum Vitae **205**

List of Figures

1.1 Schematic illustration of underlying tip leakage mechanism. 3

1.2 Trajectory of tip leakage vortex through compressor blade passage for the compressor by Javed et al.. In addition, cross section planes illustrating entropy distribution are shown. 4

1.3 Comparison between a shrouded impeller and an unshrouded/open impeller. 6

1.4 Reynolds number - friction factor -diagram based on the adapted friction model for turbomachinery provided by Casey and Robinson. 8

1.5 Impact of the 'Reynolds number effect' on the performance of three geometrically similar scaled compressors. 9

1.6 Graphical meaning of the method by Casey and Robinson; Separation of losses into a Reynolds number independent part *A* and a Reynolds number dependent part *B*. 11

1.7 Cold and hot compression of a fluid illustrated in a h-s-diagram. 11

1.8 Idealized thermodynamic comparison process of a diabatic compression. . . . 12

2.1 Cutting slice of a centrifugal compressor with control stations for calculation. . 18

2.2 Schematic velocity triangle at impeller trailing edge; Definition of flow angles α and β in meridional direction. 19

2.3 Left: Pressure ratio and efficiency as function of the mass flow rate for different speed lines. right: Head coefficient, work input coefficient and efficiency as a function of a flow coefficient for one speed line. 20

2.4 Impeller of the investigated compressor by Schiffmann. 23

2.5 Comparison of original-size impeller by Javed et al. and 4.6-times scaled up impeller. 24

2.6 Photo of the test setup by Schiffmann. 25

2.7 Photo of the test-rig consisting of compressor unit (left) and refrigeration loop (right). 26

2.8 Schematic flow chart (PID) of the test setup. 27

2.9 Magnetic coupling to connect the driving spindle with the compressor shaft. . 27

2.10 Distribution of static wall pressure measurement positions on the collector housing. 28

2.11 Isentropic total-static efficiency at outlet of vaneless diffuser as a function of time. 30

2.12 Impeller having a relative clearance ratio of 5 % after touching the collector housing. 30
2.13 Comparison of non-dimensional performance values between experimental data by Schiffmann and the one obtained from the one-dimensional model. . . 35
2.14 Deviation between 1D data and experimental data compared to the measurement error. 37
2.15 Meridional cutting view of simulated compressor components. 38
2.16 Three-dimensional view of the modeled compressor by Schiffmann. 39
2.17 Grid convergence for the total-total pressure ratio (a) and the total-total polytropic efficiency (b) as a function of grid point number 42
2.18 Comparison of the stage characteristics between SST turbulence model, SA turbulence model and experimental data. 43
2.19 Comparison of stage characteristics between CFD setup and experimental data set for the compressor by Schiffmann. 46
2.20 Relative deviation between CFD setup and experimental data as well as measurement errors. 47
2.21 Comparison between numerically determined work input coefficient and experimental one for the compressor by Javed et al.. 48
2.22 Comparison between numerical isentropic total-static head coefficient (a) and isentropic total-static efficiency (b) and experimental data at a location of 105 % times the impeller diameter in the vaneless diffuser. 49
2.23 Comparison between CFD setup and experimental data set near the outlet of the vaneless diffuser for the scaled up compressor by Javed et al.. 50

3.1 Reynolds number-friction factor-diagram: 55
3.2 Total-total polytropic head coefficient (a) and work input coefficient (b) as a function of the total-static pressure ratio for the four scaling cases. 56
3.3 Total-total polytropic head coefficient (a) and work input coefficient (b) as a function global flow coefficient at design speed for the four scaling cases. 57
3.4 Total polytropic efficiency as a function of the global flow coefficient at design speed for the four scaling cases. 58
3.5 Prediction quality of various correlations to account for Reynolds number effect for a scaling factor of 0.75 (a), 2 (b) and 4 (c). 60
3.6 Total-total polytropic efficiency and tip leakage loss as a function of the Darcy-Weissbach friction coefficient after Casey and Robinson and Dietmann and Casey plotted for a relative tip clearance of 5 %. 62
3.7 Total-total polytropic efficiency as a function of the Darcy-Weissbach friction coefficient plotted for operating points having the same total-static pressure ratio near surge (a) and operating points having the same total-static pressure ratio near choke (b). 63

3.8 (a) Evolution of the Reynolds number (see Eq. 3.6) along the mid span of the blade for test cases A to D. (b) More detailed view of (a) for compressors A and B, indicating the critical Reynolds number for end of transition according to Schlichting. 65
3.9 Reynolds number independent (a) and dependent losses (b) for five different clearance ratios as a function of the global flow coefficient. 67
3.10 Efficiency drop due to tip leakage (a) and remaining Reynolds number and relative clearance ratio independent loss (b) as a function of the global flow coefficient. 67
3.11 Total-total polytropic efficiency over the global flow coefficient obtained by the one-dimensional model. 68
3.12 Reynolds number independent (a) and depended losses (b) as a function of the global flow coefficient according to the method suggested by Casey and Robinson, using data from the one-dimensional model. 69
3.13 Total-total polytropic head coefficient (a), work input coeffcient (b) and total-total polytropic efficiency (c) as a function of the global flow coefficient, showing baseline compressor and down-scaled geometries with various relative clearance ratios. (CFD results) 70
3.14 Ratio between leakage mass flow rate and overall compressor mass flow rate (a) and tip flow coefficient (b) over the global flow coefficient for down-scaled compressors with different relative clearance ratios. (CFD results) 71
3.15 Mass flux distribution (a), normalized tip jet density (b) and relative Mach number of tip jet (c) along the main blade suction side of tip gap, showing the design example. (CFD results) 72
3.16 Diffusion ratio (a), total-static pressure ratio (b) and blade loading (c) along the 95 % blade span, showing the design example. 74

4.1 Numerically obtained total-total polytropic head coefficient (a), work input coefficient (b) and total-total polytropic efficiency (c) from impeller inlet to vaneless diffuser outlet for various clearance ratios of the compressor unit provided by Schiffmann. Tip clearance is adjusted by impellers having different blade height. 79
4.2 Numerically determined efficiency loss due to kinetic energy of the tip jet (a), tip flow coefficient (b) and normalized slip velocity (c) as a function of the global flow coefficient, showing various relative clearance ratios of the compressor unit by Schiffmann. 80
4.3 Distribution of relative Mach number at impeller trailing edge for various relative clearance ratios (compressor unit by Schiffmann). 82
4.4 Normalized entropy distribution at impeller trailing edge for various relative clearance ratios (compressor unit by Schiffmann). 83
4.5 Experimental tip gap investigation for Schiffmann compressor using shimming plates. Total-total polytropic efficiency of the compressor as a function of the global flow coefficient. Experimental results are provided by Schiffmann. 84

4.6 Numerically obtained stage characteristics for various relative tip gap ratios as a function of the global flow coefficient for the scaled up compressor by Javed et al.. 85
4.7 Distribution of relative Mach number at impeller trailing edge of scaled up compressor by Javed et al., having different relative clearance ratios. 86
4.8 Normalized entropy distribution at 105 % times the impeller diameter for the scaled up compressor by Javed et al.. 87
4.9 Normalized entropy distribution at 110 % times the impeller diameter for the scaled up compressor by Javed et al.. 88
4.10 Normalized entropy distribution at 125 % times the impeller diameter for the scaled up compressor by Javed et al.. 89
4.11 Comparison between experimental and numerical dimensionless compressor performance values for various relative tip gap ratios at impeller trailing edge (scaled up compressor by Javed et al.). 90
4.12 Comparison between experimental and numerical total-static isentropic head (a) and efficiency (b) for various relative tip gap ratios at outlet of the vaneless diffuser (compressor by Javed et al.). 91
4.13 Numerical (CFD) drop in compressor efficiency due to alteration of relative clearance ratio compared to commonly-used empirical correlations (compressor by Schiffmann). 93
4.14 Experimental drop in compressor efficiency due to alteration of relative clearance ratio compared to commonly-used empirical correlations (compressor by Schiffmann). 93
4.15 Numerical (CFD) drop in compressor efficiency due to alteration of relative clearance ratio compared to commonly-used empirical correlations (compressor by Javed et al.). 94
4.16 Experimental drop in compressor efficiency due to alteration of relative clearance ratio compared to commonly-used empirical correlations (compressor by Javed et al.). 95
4.17 Linear fitting of numerical efficiency drop caused by relative clearance alteration for the compressor unit provided by Schiffmann at different operating points. . 97
4.18 Problem of using a linear fit at high mass flow rates (ϕ_{t1}=0.05) for the compressor by Javed et al.. 98
4.19 Experimentally and numerically obtained tip clearance sensitivity parameter over the global flow coefficient for compressor provided by Schiffmann. 99
4.20 Experimentally and numerically obtained tip clearance sensitivity parameter over the global flow coefficient for compressor provided by Javed et al.. 100
4.21 Evaluation of tip clearance sensitivity parameter for geometrical compressor scaling of the unit by Schiffmann. (a) Non-corrected results; (b) Corrected results considering Reynolds number effect. 100
4.22 Leakage mass flow rate ratio as a function of the global flow coefficient for Schiffmann compressor (a) and the scaled up compressor unit provided by Javed et al. (b). 101

4.23 Aerothermal properties along the suction side of main and splitter blade tip gap as a function of the meridional tip gap length, showing the compressor unit provided by Schiffmann for various clearance ratios at their peak efficiency point. 103

4.24 Aerothermal properties along the suction side of main and splitter blade tip gap as a function of the meridional tip gap length, showing the compressor unit provided by Javed et al. for various clearance ratios at their peak efficiency point. 105

4.25 Total-static pressure ratio along the normalized meridional length at a blade span of 90 % for various clearances at their peak efficiency point (Schiffmann). 106

4.26 Total-static pressure ratio along the normalized meridional length at a blade span of 90 % for various clearances at their peak efficiency point (Javed et al.). . 106

4.27 Blade loading as a function of the normalized meridional length at 90 % blade span for various relative clearance ratios at their peak efficiency point (Schiffmann). 107

4.28 Blade loading as a function of the normalized meridional length at 90 % blade span for various relative clearance ratios at their peak efficiency point (Javed et al.). 108

4.29 Trajectories of main (red streamlines) and splitter blade (blue streamlines) tip leakage vortices for the scaled up compressor by Javed et al., having a relative clearance ratio of 3 %. 109

4.30 Trajectories of main (red streamlines) and splitter blade (blue streamlines) tip leakage vortices for the scaled up compressor by Javed et al., having a relative clearance ratio of 5 %. 110

4.31 Trajectories of main (red streamlines) and splitter blade (blue streamlines) tip leakage vortices for the scaled up compressor by Javed et al., having a relative clearance ratio of 10 %. 110

4.32 Trajectories of main (red streamlines) and splitter blade (blue streamlines) tip leakage vortices for the scaled up compressor by Javed et al., having a relative clearance ratio of 14.73 %. 111

4.33 Trajectories of main (red streamlines) and splitter blade (blue streamlines) tip leakage vortices for the scaled up compressor by Javed et al., having a relative clearance ratio of 20 %. 112

4.34 Stage characteristic for various relative tip gap ratios obtained by the one-dimensional model (compressor by Schiffmann). 114

4.35 Tip clearance sensitivity parameter as a function of the global flow coefficient. Comparison between data set of CFD and one-dimensional model. 115

4.36 Comparison between predicted tip leakage ratio by a reduced-order model provided by Aungier and CFD data. 116

5.1 Comparison between the hub and shroud end-walls of the baseline compressor and the modified hub-end-wall shape in a z-r-coordinate system. 120

5.2 Cross section areas of the baseline compressor and the modified hub-end wall shape as a function of the meridional impeller length. 121

5.3 Blade angle distributions of the baseline compressor and the different shroud blade loading distributions as a function of the normalized meridional coordinate. 122

5.4 Numerically (CFD) obtained stage characteristics as a function of the global flow coefficient for differently designed impellers with a relative clearance ratio of 14.73 %. 124

5.5 Total-total pressure ratio as a function of the global flow coefficient for differently designed impellers with a relative clearance ratio of 14.73 % (CFD). 125

5.6 Comparison between numerical and experimental stage characteristics at 105 % times the impeller diameter over the global flow coefficient for various designs (CR=14.73 %). 126

5.7 Comparison between experimental and numerical total-static isentropic head coefficient (a) and total-static isentropic efficiency (b) at outlet of the vaneless diffuser over the global flow coefficient for various designs (CR=14.73 %). 127

5.8 Numerically defined flow characteristics as a function of the global flow coefficient. Tip flow coefficient (a), normalized absolute tangential velocity (b) and diffusion ratio (c) over the global flow coefficient. 128

5.9 Relative Mach number distribution at impeller trailing edge for differently designed impeller geometries with a relative clearance ratio of 14.73 %. 130

5.10 Numerically obtained ratio between tip leakage mass flow rate and total compressor mass flow rate as a function of the global flow coefficient for the four different designs. 131

5.11 Tip mass flux, normalized density of tip jet as well as relative tip jet Mach number as a function of the normalized meridional coordinate for the four different designs. 133

5.12 Blade loading parameter along the 90 % blade span for differently designed impellers. 134

5.13 Trajectories of main (red streamlines) and splitter blade (blue streamlines) tip leakage vortices for the scaled up compressor by Javed et al. at its design point. 135

5.14 Trajectories of main (red streamlines) and splitter blade (blue streamlines) tip leakage vortices for the aft-loaded compressor at its design point. 136

5.15 Trajectories of main (red streamlines) and splitter blade (blue streamlines) tip leakage vortices for the mid-loaded compressor at its design point. 137

5.16 Trajectories of main (red streamlines) and splitter blade (blue streamlines) tip leakage vortices for the front-loaded compressor at its design point. 137

5.17 Difference between isentropic Mach number at hub and shroud for the different impeller designs as a function of the normalized meridional coordinate. 139

5.18 Tip clearance sensitivity parameter over global flow coefficient for impellers with different shroud loading distributions and the baseline geometry by Javed et al.. 141

5.19 Total-total polytropic efficiency over the relative clearance ratio for different loading distributions obtained from Eq. 4.3 and CFD. 142

A.1 End wall distribution (a) and blade angle distribution (b) at hub and shroud of compressor unit by Schiffmann. 156

A.2 End wall distribution (a) and blade angle distribution (b) at hub and shroud of original size compressor by Javed et al.. 157

A.3 Cut of the compressor shaft used in the experimental setup. 159

A.4 Assembly drawing of the whole compressor unit. 160

A.5 Iterative solution scheme of the impeller used in the one-dimensional model. . 163

A.6 Iterative solution scheme at impeller trailing edge. 164

A.7 Solution scheme of the partial differential equations in the vaneless diffuser. . . 165

A.8 Iterative solution scheme of the volute used in the one-dimensional model. . . 166

A.9 Computational grid (H-I-topology) around the main blade leading edge of the impeller by Schiffmann. 167

A.10 Computational grid (H-I-topology) around the splitter blade leading edge of the impeller by Schiffmann. 168

A.11 Computational grid (H-I-topology) around the trailing edge of the impeller by Schiffmann. 168

C.1 Comparison of experimentally and numerically determined work input coefficient for scaled up compressor by Javed et al. with CR = 5%. 178

C.2 Comparison of numerically and experimentally determined total-static isentropic head coefficient (a) and efficiency (b) for scaled up compressor by Javed et al. with CR = 5% at 105 % of d_2. 179

C.3 Comparison of numerically and experimentally determined total-static isentropic head coefficient (a) and efficiency (b) for scaled up compressor by Javed et al. with CR = 5% at outlet of vaneless diffuser. 179

C.4 Comparison of experimentally and numerically determined work input coefficient for scaled up compressor by Javed et al. with CR = 10%. 180

C.5 Comparison of numerically and experimentally determined total-static isentropic head coefficient (a) and efficiency (b) for scaled up compressor by Javed et al. with CR = 10% at 105 % of d_2. 180

C.6 Comparison of numerically and experimentally determined total-static isentropic head coefficient (a) and efficiency (b) for scaled up compressor by Javed et al. with CR = 10% at outlet of vaneless diffuser. 181

C.7 Comparison of experimentally and numerically determined work input coefficient for scaled up compressor by Javed et al. with CR = 20%. 181

C.8 Comparison of numerically and experimentally determined total-static isentropic head coefficient (a) and efficiency (b) for scaled up compressor by Javed et al. with CR = 20% at 105 % of d_2. 182

C.9 Comparison of numerically and experimentally determined total-static isentropic head coefficient (a) and efficiency (b) for scaled up compressor by Javed et al. with CR = 20% at outlet of vaneless diffuser. 182

D.1 Aft-loaded shroud configuration at 90 % blade span shown in a conformal plot (viewing direction: from hub). 183
D.2 Mid-loaded shroud configuration at 90 % blade span shown in a conformal plot (viewing direction: from hub). 184
D.3 Front-loaded shroud configuration at 90 % blade span shown in a conformal plot (viewing direction: from hub). 184
D.4 Comparison of experimentally and numerically determined work input coefficient for aft-loaded shroud loading configuration with CR = 14.73%. 187
D.5 Comparison of numerically and experimentally determined total-static isentropic head coefficient (a) and efficiency (b) for aft-loaded shroud loading configuration with CR = 14.73% at 105 % of d_2. 188
D.6 Comparison of numerically and experimentally determined total-static isentropic head coefficient (a) and efficiency (b) for aft-loaded shroud loading configuration with CR = 14.73% at outlet of vaneless diffuser. 188
D.7 Comparison of experimentally and numerically determined work input coefficient for mid-loaded shroud loading configuration with CR = 14.73%. 189
D.8 Comparison of numerically and experimentally determined total-static isentropic head coefficient (a) and efficiency (b) for mid-loaded shroud loading configuration with CR = 14.73% at 105 % of d_2. 189
D.9 Comparison of numerically and experimentally determined total-static isentropic head coefficient (a) and efficiency (b) for mid-loaded shroud loading configuration with CR = 14.73% at outlet of vaneless diffuser. 190
D.10 Comparison of experimentally and numerically determined work input coefficient for front-loaded shroud loading configuration with CR = 14.73%. 190
D.11 Comparison of numerically and experimentally determined total-static isentropic head coefficient (a) and efficiency (b) for front-loaded shroud loading configuration with CR = 14.73% at 105 % of d_2. 191
D.12 Comparison of numerically and experimentally determined total-static isentropic head coefficient (a) and efficiency (b) for front-loaded shroud loading configuration with CR = 14.73% at outlet of vaneless diffuser. 191
D.13 Isentropic Mach number distribution on the blade surfaces for the scaled up compressor by Javed et al. at its design point. 192
D.14 Isentropic Mach number distribution on the blade surfaces for the aft-loaded shroud loading configuration at its design point. 193
D.15 Isentropic Mach number distribution on the blade surfaces for the mid-loaded shroud loading configuration at its design point. 194
D.16 Isentropic Mach number distribution on the blade surfaces for the front-loaded shroud loading configuration at its design point. 195

List of Tables

2.1 Specifications of computational grids used for the mesh sensitivity study. . . . 42

3.1 Scaling factor and resulting motor speeds of the scaled compressor geometries. 54
3.2 Standard deviations of reduced-order models relative to numerical model. . . . 61
3.3 Reynolds numbers for various test cases evaluated according the pipe flow analogy model (see Lüdtke). 64

A.1 Main dimensions of compressor unit provided by Schiffmann. 155
A.2 Main dimensions of original size compressor by Javed et al.. 156
A.3 Time averaged experimental data for up-scaled compressor by Javed et al. having a relative clearance ratio of 14.73 % 169

B.1 Solver setup for scaling analysis of Schiffmanns compressor. 172

C.1 Solver setup for tip gap analysis of the up-scaled compressor provided by Javed et al.. 176
C.2 Time averaged experimental data for up-scaled compressor by Javed et al. having a relative clearance ratio of 5 %. 177
C.3 Time averaged experimental data for up-scaled compressor by Javed et al. having a relative clearance ratio of 10 %. 177
C.4 Time averaged experimental data for up-scaled compressor by Javed et al. having a relative clearance ratio of 20 %. 178

D.1 Solver setup for the shroud blade loading investigation applied for the aft-, the mid- and the front-loaded configuration. 185
D.2 Time averaged experimental data for the up-scaled compressor having an aft-loaded shroud loading distribution. 186
D.3 Time averaged experimental data for the up-scaled compressor having a mid-loaded shroud loading distribution. 186
D.4 Time averaged experimental data for the up-scaled compressor having a front-loaded shroud loading distribution. 187

Nomenclature

Greek Symbols

α	Absolute flow angle with respect to meridional direction [°]
β	Relative flow angle with respect to meridional direction [°]
Δ	Difference
δ	Boundary layer thickness $[m]$
ϵ	Turbulent dissipation rate (see Eq. 2.25) $[\frac{m^2}{s^3}]$
η	Efficiency [-]
λ	Work input coefficient [-]
μ	Dynamic viscosity $[Pas]$
μ_t	Turbulent dynamic viscosity $[Pas]$
ν	Kinematic viscosity $[\frac{m^2}{s}]$
ω	Angular velocity $[\frac{rad}{s}]$
ϕ	Flow coefficient [-]
ϕ_{t1}	Global flow coefficient [-]
Π	Pressure ratio [-]
ψ	Head coefficient [-]
ρ	Density $[\frac{kg}{m^3}]$
σ	Slip factor [-]
τ	Sheer stress $[\frac{N}{m^2}]$
ξ	Angle of tip leakage jet (Eq. 1.5) [°]
ξ	Specific loss $[\frac{kJ}{kgK}]$

Nomenclature

Roman Symbols

$\dot{m}$	Mass flow rate $[\frac{kg}{s}]$
$\dot{Q}$	Heat flux $[W]$
A	Area $[m^2]$
A	Reynolds number independent losses [-]
a	Parameter (Eq. 1.1) [-]
a	Reynolds number independent losses in Eq. 1.9 [-]
a	Speed of sound $[\frac{m}{s}]$
B	Reynolds number dependent losses [-]
b	Blade height $[m]$
BL	Blade loading parameter [-]
c	Absolute velocity $[\frac{m}{s}]$
c_μ	Constant of standard k-ϵ-turbulence-model [-]
c_τ	Friction velocity (see Eq. 2.21) $[\frac{m}{s}]$
C_D	Discharge coefficient (Eq. 1.2) [-]
c_f	Fanning friction factor [-]
C_{ref}	Slope of flow coefficient shift in Eq. 1.12 [-]
cp	Pressure recovery coefficient [-]
CR	Relative clearance ratio at trailing edge t_2/b_2 [-]
d	Diameter $[m]$
DR	Diffusion ratio [-]
e	Specific energy $[\frac{kJ}{kg}]$
F	Force $[N]$
f	Darcy-Weissbach friction factor [-]
h	Specific enthalpy $[\frac{kJ}{kg}]$
j	Power loss $[\frac{kJ}{kg}]$
k	Blockage factor [-]

k	Constant for vaneless diffuser friction (see Eq. 2.17) [-]
k	Turbulent kinetic energy (see Eq. 2.24) $[\frac{m^2}{s^2}]$
l	Length $[m]$
L_{hyd}	Hydraulic/characteristic length $[m]$
M	Meridional coordinate $[m]$
m	Exponent (see Eq. 1.8) [-]
m_{Cl}	Tip clearance sensitivity parameter [-]
Ma	Mach number [-]
Ma_{u2}	Rotational Mach number [-]
n	Exponent (see Eq. 1.9) [-]
n	Rotor speed $[\frac{1}{s}]$
P	Power $[W]$
p	Coefficient for friction model (see Eq. B.3) [-]
p	Pressure $[Pa]$
q	Specific heat flux $[\frac{kJ}{kg}]$
R	Rothalpy $[\frac{kJ}{kg}]$
r	Radius $[m]$
Re	Reynolds number [-]
S	Standard deviation
s	Specific entropy $[\frac{kJ}{kgK}]$
T	Temperature $[K]$
t	Exponent for friction model (see Eq. B.4) [-]
t	Time (see Fig. 2.11) $[s]$
t	Tip clearance $[m]$
u	Rotational velocity $[\frac{m}{s}]$
w	Relative velocity $[\frac{m}{s}]$
y	Distance of first near wall cell (see Eq. 2.21) $[m]$

y	Polytropic work $[\frac{kJ}{kg}]$
y^+	Dimensionless distance of first near wall cell (see Eq. 2.21) [-]

Superscripts

$\bar{\ }$	Variation (see Eq. 2.24)
$\vec{\ }$	Vector
’	Relative thermodynamic properties

Subscripts

∞	Ideal conditions
0	0mm-Clearance case or compressor inlet
1	Impeller leading edge
2	Impeller trailing edge
3	Outlet of vaneless diffuser
4	Volute outlet
Bl	Blade
Cl	Tip clearance
cr	Critical/infinite conditions in Eq. 1.9
dia	Diabatic operation
exp	Expansion
h	Hub
in	Inlet domain
is	Isentropic
kin	Kinetic
lam	Laminar
m	Meridional/radial direction
Max	Maximum
n	Direction normal to a surface
out	Outlet domain

pol	Polytropic change in state
PS	Blade pressure side
ref	Reference/datum case
s	Shroud
Sp	Volute/Spiral
SS	Blade suction side
t	Total
TE	Impeller trailing edge
th	Impeller throat
turb	Turbulent
u	Tangential velocity component
VLD	Vaneless diffuser
Vol	Volute/Scroll

Other Symbols

∂	Partial differential operator
d	Ordinary differential operator
BEP	Best efficiency point
CFD	Computational fluid dynamics
Exp.	Experiment
ICAAMC	International Compressed Air and Allied Machinery Committee
PID	Piping and instrumentation diagram
RANS	Reynolds averaged Navier-Stokes equations

1 Introduction

The worldwide climate change as a result of the continuous increase of global warming gases like CO_2 is one of the main issues of the 21^{st} century (refer to Kooten [1], Herzberg et al. [2] and Ritter and Mann [3]). The use of renewable energy sources is a possibility to mitigate the progression of climate change (refer to Edenhofer et al. [4] and Turner [5]). Nonetheless, various challenges in terms of distribution and storage of renewable energies compared to a classical way of energy conversion are present (refer to Denholm et al. [6], Beaudin et al. [7] and Aneke and Wang [8]). For instance, the large power density of fossil energy sources used in the last decades yielded mainly a centralized energy conversion provided by large power plants. These large centralized units are operated in a continuous way, thus providing a base level of the energy consumption (refer to Hancher et al. [9]). Most of the renewable energy sources do not allow such operational mode due to their fluctuations (refer to Connolly et al. [10] and Bull [11]). From this point of view, decentralized energy conversion might be a good choice to integrate the use of renewable energies. Decentralized energy conversion, however, requires less power thus leading to machines having small geometrical dimensions.

Thermal turbomachinery plays a major role in converting energy, since these machines offer a continuous aerodynamic operation working principle and a superior efficiency compared to positive displacement compression/expansion machines. A dynamic machine compresses/expands a working fluid from a starting pressure to an end pressure thus the same head is relatively transferred/extracted to/from the fluid independently of the machine size. The geometric feature size, however, decreases, hence leading to increased rotor speeds. Recent improvements in gas bearing and active magnetic bearing technologies, however, allow handling high rotor speeds, thus reduced-scale turbomachinery becomes realizable.

For instance, Schiffmann [12, 13, 14, 15] has operated a domestic heat pump using a reduced-scale centrifugal compressor and achieved a higher system performance compared to classical compressor technologies such as reciprocating, scroll or screw compressors. A centrifugal compressor with an impeller diameter of 20 mm was used in this application, which had a design speed of 180 000 rpm. The rotor was supported on gas lubricated bearings, offering oil-free and thus maintance-free operation. Further examples of reduced-scale turbomachinery are micro-gasturbines as reported in Sirakov [16], an ORC-driven heat pump by Demierre et al. [17], Mounier and Schiffmann [18] and Mounier [19] and a reduced-scale fan for fuel cell applications by Wagner [20] and Wagner et al. [21]. These examples demonstrate that ultra-compact and high-spinning turbomachinery is a key product in decentralized energy conversion.

Besides the high rotor speeds, manufacturing tolerances and required surface quality are other challenging factors of reduced-scale turbomachinery. Already small geometrical variations due to manufacturing tolerances have a large impact on the machine performance. From an aerodynamic point of view, the small feature size leads to low Reynolds numbers, resulting in increased relative surface friction. As a consequence, reduced-scale turbomachinery achieves lower efficiencies compared to geometrically similar machines at larger scale.

1.1 Compressor performance deterioration due to reduced feature size

Down-scaling a centrifugal compressor leads to a deterioration of compressor performance caused by the reduced feature size as well as manufacturing and assembly issues. Schiffmann [12, 13, 14, 15] and Sirakov [16] have summarized the issues related to reduced-feature size compressors as follows:

1. Increased relative tip clearance ratios to avoid touchdown between the impeller and the shroud decrease compressor performance. In addition, Sirakov [16] has observed a modified flow structure in the tip gap occurring at minimized feature sizes, which is similar to a Couette type of flow. This indicates a strong interaction of the tip leakage with the shroud end-wall and creates additional losses.

2. Higher frictional losses due to lower Reynolds numbers and higher relative surface roughness deteriorate the compressor performance at reduced scale.

3. Due to the increased surface-to-volume ratio of a reduced-scale compressor, the compressor becomes more sensitive for heat addition. As a consequence, the compressor flow cannot be treated as adiabatic anymore, what is usually done in larger scale compressors.

The following subsections give a summary of the mentioned issues related to down-scaling a compressor. The physics behind as well as the state of the art modeling techniques are presented.

1.1.1 Underlying phenomena in relative large tip gaps

Tip leakage is a phenomenon in turbomachinery which occurs for unshrouded/open impellers in the tip gap between impeller blades and the shroud. It is a secondary flow which deteriorates the main flow and thus the compressor performance. Literature considers tip leakage jet as a result of the pressure difference between pressure and suction side of a blade. Depending on the blade geometry, the tip jet separates at the blade tip forming a vena-contracta and is accelerated. The tip jet enters the suction side of the blade and mixes with the main flow building a vortical structure. The mixing of the main flow and the re-entering of this tip jet causes an entropy increase and is thus considered as an internal loss. The mechanism is schematically illustrated in Fig. 1.1 as suggested by Schabowski and Hodson [22].

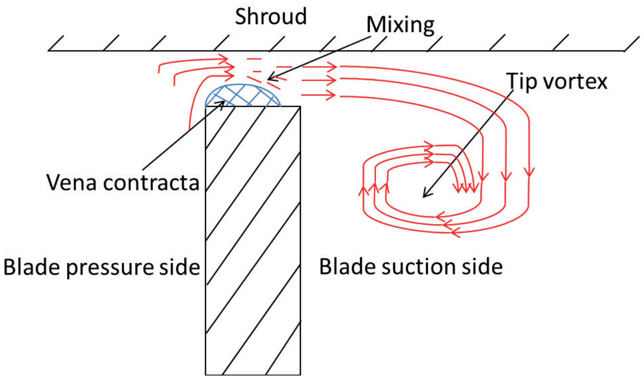

Figure 1.1: Schematic illustration of underlying tip leakage mechanism.

The flow in an impeller blade with tip clearance can be compared to the vortex system of an air plane wing leading to induced drag. Due to different velocity gradients in the boundary layers around the blade pressure and suction side, there is an unequal distribution of circulation around the blade. Since there is a no-slip condition on velocity on any contour on the casing over the tip gap, no circulation occurs on the casing contour, thus a vortex line cannot end in the casing contour. However, a finite vortex line cannot exist according to Helmholtz' first vortex law [23, 24], thus it needs to end in infinite or has to be part of a closed vortex system. A free vortex therefore builds in the tip gap and trails downstream the compressor blade. This free vortex causes an induced drag due to its downward velocity. The downward velocity of the free vortex decreases when it is trailing downstream, thus the shear layer has a tendency to roll up downstream in a vortical structure what is schematically illustrated in Fig. 1.1.

As a consequence, a tip vortex rolls up along the blade tip behind the leading edge of the impeller main blade. This vortex grows in size along the compressor blade in the inducer and propagates downstream the blade channel. According to Kang and Hirsch [25, 26], the trajectory of this tip leakage vortex is governed by Coriolis and centrifugal forces as well as the strength of the tip leakage jet at the trailing edge of the impeller. As soon Coriolis and centrifugal forces become more pronounced (radial part of the impeller), pressure gradients between the blade pressure and the suction side of the adjacent blade as well as between hub and shroud are generated. The tip leakage vortex is pressed by these pressure gradients against the suction side of the blades. In addition to boundary layer blockage, the tip vortex creates additional flow blockage. Hence, less diffusion and less pressure rise is achieved. The tip vortex is considered to be a phenomenon, which is induced by tip leakage.

In addition, the streamlines of main and splitter blade tip leakage vortices intersect cross section planes of the blade passage at a position, where most of the compressor losses are located. Fig. 1.2 shows the trajectories of main (red) and splitter blade (blue) tip leakage vortex as well as the entropy distribution of two different cross sections in the impeller blade passage for the compressor provided by Javed et al. [27] at its design point, indicating that tip leakage vortices intersect the zones of high entropy distribution and corroborates the amount of entropy in this zone. Hence, the homogeneity of the exhaust flow pattern as well as the compressor efficiency depends on the position of these vortex cores.

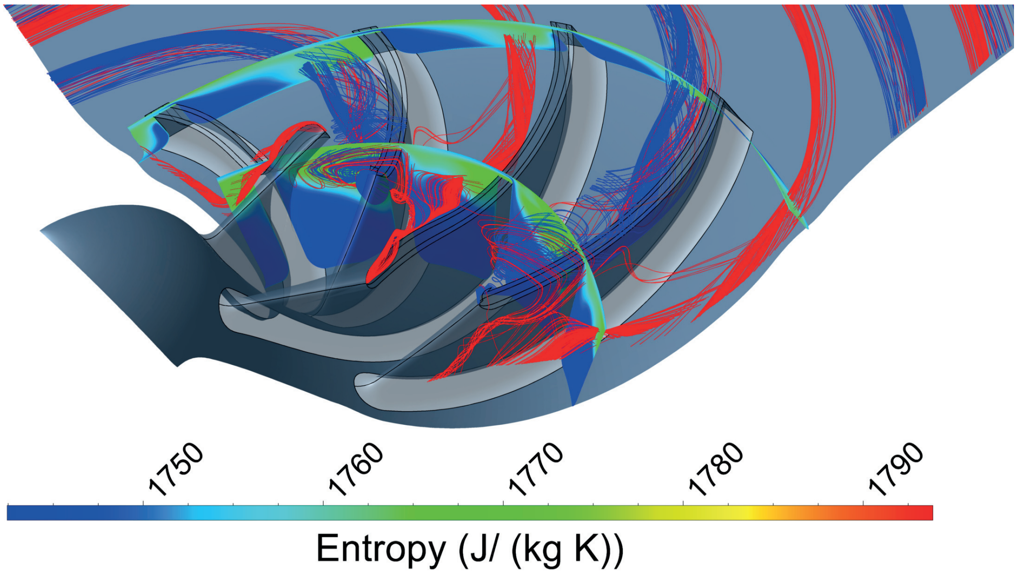

Figure 1.2: Trajectory of tip leakage vortex through compressor blade passage for the compressor by Javed et al. [27]. In addition, cross section planes illustrating entropy distribution are shown.

According to Chen et al. [28], modeling techniques of tip clearance flow are categorized into three categories:

1. Tip leakage phenomenon is modeled as a jet driven by the pressure difference between pressure and suction side of the blade. It is assumed that the whole kinetic energy of the tip jet is lost due to mixing.
2. The second approach uses the lifting line analysis and the effect of the induced drag of the trailing vortex system is considered. The method needs, however, empirical correlations which strongly depend on the specific problem.
3. A direct modeling of the tip leakage and its impact on the main flow is achieved by solving Reynolds-averaged Navier Stokes equations on a discrete domain (CFD).

Besides the physical approaches to model tip leakage, empirical correlations exist, which predict the drop in efficiency due to a change in clearance ratio. Pfleiderer and Petermann [29] as well as Eckert and Schnell [30] suggest a linear correlation to model the drop in efficiency depending on the tip gap width t (see Eq. 1.1). Further correlations are the one of Pampreen [31] and Schmidt-Theuner and Mattern [32].

$$\frac{\Delta\eta_{pol,tt}}{\eta_{pol,tt,0}} = -\frac{2at}{(b_1 + b_2)} \tag{1.1}$$

Brasz [33] suggested, that the sensitivity of the compressor caused by alteration of its clearance ratio is more pronounced at low clearance ratios. The compressor becomes less sensitive to a change in clearance ratio at higher relative clearance ratios. This disagrees with the mentioned linear modeling approaches and the question arises how the compressor reacts when operated at large relative clearance ratios.

A more physical insight into tip leakage phenomenon is given by one-dimensional models. Senoo and Ishida [34, 35] suggest to consider tip leakage as a mechanism driven by the pressure difference of blade pressure and suction side. Its velocity is derived from an incompressible Bernoulli approach, where a discharge coefficient C_D is considered (see Eq. 1.2):

$$w_{Cl,n} = C_D\sqrt{\left(\frac{2\Delta p}{\rho}\right)} \tag{1.2}$$

The incremental tip leakage mass flow rate along the blade is given by Eq. 1.3:

$$d\dot{m}_{Cl} = \rho t w_{Cl,n} dl \tag{1.3}$$

Two different assumptions about mixing of the tip jet with the main flow have been suggested. The first one assumes a partial mixing, where the whole kinetic energy of the tip jet normal to the blade is lost. This assumption is supported by Senoo and Ishida [34, 35]. In this case, the entropy generation of the main flow is expressed by Eq. 1.4.

$$\dot{m}T ds = \frac{1}{2}\dot{m}_{Cl} w_{Cl,n}^2 \tag{1.4}$$

The second approach assumes a complete mixing of the tip jet with the main flow (see Storer and Cumpsty [36]). According to Denton [37], the entropy generation of the main flow in this case is expressed by Eq. 1.5, where ξ represents the flow angle of the tip jet with respect to the mainstream.

$$\dot{m}T ds = \frac{1}{2}\dot{m}_{Cl} w_{Cl,n}^2 sin^2(\xi) + \frac{1}{2}\dot{m}_{Cl}\left(w_{Cl,n} - w_{Cl,n} cos(\xi)\right)^2 \tag{1.5}$$

Aknouche [38], however, shows numerically that the first assumption is more appropriate in centrifugal compressors, since the tip jet is not completely mixed out with the main flow. A low reduced static pressure region at the shroud suction side of the blade is growing from leading to trailing edge. This indicates a partial mixing of the tip jet with the main flow, which supports the theory of Senoo and Ishida [34, 35].

Sirakov [16] has identified a flow structure of the tip leakage flow in the clearance of reduced-scale compressors which is similar to a Couette-type of flow. This suggests an interaction of the tip leakage jet with the shroud end-wall. Besides the acceleration of the tip jet through the pressure difference of the blade, tip jet gets further accelerated by the shroud end-wall. Following Eq. 1.4, tip leakage loss depends on the tip jet velocity thus higher losses are expected in case the shroud end-wall effect plays a role.

In order to avoid tip leakage flows from pressure to suction side of the blade, the impeller needs to be shrouded. Nonetheless, a leakage mass flow occurs between the impeller outlet and impeller inlet, thus a rotary seal has to be used. Shrouding the impeller is normally done for low flow coefficient compressors, thus the impeller becomes inducerless. As a consequence, the impeller is shorter and the cover can be milled together with the blades. In addition, mechanical stress determines if an impeller can be designed shrouded. Furthermore, shrouded impellers are mainly used when sufficiently small tip clearance cannot be ensured, i.e. due to thermal elongation in multi-stage compressors. Fig. 1.3 provides a comparison of a shrouded and an unshrouded/open impeller.

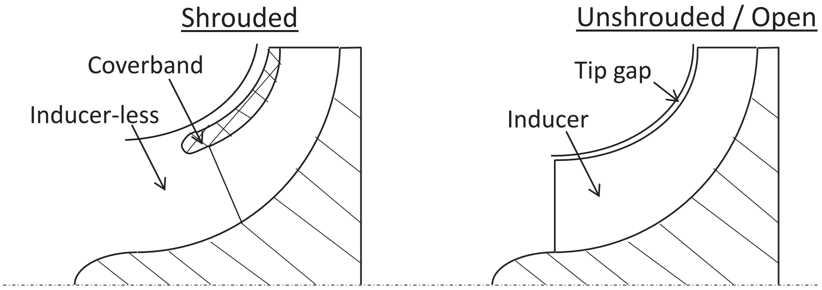

Figure 1.3: Comparison between a shrouded impeller and an unshrouded/open impeller.

Even though tip leakage is avoided due to the coverband, literature indicates that an unshrouded impeller shows superior performance compared to a similar shrouded one. Harada [39] has performed experimental tests of shrouded and unshrouded impellers. In this case the shrouded impeller was realized by welding a coverband on the unshrouded impeller after testing it. The results suggest, that the shrouded impeller showed an inferior performance at part-load and rotating stall was occurring earlier as at the unshrouded configuration, suggesting less stability. A possible explanation for this behavior is given by Dalbert et al. [40]. They performed a CFD simulation of a shrouded and an unshrouded impeller with the same blading. The shrouded impeller showed a zone of low relative velocity near the shroud suction side corner, whereas in the unshrouded impeller the low momentum fluid is pushed to the

center of the blade passage by tip leakage. The shroud suction side is the critical position in the impeller in terms of stability. According to jet-wake theory suggested by Dean and Senoo [41], low momentum fluid is pressed to shroud suction side corner of the blade caused by Coriolis and centrifugal forces as well as secondary flows in the boundary layers. In case the adverse pressure gradient along the impeller blade is too large, the flow separates at the shroud suction side thus the compressor gets unstable. In case of an unshrouded impeller, tip jet works against the accumulation of low momentum fluid at shroud suction side corner thus instability onset is shifted towards lower mass flow rates. The theory of Dalbert et al. [40] got experimentally corroborated by Hamkins and Flack [42], who made similar observations. Furthermore, Offtinger [43] has figured out that welding the shroud on an unshrouded impeller has always negative effects on the inducer flow, since the shroud cover shows more pronounced losses. Hence, it is not recommended to use a shrouded inducer-type impeller.
As suggested by literature, shrouding an impeller does not have beneficial effects on the compressor performance and stability. On the other hand, Sirakov [16] claims, that shrouding an impeller improves performance when large relative tip gaps as in reduced-scale turbomachinery are present.

1.1.2 Low Reynolds number centrifugal compressors

The friction factor increases with a decrease in Reynolds number. This effect is illustrated in a Reynolds number-friction factor-diagram, which has been provided by Moody [44], actually elaborated for pipes, since impeller channel behave similar, although no fully developed flow profile is found. As a consequence, higher frictional losses occur in smaller machines leading to a deterioration of efficiency.
Compressor literature is not coherent about the definition of a global Reynolds number, since it is depending on the analogy model of boundary layers, namely the pipe flow or flat plate theory. Some authors model friction in turbomachinery according the pipe flow theory [45, 46, 47]. Others model frictional effects according the flat plate theory [48, 49, 50, 51]. Since boundary layers along a compressor blade are not merged as in a pipe, the flat plate analogy model seems more suitable.
Following the definition of Reynolds number suggested by Dietmann and Casey [50, 51] in Eq. 1.6,

$$Re = \frac{w_1 L_{hyd} \rho_{t1}}{\mu_{t,1}} = \frac{w_1 L_{hyd}}{\nu_{t,1}} \tag{1.6}$$

a smaller compressor has a lower Reynolds number compared to a geometrically similar scaled up version. At the same time, the relative surface roughness increases by minimizing the feature size. Both lower Reynolds number and higher relative surface roughness yield higher frictional losses. In order to illustrate this effect, a Reynolds number-friction factor-diagram based on the friction model of Casey and Robinson [49] is provided in Fig. 1.4.

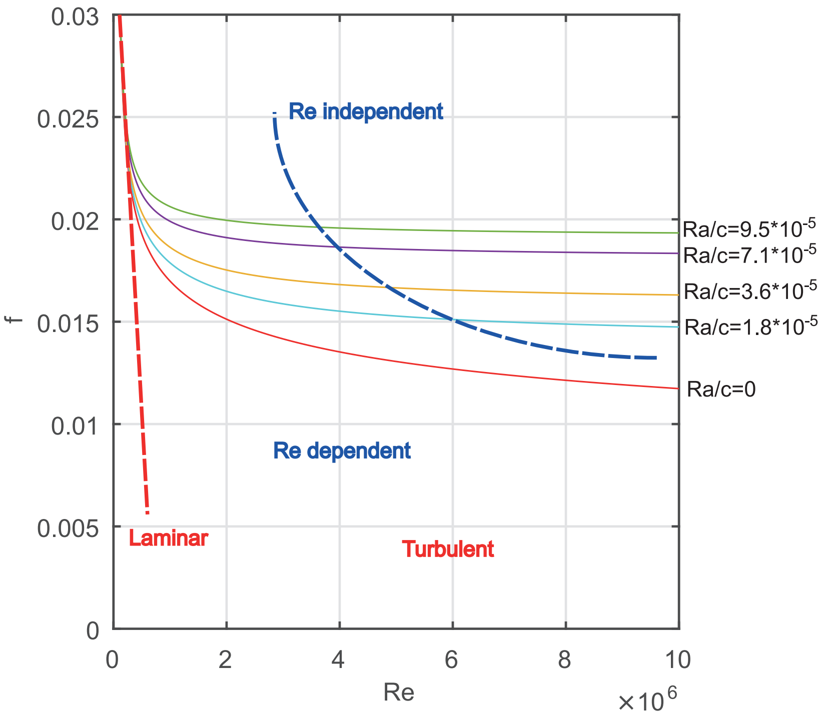

Figure 1.4: Reynolds number - friction factor -diagram based on the adapted friction model for turbomachinery provided by Casey and Robinson [49].

Down-scaling a compressor under consideration of similarity in rotational Mach number and global flow coefficient, deteriorates the performance of the compressor having the smaller feature size. At the same time, an operating point is shifted towards lower mass flow rates due to a higher relative boundary layer blockage. This so-called 'Reynolds-number effect' is schematically illustrated in Fig. 1.5. Three different geometrically similar scaled compressors are shown, which provide the same head. Due to the Reynolds number effect, best efficiency points are deteriorated and shifted towards lower mass flow rates by decreasing compressors feature size.

The impact of compressor scaling on its performance is a field, which already has a long history. One of the first correlations to predict the change in efficiency by scaling was suggested by Moody [52, 44]. He correlated the change in efficiency to the change of the impeller Reynolds number defined by the impeller tip diameter d_2. In case of same inlet thermodynamic properties, the change in efficiency is merely correlated to the change of impeller diameter. Moody's equation is presented in Eq. 1.7:

$$\frac{1-\eta}{1-\eta_{ref}} = \left(\frac{d_{ref}}{d}\right)^{0.25} \tag{1.7}$$

Pfleiderer and Petermann [29] were the first authors who correlated the change in efficiency to alteration of the Reynolds number. They suggested Eq. 1.8 to model the change in efficiency

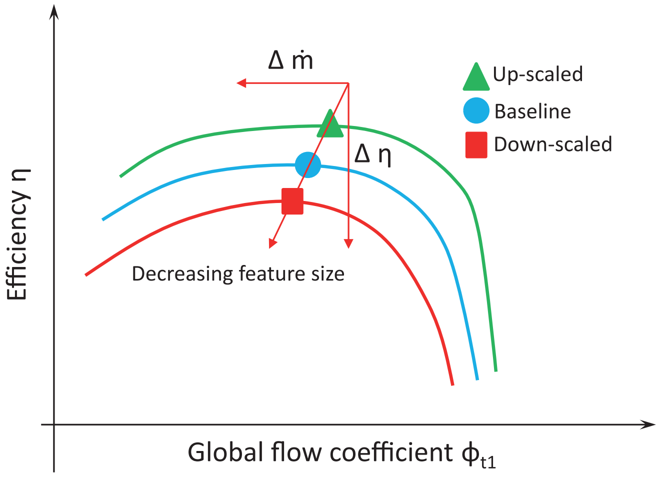

Figure 1.5: Impact of the ’Reynolds number effect’ on the performance of three geometrically similar scaled compressors.

by compressor scaling. The exponent m is an empirical one, which strongly depends on the machine type and is unknown in advance. In most of the cases, the exponent m is set to 0.25 as suggested in Eq. 1.7

$$\frac{1-\eta}{1-\eta_{ref}} = \left(\frac{Re_{ref,d2}}{Re_{d2}}\right)^m \tag{1.8}$$

Ackeret and Medici [53] were the first authors, who divided the efficiency drop in a Reynolds number dependent and a Reynolds number independent part. It is assumed that one part of the compressor losses is independent of the Reynolds number (e.g. incidence losses, recirculation losses, losses due to tip clearance, etc.) and the other part directly scales with the Reynolds number. The correlation (see Eq. 1.9) is still applied in compressor design and testing, but has some drawbacks. The variable a and the exponent n strongly depend on the machine type. Empirical knowledge is required by applying this correlation for scaling compressors.

$$\frac{1-\eta}{1-\eta_{ref}} = (1-a) + a\left(\frac{Re_{ref,d2}}{Re_{d2}}\right)^n \tag{1.9}$$

In addition, Wright [54] figured out, that the exponents m and n strongly depend on the surface roughness of the machine. Based on Wright’s findings, Strub et al. [55] published a Reynols number correction approach. It allows to correct test data from the actual case to a reference case thus used for comparing different inlet conditions or geometrical feature sizes. This correction procedure is also proposed by ICAAMC and commonly used in compressor industry. The Reynolds number in Eq. 1.10 is defined by assuming $2b_2$ (the tip blade span) as characteristic length and $\frac{u_2}{2}$ as characteristic velocity. A pipe friction model is used as analogous model to evaluate the friction factors. The pipe friction factors are defined according to the Colebrook-White formula.

$$\frac{1-\eta}{1-\eta_{ref}} = \frac{0.3+0.7\frac{c_f}{c_{f,cr}}}{0.3+0.7\frac{c_{f,ref}}{c_{f,ref,cr}}} \tag{1.10}$$

A different approach, which does not require prior knowledge about the magnitude of empirical variables, is suggested by Casey and Robinson [49]. Their equation correlates the change in efficiency, but no reference efficiency case is required as for the previous correlations. Furthermore, the flat plate theory is used as analogy model to evaluate friction factors using Gülichs [48] equations. Their approach was improved by Dietmann and Casey [50, 51] by calibrating their correlation with a large set of test data. Furthermore, a correlation to model the shift in global flow coefficient due to Reynolds number effect is suggested. The drop in efficiency and the shift of the flow coefficient due to relative boundary layer blockage is modeled by Eq. 1.11 and Eq. 1.12 ,respectively.

$$\Delta\eta_{pol} = -B_{ref}\frac{\Delta f}{f_{ref}} \qquad B_{ref} = 0.05+\frac{0.002}{\phi_{t1}+0.0025} \tag{1.11}$$

$$\frac{\Delta\phi_{t1}}{\phi_{t1}} = -C_{ref}\frac{\Delta f}{f_{ref}} \qquad C_{ref} = 0.05+\frac{0.000025}{\left(\phi_{t1}+0.018\right)^{2.45}} \tag{1.12}$$

Since the method of Casey and Robinson [49] is used in chapter 3, its origin and graphical understanding is briefly described.

Method of Casey and Robinson

Based on a loss analysis of Traupel [56], the compressor losses can be written as shown in Eq. 1.13:

$$1-\eta_{pol} = \frac{\int T ds}{\Delta h_t} = \frac{j_a}{\Delta h_t} + \frac{j_b}{\Delta h_t} = A + B \tag{1.13}$$

Hence, the compressor losses are separated in a Reynolds number independent part A and a Reynolds number dependent part B. The method is represented graphically by drawing the polytropic efficiency of differently geometrically similar scaled compressors as a function of the friction coefficient. All operating points showing same rotational Mach number and head are connected by a linear relationship (see Eq. 1.11 and Fig. 1.6). The slope of the curve represents the term $\frac{B_{ref}}{f_{ref}}$. The y-intercept is the case were no friction occurs what corresponds to the Reynolds number independent losses A.

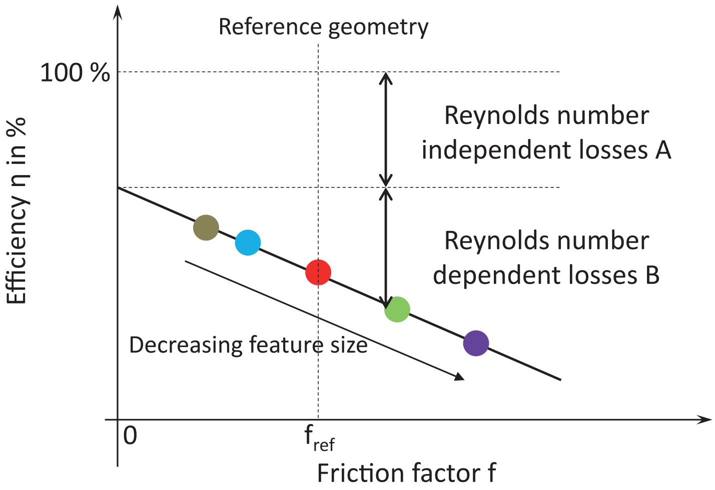
Reference geometry
100 %
Efficiency η in %
Reynolds number independent losses A
Reynolds number dependent losses B
Decreasing feature size
0
f_ref
Friction factor f

Figure 1.6: Graphical meaning of the method by Casey and Robinson [49]; Separation of losses into a Reynolds number independent part *A* and a Reynolds number dependent part *B*.

1.1.3 Diabatic compressor operation

The surface-to-volume ratio is increasing with a decrease of machine size. As a consequence, a smaller compressor is more sensitive to heat addition, since more surface area is available to transfer heat into a fluid volume. Additional heat in the compressor increases the required input power. This yields a reduction of the compressor efficiency as suggested by Eq. 2.4. Fig. 1.7 shows a h-s-diagram illustrating compression process with the same compressor at a similar pressure ratio. The blue solid line shows a compression at low temperatures whereas the red dashed line shows a compression at higher temperatures. Since isobars diverge with an increase of temperature in a h-s-diagram, more input power is required to obtain the same pressure ratio of the fluid at a higher temperature.

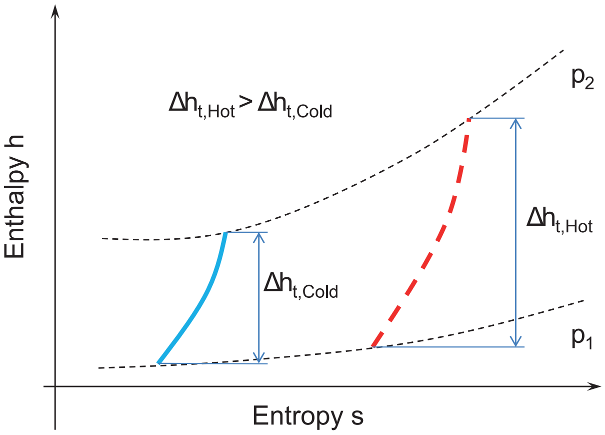
$\Delta h_{t,Hot} > \Delta h_{t,Cold}$
p_2
Enthalpy h
$\Delta h_{t,Hot}$
$\Delta h_{t,Cold}$
p_1
Entropy s

Figure 1.7: Cold and hot compression of a fluid illustrated in a h-s-diagram.

This effect is observed by comparing the measured efficiency of a turbocharger with the adiabatic efficiency. If the compressor is heated, the efficiency is lower than the adiabatic one and vice versa (see Sowayan [57]). Gong et al. [58] figured out, that reduced-scale compressors show a more sensitive behavior in heat addition than a similar up-scaled one due to the high surface-to-volume ratio. They mentioned, that depending on the configuration an efficiency drop of up to 20 % is expected compared to the adiabatic case.

According to Shaaban and Seume [59], heat addition in the compression process is considered to be conveyed/removed isobarically before and after the impeller. This idealised thermodynamic comparison process is schematically shown in Fig. 1.8. In this case, heat is added isobarically before and isobarically removed after the impeller. The compression process itself is considered as an isentropic process.

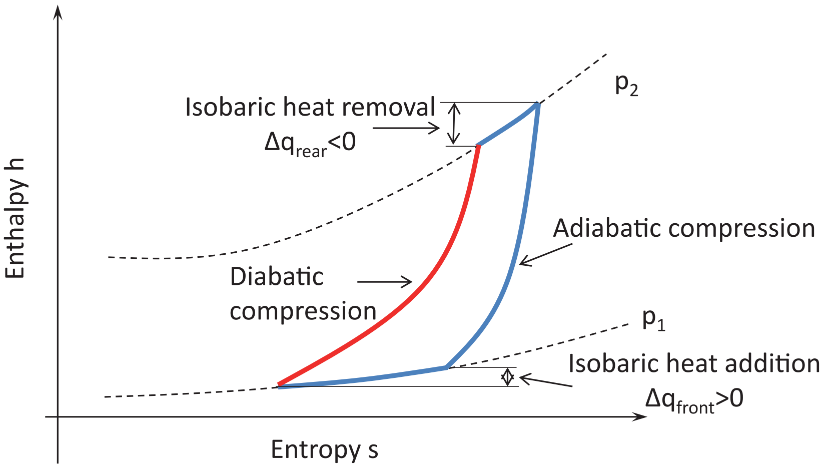

Figure 1.8: Idealized thermodynamic comparison process of a diabatic compression.

The isentropic definition of head coefficient and efficiency, respectively, is not suitable to account for diabatic conditions during the compression process. Casey and Fesich [60] and Sirakov and Casey [61] suggest to use the polytropic efficiency definition. In addition, they provide a procedure to evaluate the adiabatic efficiency from the measured diabatic one, which is based on the assumption that heat addition does not affect the pressure rise in the impeller. The adiabatic polytropic efficiency is derived from the measured one (including heat transfer) by Eq. 1.14:

$$\eta_{pol} = \frac{1}{\frac{1}{\eta_{pol,dia}} - \frac{q_{12}}{y_{12}}} \tag{1.14}$$

The work input coefficient including heat transfer consists of the work input coefficient without heat transfer and normalized added heat (see Eq. 1.15):

$$\lambda_{dia} - \lambda = \frac{q_{12}}{u_2^2} \tag{1.15}$$

Combining Eq. 1.14 and Eq. 1.15, the adiabatic polytropic efficiency is derived in Eq. 1.16.

$$\eta_{pol} = \frac{1}{\frac{1}{\eta_{pol,dia}} - \frac{\lambda_{dia}-\lambda}{\psi_{pol}}} \tag{1.16}$$

The increase in work input coefficient due to heat is related to the global flow coefficient leading to Eq. 1.17:

$$\lambda_{dia} - \lambda = \frac{q_{12}}{u_2^2} = \frac{\dot{Q}}{\rho_{t1}\phi_{t1}u_2^3 d_2^2} = \frac{\dot{Q}}{\rho_{t1}\phi_{t1}Ma_{u2}^3 a_{t1}^3 d_2^2} \approx \frac{k}{\phi_{t1}Ma_{u2}^3} \tag{1.17}$$

Eq. 1.17 shows that the increase in work input coefficient is proprotional to a constant k, $1/\phi_{t1}$ and $1/Ma_{u2}^3$. As a consequence, the compressor efficiency is more affected by heat at low mass flow rates and low rotational speeds. Furthermore, increase in work input coefficient is more pronounced for smaller compressors, since the denominator of Eq. 1.17 contains the impeller diameter d_2.

Yamagata et al. [62] conducted a CHT-analysis of a high-temperature turbocharger impeller. The computational results were experimentally validated using a radiation thermometer. The authors figured out, that most of the heat is added in the clearance between the impeller back face and the housing due to windage effects at the trailing edge of the impeller. This is also confirmed by numerical investigations conducted by Bohn et al. [63] and supports the thermodynamic comparison model shown in Fig. 1.8.

Ma and Xi [64] have numerically investigated three similar but differently scaled impellers. They concluded that the smallest version having the lowest Reynolds number is most affected by heat transfer. In contrast to the approach of Casey and Sirakov [61] and Casey and Fesich[60], the results suggest that internal loss mechanisms are additionally affected by heat transfer. Larger boundary layers were observed in the diabatic cases compared to the adiabatic cases in addition to a higher entropy generation.

1.2 Problem Statement

The centrifugal compressors, which are subject of this thesis, are used in domestic scale heat pump systems and operate with an input power of a few kilowatts. Hence, the compressor becomes very compact and high rotational speeds are needed to achieve the required pressure ratio. For instance, the compressor by Schiffmann [12, 13, 14, 15] has an impeller diameter of 20 mm and spins with 180 000 rpm at its design speed. An even smaller compressor system is the one designed by Javed et al. [27]. The compressor has an impeller diameter of around 15 mm and is spinning with 227 000 rpm at its design speed. Both compressors are considered to be reduced-scale.

The performance drop of reduced-scale machines is related primarily to manufacturing issues. For instance, the relative surface roughness increases with reducing scale and more friction losses occur. In addition, small geometrical deviations due to manufacturing have a large impact on the compressor performance. As a consequence, the relative shroud tip gap between the impeller and the volute housing to allow free spinning of the rotor is large compared to larger machines, what leads to a decrease of compressor performance.

Furthermore, the increased surface-to-volume ratio of the small compressor makes the machine more sensitive to heat addition, which results in an increased input power. As a consequence, the efficiency decreases during operation in case heat is added to the compressor.

Reduced-order models to capture these scaling effects exist. Nonetheless, these models are mostly validated for larger-scale machines. Hence, the question arises whether the prediction quality of these models is satisfactory for reduced-scale machines.

In addition, commonly-used design strategies for centrifugal compressors are strongly empirical. These guidelines are mostly derived from larger-scale machines, thus it is not guaranteed whether they are applicable for design of reduced-scale machines. Further, since most of the large scale machines operate at small relative tip clearances (CR < 5 %), it is unclear what effect larger relative clearances have on the compressor performance, and whether there are means to mitigate these losses by an appropriate blade design.

1.3 Objectives

Limited experience about performance prediction and design of small-scale compressor systems running on relative large clearance ratios exist. This has motivated the author to investigate the behavior of reduced-scale centrifugal compressors and to answer the following research questions:

1. What is the impact of reducing the scale on the compressor performance and what are the dominating loss mechanisms?
2. Are reduced-order models, which are available in the literature well adapted to predict performance of reduced-scale compressors?
3. Is there a best design strategy to mitigate tip leakage induced phenomena for reduced-scale compressors? Is an adaption of commonly used empirical compressor design guidelines required?

1.4 Used Methodologies

In order to answer the research questions, a technical road map for each question is postulated:

1. The impact of reduced feature size on the compressor performance is analyzed by geometrically scaling of a centrifugal compressor. In addition, the tip gap size is varied, in order to investigate the impact of tip leakage on the compressor performance. This

procedure enables the quantification of the impact of low Reynolds numbers and large relative tip clearance ratios on the compressor performance and to identify the main issues related to a reduction of compressor feature size.

2. The validity of empirical models to predict deteriorating effects of low Reynolds number and large relative clearance ratios on the performance of a centrifugal compressor is assessed. Based on experimental and numerical findings, new models for performance prediction are provided.

3. Various compressor designs are investigated to mitigate tip leakage effects. Impellers with different shroud blade angle distributions and a modified end-wall distribution are investigated to assess their effect on tip leakage induced losses. This procedure is performed both numerically and experimentally in view of devising new design guidelines for small-scale centrifugal compressors.

1.5 Structure of the thesis

The methods, which have been used in this thesis, are described in chapter 2. The chapter starts with an introduction into compressor aero- and thermodynamics, followed by a brief description of dimensionless performance values, which are used in this thesis.
Design features of the two investigated compressor geometries are presented, namely the centrifugal compressors by Schiffmann [12, 13, 14, 15] and Javed et al. [27].
The chapter continues with descriptions of the experimental approach by Schiffmann [12, 13, 14, 15] and an own experimental approach for investigation of a scaled-up version of the compressor by Javed et al. [27].
In a next step, a one-dimensional model to predict performance of a centrifugal compressor is described. The model is mainly based on the approach provided by Whitfield and Baines [46]. Nonetheless, slight changes are applied to this model, in order to increase the prediction accuracy.
The CFD approach beginning from computational mesh creation, solver setup and validation with experimental setup is described in chapter 2.

A scaling analysis of Schiffmann's [12, 13, 14, 15] compressor is performed in chapter 3. This analysis shows the impact of Reynolds number variations on the compressor performance. Empirical correlations to predict the expected performance by scaling compressors are investigated.
In addition, the Reynolds number independence of phenomena related to tip leakage is shown in this chapter. A design example, where a baseline compressor is down-scaled with an increase of its relative clearance ratio demonstrates, that increased relative clearance ratio is a major contributor to performance deterioration by scaling a compressor. Design guidelines about how to improve compressor design when dealing with relative large clearance ratios are given.
The chapter ends by performing a plausibility check of the one-dimensional compressor

model in terms of performance prediction for geometrical compressor scaling.

In chapter 4, the behavior of a centrifugal compressor in terms of altering its relative clearance ratio is assessed. In a first step, the performance deteriorating impact of tip leakage on the flow pattern is analyzed. The analysis is performed for both compressors, the one by Schiffmann [12, 13, 14, 15] and the one by Javed et al. [27].
Furthermore, empirical correlations to account for tip leakage losses are assessed. Here, a tip clearance sensitivity parameter is introduced, which allows modeling the compressor sensitivity by altering the relative clearance ratio in the entire compressor operating range.
A more deep insight into the compressor flow by using CFD data allowed identifying the driving mechanisms of tip leakage. The shroud blade loading and the diffusion rate in the impeller are the main drivers of tip leakage. Both parameters are affected by compressor design, namely hub and shroud end-wall shape and shroud blade angle distribution.
The chapter closes by analyzing the plausibility of the one-dimensional compressor model in terms of performance prediction by adapting the relative tip clearance ratio.

The impact of end-wall contours and shroud blade angle distribution on the compressor performance is investigated in chapter 5. Using the compressor of Javed et al. [27] as a reference geometry, the hub end-wall shape and shroud blade angle distribution are modified, in order to study the impact of these design features on compressor performance with special regards to tip leakage induced phenomena. It has been figured out, that a design optimized for tip leakage induced phenomena is a trade-off between tip leakage itself and an optimal guidance of tip leakage vortices as well as secondary flows. Here, a mid-loaded shroud loading configuration offered a superior efficiency compared to an aft- and a front-loaded configuration. The difference in efficiency of the different loading configurations is suggested having a large impact for compressors operating at large relative clearance ratios. At small relative clearance ratios, however, the shroud blade angle distribution suggests having only a minor impact on the compressor performance.

The PhD-thesis finishes with a conclusion and a discussion of further steps.

2 Methods

The methods, which were used for performance investigation of reduced-scale centrifugal compressors, are described in the following chapter. Three different approaches are used and compared, namely experimental and numerical one, such as CFD and a one-dimensional compressor model.

2.1 Aero-thermal working principle of a centrifugal compressor stage

A centrifugal compressor operates along a continuous aerodynamic working principle and processes a compressible flow, thus it is classified as a thermal turbomachine. The working fluid is sucked by the rotating impeller. In order to achieve a static pressure rise in the impeller, the absolute flow is accelerated and the relative flow decelerated. Hence, the flow has a high kinetic energy downstream of the impeller. This kinetic energy is transformed into potential energy (pressure rise) by a diffuser. Depending on the compressors application, the diffuser is vaneless or vaned. A volute or collector is located after the diffuser in a single stage compressor. The flow is collected and homogenized in this component. In case of a multistage compressor, the flow is conveyed to the next stage through a return channel. The return channel is like the diffuser vaned or vaneless. An inlet guide vane system (IGV) is an additional component, which is normally used in front of the first compressor stage. The pre-swirl of the incoming flow changes by changing the angle of the IGV-blades, which has an impact on the work transferred to the fluid as shown in Eq. 2.1. This setup allows to shift operating points to different flow rates.

Fig. 2.1 shows the cut of a single stage centrifugal compressor. The compressor consists of an inlet port, an impeller, a vaneless diffuser and a volute/collector. This compressor setup is used in this thesis. In addition, the stations, where the thermodynamic and aerodynamic properties of the compressor are evaluated, are shown in Fig. 2.1. Station 0 represents the compressor inlet, station 1 the impeller leading edge, station 2 the impeller trailing edge, station 3 the outlet of the diffuser and station 4 the compressor outlet. The numeration of these stations is kept same in the remainder of this thesis.

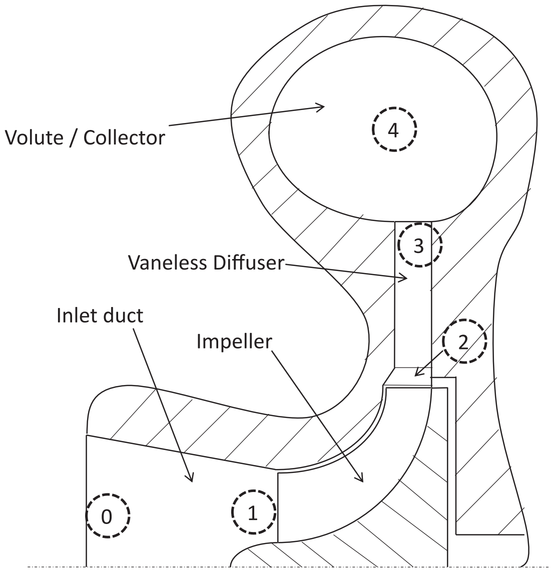

Figure 2.1: Cutting slice of a centrifugal compressor with control stations for calculation.

The basic aerodynamic principle of a centrifugal compressor is illustrated by Euler's equation (see Eq. 2.1). In order to achieve a positive total enthalpy difference of the fluid, the relative flow (w) is decelerated in the impeller. This corresponds to an acceleration of flow in the absolute frame of reference (c). The last term $u_2 - u_1$ in Eq. 2.1 is important in radial turbomachinery, since an enthalpy rise occurs due to a difference in rotational speed between inlet and outlet of the machine. This so called 'centrifugal effect' is loss-free and accounts for about 40 % of the head rise in the impeller (see Casey [65]). As a consequence, a centrifugal compressor achieves higher pressure ratios than an axial machine.

$$\Delta h_{t,12} = \frac{1}{2}\left(\left(w_1^2 - w_2^2\right) + \left(c_2^2 - c_1^2\right) + \left(u_2^2 - u_1^2\right)\right) = c_{u,2}u_2 - c_{u,1}u_1 \tag{2.1}$$

Since the impeller is rotating, relative velocities and relative total thermodynamic properties are observed in the rotating frame of reference. The transformation from an absolute system into a relative system is done by applying a Galilei transformation, which yields the concept of velocity triangles (Eq. 2.2). The absolute and relative velocities can be further split into a tangential and meridional/radial component by applying pythagoras' law. Fig. 2.2 shows a typical velocity triangle of a compressor at the impeller trailing edge. Absolute and relative flow angles are defined from the meridional/radial direction in this thesis, as shown in Fig. 2.2.

$$\vec{c} = \vec{w} + \vec{u} \tag{2.2}$$

In order to compare performance of compressors, which operate at different boundary conditions or have different geometrical scale, the application of non-dimensional performance

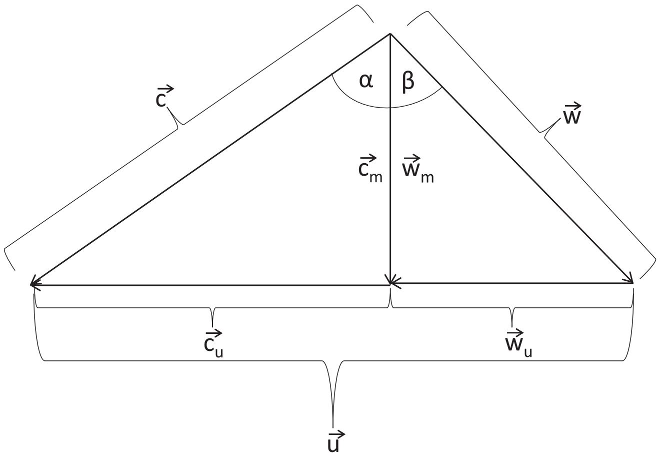

Figure 2.2: Schematic velocity triangle at impeller trailing edge; Definition of flow angles α and β in meridional direction.

values is common practice in compressor aerodynamics. For instance, by normalizing Eq. 2.1 with u_2^2 the blade work input coefficient is obtained. This corresponds to a dimensionless compressor power. By applying trigonometrical relations, the blade work input is calculated by Eq. 2.3 as follows:

$$\lambda_{Bl} = \frac{\Delta h_{t,12}}{u_2^2} = \frac{c_{u,2}}{u_2} - \frac{c_{u,1} u_1}{u_2^2} = \sigma\left(1 + k\phi_2 tan(\beta_{2,Bl})\right) - \frac{c_{u,1} u_1}{u_2^2} \tag{2.3}$$

The blade work input coefficient describes the specific work, which is needed to achieve a required enthalpy rise. It is the main part of the total compressor input power. As can be seen in Eq. 2.3, the blade work input is decreased by the slip velocity and boundary layer blockage, represented by the slip factor σ and a blockage factor k, respectively. Thus additional power is required to obtain the same head rise.

Additional effects, which further increase the required compressor input power, are present. Disk friction in the gap between impeller back face and housing increases the input power. Disk friction also occurs for a shrouded impeller (see subsection 1.1.1) between the impeller cover band and the housing. In addition, strongly loaded compressor wheels show flow recirculation from the diffuser into the impeller at part-load. These recirculation additionally increase the input power of the compressor. Other effects, which have direct impact on the compressor input power, are heat transfer effects, which are further discussed in subsection 1.1.3. Since all of these additional losses increase the required input power but have no net effect on the pressure rise of a compressor, they are called external losses.

On the other hand, internal losses deteriorate the head achieved in the compressor. The main contributor of these internal loss mechanisms is the skin friction loss between fluid and wall, occurring in each component. In addition, flows are present which have another flow direction as the main flow and are called secondary flows. For instance, the blade vortex due to the different curvature of hub and shroud end-walls, the passage vortex generated

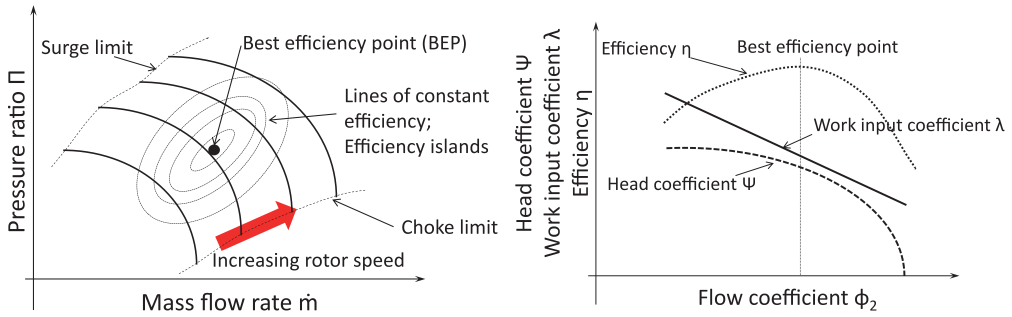

Figure 2.3: Left: Pressure ratio and efficiency as function of the mass flow rate for different speed lines.
right: Head coefficient, work input coefficient and efficiency as a function of a flow coefficient for one speed line.

by the pressure difference between the blade pressure and the suction side of the adjacent blade and tip leakage jet and vortex are representatives for secondary flows. These flows further increase the entropy generation in the main flow, thus compressor performance is deteriorated. The incidence loss at the leading edge of the impeller is another internal loss mechanism. It considers the loss caused by the misalignment between the entering flow and the blade metal angle. Further internal loss mechanisms are present which are described in-depth by Aungier [45] and Whitfield and Baines [46].
In order to correlate these internal loss mechanisms, a thermodynamic baseline process is required for comparison. Depending on the application, an isentropic, a polytropic or an isothermal change in state is defined. A polytropic change in state is often preferred in turbomachinery design, since it shows the true aerodynamic performance, independently of the inlet conditions. By normalizing the work which is transferred to the fluid by this ideal change of state with u_2^2, the head coefficient ψ is obtained.
Compressor performance is commonly presented as pressure ratio as a function of the mass flow rate for different speed lines. Lines of constant efficiency are often plotted in the same map. A dimensionless form of a compressor map is a stage characteristic, which illustrates the work input coefficient λ, head coefficient ψ and efficiency η as a function of a flow coefficient. Fig. 2.3 shows a typical compressor map and a dimensionless characteristic for one speed line.

2.2 Dimensionless performance values in centrifugal compressor theory

In order to compare machines of different size and/or different operating conditions, it is common practice to use dimensionless performance values.
The work input λ and head coefficient ψ are linked to the compressor efficiency by Eq. 2.4.

$$\eta = \frac{\psi}{\lambda} \tag{2.4}$$

The efficiency can be defined as total-total, total-static or static-static, depending on the thermodynamic change of state that are considered at the inlet and exhaust.
The polytropic work included in the polytropic head coefficient ($\psi_{pol,} = \frac{\Delta h_{pol}}{u_2^2}$) is calculated by the approximation method provided by Mallen and Saville [66], such as shown in Eq. 2.5.

$$\Delta h_{pol} = h_{out} - h_{in} - \frac{(s_{out} - s_{in})(T_{out} - T_{in})}{log\left(\frac{T_{out}}{T_{in}}\right)} \tag{2.5}$$

Besides the polytropic change in state, an isentropic change in state is used in this work, in order to compare experimental results with CFD data. The isentropic work is obtained from an isentropic enthalpy difference Δh_{is}, which considers an isentropic and adiabatic compression from compressor inlet to the desired control station.
A dimensionless form of the mass flow rate is the flow coefficient, which is derived from the Strouhal number. The flow coefficient at the trailing edge of the impeller is defined according to Eq. 2.6.

$$\phi_2 = \frac{\dot{m}}{\rho_2 A u_2} = \frac{k c_{m2}}{u_2} \tag{2.6}$$

Since the static values ρ_2 or c_{m2} and k are difficult to measure, it is more convenient to define a global flow coefficient. It correlates the volume flow rate at the inlet to the tip diameter of the compressor wheel (Eq. 2.7).

$$\phi_{t1} = \frac{\dot{m}}{\rho_{t1} A u_2} = \frac{\dot{m}}{\rho_{t1} d_2^2 u_2} \tag{2.7}$$

The rotational Mach number (machine Mach number) is a non-dimensional form of the rotational speed. It represents the ratio between the tangential tip speed u_2 and the total inlet speed of sound (see Eq. 2.8):

$$Ma_{u2} = \frac{u_2}{a_{t1}} \tag{2.8}$$

Another definition of a compressor flow coefficient exist. The global flow coefficient ϕ_{t1} is normalized by a_{t1} instead of u_2, such as presented in Eq. 2.9. This parameter is commonly used as dimensionless mass flow rate in compressor maps and is the product of global flow coefficient ϕ_{t1} and rotational Mach number Ma_{u2}.

$$\phi_{at1} = \frac{\dot{m}}{\rho_{t1} A a_{t1}} = \phi_{t1} Ma_{u2} \tag{2.9}$$

The ratio of inertial forces to viscous forces in the fluid is represented by the Reynolds number (see Eq. 2.10). As discussed in subsection 1.1.2, the definition of a global Reynolds number for a centrifugal compressor is not clearly defined. Some authors use a pipe friction model and others the flat plate theory to model skin friction in a centrifugal compressor.

$$Re = \frac{F_{inertia}}{F_{viscous}} \tag{2.10}$$

As shown in Eq. 2.3, the compressor power is reduced due to slip velocity caused by the relative eddy acting in the impeller. Eq. 2.11 shows the slip factor which is the ratio of actual absolute tangential velocity to tangential velocity considering no slip at trailing edge.

$$\sigma = \frac{c_{u2}}{c_{u2,\infty}} \tag{2.11}$$

Due to Coriolis and centrifugal forces in the radial part of the impeller, the relative flow velocity at the suction side of the blade is higher than on the blade pressure side. As a consequence, a pressure difference occurs between the blade pressure and suction surfaces, which is related to the compressor blade work input. Furthermore, a pressure difference between the blade surfaces also occurs due to curvature, i.e. turning of the blade. The blade loading parameter BL is defined according to Eq. 2.12 as suggested by Lüdtke [47]. The blade loading parameter represents the ratio between the relative velocity difference at blade suction side and pressure side to the mean average of both relative velocities. The parameter is derived from an inviscid case were the relative velocity at suction side is highest. For viscid flows, however, the relative velocity directly on the blade surface is zero due to the no-slip condition. Nonetheless, the relative isentropic Mach number Ma_{is} (see Numeca [67]), which is derived from rothalpy and isentropic enthalpy, allows to calculate a fictive speed on the blade surfaces.

$$BL = \frac{w_{SS} - w_{PS}}{\bar{w}} \qquad \bar{w} = \frac{w_{SS} + w_{PS}}{2} \tag{2.12}$$

Another parameter, which serves as indicator for pressure rise and possible flow separation is the diffusion ratio DR. It corresponds to the ratio of relative inlet velocity w_1 to the relative velocity anywhere in the compressor. According to Eq. 2.13, the relative flow is decelerated ($DR > 1$) and accelerated ($DR \leq 1$).

$$DR = \frac{w_1}{w} \tag{2.13}$$

The relative clearance ratio, which is used in this thesis, is defined as ratio between the absolute tip gap size and the blade height at impeller trailing edge, as suggested by Eq. 2.14:

$$CR = \frac{t_2}{b_2} \tag{2.14}$$

2.3 Investigated compressor geometries

2.3.1 Compressor by Schiffmann

The investigated compressor by Schiffmann [12, 13, 14, 15] is a first stage of a two-stage compressor unit for a refrigeration cycle, operating with R134a. The compressor consists of an inlet section, an impeller, a vaneless diffuser and a volute. At its design speed of 180 000 rpm the compressor achieves a pressure ratio (total-total) of 2.3.

The impeller wheel consists of 18 blades (9 main blades / 9 splitter blades) and has a back-swept blading with a blade angle of -48.9° with respect to meridional/radial direction.

The vaneless diffuser has no pinch, but the diffuser with a diameter ratio of 1.65 is tapered at its shroud from diffuser inlet until its outlet, thus the diffuser width decreases from inlet to outlet. The scroll part of the volute features a rectangular cross section area followed by a conical exit diffuser having a circular shape. Fig. 2.4 shows a photo of the investigated impeller. More details about design and optimization of the compressor geometry are provided by Schiffmann [12, 13, 14, 15].

The main dimensions of the compressor unit as well as end-wall shape in z-r-coordinates and blade angle distribution as a function of the meridional impeller length are summarized in A.1.1.

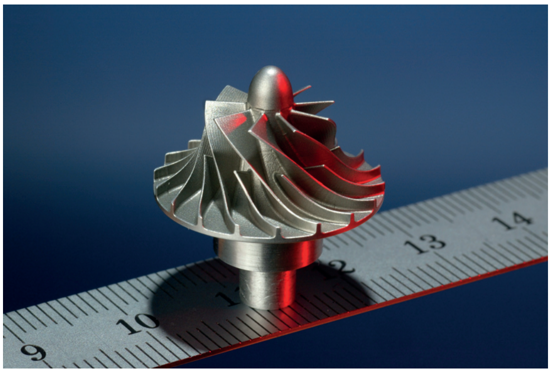

Figure 2.4: Impeller of the investigated compressor by Schiffmann [12, 13, 14, 15].

2.3.2 Compressor by Javed et al.

The compressor by Javed et al. [27] is the first stage of a two-stage compressor for a domestic refrigeration application, processing refrigerant R134a. The compressor features an inlet duct, the impeller, a vaneless diffuser and a volute. The compressor achieves a nominal pressure ratio of 2.3 at a rotational speed of 227 000 rpm and at a global flow coefficient of ϕ_{t1}=0.042.

The impeller wheel consists of 16 blades (8 main blades/ 8 splitter blades). The blades are back-swept with a blade angle of -45°.

The vaneless diffuser is designed with a strong shroud pinch at the inlet of the vaneless diffuser, in order to accelerate the disturbed flow after the impeller in the diffuser, minimizing recirculation back into the impeller. The vaneless diffuser has a diameter ratio of around 1.65. The original design by Javed et al. [27] has a volute. Its cross section is a tunnel shaped type (rectangular + half a circle). In addition to the volute, a collector with a similar cross section shape as the volute has been designed, in order to achieve a more homogenized flow at compressor off-design conditions. However, the cross section area of the collector is four times the cross section area of the volute throat ($A_{Coll} = 4A_{Vol,th}$).

All dimensions as well as hub and shroud end-wall distribution in z-r-coordinates and blade angle distribution as a function of the meridional impeller length are provided in A.1.2.

2.3.3 Scaled up version of compressor by Javed et al. (scaling factor 4.6)

In order to perform more detailed aerodynamic flow measurements, the compressor by Javed et al. [27] was geometrically scaled up by applying a scaling factor of 4.6. End-wall distribution and blade angle distribution are geometrically similar to the down-scaled version and are given in A.1.2.

A collector is used instead of a volute. The collector has an equally distributed cross section area and the cross section area is four times bigger than the volute throat area. This setup allows to test the compressor at off-design conditions avoiding strong upstream effects caused by the different area distribution of a volute.

Fig. 2.5 shows a comparison of the original size impeller by Javed et al. [27] and the 4.6-times scaled up design.

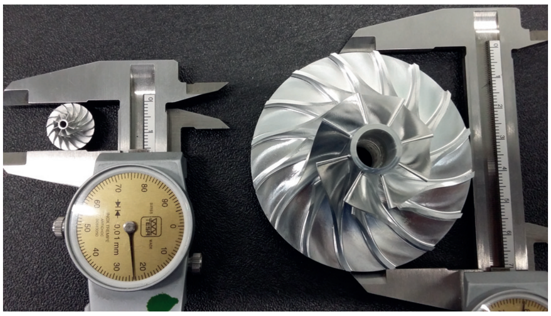

Figure 2.5: Comparison of original-size impeller by Javed et al. [27] and 4.6-times scaled up impeller.

2.4 Experimental procedure

Both compressor geometries have been experimentally investigated, in order to allow a comparison between numerical models and experimental data. The following section describes the experimental approach by Schiffmann [12, 13, 14, 15] and the experimental approach for investigation of the scaled up compressor geometry by Javed et al. [27].

2.4.1 Experimental approach by Schiffmann

The experimental investigation of the reduced-scale centrifugal compressor by Schiffmann [12, 13, 14, 15] has been performed on a fully hermetic test rig. The compressor mass flow was controlled by an electric expansion valve, located downstream of the compressor. The mass flow was measured by an Coriolis mass flow meter, which was located between the compressor outlet and the expansion valve. A condenser is located downstream the expansion valve, which is partially filled with liquid refrigerant. As a consequence, the fluid in the heat exchanger is in the two-phase region, where pressure and temperature are linked, thus stabilizing inlet conditions. The condenser is cooled by an external cold source. Hence, the desired inlet pressure of the compressor test rig is adjusted by the cold source temperature. Overall compressor efficiency was determined using static and total pressure probes as well as total temperature probes located in front and after the compressor. The rotational speed was measured via electric motor and drive. Temperature and pressure sensors were calibrated with an accuracy of ± 2000 Pa and ± 0.2 K, respectively. The test rig is illustrated in Fig. 2.6.

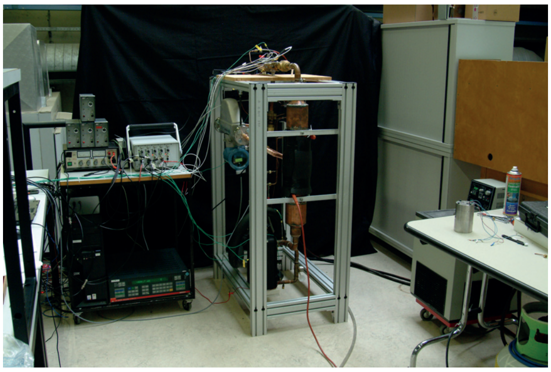

Figure 2.6: Photo of the test setup by Schiffmann [12, 13, 14, 15].

2.4.2 Experimental compressor setup for testing the scaled up compressor by Javed et al.

A scaled up compressor test rig of the reduced-scale centrifugal compressor by Javed et al. [27] has been designed and all geometrical variations of the impeller wheel (see chapter 4 and chapter 5) have been tested on that test-stand. The test unit consists of two main parts, namely the compressor unit and the refrigeration loop. A photo of both is provided in Fig. 2.7.

The main components of the test-rig are the compressor unit, an expansion valve, a heat exchanger and a heated separator. A PID is provided in Fig. 2.8. R134a is conveyed to the impeller after passing a heated separator, in order to obtain superheated and liquid droplet free vapor. The heating power of the separator is controlled by a solid state relay, in order to adapt the compressor inlet temperature. In addition, the flow can be by-passed through a filter drier, to clean the cycle if needed. The mass flow rate of the compressor is controlled by an electrical expansion valve located downstream of the compressor exhaust. The fluid is

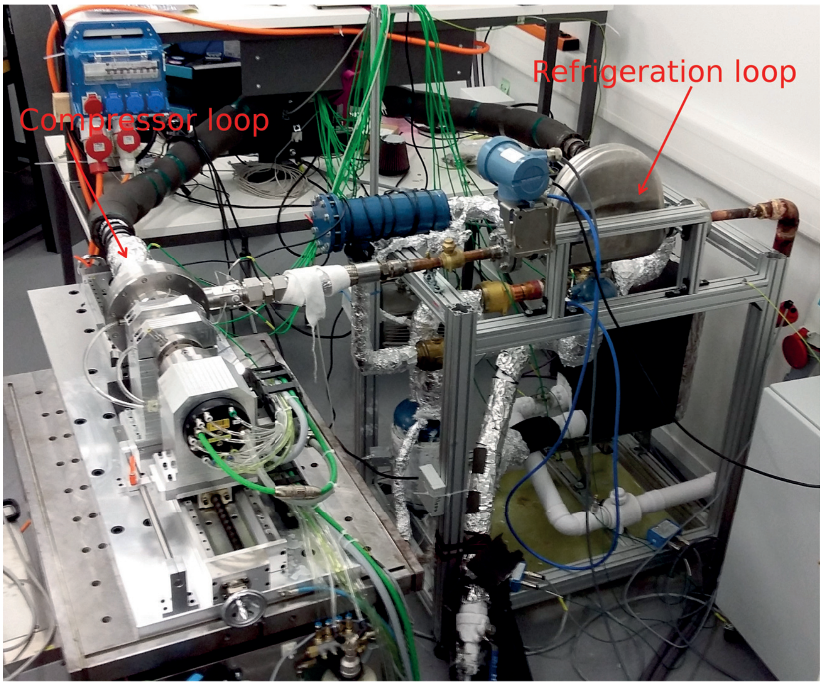

Figure 2.7: Photo of the test-rig consisting of compressor unit (left) and refrigeration loop (right).

passed through the expansion valve into a heat exchanger, where the power introduced into the cycle by the compressor and heated separator is removed. A 40 kW refrigeration machine is used for this purpose.

The compressor is driven by an electrical spindle. This spindle is connected to the compressor shaft via magnetic coupling. This setup has two benefits: (1) an optimal sealing of the compressor housing to the environment and (2) the heat of the motor is not introduced into the compressor system. The bearing temperature of the compressor is controlled by a Pt100 temperature sensor and a thermostat, thus the temperature difference between inner and outer ring of the bearing does not exceed 5 K. Fig. 2.9 shows the connection of compressor shaft with spindle using a magnetic coupling.

Total temperature is measured by three thermocouples (K-type) at the compressor inlet. All thermocouples used at this position have the same immersion depth of six times the thermocouple diameter.
At the outlet of the collector, the total temperature is measured via three thermocouples (K-type) having different immersion depth. The immersion depth was chosen to be 6, 7.5 and 9 times the thermocouple diameter.
In addition, the total temperature is also measured by three different thermocouples at the inlet and outlet of the heat exchanger. The temperature of the water-glycol mixture of the cold-store is tracked with one thermocouple at inlet and outlet of the corresponding heat exchanger side.

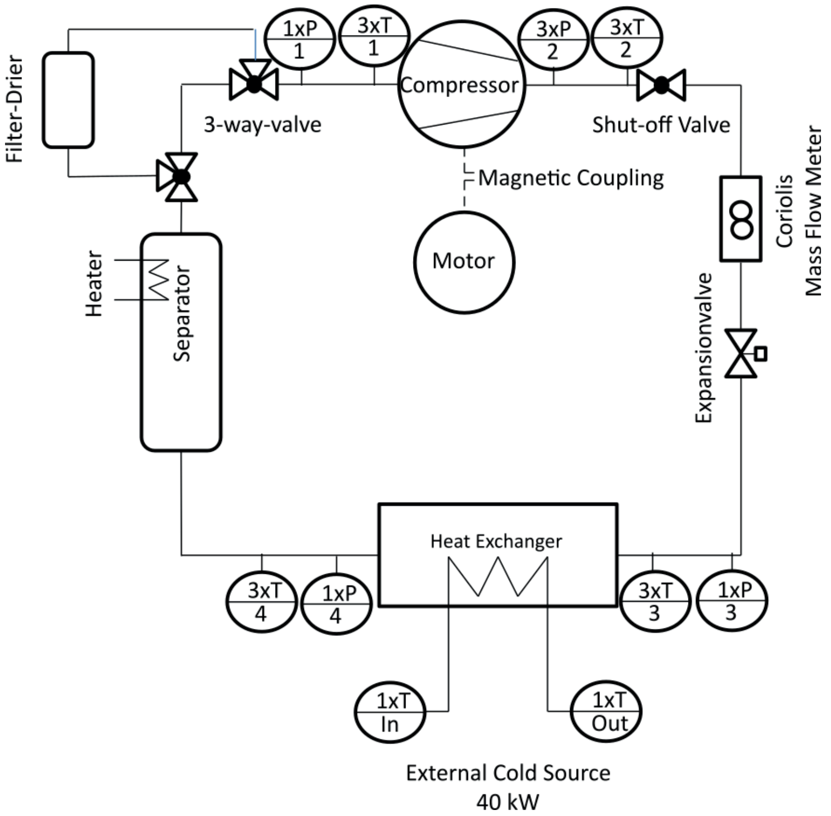
1xP
1
3xT
1
3xP
2
3xT
2
Filter-Drier
3-way-valve
Compressor
Shut-off Valve
Magnetic Coupling
Coriolis
Mass Flow Meter
Heater
Separator
Motor
Expansionvalve
Heat Exchanger
3xT
4
1xP
4
3xT
3
1xP
3
1xT
In
1xT
Out
External Cold Source
40 kW

Figure 2.8: Schematic flow chart (PID) of the test setup.

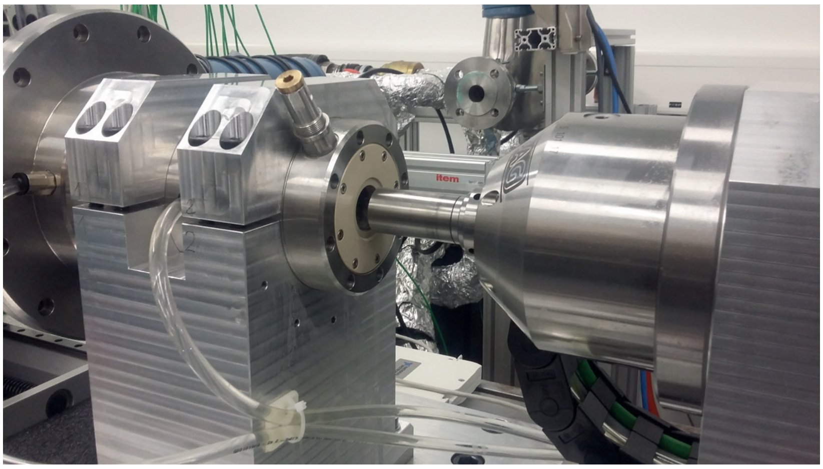

Figure 2.9: Magnetic coupling to connect the driving spindle with the compressor shaft.

Static pressure is measured by static wall pressure measurements using a differential pressure scanner. Static pressure is measured at various positions along the compressor unit, such as schematically illustrated in Fig. 2.10. At impeller trailing edge, at the outlet of vaneless diffuser and at the collector, three static wall pressure measurements are equally distributed around the circumference. Six static wall pressure measurement positions are located at the inlet, where three are connected to one pressure channel thus resulting in two pressure signals of the differential pressure scanner. Six static pressure measurement positions are equally distributed at the outlet tube of the compressor, where two measurement positions are connected thus resulting in three different pressure signals of the differential pressure scanner. The pressure scanner measures the differential pressure between each channel and the reference channel, which measures the ambient air pressure. Hence, an additional pressure transducer to measure the ambient air pressure is used, in order to obtain the absolute pressures.

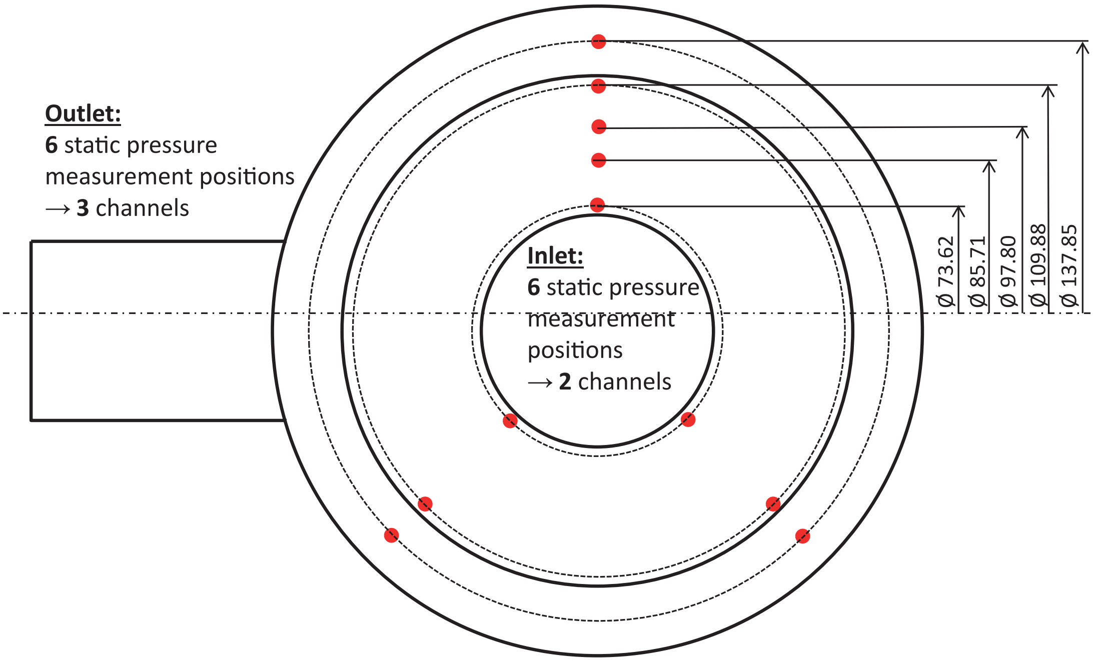

Figure 2.10: Distribution of static wall pressure measurement positions on the collector housing.

Static pressure at inlet and outlet of the heat exchanger is measured by an absolute pressure transducer.
Motor speeds and torque of the compressor is identified via the the digital signals available from the electric drive control.
Specific details about test-rig setup including information about thermocouples, static pressure measurement and compressor drive are provided in appendix A.2.

Conduction of experiments

Various experiments with different impeller geometries (see subsection 2.6.4, chapter 4 and chapter 5) have been conducted on the test-rig described above.
In a first step, the up-scaled compressor geometry by Javed et al. [27] having a relative tip clearance ratio of 14.73 % has been characterized experimentally. Results of the design speed line having a rotational speed of 50 000 rpm are presented in this thesis. The measurement of this speed line has been performed as follows:

1. The cold store temperature has been set to -15°C, corresponding to a pressure of 1.75 bar.
2. The thermostat for bearing cooling is adjusted to 48°C, in order to keep the temperature difference between the inner and outer ring of the ball bearings below 5K. The compressor is started running at a speed of 50 000 rpm.
3. The electric expansion valve is fully opened thus the maximum mass flow rate passes through the compressor. The heating collar around the separator is supplied with a power level, that depends on the desired degree of superheat. In case of the design speed line, the heater runs at 35 % of its maximum power, leading to a superheat of 5 K and a compressor inlet temperature of -8 °C. A waiting time of around one hour was required until inlet and outlet temperature converge to stationary values.
4. An additional waiting time of around 10-15 minutes is required for each operating point until the efficiencies converge. Fig. 2.11 shows the efficiency as function of time. The efficiency is over-estimated and converges after 10 minutes. Each operating point is tracked by collecting all pressure and temperature signals over a period of 200 data acquisitions. This corresponds to a time of around 30 seconds.
5. The electric expansion valve is closed in 5 %-steps until a nozzle position of around 70 %. From this point on, the expansion valve is throttled by 2.5 % towards smaller mass flow rates. The heater power needs to be continuously adapted, in order to maintain the same inlet temperature. Nonetheless, using this setup did not allow to maintain the same inlet temperature, since the inlet temperature increased towards smaller mass flow rates.
6. The static-static pressure ratio is tracked during the test and serves as an indicator for reaching the unstable surge region. As soon this static-static pressure ratio drops, the test is stopped, in order to avoid surge.

In a next step, the scaled up compressor by Javed et al. [27] was tested with relative clearance ratios of 10 % and 20 %. The measurements were conducted as described before.
The front-, mid- and aft-loaded compressor geometries (see chapter 5) were tested according the same measurement scheme.

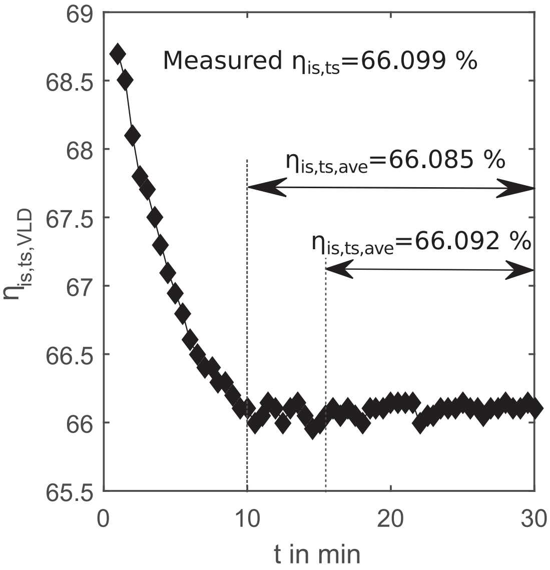

Figure 2.11: Isentropic total-static efficiency at outlet of vaneless diffuser as a function of time.

In a last step, the scaled up compressor by Javed et al. [27] was tested for a clearance ratio of 5 %. Nonetheless, at the design speed line of 50 000 rpm, the impeller touched the collector housing, thus the compressor test was stopped immediately. Fig. 2.12 shows the impeller after it touched the collector housing. Although the impeller tip was severely damaged due to this crash and was not usable anymore, the collector could be repaired by surface polishing.

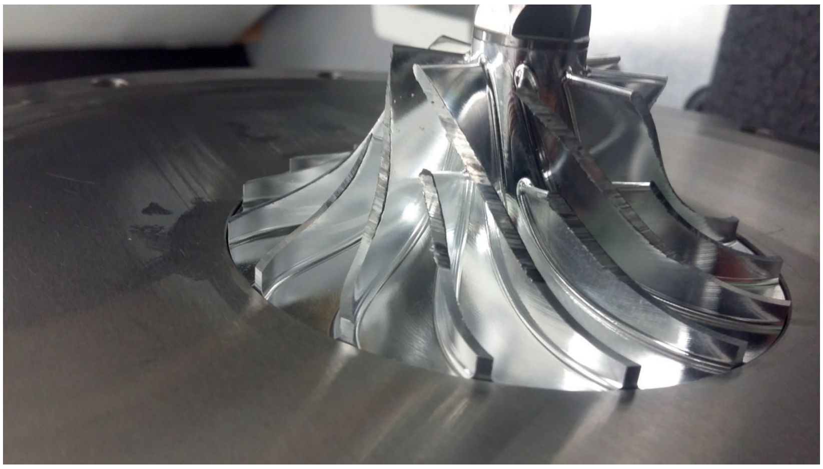

Figure 2.12: Impeller having a relative clearance ratio of 5 % after touching the collector housing.

Limitations of test-rig

In a first step, the static pressure at various positions along the compressor unit as well as total temperature at inlet and outlet of the compressor is measured. This setup does not allow to define the efficiency of the compressor, since the entropy is not fully defined. A total pressure probe would be required. Nonetheless, installing of such probes in the hermetic rig has been figured out to be a difficult task, since sealing of traverse probes in such high pressure is difficult. Therefore, the overall efficiency is estimated by a reduced-order model which assumes an axial inflow at inlet and outlet of the compressor as well as knowledge about the flow blockage.

The determination of the right working fluid charge has been figured out to be a difficult task, since limited knowledge is available of operating a compressor in a clockwise cycle as presented in Fig. 2.8. In case of too much refrigerant, the compressor sucks a vacuum in the heat exchanger, since the refrigerant is not able to evaporate quickly enough to maintain the mass flow needed by the compressor. As a consequence, the compressor sucks liquid refrigerant at higher speed lines. In order to find the right amount of refrigerant, a certain amount of refrigerant was filled in the rig and tests were conducted at the highest speed line. In case the compressor started sucking liquid refrigerant, the test was stopped and a small amount of refrigerant was removed. The inlet temperature served as an indicator for this behavior, since all thermocouples at inlet show an intense drop of temperature. This procedure was repeated until a stable operation of the compressor at its highest speed line was achieved. An amount of 700-750 g of refrigerant has been determined to be sufficient to guarantee a stable operation for a total heat exchanger volume of 14 liter.

Compared to numerical results (see subsection 2.6.4), the choke region of the compressor could not be examined due to the high pressure loss of the refrigeration loop.

2.5 One-dimensional centrifugal compressor model

A one-dimensional centrifugal compressor performance prediction model has been developed, which is mostly based on Whitfield and Baines [46]. The model consists of three different components, namely impeller, vaneless diffuser and volute. It predicts thermodynamic as well as aerodynamic properties at defined control stations along the flow path on the rms-streamline (see Fig. 2.1). The model is based on conservation of continuity and energy, considering empirical internal and external losses.

The loss in head coefficient is modeled by an isentropic head loss coefficient as suggested by Balje [68]. In case of the impeller, this loss coefficient is applied to the loss in relative total enthalpy. For this purpose, the relative total enthalpy at impeller trailing edge is obtained from rothalpy R, which according to Wu [69] is conserved in rotating systems. The rothalpy is defined by Eq. 2.15 (see e.g. Aungier [45]).

$$R = h_t - \omega r c_u = h_t^{'} - \frac{(\omega r)^2}{2} \tag{2.15}$$

2.5.1 Impeller modeling

The impeller model is based on an iterative solution of continuity and energy equation. Various empirically derived loss mechanisms to account for loss in isentropic head coefficient are considered during the solution procedure. The impeller is divided into different control stations, which are located at the inlet, the leading edge, the impeller throat, the trailing edge and the inlet of the vaneless diffuser (see Fig. 2.1). The calculation of the impeller is conducted at the rms streamline, which divides the mass flow rate into two equal parts, thus corresponding to the so-called rms- or Euler-diameter.

An incidence loss occurs at the leading edge of the impeller, which is the loss associated to the misalignment between the flow and the blade metal angle. The incidence loss is modeled as suggested by Galvas [70]. Besides the evaluation of aerodynamic properties at the rms-diameter, flow velocities are additionally calculated at hub and shroud to account for possible shock losses.

Furthermore, an iterative solution of continuity and energy equation is performed at the impeller throat, in order to account for potential impeller choke.

In order to offer rapid convergence at the impeller trailing edge through a good initial solution, a static density at the trailing edge of the impeller is obtained from loss-free calculations. In this situation, meridional velocity at impeller trailing edge is calculated from continuity equation, considering a blockage factor. The Euler work (Eq. 2.3) is calculated by considering slip as proposed by Wiesner [71], thus tangential absolute and relative velocities are computed.

Three different internal loss mechanisms are considered, namely skin friction loss, blade loading and diffusion loss and tip clearance loss. The skin friction loss is modeled as suggested by Jansen [72] and Coppage et al. [73], where the friction factors are evaluated applying the Colebrook-White equation. The analogy model behind the modeling of surface friction is based on a pipe-flow model. Jansen [72] and Coppage et al. [73] suggest modeling blade loading and diffusion losses as Lieblein et al. [74] propose for axial compressors. Blade loading and diffusion loss, however, are implemented as suggested by Rodgers [75, 76]. The tip clearance loss is modeled as suggested by Jansen [72], where tip leakage jet undergoes a sudden compression followed by a sudden expansion.

As reported in Beinecke [77], the compressor flow underlies a sudden expansion from trailing egde into the vaneless diffuser. External loss mechanisms like the one associated to disk friction are considered at this position. The flow is modeled as a Borda-Carnot shock. Equations for this expansion are provided by Greitzer et al. [23], Whitfield and Baines [46] and Beinecke [77]. External loss mechanisms are disk friction as suggested by Daily and Neece [78, 79] and recirculation as suggested by Coppage et al. [73]. Besides continuity and energy equation, momentum in radial/meridional direction is considered. Further details about this effect can be found in Whitfield and Baines [46], Aungier [45], Greitzer et al. [23], Japikse [80] and Beinecke [77].

The iterative solution procedure of the whole impeller is provided in A.3. In addition, the iterative solution procedure of the impeller trailing edge considering internal loss mechanisms is exemplary provided in A.3.

2.5.2 Model of vaneless diffuser

Compared to the modeling procedure of impeller and volute, the vaneless diffuser is modeled by a different approach. Differential equations as suggested by Stanitz [81] and Dubitsky and Japikse [82] are solved by a second order central difference scheme. In addition, the blockage/distortion due to boundary layer growth in the vaneless diffuser is considered. An approach suggested by Aungier [45] to account for blockage in the vaneless diffuser is used. As a consequence, the continuity equation as suggested by Stanitz [81] is re-arranged to account for blockage effects, what is shown in Eq. 2.16.

$$\frac{1}{\rho}\frac{d\rho}{dr} + \frac{1}{c_m}\frac{dc_m}{dr} + \frac{1}{b}\frac{db}{dr} + \frac{1}{k}\frac{dk}{dr} + \frac{1}{r} = 0 \tag{2.16}$$

The boundary layer thickness is further used as a hydraulic diameter to calculate the friction coefficient based on the skin friction correlation provided by Japikse [80]. Eq. 2.17 shows this friction factor correlation for a vaneless diffuser as proposed by Japikse [80]. The value k is set to 0.01.

$$c_f = k\left(\frac{1.8\cdot 10^5}{Re}\right)^{0.2} \tag{2.17}$$

The solution procedure of the vaneless diffuser is schematically illustrated in A.3.

2.5.3 Volute/scroll model

Aerodynamic losses occurring in the volute are considered by a pressure recovery coefficient (Eq. 2.18). It describes the losses in the scroll part as well as in the conical exit diffuser as proposed by Schreiber [83]. A complete loss of meridional velocity component as well as a sudden expansion loss of the tangential velocity component from inlet to outlet of the volutes spiral is assumed. The kinetic energy at the outlet of the conical diffuser is expected to be a loss.

$$\begin{gathered} cp_{Vol} = 1 - e_{kin,out} - \xi_m - \xi_{exp} = \\ 1 - \left(\frac{cos(\alpha_3)}{A_{r4}}\right)^2 - cos(\alpha_3)^2 - \left(sin(\alpha_3) - \frac{cos(\alpha_3)}{A_{rsp}}\right)^2 \end{gathered} \tag{2.18}$$

The area ratios in Eq. 2.18 are defined as $A_{r4} = A_4/A_3$ and $A_{rsp} = A_{sp}/A_3$.
In order to account for compressibility effects in the volute, continuity equation as well as energy equation are solved iteratively until the static density converges. The iterative solution procedure of the volute is provided in A.3.
In addition, two alternative models to model volute performance have been implemented, namely the one by Japikse [80] and the one by Weber and Koronowski [84].

2.5.4 Performance map prediction

In order to create a compressor performance map, the implemented one-dimensional model of each component are combined. Hence, the outlet conditions of an upstream component are the inlet conditions of the following downstream component. The local relative/absolute Mach number is checked to account for compressor choking at each control station of all components. Nonetheless, the most relevant station for compressor choking is the impeller throat, which corresponds to the smallest cross section area of the impeller located behind the leading edge.

Surge occurs at low mass flow rate, where different instability phenomena exist. By throttling the mass flow rate of a compressor, the first unstable phenomenon which occurs is so called 'rotating stall'. It describes flow separations in the impeller or the diffuser, leading to partial recirculation from diffuser into the impeller. The compressor is still able to deliver a pressure rise. In case the mass flow is throttled further down, the rotating stall cells grow in size and complete flow separation occurs. As a consequence, the compressor produces pulsating flows from outlet to its inlet and the pressure rise decreases.

A possible stall behavior in the inducer of the impeller is suggested by Aungier [45]. His model assumes that inducer stall is expected when the diffusion from the shroud inlet to the throat of the impeller is too strong (see Eq. 2.19). As a consequence, the inducer stall leads to so called rotating stall - the onset of unstable compressor operation.

$$\frac{w_{1s}}{w_{th}} \geq 1.75 \tag{2.19}$$

In addition, the slope of the total-total head coefficient is analyzed. According to Beinecke [77], onset of surge is located at the maximum turning point of the total-total head coefficient (see Eq. 2.20). Strong backflows in the compressor start to occur by overcoming this maximum turning point.

$$\frac{d\psi_{pol,tt}}{d\phi_{t1}} = 0 \tag{2.20}$$

2.5.5 Validation of one-dimensional model

The one-dimensional model is compared with experimental data provided by Schiffmann [12, 13, 14, 15]. All empirical internal and external loss mechanisms are weighted by a weighting factor, in order to allow for calibration of the one-dimensional model. Weighting factors of 1 are used in a first step for all empirical loss models.

Fig. 2.13 shows the dimensionless performance values total-total polytropic head coefficient $\psi_{pol,tt}$, work input coefficient λ and total-total polytropic efficiency $\eta_{pol,tt}$ as a function of percentage design mass flow rate of the experimental results compared to the results obtained from the one-dimensional model (uncalibrated). The dimensionless performance values are evaluated for three different machine Mach numbers, namely $Ma_{u2} = 1.06$, $Ma_{u2} = 1.27$ and $Ma_{u2} = 1.48$. Experimental results are presented as black circles (polytropic total-total head coefficient), red diamonds (work input coefficient) and blue squares (polytropic total-total efficiency). Numerical results are presented as black line (polytropic total-total head coefficient), red dashed line (work input coefficient) and blue dash-dotted line (polytropic total-total efficiency). In addition, the onset of inducer stall according to Eq. 2.19 is marked as dashed line in all three graphs.

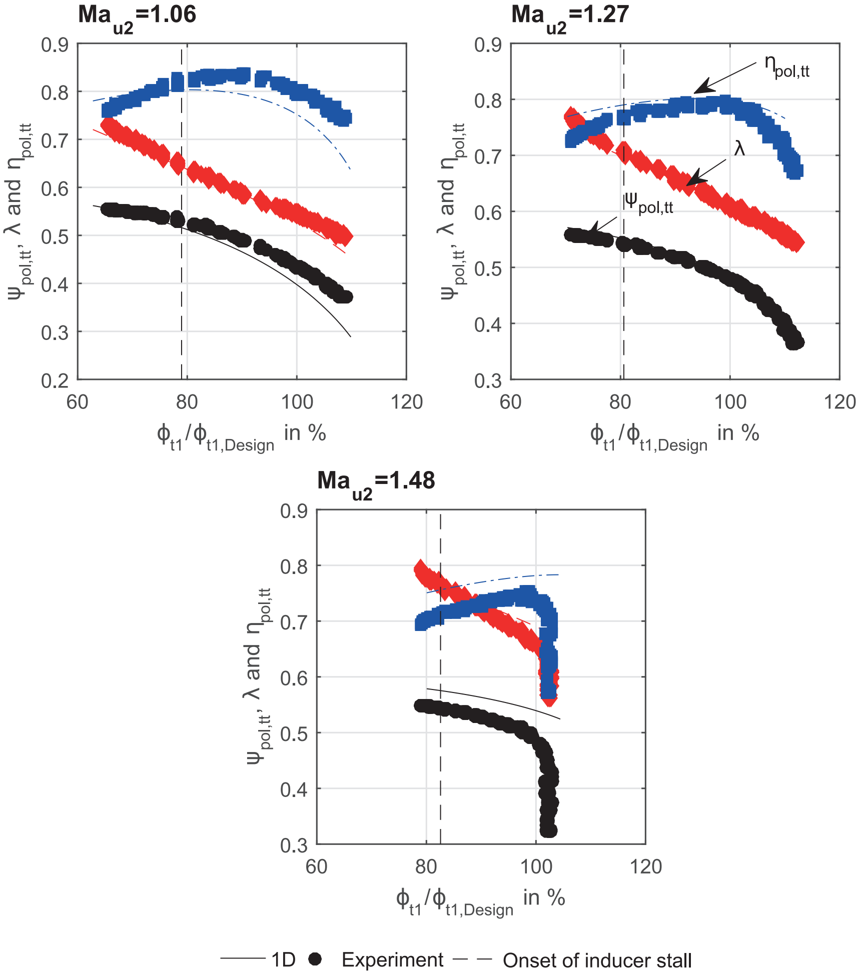

Figure 2.13: Comparison of non-dimensional performance values between experimental data by Schiffmann [12, 13, 14] and the one obtained from the one-dimensional model.

The polytropic total-total head coefficient is under-estimated for the lowest speed line of $Ma_{u2} = 1.06$ towards high mass flow rates, suggesting an over-estimation of internal losses. Work input coefficient is accurately predicted in the design range of this speed line, but it is under-estimated at high and low mass flow rates. The under-prediction of λ towards lower mass flow rates suggest that external loss mechanism are under-estimated. Especially disk friction loss is more pronounced towards lower mass flow rates, what explains the higher

experimental work input towards surge compared to the one-dimensional model. The polytropic total-total efficiency follows a similar trend as the head coefficient, but the location of the best efficiency point is in accordance with experimental data.
The validation of the design speed line ($Ma_{u2} = 1.27$) suggests a good prediction quality in terms of total-total polytropic head coefficient and work input coefficient. Hence, total-total polytropic efficiency is accurately predicted along the operating range and the location of the best efficiency point is in line with experimental data. The one-dimensional model, however, slightly over-estimates efficiency towards smaller and higher mass flow rates than the design point.
The speed line of $Ma_{u2} = 1.48$ suggests a strong over-estimation in terms of head and work input coefficient. The over-prediction of work input coefficient is most likely caused by an under-estimation of trailing edge blockage, since a constant value of 0.88 as suggested by Whitfield and Baines [46] is used for trailing edge blockage. Over-estimation of polytropic head coefficient suggests an under-estimation of internal loss mechanisms, thus resulting in lower total pressure losses as suggested by experimental data. Nonetheless, the numerical data set features the same slope as experimental data.
In order to further illustrate the discrepancies between the one-dimensional model and experimental data, the relative deviation between the one-dimensional model and experimental data is shown in Fig. 2.14, presented as a black solid line. For the sake of comparison, experimental data was fitted by a polynomial of 4^{th} degree to allow comparison of data for one specific flow rate. In addition, the measurement error for total-total polytropic head coefficient and work input coefficient calculated according the Gaussian error propagation is additionally shown in Fig. 2.14 and is presented as red dashed lines. Fig. 2.14 further supports the findings discussed above.

A comparison between performance data produced by one-dimensional model and experimental data for the compressor provided by Schiffmann [12, 13, 14, 15] shows a good agreement in terms of prediction of work input and head coefficient for the design speed line. Nonetheless, performance prediction lower and higher than design speed show the need of adapting and calibrating the one-dimensional compressor model. For this purpose, the reduced-order model might be calibrated using experimental data. Here, the calibration weights might be adapted by a multi-objective optimizer, in order to best fit the experimental results for all speed lines.

2.6 Computational Fluid Dynamics

Computational fluid dynamics (CFD) is used for investigation of the three-dimensional compressor flow. In order to solve the three-dimensional Reynolds-averaged Navier-Stokes (RANS) equations, the simulation software Fine/Turbo provided by Numeca International [67] is used. This software is dedicated to turbomachinery specific problems. Besides the flow solver, software packages for pre-processing and post-processing are provided.

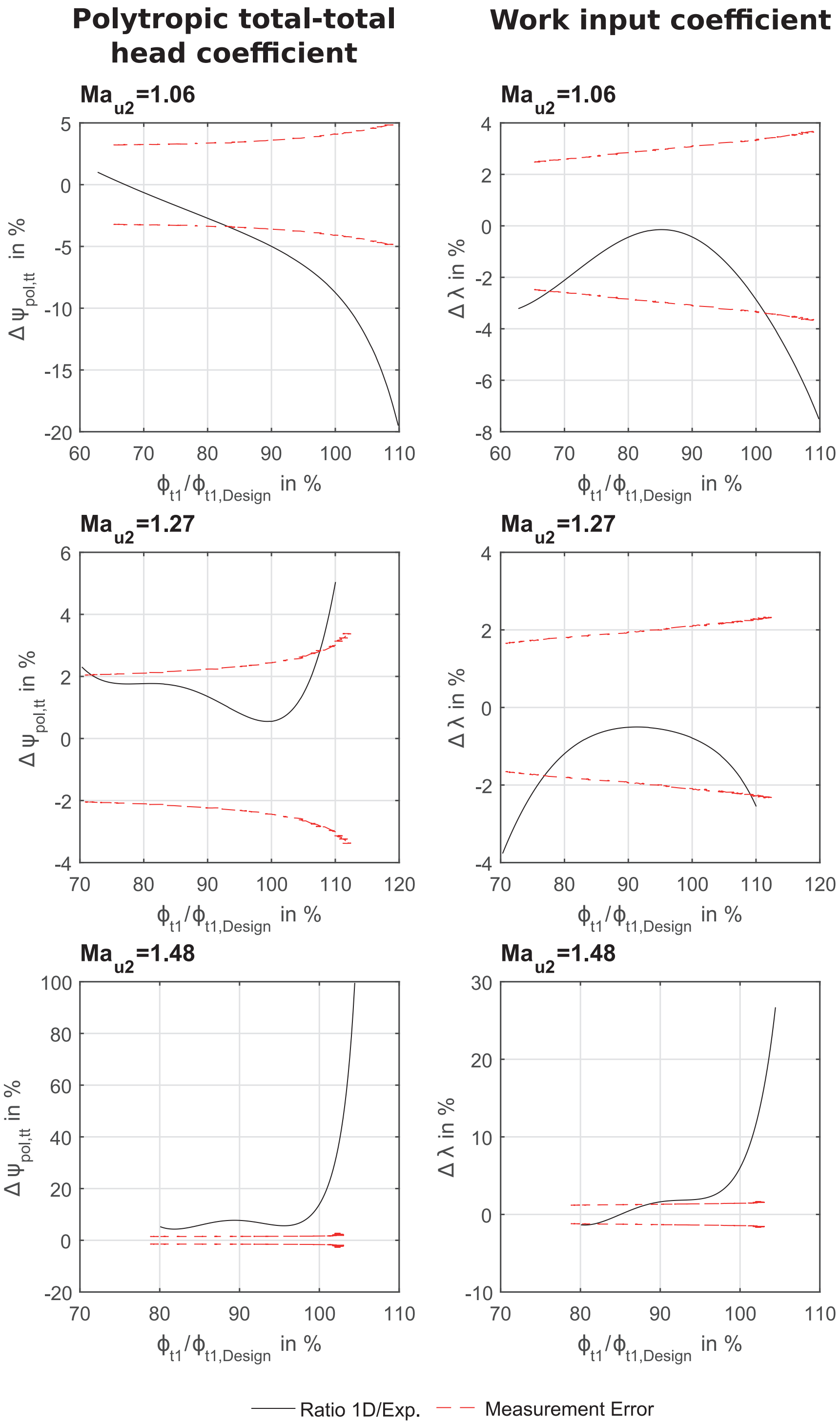

Figure 2.14: Deviation between 1D data and experimental data compared to the measurement error.

2.6.1 Creating the computational grid

The computational grid on which the RANS are solved is created by using the meshing software Autogrid, which is a dedicated meshing tool for turbomachinery provided by Numeca [67]. The used flow solver Fine/Turbo requires a structured grid. The computational domain consists of an inlet duct, the impeller and the vaneless diffuser. The impact of the asymmetric volute or collector, however, is not modeled in CFD. A single blade passage including one main and splitter blade is modeled thus periodic boundary conditions are used. Hence, a circular section of inlet duct and vaneless diffuser is combined with the impeller mesh. Fig. 2.15 and Fig. 2.16 show the mesh setup for the compressor provided by Schiffmann [12, 13, 14, 15] (see subsection 2.3.1). A similar mesh setup is used for the compressor geometry provided by Javed et al. [27] (see subsections 2.3.2 and 2.3.3).

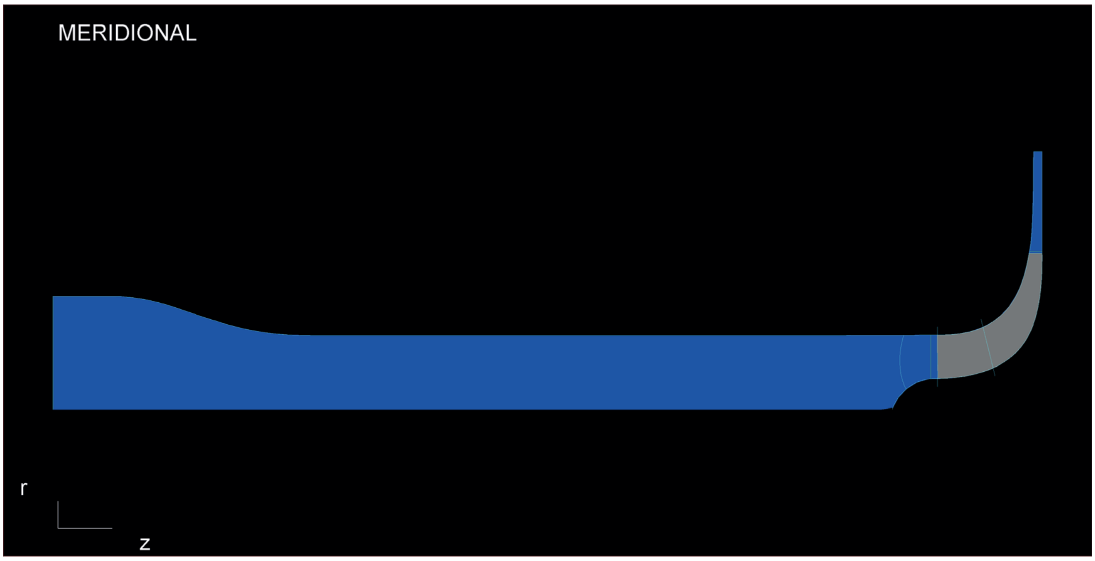

Figure 2.15: Meridional cutting view of simulated compressor components.

Since a low-Reynolds number turbulence model (no wall functions) is used, the computational grid requires a dimensionless wall distance y^+ of less than 10 where a value of 1 is desirable. Numeca [67] recommends to use a maximum non-dimensional wall distance of $y^+ = 5$. The dimensionless distance of the first node in the viscous sublayer of the boundary layer is calculated by Eq. 2.21.

$$y^+ = \frac{y c_\tau}{\mu} \tag{2.21}$$

The friction velocity is defined by Eq. 2.22:

$$c_\tau = \sqrt{\frac{\tau_{wall}}{\rho}} = \sqrt{\frac{1}{2} c_{ref}^2 c_f} \tag{2.22}$$

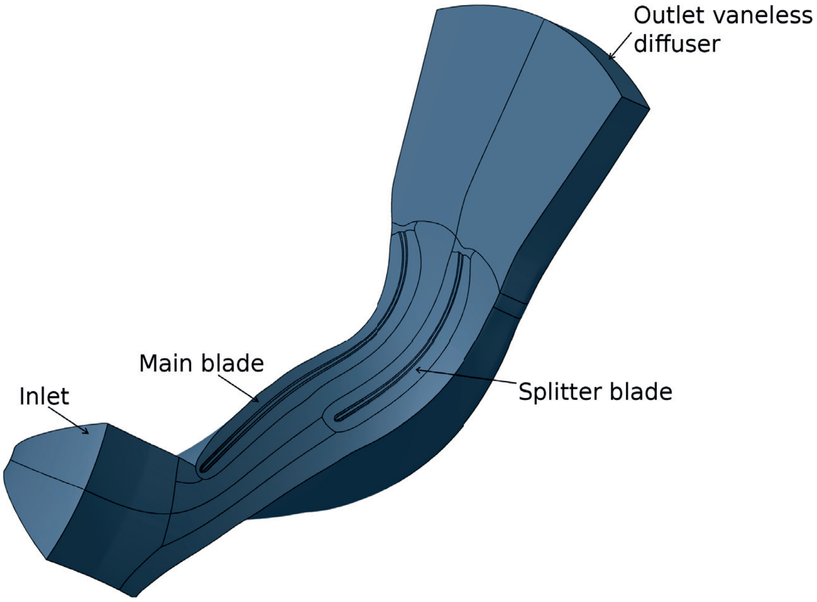

Figure 2.16: Three-dimensional view of the modeled compressor by Schiffmann [12, 13, 14, 15].

The skin friction coefficient can be estimated by applying the $1/7^{th}$ power law for boundary layer profiles (see Eq. 2.23) based on the Reynolds number.

$$c_f = \frac{0.027}{Re^{\frac{1}{7}}} \tag{2.23}$$

Here, the Reynolds number is calculated by the rotational speed at the compressor tip u_2, the impeller outlet diameter d_2 and the total inlet conditions as suggested by Numeca [67]. Eventually, Eq. 2.21 is used to determine the absolute wall distance y of the first near-wall cell. Simulations are performed using refrigerant R134a, which has a higher density and a lower kinematic viscosity compared to air. As a consequence, the absolute wall distance to achieve a dimensionless distance of 1 or less is very small. Hence, to guarantee the required mesh quality in terms of aspect ratio, expansion ratio and orthogonality, a higher mesh count is required compared to a similar air compressor.

An H-I-type mesh is used for building the computational grid in the impeller, which provides a higher mesh quality for applications having splitter blades compared to a commonly used O-4H-type mesh. The surface meshes at impeller main blade leading edge, at leading edge of the splitter blade and at the trailing edge are presented in A.4.

2.6.2 Boundary conditions and solver setup

The three-dimensional Reynolds-averaged Navier Stoke equations are solved using the solver Euranus/Turbo provided by Numeca [67]. R134a is used as working fluid and is modeled as condensable gas. The fluid properties are obtained by interpolation from a thermodynamic table provided by NIST [85].

A total temperature as well as total pressure boundary condition is imposed at the inlet. In addition, the flow angle with respect to the axial direction is specified and set to zero, thus assuming pure axial inflow. Since a low Reynolds-number k-omega SST turbulence model (Menter [86]) is used, the turbulent kinetic energy k and the turbulent dissipation rate ϵ are required as inlet boundary conditions. The turbulent kinetic energy is estimated from the turbulent intensity which is assumed to be 5 % according to recommendations by Numeca [67] for turbomachinery specific problems at the compressor inlet. The turbulent kinetic energy is calculated by Eq. 2.24:

$$k = \frac{3}{2}\left(\sqrt{\bar{c}}^2\right) \tag{2.24}$$

Two different approaches are used for calculation of the turbulent dissipation rate ϵ. The first one assumes a predefined turbulent length scale l, which is a measure for the size of large-energy containing eddies. Numeca [67] recommends to estimate the turbulent length scale l as around 10 % of the hydraulic diameter of the inlet section. The turbulent dissipation is therefore calculated by Eq. 2.25:

$$\epsilon = \frac{c_\mu^{0.75} k^{1.5}}{l} \tag{2.25}$$

The second approach for definition of turbulent dissipation rate is the specification of the turbulent viscosity ratio μ_t/μ. Numeca [67] recommends to set the turbulent viscosity ratio for turbomachinery specific problems to around 50. The turbulent dissipation rate is calculated by Eq. 2.26:

$$\epsilon = C_\mu \frac{\mu}{\mu_t} \frac{\rho_{ref} k^2}{\mu} \tag{2.26}$$

It is advised to calculate the turbulent dissipation rate by Eq. 2.25 and Eq. 2.26 and compare the results, since both equations require empiric parameters. For the investigated centrifugal compressors, both approaches lead to similar values. On the other hand, own experience as well as observations by Numeca [67] have shown that numerical results are not very dependent on the choice of turbulent dissipation ratio ϵ.

An averaged static pressure boundary condition is imposed at the outlet and is varied in order to change the compressor operating points along a speed line. An alternative outlet boundary condition is imposing the mass flow rate. Nonetheless, the average static pressure boundary condition provided a more stable convergence than the mass flow boundary condition, the residuals converged earlier. Back flows which reenter the outlet domain are suppressed by using a back flow treatment, which blocks part of the outlet using a slip (Euler) wall. The back flow treatment, however, is deactivated towards the end of the simulation, since the flow gets artificially distorted, which would influence the results.

All walls are treated as adiabatic having a no-slip condition. The blades are set as fully rotating as well as the impeller hub surface. The shroud was set as non-rotating. Disk friction is not modeled in CFD, but results are corrected by using the reduced-order approach suggested by Daily and Nece [78, 79], in order to compare with experimental results. Correction for disk friction is applied for CFD data presented in subsection 2.6.4.

Numerical convergence is determined by Numeca's [67] definition of global residual as well as stabilization of the total-total pressure ratio and total-total polytropic efficiency. Furthermore, mass conservation is maintained and solutions with a difference of less than 0.5 % between inlet and outlet mass flow rate are considered to be converged. Convergence was achieved at around 1000 iterations for operating points close to the design point as well as operating point towards high mass flow rates. 1300 iterations were required to obtain convergence at off-design operating points towards smaller mass flow rates. The global residuals drop by around 4 up to 5 orders of magnitude at design and overload conditions without showing an oscillating behavior. The global residuals at part-load fall by around 2 up to 3 orders of magnitude before strong oscillations occurred. These strong oscillations suggested the onset of transient phenomena, which cannot be captured with the used steady-state approach.

A multigrid approach is used to procure convergence by having a good initial solution. Two lower grid levels are used and on each grid level 100 iterations are performed.

2.6.3 Mesh sensitivity study and comparison of two turbulence models

In order to verify the numerical setup, a grid independence study has been performed. The mesh sensitivity study has been performed on the centrifugal compressor by Schiffmann [12, 13, 14, 15] (subsection 2.3.1). The numerical study is performed for the inlet section, the impeller and the vaneless diffuser. Therefore, the computational grids have been created for a 40-degree section of the inlet pipe, one impeller blade passage and a 40-degree section of the vaneless diffuser. Periodic boundary conditions have been used for the side patches of the passage model, assuming an equal flow distribution in each impeller blade passage. The mesh setup was chosen according to subsection 2.6.1 and a low Reynolds number SST turbulence model was used, requiring a dimensionless wall distance of $y^+ \leq 5$. As stated previously, the used fluid leads to a small absolute near wall cell height. On the other hand, the used flow solver Euranus/Turbo by Numeca [67] has limitations according to aspect ratio, orthogonality and expansion ratio in the boundary layers, which should not be exceeded. From that point of view, the coarsest mesh achieved for this mesh sensitivity study, which is still in the solver restrictions, has a total cell count of around five million grid points. Six different computational grids have been investigated, listed in Table 2.1.

Convergence was determined according to subsection 2.6.2. Fig. 2.17 a) shows total-total pressure ratio and Fig. 2.17 b) the total-total polytropic efficiency as function of the number of grid points. The total-total pressure ratio is accurately predicted by all used mesh configura-

Table 2.1: Specifications of computational grids used for the mesh sensitivity study.

Case	**Cell count in Mio.**	**Min. orth. in**	**Max. exp. ratio**	**Max. asp. ratio**
A	4.97	13.03	2.67	4690
B	6.23	13.47	2.43	4230
C	7.61	14.13	2.15	3610
D	9.89	14.48	2.07	3460
E	12.34	14.92	1.98	3390
F	16.25	15.16	1.92	3340

tions independent of the cell count. However, the total-total polytropic efficiency increases with increasing cell count and starts to stagnate at a cell count of around 7.61 million. In this case, the relative deviation between mesh *C* and mesh *F* is around 0.31 % for the total-total pressure ratio and around 0.34 % for the total-total polytropic efficiency, respectively.

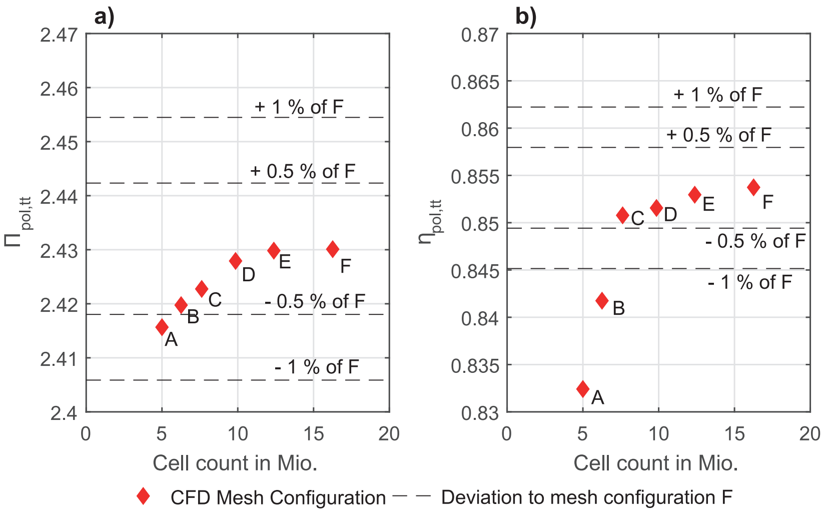

Figure 2.17: Grid convergence for the total-total pressure ratio (a) and the total-total polytropic efficiency (b) as a function of grid point number

As a consequence, the computational grid having a cell count of 7.61 million has been selected to simulate the compressor by Schiffmann [12, 13, 14, 15]. The compressor geometry by Javed et al. [27] is meshed with a similar mesh setup, in order to achieve similar values in terms of aspect ratio, expansion ratio and orthogonality.

Besides the size of computational grid, the used turbulence model has an impact on the flow solution. Numeca [67] recommends to use the Spalart-Allmaras (SA) [87] turbulence model for their flow solver in terms of memory usage and convergence behavior. However, compared to Menter's [86] SST model the SA-model does not model accurately at compressor off-design as suggested by Numeca [67]. Nonetheless, Spalart-Allmaras turbulence model requires less memory usage and is less dependent on the mesh quality. From that perspective, both turbulence models have been compared. In a similar way as for the mesh sensitivity study, the compressor by Schiffmann [12, 13, 14, 15] has been selected for this investigation. Experimental data set have been used for verification of the numerical setup. In order to compare numerical results with experimental results, the impact of the volute was considered by a reduced-order model provided by Japikse [80] and disk friction was modeled according to Daily and Nece [78, 79]. Fig. 2.18 a) shows the total-total polytropic head coefficient, Fig. 2.18 b) the work input coefficient and Fig. 2.18 c) the total-total polytropic efficiency as a function of the global flow coefficient. Experimental results are marked as black circles, numerical results of the SST-turbulence model are marked as red solid line having diamonds and the numerical results of the SA-turbulence model are marked as blue dotted line having squares.

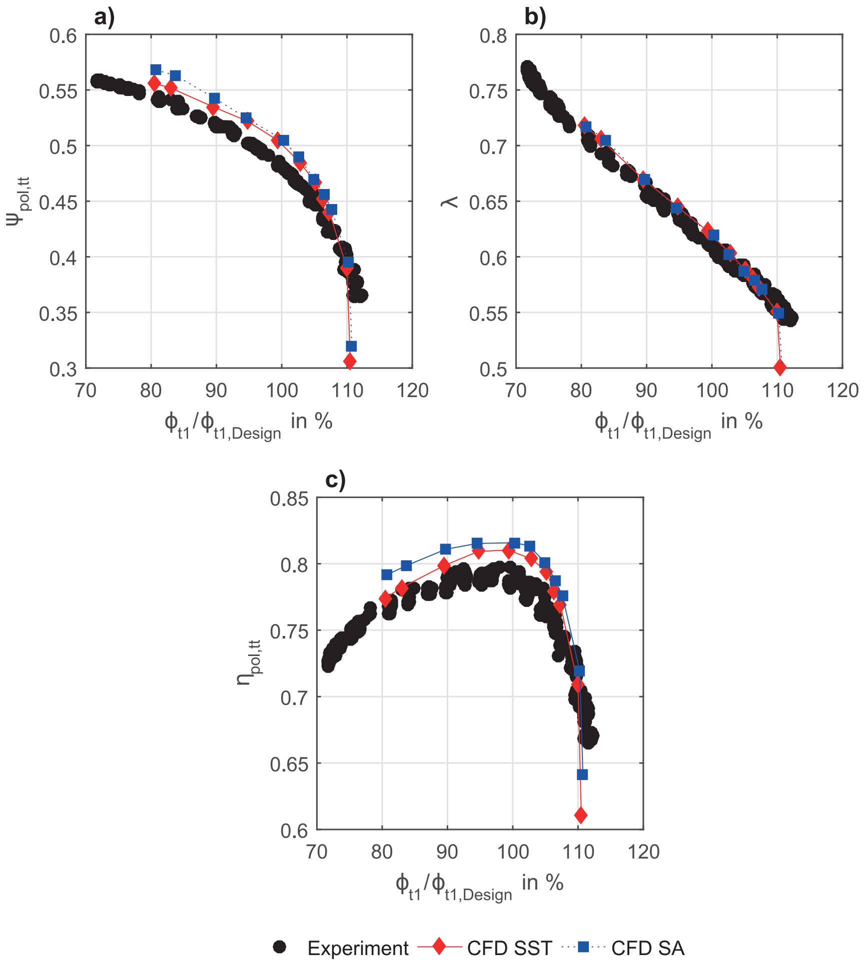

Figure 2.18: Comparison of the stage characteristics between SST turbulence model, SA turbulence model and experimental data.

Fig. 2.18 a) clearly shows that Spalart-Allmaras (SA)-turbulence model over-estimates the total-total polytropic head coefficient over the whole operating range. From the best efficiency point towards choking, the slope of the head coefficient predicted by the Spalart-Allmaras turbulence model is similar to the experimental data set. Nonetheless, the slope of head coefficient towards surge is different and the drop in efficiency relative to the best efficiency

point is less pronounced. Menters SST-turbulence model, however, accurately predicts the total-total head coefficient over the whole operating range with a slight tendency to over-prediction. A similar trend in prediction as for the whole compressor is observed at the outlet of the vaneless diffuser, thus the impact of the reduced-order models by Japikse [80] and by Daily and Nece [78, 79] is negligible concerning recommendations about the turbulence model.
Fig. 2.18 b) suggests, that both turbulence models deliver the same order of accuracy in terms of the prediction of work input coefficient, suggesting similar blockage prediction for both turbulence models.
As a consequence of Fig. 2.18 a) and Fig. 2.18 b), the total-total polytropic efficiency (see Fig. 2.18 c)) is over-predicted over the whole operating range by the SA-turbulence model compared to Menter's SST-model. In addition, the slope of total-total polytropic efficiency towards smaller mass flow rates does not follow the trend suggested by experimental data when using the SA-turbulence model. Nonetheless, the location of the peak efficiency point is well predicted by both turbulence model at similar flow rates.

The study of two low Reynolds number turbulence models suggested to use Menter's SST [86] model instead of the Spalart-Allmaras [87] model, since a more accurate prediction especially at off-design was observed. As a consequence, all numerical simulation which have been performed in that thesis are using Menter's low Reynolds number SST turbulence model.

2.6.4 Validation of the numerical setup

Validation with experimental data provided by Schiffmann:

The prediction quality of the numerical setup is compared with experimental data set provided by Schiffmann [12, 13, 14, 15]. Since the numerical computation is performed without considering the impact of the volute and disk friction, reduced-order models by Japikse [80] and Daily and Nece [78, 79], respectively, have been used. Numerical values obtained at the outlet of the vaneless diffuser are used as input values for the reduced-order volute model by Japikse [80].
Fig. 2.19 shows the comparison between experimental data and numerical data at the design speed of 180 000 rpm, corresponding to a rotational Mach number of 1.27. Fig. 2.19 a) shows the total-total polytropic head coefficient, Fig. 2.19 b) the work input coefficient and Fig. 2.19 c) the total-total polytropic efficiency as a function of percentage design mass flow rate. Experimental data is shown as black dots and numerical data as red solid lines with diamonds. The polytropic total-total head coefficient shown in Fig. 2.19 a) suggests a good qualitative agreement. However, numerical data is consistently higher than the experimental one. A contributor to the deviation could be the under-prediction of blockage in the rotor passage, leading to increased diffusion and consequently higher head. Reduced numerical blockage can source from the simplification of hydraulically smooth walls. Another contributor could be altered turbulence dissipation relative to real conditions, leading to faster mixing and decay

of secondary flows in the simulation. In addition, the volute was not considered in the CFD simulation, thus the distorting impact of the volute on upstream components is neglected. Furthermore, inaccuracies in the reduced order volute model could contribute to deviations between model and experiment. At maximum flow rate, the numerical model deviates from the experiment. This can be explained by the influence of manufacturing tolerances and will be discussed more detailed below.
As can be seen from Fig. 2.19 b), good agreement between experiment and numerical data was achieved in terms of work input coefficient over the whole operating range. In general, the numerical data provided marginally higher work input. Reasons could be a deviation in predicted secondary flows or heat transfer in the experiment, what was not captured in the numerical setup.
Polytropic total-total efficiency, shown in Fig. 2.19 c), presents the product of head and work coefficient. As a result, the numerically obtained efficiency yields marginally higher values over the operating range, with a strong deterioration at choke due to manufacturing deviations. Qualitatively, the location of peak efficiency could be reproduced by the virtual model.

Schiffmann [12] mentions a probe accuracy of ± 0.2 K for the temperature measurement and ± 2000 Pa for the total and static pressure measurement. Applying the Gaussian error propagation to the experimental data, the measurement error is calculated for the total-total polytropic head coefficient and work input coefficient. Since a real gas is considered, where the thermophysical properties are evaluated by NIST [85] for a given temperature and pressure value, the Gaussian error propagation is solved numerically. Eq. 2.27 shows this procedure for the work input coefficient, where inlet and outlet total enthalpy depend on the total inlet pressure and total inlet temperature as well as total outlet pressure and total outlet temperature, respectively. The measurement error is shown in Fig. 2.20 for the total-total polytropic head coefficient (Fig. 2.20 a)) and the work input coefficient (Fig. 2.20 b)) as a function of percentage design flow coefficient. It is presented as black solid line. In addition, the relative deviation between numerical data set and experimental data set is illustrated as red diamonds. An error for the CFD simulations exist, what has been shown in the grid independence study in the previous subsection. A grid independence study, however, has only been performed for the design point of the compressor provided by Schiffmann [12, 13, 14, 15]. Hence, the numerical error for other operating points than the design point are unknown. Nonetheless, considering further errors, which result from simplifications concerning the solution scheme of the RANS, the relative error in CFD simulations might be located between 0.5 and 1 %. The error in CFD simulations, however, is not shown in this thesis, since an accurate determination of all errors is impossible and too time consumptive. Nonetheless, one have to keep in mind that an error exist in CFD simulations.

$$\Delta\lambda = \frac{\partial\lambda}{\partial p_{t1}}\Delta p_{t1} + \frac{\partial\lambda}{\partial T_{t1}}\Delta T_{t1} + \frac{\partial\lambda}{\partial p_{t2}}\Delta p_{t2} + \frac{\partial\lambda}{\partial T_{t2}}\Delta T_{t2} \tag{2.27}$$

Fig. 2.20 a) clearly suggests, that the total-total polytropic head coefficient is over-estimated by CFD compared to experimental data, since the deviation between CFD and experiment

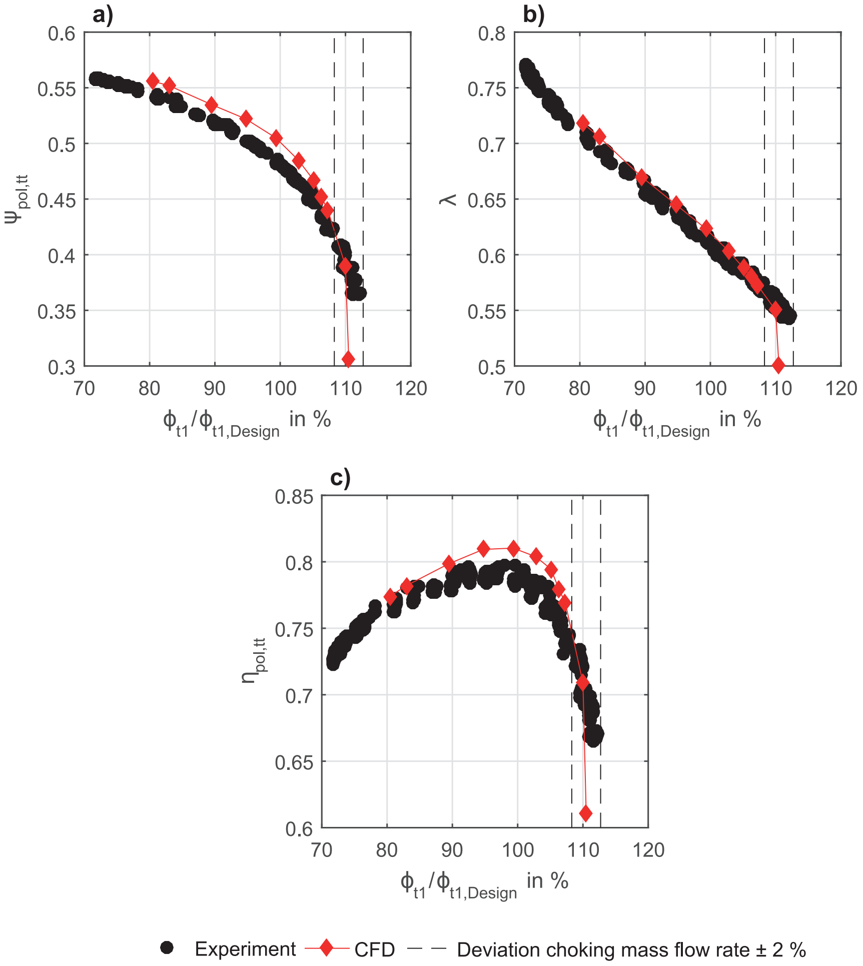

Figure 2.19: Comparison of stage characteristics between CFD setup and experimental data set for the compressor by Schiffmann [12, 13, 14, 15].

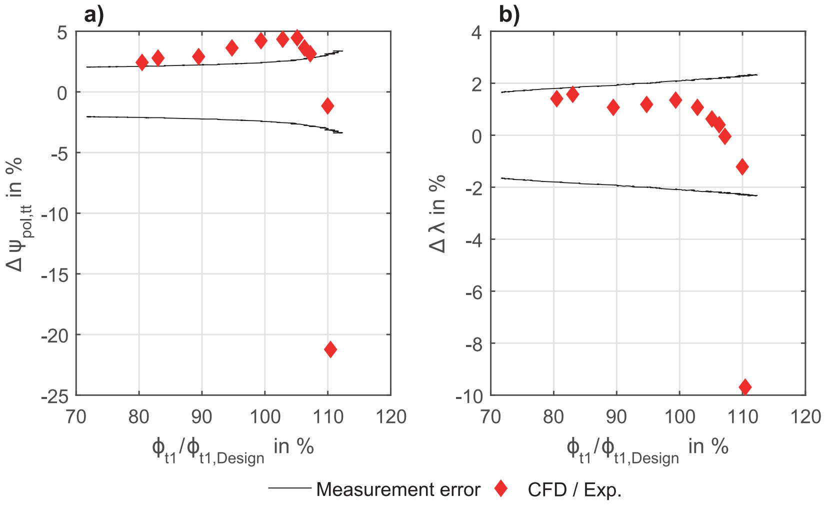

Figure 2.20: Relative deviation between CFD setup and experimental data as well as measurement errors.

is marginally higher as the determined measurement error. CFD predicts the work input coefficient (see Fig. 2.20 b)) in the range where the measurement error is located, thus CFD accurately predicts the work input coefficient.

As shown in Fig. 2.19 and Fig. 2.20, simulation and experiment show a significant deviation around the choking region. This behavior is likely due to manufacturing variations. Small errors during the flank milling process of impeller blades lead to errors in rotor throat area. As a consequence, the machine chokes at a different flow rate. In order to quantify this effect, a reduced-order approach by Lüdtke [17] for calculation of choking mass flow rate was used and a possible difference of 2 % in throat area relative to the ideal one was determined. An alteration of choking mass flow of ± 2 % was calculated and marked as black dashed vertical lines in Fig. 2.19. As can be seen, the deviation in choking mass flow between simulation and experiment lies within the manufacturing variation band. As a consequence, the choke region is excluded from the validation.

For the remaining characteristic, the virtual model provides sufficient accuracy and can be taken as validated. The numerical investigation done in chapter 3 as well as chapter 4 is conducted using this validated numerical setup.

Validation with experimental data obtained from scaled up compressor by Javed et al.:

The numerical setup of the scaled up compressor by Javed et al. [27] is validated using experimental data. The experimental data were obtained with the experimental setup described in subsection 2.4.2. Since no total pressure probes are installed, efficiency is not directly accessible by experimental data. For this purpose, a reduced-order model has been used in order to calculate all thermodynamic conditions (static and total) from the measured total temperature and the measured static pressure. It has to be noted that the total temperature is assumed to be equal than the measured temperature, neglecting heat transfer effects in the thermocouple, which are normally corrected by a recovery factor. The used reduced-order model is based on the fact, that thermodynamic static and total conditions are located at the same entropy thus finding all thermodynamic properties by an iterative approach. Therefore, a blockage value of 0.98 is assumed at the inlet measurement domain and an outlet blockage of 0.9 is assumed at the outlet measurement domain for the reduced-order model. The reduced-order model cannot be applied at other measurement positions (e.g. trailing edge or outlet of the vaneless diffuser), since the assumption of axial flow is not valid at these positions. The time-averaged experimental data of the up-scaled compressor by Javed et al. [27] is tabulated in appendix A. In addition, the work input coefficient obtained from CFD is corrected by the increased power caused by disk friction, what is taken into account by a reduced-order model provided by Daily and Nece [78, 79].

Compared to previously described experiment by Schiffmann [12, 13, 14, 15], the experimental setup uses a collector instead of a volute. The reduced-order volute model to correct numerical data of CFD is not suitable for the collector, since the collector shows a different loss behavior. Furthermore, the experimental setup does not allow to define an experimentally calibrated reduced-order collector model, since total pressure probes are missing at outlet of vaneless diffuser and the collector.

The work input coefficient is calculated from experimental data (inlet total temperature and static pressure as well as outlet total temperature and static pressure) using the reduced-order model to find the corresponding total pressure values at inlet and outlet of the compressor. Fig. 2.21 shows the numerically predicted work input coefficient (red solid line) compared to experimental data (indicated by black error bars) for the design speed line of 50 000 rpm. In addition, the measurement error for work input coefficient (vertically) determined according Eq. 2.27 and the measurement error for global flow coefficient (horizontally) are illustrated in Fig. 2.21, indicated by error bars. This color code is kept for the rest of this subsection.

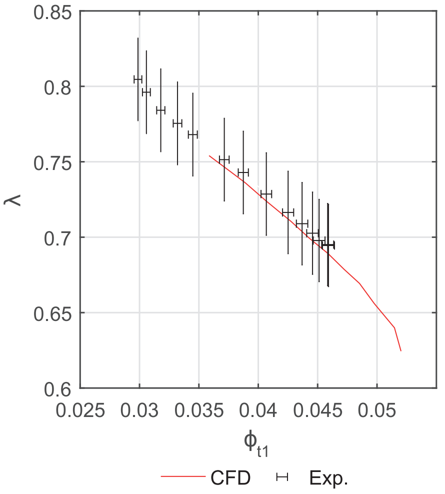

Figure 2.21: Comparison between numerically determined work input coefficient and experimental one for the compressor by Javed et al. [27].

As can be seen by Fig. 2.21, the numerically predicted work input coefficient is in line with the experimental data set. The experimental work input coefficient is slightly under-predicted by CFD, what is mostly caused by additional heat introduced into the system by the bearing cooling occurring during the experimental test. The pressure loss of the refrigeration loop did not allow to run the experiment at higher mass flow rates, thus the numerical data set cannot be validated in that region. On the other hand, the steady-state numerical model has shown convergence issues towards smaller mass flow rates as indicated in Fig. 2.21. The steady-state numerical model was not suitable to simulate operating points at lower mass flow rates, since convergence was not achieved by that approach anymore.

In a next step, the total-static isentropic head coefficient is calculated by the measured static pressure at a measurement station, which is located at 105 % of the impeller diameter. Fig. 2.22 shows the comparison between CFD data and numerical data.

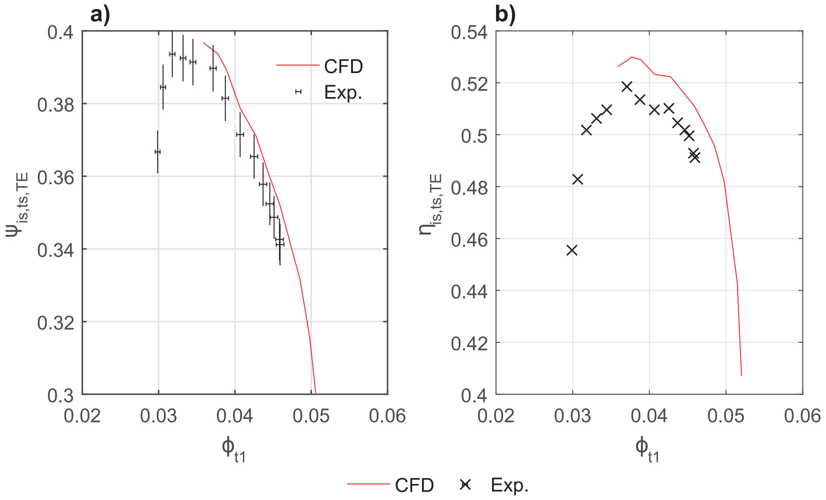

Figure 2.22: Comparison between numerical isentropic total-static head coefficient (a) and isentropic total-static efficiency (b) and experimental data at a location of 105 % times the impeller diameter in the vaneless diffuser.

The numerically predicted isentropic total-static head coefficient (see Fig. 2.22 a)) is slightly over-predicted compared to experiment. However, it is still located within the uncertainty range, thus suggesting an accurate prediction of total-static isentropic head coefficient by CFD. The over-prediction of the head coefficient mostly sources from simplifications done in the CFD model. For instance, surface roughness was neglected in CFD, thus the loss due to wall friction is under-estimated. Another contributor to this deviation is the presence of the collector. Experimental data suggests, that the collector causes an unequal circumferential pressure distribution. This unequal pressure distribution causes a distorting effect on the upstream components. This distorting effect of the collector was observed up to the trailing edge of the impeller in experiments. Nonetheless, the numerical data set suggests a similar trend of isentropic total-static head coefficient, thus the numerical model can be taken as validated at this location.

Caused by the over-prediction of total-static isentropic head coefficient, the total-static isentropic efficiency (see Fig. 2.22 b)) is over-estimated by the virtual model. This numerical over-prediction corresponds to 1 efficiency point between the inlet measurement position and the measurement position, which is located 105 % of the impeller tip diameter.

Furthermore, the total-static isentropic head coefficient is calculated from the measured static pressure near the outlet of the vaneless diffuser. Fig. 2.23 shows a comparison between numerical data set and experimental data set.

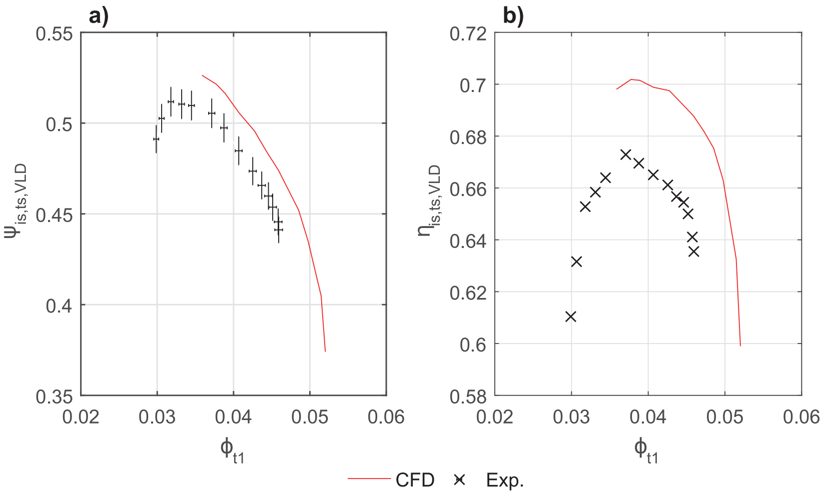

Figure 2.23: Comparison between CFD setup and experimental data set near the outlet of the vaneless diffuser for the scaled up compressor by Javed et al. [27].

Fig. 2.23 a) clearly suggests an over-prediction of total-static head coefficient by the numerical setup compared to the experimental data set. The distorting effect of the collector is more pronounced compared to the location located behind the trailing edge of the impeller and the pressure rise is more deteriorated at this position. Nonetheless, the numerical data set features a similar slope as suggested by experimental data.

As a consequence, CFD over-estimates the total-static isentropic efficiency between the inlet measurement position and the measurement position before the outlet of the vaneless diffuser between 2 and 3 efficiency points (see Fig. 2.23 b)).

The validation of the numerical setup with experimental data suggested slight discrepancies between numerical data set and experiments. The work input coefficient which is mostly determined by the rotating impeller is accurately predicted by CFD. Nonetheless, the total-static isentropic head coefficient is over-estimated by the virtual model and this effect is amplified close to the asymmetric collector. However, both numerical and experimental data feature the same trend, thus the numerical model is used for further investigation of this compressor done in chapter 4 and 5.

In addition, further experimental results for different relative clearance ratios of this compressor (see chapter 4) and different shroud blade angle distributions (see chapter 5) have been conducted and validated using experimental data (see appendix C and appendix D). A similar trend in validation as presented in this subsection has been observed and further supports the quality of the numerical model.

Overall, the comparison of numerical models (CFD) to experimental data provided by Schiffmann [12, 13, 14, 15] and Javed et al. [27] suggested a remarkable agreement for both compressor geometries. Work input coefficient is accurately predicted and the head coefficients are over-estimated, which is caused by simplifications of the numerical setup. The trend and slope of the efficiency curves as well as the accurate prediction of the peak efficiency point, however, are in line with experimental data, thus the numerical models of different compressor geometries can be taken as validated. These numerical models are used in chapter 3, chapter 4 and chapter 5.

3 Scaling analysis of a centrifugal compressor

The impact of geometrical centrifugal compressor scaling on its performance is described in this chapter. Empirical correlations to account for performance deterioration caused by geometrical scaling of a centrifugal compressor are assessed in the operating range of the design speed line. An approach provided by Casey and Robinson [49] is assessed and further used to develop a new correlation, which allows to predict performance of scaled compressor geometries as a function of the global flow coefficient.

In a next step, the relative tip clearance ratio is altered for differently scaled impellers. Compressor literature is coherent in seeing the pressure difference between the blade pressure and the blade suction side as the main driver of tip leakage jet. This phenomenon is independent of the Reynolds number, since it only depends on the pressure difference between the blade surfaces. Nonetheless, the tip leakage jet also interacts with the shroud boundary layer and mixes with the main flow by re-entering the blade channel. These are Reynolds number dependent processes. Hence, the question arises whether these effects impact the clearance losses by scaling an impeller and cause increased performance deterioration, especially towards reduced-scale.

In a last step, a design example is given which illustrates down-scaling a compressor by changing its relative clearance ratio. The results suggest that the expected performance deterioration is related rather to a change of relative clearance at trailing edge than to a change of compressors Reynolds number. Based on a flow pattern analysis, design guidelines for dealing with large relative clearance ratios are given.

The results of this chapter have been submitted to the journal of turbomachinery (ASME).

3.1 Impact of low Reynolds numbers on compressor performance

3.1.1 Geometrical scaling of the reduced-scale centrifugal compressor by Schiffmann

The impact of geometrical compressor scaling on the performance of the compressor provided by Schiffmann [12, 13, 14, 15] is assessed numerically. Therefore, the compressor unit was

scaled into 3 different geometrical feature sizes. The scaling factors were selected to be 0.75 (A), 1 (B), 2 (C) and 4 (D) and the main specifications of each geometry are listed in Table 3.1. In order to obtain similar head and pressure ratios for different scaling cases, the rotational Mach number (see Eq. 2.8) was held constant. The relative tip clearance ratio was kept constant at 5 % in a first step and was varied in a second step, ranging from 3 % to 15 %. The Reynolds number shown in Table 3.1 is evaluated according to Dietmann and Casey [50, 51] (see Eq. 1.6), where the arithmetic average between meridional blade length M of hub and shroud is taken as a characteristic length of the impeller.
The solver setup for this analysis is presented in appendix B.

Table 3.1: Scaling factor and resulting motor speeds of the scaled compressor geometries.

Test case		**A**	**B**	**C**	**D**
Geometric scale	[-]	0.75	1.	2.	4.
Relative tip gap	[%]	5	5	5	5
n	[krpm]	240	180	90	45
$\boldsymbol{M_{u2}}$	[-]	1.27	1.27	1.27	1.27
Design point $\boldsymbol{Re}$	$[-]*10^5$	6.47	8.66	17.9	35.2

3.1.2 Verification of scaling approach

Fig. 3.1.2 shows the location of best efficiency points in a friction factor-Reynolds number diagram as red diamonds, evaluated using the friction model provided by Dietmann and Casey [50, 51] (see appendix B). The rotational Mach number for all four different scaling cases is maintained constant, thus leading to different rotor speeds as well as different Reynolds numbers caused by the varying characteristic length of each scaled impeller. The walls are assumed to be hydraulically smooth in the numerical setup (CFD).

By maintaining the same rotational Mach number for each scaling case, a constant total-total polytropic head coefficient is achieved. Fig. 3.2 a) shows the total-total polytropic head coefficient as a function of the total-static pressure ratio and suggests constant head rise for a given total-static pressure ratio. All compressors achieve the same head rise, the operating point, however, is shifted towards smaller mass flow rates with a decrease of feature size. The scaling case A is plotted as green stars, the baseline configuration (B) as black dots, the scaling case C as red crosses and scaling case D as blue diamonds. This color code is kept for the remainder of this chapter. In addition, the design point is drawn as dashed vertical line in Fig. 3.2. The compressor operates at choke towards the left of this diagram and close to surge towards the right of Fig. 3.2.

Fig. 3.2 b) shows the work input coefficient as a function of the total-static pressure ratio. The work input decreases with geometrical scale, thus larger scale compressors show increased efficiency. This is caused by the so-called Reynolds number effect (see Dietmann and Casey [50, 51]), which causes a deterioration in efficiency as well as shift of an operating point towards smaller flow rates.

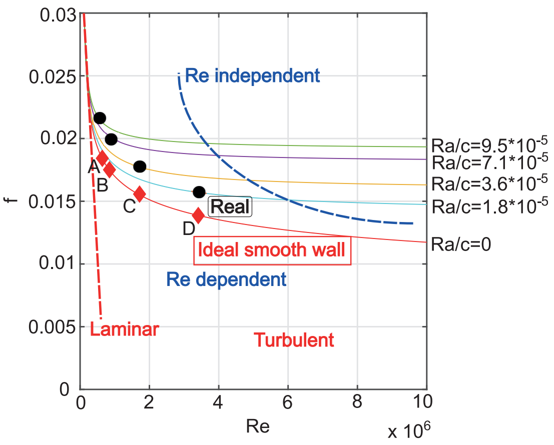

Figure 3.1: Reynolds number-friction factor-diagram:
Red dashed line: separation between laminar and turbulent flow **Blue dashed line:** Separation between Re dependent and Re independent friction factor **Black points:** Compressor operating points in real machine **Red points:** Compressor operating points idealized with smooth wall

3.1.3 Performance alteration caused by Reynolds number effect

Fig. 3.3 a) and b) and Fig. 3.4 show a comparison of compressor performance in terms of total-total polytropic head, work input coefficient and total-total polytropic efficiency. The dimensionless performance values are plotted against the global flow coefficient for a rotational Mach number of 1.27.

Fig. 3.3 a) suggests, that all scaling cases feature the same slope of total-total polytropic head coefficient, but the curves are shifted towards lower flow coefficients with decreasing scale. As a consequence, by operating two similar compressors of different scale in such way that the head remains constant, the larger one operates at higher flow coefficients.
By comparing the work input coefficient of all scaling cases, Fig. 3.3 b) shows a virtually identical distribution. Since the work input coefficient mainly depends on the blade outlet angle, a geometrical feature which remained constant across the scaling exercise, different scaling cases achieve the same work input for a given flow coefficient.

Fig. 3.4 clearly suggests, that the total-total polytropic efficiency and the global flow coefficient of one operating point is shifted towards higher values by increasing compressors feature size. The red triangular drawn in Fig. 3.4 demonstrates this effect for the best efficiency points.
Two main effects cause efficiency deterioration by decreasing the feature size, namely the relative surface roughness and the Reynolds number effect. The former increases by decreasing the geometrical size of the compressor, yielding higher frictional losses. However, the numerical results are obtained assuming hydraulically smooth walls, thus the impact of increased relative surface roughness is not captured. From this point of view, the drop in efficiency due to a decrease in feature size is entirely attributed to alteration of the Reynolds number.
The shift of an operating point towards smaller flow rates by down-scaling the compressor

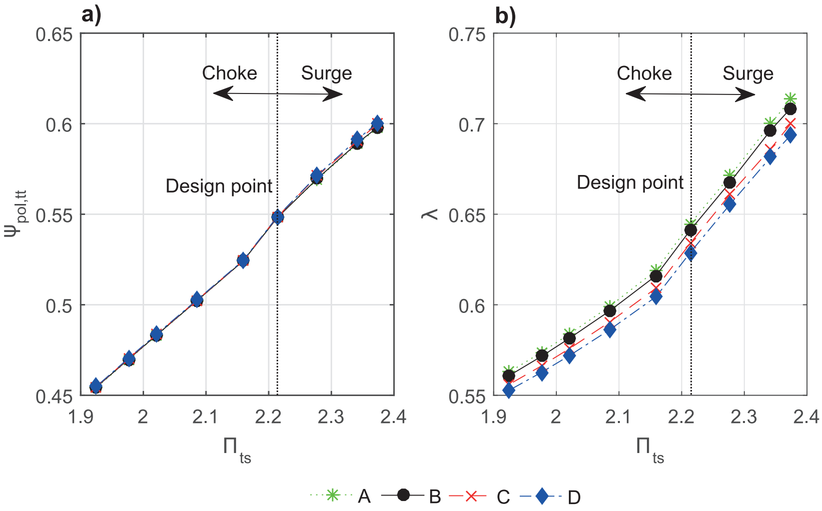

Figure 3.2: Total-total polytropic head coefficient (a) and work input coefficient (b) as a function of the total-static pressure ratio for the four scaling cases.

is caused by the different boundary layer thickness, thus indirectly related to the Reynolds number effect. Since the friction factor increases with a decreasing size, the boundary layers are relatively thicker, thus yielding an increased flow blockage. More explanation about this effect is provided in appendix B.

This scaling analysis suggests, that an accurate prediction of scaled compressor performance needs to take both the deterioration in efficiency and the shift of operational points into account. The next subsection provides an assessment of empirical correlations available in literature as well as an alternative model of the author.

3.1.4 Assessment of empirical correlations used for scaling

This subsection assesses the performance prediction of various empirical correlations to account for performance alteration caused by geometrical compressor scaling. The assessed empirical correlations are the one by Moody [52, 44] (see Eq. 1.7), Ackeret and Medici [53] (see Eq. 1.9) and Dietmann and Casey [50, 51] (see Eq. 1.11 and Eq. 1.12). In addition, an alternative model based on models by Casey and Robinson [49] and Dietmann and Casey [50, 51] is suggested.

Fig. 3.2 a) suggests same total-total head coefficients for same total-static pressure ratios. Hence, the head coefficient is not contributing to the deterioration of efficiency for operating points, which achieve same head and pressure rise. The work input, however, increases with a decrease of compressors feature size, thus compressor efficiency is lowered. Hence, the change in efficiency can be modeled as a function of the change in work input coefficient, where the change in work input coefficient is depending on the global flow coefficient. Eq. 3.1 provides the modeling of change in efficiency depending on the corresponding change of

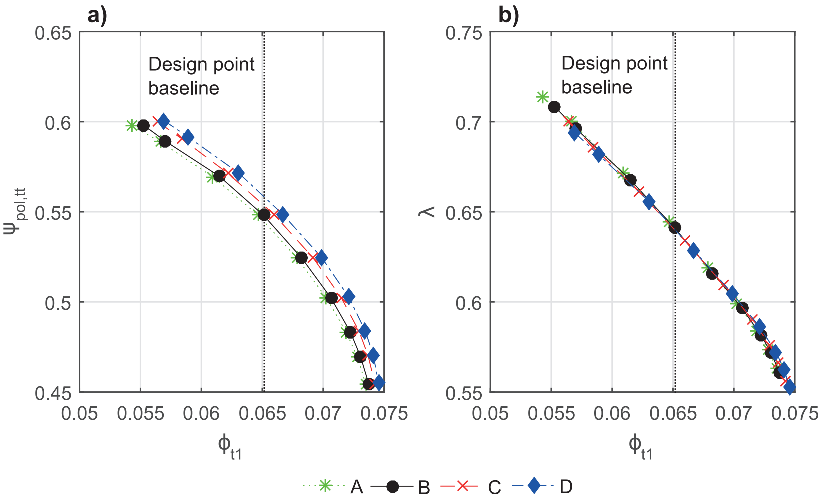

Figure 3.3: Total-total polytropic head coefficient (a) and work input coefficient (b) as a function global flow coefficient at design speed for the four scaling cases.

work input coefficient.

$$\begin{aligned}\Delta\eta_{pol,tt} = \eta_{Scale} - \eta_{ref} = \frac{\psi_{pol,tt,Scale}}{\lambda_{Scale}} - \frac{\psi_{pol,tt,ref}}{\lambda_{ref}} = \\ -\eta_{ref}\frac{\lambda_{Scale}-\lambda_{ref}}{\lambda_{Scale}} = -\eta_{ref}\frac{\Delta\lambda}{\lambda_{ref}+\Delta\lambda}\end{aligned} \tag{3.1}$$

It has to be noted, that Eq. 3.1 is only valid if the impact of relative surface roughness is neglected, leading to the same head coefficients for a given total-static pressure ratio. The change of the work input coefficient is modeled similarly as the change in efficiency as suggested by Dietmann and Casey [50, 51]. Fig. 3.6 and Fig. 3.7 suggest a linear dependence of efficiency as a function of the Darcy-Weisbach friction coefficient. Since the head coefficient is constant for an operating point with same total-static pressure ratio, the work input coefficient also depends linearly on the Darcy-Weisbach friction coefficient. Hence, the slope of this linear function represents the change in work input coefficient. Performing this for operating points having the same total-static pressure ratio in the operating range of the compressor, the change in work input coefficient depending on the global flow coefficient is obtained.

In a similar manner as done for parameters B_{ref} and C_{ref} (Eq. 1.11 and Eq. 1.12), a parameter E_{ref} is introduced, which models the slope of the work input curve according to Eq. 3.2. This parameter is evaluated for operating points showing the same total-static pressure rise and head, respectively, thus depending on the global flow coefficient. The parameter E_{ref} is fitted by a polynomial of 5^{th} order. The friction factors shown in Eq. 3.2 are evaluated according the

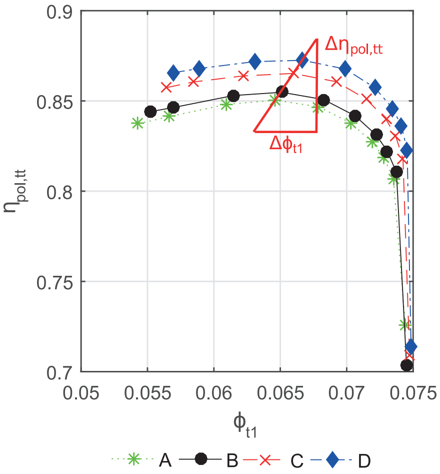

Figure 3.4: Total polytropic efficiency as a function of the global flow coefficient at design speed for the four scaling cases.

surface friction model provided by Dietmann and Casey [50, 51] (see appendix B).

$$\Delta\lambda = -E_{ref}\frac{\Delta f}{f_{ref}}$$

$$E_{ref} = -0.0045X^5 - 0.0048X^4 + 0.0134X^3 + 0.0108X^2 + 0.0026X - 0.0592 \tag{3.2}$$

$$X = \left(\frac{\phi_{t1ref} - 0.0663}{0.007}\right)$$

The parameter C_{ref} is modeled in a similar approach as the parameter E_{ref} (see Eq. 3.2) and is fitted by a polynomial of 5^{th} degree. Eq. 3.3 shows an equation to correlate the parameter C_{ref} as a function of the global flow coefficient.

$$\frac{\Delta\phi_{t1}}{\phi_{t1}} = -C_{ref}\frac{\Delta f}{f_{ref}}$$

$$C_{ref} = 0.0024X^5 - 0.0061X^4 - 0.0341X^3 - 0.0088X^2 - 0.0059X + 0.1174 \tag{3.3}$$

$$X = \left(\frac{\phi_{t1ref} - 0.0663}{0.007}\right)$$

The empirical models introduced in subsection 1.1.2 are assessed by using performance data of baseline case B as input (reference) and the performance data of scaled cases A, C and D as output. Total-total efficiency predicted by the empirical model is then compared to CFD data. Two different sets of parameters a and n have been investigated for Ackeret and Medici's [53] model, since the model strongly depends on these parameters. Pfleiderer and Petermann [29] suggest ranges for both parameters a and n. Hence, two scenarios are investigated for Ackeret and Medici's [53] correlation, where the limiting values suggested by Pfleiderer and

Petermann [29] are considered. In the first scenario (Pfleiderer1), the values have been chosen as 0.7 for a and 4 for n. In the second scenario (Pfleiderer2), the parameter a is set to 0.5 and n to 7. Both parameter sets are presented in Eq. 3.4.

$$\begin{aligned} \frac{1-\eta}{1-\eta_{ref}} &= 0.3 + (1-0.3)\left(\frac{Re_{ref,d2}}{Re_{d2}}\right)^{\frac{1}{4}} \quad \text{(Pfleiderer1)} \\ \frac{1-\eta}{1-\eta_{ref}} &= 0.5 + (1-0.5)\left(\frac{Re_{ref,d2}}{Re_{d2}}\right)^{\frac{1}{7}} \quad \text{(Pfleiderer2)} \end{aligned} \tag{3.4}$$

Fig. 3.5 shows the resulting total-total polytropic efficiency over the global flow coefficient for the three different scaling cases. CFD results are drawn as black dots, Moody's [52, 44] model is illustrated as green stars, Ackeret and Medicis' [53] model with two different parameter choices in blue squares and diamonds, Dietmann and Caseys' [50, 51] model is presented as red crosses and the authors approach is shown as pink squares.

In general, all empirical model reproduce the shape of the CFD performance curve of the baseline compressor for the scaled cases. However, deviations to CFD data occur in terms of efficiency magnitude and shift of peak efficiency.

The empirical model provided by Moody [52, 44] shows a strong offset in efficiency for all scaling cases. The down-scaled case A is strongly under-predicted and the up-scaled cases C and D are over-predicted. Since Moody's [52, 44] model only depends on the impeller outlet diameter ratio of differently scaled cases, this value is not suitable to account for alteration of performance caused by different Reynolds numbers. In addition, Moody's [52, 44] model does not account for shift in flow coefficient, thus this effect is not captured.

Fig. 3.5 shows the strong parameter dependency of a and n occurring at Ackeret and Medici's [53] model. Since these parameters are not known during the design process, a compressor designer needs to take care on how he chooses these parameters. The scenario "'Pfleiderer2"' suggests and increased error in efficiency, which is amplified by increasing the scaling factor, thus the scaling case D shows the strongest deviations. The scenario "'Pfleiderer1"' is yielding increased accuracy compared to CFD data, however, the model leads to an under-prediction of efficiency with increasing scale. Since their model does not include a flow coefficient correction, the shift in flow coefficient is not captured.

Dietmann and Caseys' [50, 51] model provides a good quality in terms of efficiency prediction for all scaling cases. The Reynolds number in this model is evaluated using the chord length as characteristic length, which seems to be a better metric to characterize the Reynolds number effect compared to the other models, which use impeller outlet diameter as characteristic length. Slight deviations towards smaller mass flow rates are observed for this model, indicated by an under-prediction occurring at up-scaled cases and an over-prediction at down-scaled case. One possible contributor could be that Dietmann and Caseys' [50, 51] model is obtained from experimental results of full compressor stages, including asymmetric parts like the

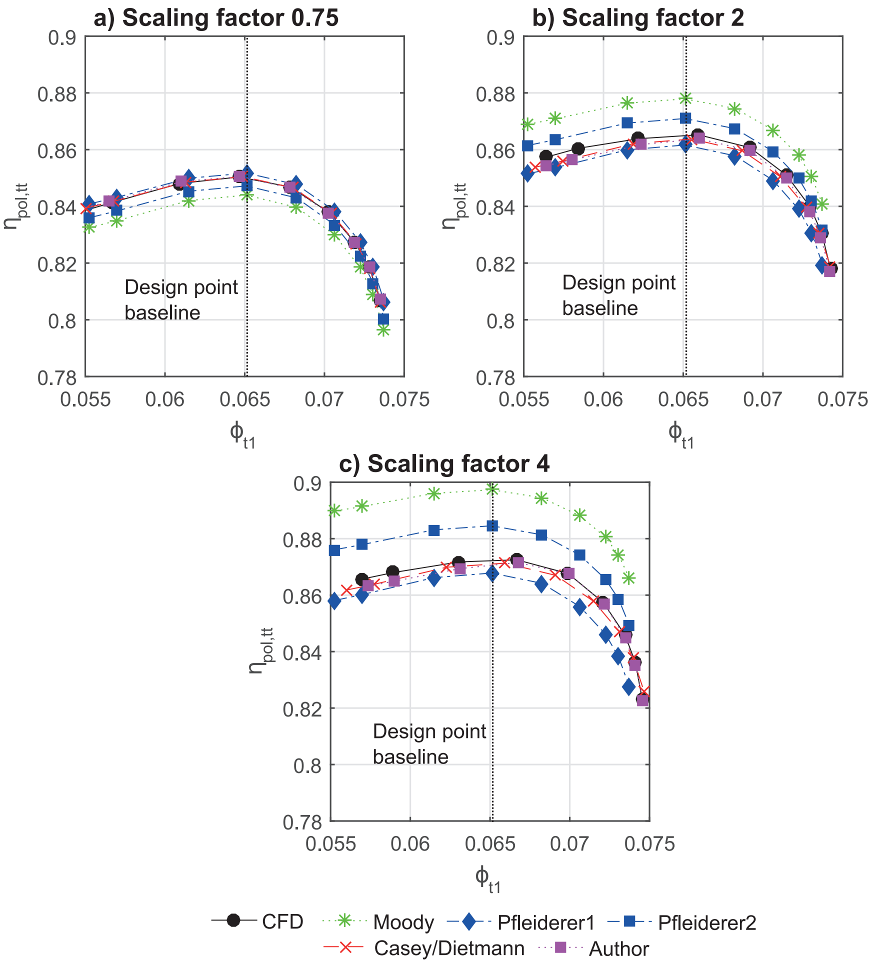

Figure 3.5: Prediction quality of various correlations to account for Reynolds number effect for a scaling factor of 0.75 (a), 2 (b) and 4 (c).

volute. The volute has a strong impact on component matching as well as on the shape of the resulting performance curve. The numerical model used to simulate the Reynolds number effect, however, consists of impeller and vaneless diffuser, without considering the effect of the volute. The shift of the best efficiency points is captured by Dietmann and Caseys' [50, 51] model, however, it suggests a less pronounced shift of operating points compared to CFD results, showing the strongest deviations for case D. Dietmann and Caseys' [50, 51] model is calibrated with test data additionally including the impact of relative surface roughness, however, the presented numerical model is performed using hydraulically smooth walls. As a consequence, boundary layer growth and blockage is reduced compared to reality, what serves as explanation for the discrepancy of Dietmann and Caseys' [50, 51] model in terms of flow coefficient shift.

The author's model shows the best agreement between numerical data and data predicted by this reduced-order model. The results are almost identical with the one of Dietmann and

Caseys' [50, 51] model at low flow rates. Nonetheless, an improved prediction quality of shift in flow coefficient compared to Dietmann and Caseys' [50, 51] model is observed towards higher flow coefficients. The author's model, however, is derived from the investigated compressor geometry, thus Dietmann and Caseys' model [50, 51] shows more general validity, since their model is derived from a large amount of test cases.
The standard deviation between CFD data and data of the reduced-order models is listed in Table 3.2.

Table 3.2: Standard deviations of reduced-order models relative to numerical model.

Test case		C	D	A
Model	Parameter	Std deviation $\Delta\ S$ in %		
Moody	η	2.0	3.8	1.0
Pfleiderer1	η	0.5	0.6	0.2
Pfleiderer2	η	1.1	2.1	0.5
Dietmann	η	0.3	0.3	0.1
	ϕ_{t1}	0.9	1.2	0.6
Author	η	0.3	0.2	0.1
	ϕ_{t1}	0.2	0.3	0.3

3.1.5 Quality of used modeling approach

It was demonstrated in the previous subsection, that Dietmann and Caseys' [50, 51] as well as the author's model accurately predict the change in compressor performance caused by the Reynolds effect in the entire operating range of the investigated compressor. Both approaches use a model provided by Casey and Robinson [49]. The change of compressor efficiency due to an alteration of Reynolds number is modeled as linear relationship depending on the friction factor. Therefore, a flat plate model for surface friction suggested by Gülich [48] was adapted to match with compressor data. Details about this modified friction model can be found in Dietmann and Casey [50, 51] and the equations to calculate the friction factor of a compressor are summarized in appendix B.

The polytropic efficiency is shown for all four scaling cases at their design point as a function of the friction factor in Fig. 3.6. As suggested by this graph, all efficiencies can be connected by a line, thus the linear modeling approach of Casey and Robinson [49] can be confirmed for this particular compressor. In addition, it demonstrates the practicability of Gülichs [48] friction model for radial turbomachinery.

The y-intercept of the line, which connects the efficiency of all scaling cases, represents a situation where the friction factor is zero and no surface roughness occurs, thus the compressor performance is only deteriorated by losses which are independent of the friction factor. These losses are called Reynolds number independent losses.
In order to confirm the order of magnitude of Reynolds number independent losses, an addi-

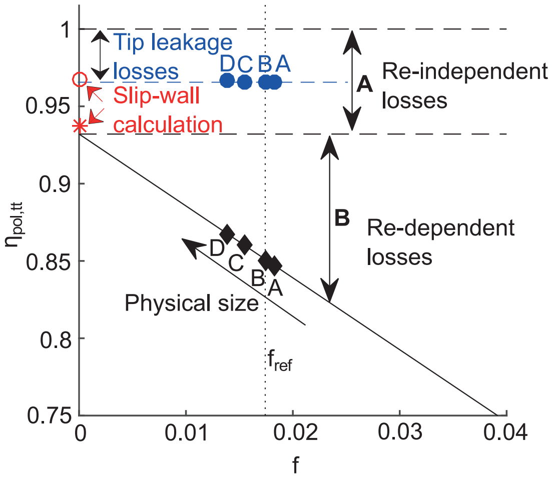

Figure 3.6: Total-total polytropic efficiency and tip leakage loss as a function of the Darcy-Weissbach friction coefficient after Casey and Robinson [49] and Dietmann and Casey [50, 51] plotted for a relative tip clearance of 5 %.

tional numerical simulation has been performed, where all surfaces are treated as slip walls. Hence, the compressor performance is only governed by Reynolds number independent losses in this numerical setup. The point is marked as red star in Fig. 3.6. The efficiency drop of the slip-wall simulation is suggested to be 6.28 % and the expected efficiency drop determined using the method of Casey and Robinson is 6.79 %, thus yielding a deviation of around 8 %, corresponding to an over-prediction of 0.51 efficiency points for the modeling approach of Casey and Robinson [49]. This further demonstrates the good prediction quality of Casey and Robinsons' [49] model.

In order to determine the efficiency drop associated to tip leakage, Eq. 3.5 is used, assuming that the whole kinetic energy of the tip jet normal to the tip gap is lost due to mixing with the main flow (see Eq. 1.4).

$$\Delta\eta_{Cl} = \frac{P_{Cl}}{P_{total}} \tag{3.5}$$

The losses related to tip leakage of the different scaling cases are illustrated as blue dots in Fig. 3.6. Since all of the points can be connected by a horizontal line, the loss of kinetic tip jet energy is suggested to be Reynolds number independent. Furthermore, the loss of kinetic tip jet energy was also determined for the slip-wall simulation and is marked as red circle in Fig. 3.6 on its ordinate. All five points have a standard deviation of 0.44 %, suggesting that all losses which are related to tip leakage are independent of the Reynolds number.

Furthermore, Fig. 3.7 a) and b) show the total-total polytropic efficiency as a function of the friction factor for one operating point near surge (Fig. 3.7 a)) and one operating point near choke (Fig. 3.7 b)). It suggests that other operating points having the same total-static pressure ratio also linearly depend on the friction factor, thus the prediction range of the model provided by Casey and Robinson [49] and Dietmann and Casey [50, 51], respectively, can be extended to off-design operating points.

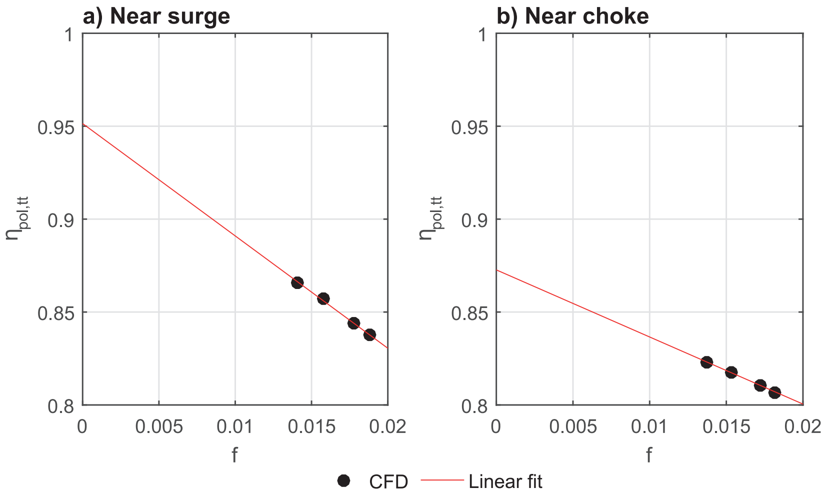

Figure 3.7: Total-total polytropic efficiency as a function of the Darcy-Weissbach friction coefficient plotted for operating points having the same total-static pressure ratio near surge (a) and operating points having the same total-static pressure ratio near choke (b).

This subsection clearly shows, that the model by Casey and Robinson [49] combined with an adapted flat plate friction model suggested by Gülich [48] is well suited to predict efficiency deterioration caused by altering the Reynolds number. Furthermore, it has been figured out that Casey and Robinsons' [49] linear approach can be applied for operating points having the same total-static pressure ratio in the entire compressor operating range. In addition, the investigation of tip leakage losses demonstrated a Reynolds number independence of tip leakage losses for the design point by assuming that all kinetic energy of the tip jet normal to the tip gap is lost.

3.1.6 The role of transition

A significant change of the boundary layer profile occurs with an increase of the Reynolds number, where the boundary layer profiles change from a laminar profile to a turbulent profile. The zone in between these two profiles is called transition zone where turbulence originates. Transition occurs in internal as well as external flows. For instance, the boundary layer profile along a flat plate shows the following behavior as described in Schlichting [88]: Firstly, a laminar boundary layer profile evolves along the flat plate. The Reynolds number along the flat plate increases with an increase of the distance between a position on the flat plate and its leading edge. Two dimensional Tollmien-Schlichting instability waves occur at the so called indifference point, where the transition starts. Three dimensional instabilities - so called Λ-vortices - develop further downstream of the flat plate, these Λ-vortices are then separated by turbulent spots, what is the completion of transition, and the boundary layer becomes turbulent.

The impact of transition on the numerical results has been neglected in this thesis. However, transition might have a certain impact on the compressor performance, since the friction coefficient changes dramatically in the region, where transition occurs. Following the flat plate theory, the boundary layer along a flat plate is firstly laminar, followed by a region, where transition occurs, and becomes then turbulent. On the one hand, the characteristic Reynolds number for the flat plate contains the distance between leading edge and a certain position of the flat plate. On the other hand, a critical Reynolds number is defined according to Schlichting [88], where the transition ends and the boundary layer becomes turbulent. Hence, the transition zone in a reduced-scale compressor is shifted to the rear part of the impeller blade compared to a larger size compressor and increased frictional losses and boundary layer blockage occur.

Since reduced-scale centrifugal compressors having tip diameters of less than 20 mm are investigated in this scaling analysis, transition might have a certain impact on the compressor performance. The role of transition has been, however, neglected in the numerical studies of this PhD thesis. The question therefore arises, whether the numerical approach neglecting transition can be justified.

In a first step, the Reynolds number is calculated according the analogy model, which considers the boundary layer profiles in the impeller passage similar to the one in a pipe flow, where the characteristic velocity and characteristic length, according to Lüdtke [47], are chosen to $\frac{u_2}{2}$ and $2b_2$, respectively. Table. 3.3 shows the Reynolds numbers for the different scaling cases A to D.

Table 3.3: Reynolds numbers for various test cases evaluated according the pipe flow analogy model (see Lüdtke [47]).

Test case		**A**	**B**	**C**	**D**
Design point *Re*	$[-]*10^5$	1.11	1.48	2.96	5.91

The critical Reynolds number for pipe flow, where the boundary layer becomes turbulent, is $Re_{crit} = 2300$ according to Schlichting [88]. Aungier [45] defines the critical Reynolds number for termination of transition between 2000 and 4000. As suggested by Table 3.3, the smallest Reynolds number of case A is around 25 up to 50 times higher than the critical Reynolds numbers thus the role of transition is negligible following the analogy model of pipe flow.

As stated in subsection 1.1.2, the boundary layer profiles along the blades in turbomachinery are more similar to the one of a flat plate compared to a pipe flow, thus the role of transition needs to be also investigated according the flat plate theory. Schlichting [88] defines the Reynolds number along a flat plate according to Eq. 3.6:

$$Re = \frac{w_\infty M}{\nu} \tag{3.6}$$

As suggested by Schlichting [88], the critical Reynolds number, where the transition zone ends and the boundary layers become turbulent occurs between Reynolds numbers of $Re_{crit} =$

350000 – 1000000. As indicated by Table 3.1, the machine Reynolds number of cases A and B is located in the range of critical Reynolds numbers of the transition zone.

In a next step, the Reynolds number is evaluated along the mid span for cases A to D. Fig. 3.8 a) and b) shows the Reynolds number as a function of the normalized length of the mid span for compressor test cases A to D. The range of critical Reynolds number for flat plates (according to Schlichting [88]) is additionally plotted in Fig. 3.8, in order to demonstrate the role of transition. Fig. 3.8 b) provides a more detailed view of Fig. 3.8 a) for the test cases A and B.

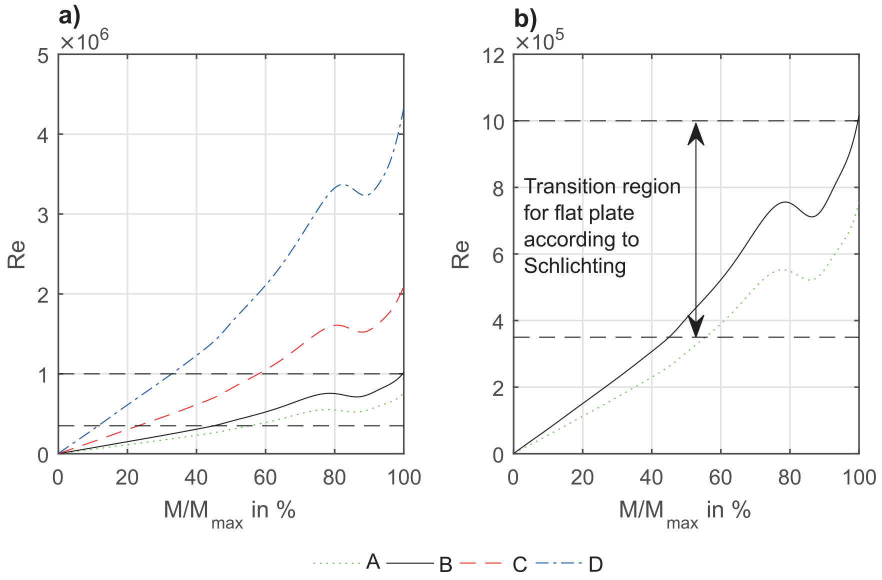

Figure 3.8: (a) Evolution of the Reynolds number (see Eq. 3.6) along the mid span of the blade for test cases A to D. (b) More detailed view of (a) for compressors A and B, indicating the critical Reynolds number for end of transition according to Schlichting [88].

As indicated by Fig. 3.8 a) and b), the role of transition becomes of importance for compressors B and A. Depending on the critical Reynolds number, transition occurs either up to 50 % of the normalized blade length or along the entire blade.

Along a compressor blade, however, other mechanisms like curvature and secondary flows are present, which further shift the critical Reynolds number to lower values. Furthermore, Schlichting [88] claims that the boundary layer stays laminar in case the pressure gradient decreases (nozzle) and an increase of the pressure gradient results in an instantly transition (diffuser). As a consequence, transition in a compressor is terminated earlier than along a flat plate and plays a less important role in a centrifugal compressor, since the flow mechanisms in a centrifugal compressor tend to amplify the onset of transition. For instance, case C represents the feature size of an automotive turbocharger and transition might have a certain impact according to Fig. 3.8 a). However, empirical knowledge shows that transition is negligible for such size, even though the Reynolds number are smaller than the ones for the impellers presented in this work.

Furthermore, Dietmann [51] has compared a numerical study using a turbulence model with a numerical study using a transition model (intermittency model) for a reduced-scale air-compressor. Dietmann's [51] compressor had a similar size than the baseline compressor B. The Reynolds numbers in Dietmann's [51] study, however, are smaller than in this thesis, what is caused by the lower density of air. Hence, the transition might play an even more important role in Dietmann's [51] study than in this thesis. Nonetheless, a remarkable difference between CFD simulation considering transition and the one neglecting transition has not been figured out by Dietmann [51] thus the study has been performed neglecting transition.

Although transition might play a certain role for the compressor versions having the smallest feature size, the effect on the global performance is not significant, which is further supported by the good agreement between experimental and numerical data for the reduced-scale compressor provided by Schiffmann [12, 13, 14, 15] (see subsection 2.6.4). Nonetheless, the role of transition needs to be further investigated, since it has a certain impact on the boundary layers and hence performance and stability of a centrifugal compressor.

3.2 Reynolds number independence of tip leakage loss

It has been shown above that the tip leakage loss is independent of the scaling factor at the design point of the compressor, having a relative tip clearance ratio of 5 %.

In a next step, relative tip clearance ratio is altered, ranging from 3 up to 15 %. For each relative clearance ratio, the compressors were scaled by applying the scaling factors 0.75 (A), 1 (B), 2 (C) and 4 (D). Same operating points were defined to have the same total-static pressure ratio and the analysis is performed in the operating range of the design speed line.

The method by Casey and Robinson [49], which is explained in subsection 1.1.2, is applied for each clearance ratio in the operating range of the compressor. Reynolds number independent losses A and Reynolds number dependent losses B_{ref} are defined for operating points having the same total-static pressure ratio, shown in Fig. 3.9 a) and Fig. 3.9 b), respectively. The following color code is used in this section: A relative clearance ratio of 3 % is presented as blue diamonds, a relative clearance ratio of 5 % as black circles, a relative clearance ratio of 7.5 % as red cross, a relative clearance ratio of 10 % as green square and a relative clearance ratio of 15 % as magenta triangle.

Fig. 3.9 a) suggests an increase of the Reynolds number independent losses A with an increase in relative tip clearance ratio. Furthermore, Fig. 3.9 b) suggests that the relative clearance ratio has no impact on the Reynolds number dependent losses, since all points collapse to one curve.
In addition, the efficiency drop due to tip leakage (see Eq. 3.5) was calculated for each clearance ratio thus further splitting up the Reynolds number independent loss. Fig. 3.10 shows the loss related to tip leakage $\Delta\eta_{Cl}$ and suggests, that the tip leakage loss scales with relative clearance ratio. The remaining Reynolds number independent loss $A - \Delta\eta_{Cl}$ suggest a clearance ratio

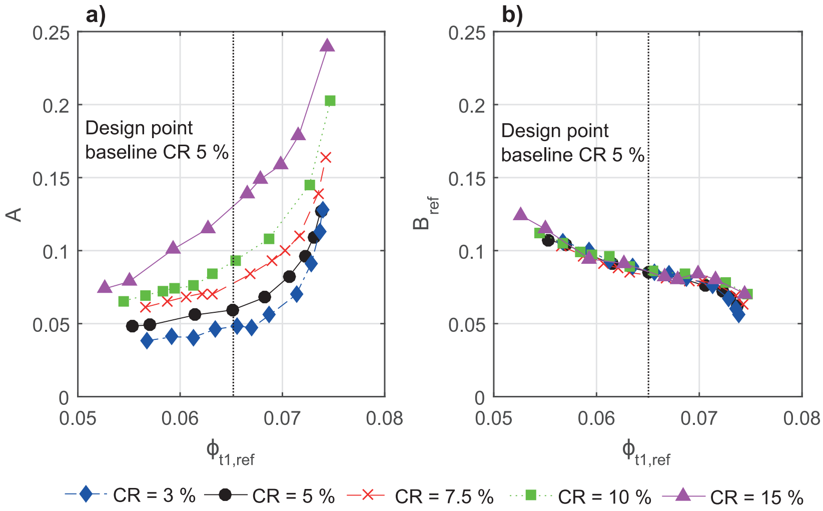

Figure 3.9: Reynolds number independent (a) and dependent losses (b) for five different clearance ratios as a function of the global flow coefficient.

independent behavior of this loss in the entire operating range of the compressor. This allows to introduce a further loss breakdown of the Reynolds number independent losses into losses, which are depending on the relative clearance ratio and losses which are independent.

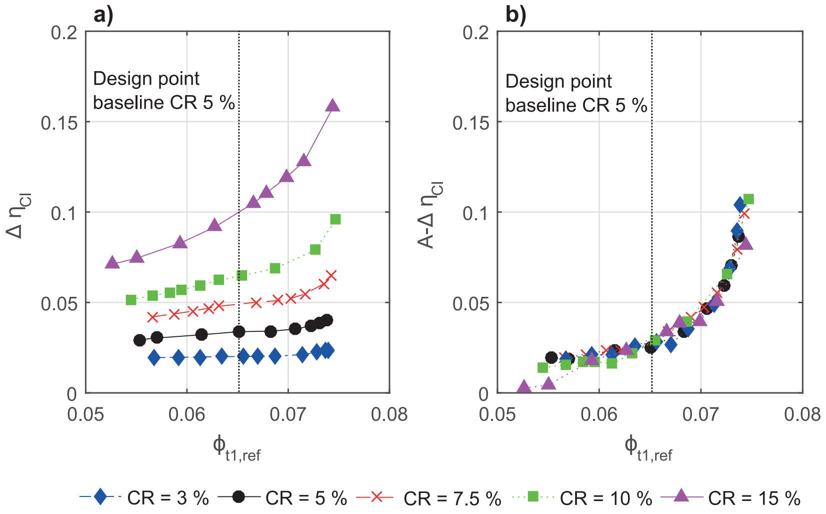

Figure 3.10: Efficiency drop due to tip leakage (a) and remaining Reynolds number and relative clearance ratio independent loss (b) as a function of the global flow coefficient.

Since B_{ref} and $(A-\Delta\eta_{Cl})$ all collapse with the same curve, this analysis suggests that the tip leakage losses are independent of scale such as incidence loss or deceleration loss, which are mainly depending on the blade loading. The tip clearance loss merely provides a loss offset to the departure of Re-dependent losses on the y-axis, an offset, which scales with the clearance. Thus a compressor designer does not need to consider further performance penalization by down-scaling a compressor as long as the relative clearance ratio is kept constant. As a consequence, design optimizations with respect to tip leakage done at larger scale can be directly used at reduced-scale.

3.3 Plausibility check of one-dimensional centrifugal compressor model (see section 2.5)

Besides the empirical modeling approaches, the performance prediction of the scaled compressor geometries is investigated by the one-dimensional model presented in section 2.5. The one-dimensional model is based on empirical loss correlations, thus capturing the previously mentioned effects of scaling is not necessarily verified. Hence, a plausibility check of the one-dimensional model has been performed by altering compressors feature size and relative clearance ratio.

Since the one-dimensional model was validated with experimental data provided by Schiffmann [12, 13, 14, 15], the scaling analysis is performed for this particular compressor including surface roughness and a volute. In addition, disk friction was included and the absolute sand roughness of the surface was set to $2.5 \cdot 10^{-6}$m.

Fig. 3.11 shows the total-total polytropic efficiency as a function of the global flow coefficient for four different scaling cases with a relative tip clearance ratio of 5 %. The one-dimensional model captures both the deterioration of efficiency and the shift of operating points towards lower flow coefficients with reducing the compressor feature size. The efficiency drop and the flow coefficient shift at the BEP is indicated by the red triangle in Fig. 3.11.

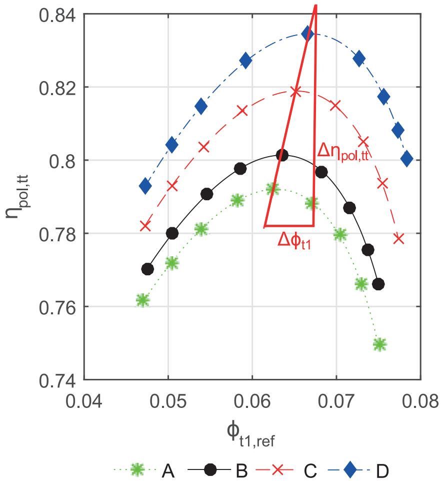

Figure 3.11: Total-total polytropic efficiency over the global flow coefficient obtained by the one-dimensional model.

Fig. 3.12 a) shows the Reynolds number independent losses A and Fig. 3.12 b) the Reynolds number dependent losses B_{ref} as a function of the global flow coefficient as predicted by the one-dimensional model for clearance ratios ranging from 3 % up to 15 %. The Reynolds number independent losses increase with an increase of flow coefficient independent of the clearance ratio. Reynolds number independent losses are increased in case the relative clearance ratio gets larger. A comparison with the distribution of Reynolds number independent losses of CFD data (see Fig. 3.9) suggests, that the one-dimensional model provides Reynolds number independent losses in the same order of magnitude.

The Reynolds number dependent losses in Fig. 3.12 b) decrease with an increase of the flow coefficient as suggested by CFD data. Predicted Reynolds number dependent losses are in the same order of magnitude as suggested by CFD data. Hence, the one-dimensional model is able to capture effects occurring at scaling and provides compared to CFD data a good prediction of the mentioned losses.

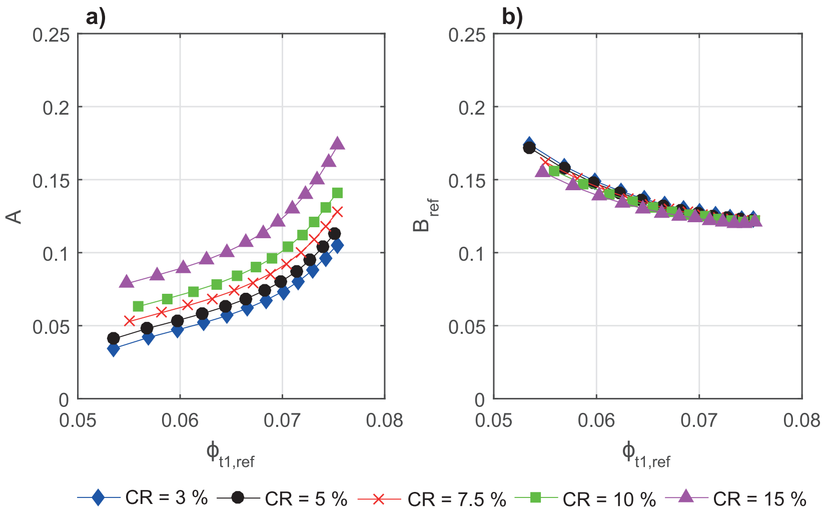

Figure 3.12: Reynolds number independent (a) and depended losses (b) as a function of the global flow coefficient according to the method suggested by Casey and Robinson [49], using data from the one-dimensional model.

3.4 Down-scaling a compressor under consideration of tip clearance alteration

It has been shown in one of the previous sections, that besides the Reynolds number effect no further drop in efficiency occurs while geometrically similar down-scaling a centrifugal compressor. However, down-scaling a compressor is most likely not happening at a constant relative clearance ratio. It is more likely that the relative clearance ratio needs to be increased due to manufacturing, assembly and rotordynamic issues. Since a compressor design normally starts from a 0-mm clearance compressor, large relative clearance ratios have an effect on the location of the desired peak efficiency point. Therefore, a compressor designer needs knowledge about mitigating deteriorating tip leakage induced phenomena by compressor design strategies.

In order to demonstrate a procedure, the baseline compressor B having a relative clearance ratio of 5 % is down-scaled to the size of compressor A (scaling factor 0.75) having relative

clearance ratio of 5%, 7.5 % and 10 %.
Fig. 3.13 shows the dimensionless performance values obtained from CFD in terms of total-total polytropic head coeffcient (Fig. 3.13 a)), work input coefficient (Fig. 3.13 b)) and total-total polytropic efficiency (Fig. 3.13 c)) as a function of the global flow coefficient for the baseline compressor B (black circles) and the compressor A (red cross) with a relative clearance ratio of 5 %, the compressor A with a relative clearance ratio of 7.5 % (blue diamonds) and the compressor A having a relative clearance ratio of 10 % (green squares).

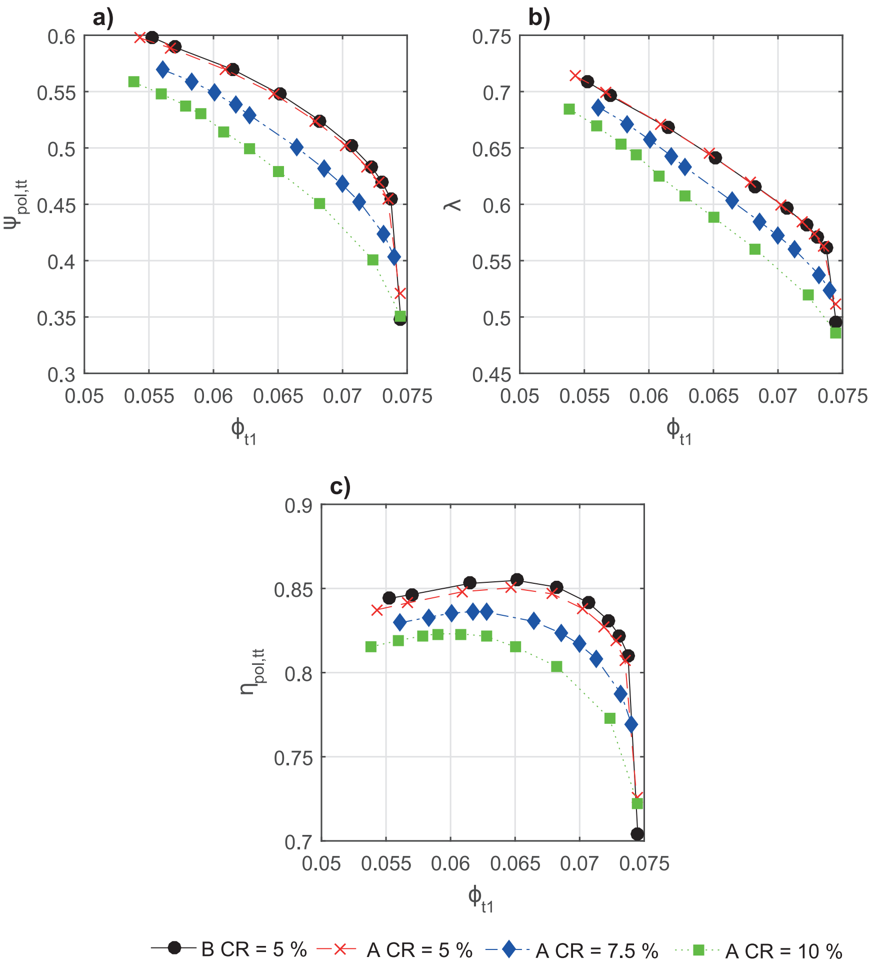

Figure 3.13: Total-total polytropic head coefficient (a), work input coeffcient (b) and total-total polytropic efficiency (c) as a function of the global flow coefficient, showing baseline compressor and down-scaled geometries with various relative clearance ratios. (CFD results)

The polytropic head (Fig. 3.13 a)) decreases with increasing relative clearance ratio, which is mostly related to the area increase of tip gap area, thus tip leakage mass flow is additionally increased. The work input coefficient decreases with an increase of relative tip clearance ratio. This is related to the increased blockage and slip induced by tip leakage jet and main and splitter blade tip leakage vortices. As a consequence, work input is reduced and more input power is required to achieve the same head (see Eq. 2.3). Both effects result in a reduction of compressor efficiency with a shift of compressor operating points towards smaller flow rates, as shown in Fig. 3.13 c). Fig. 3.13 c) suggests that changing the geometrical scale of the compressor by keeping the relative clearance ratio constant, leads to an efficiency reduction of 0.6 efficiency points and the flow coefficient is shifted by 0.76 % compared to the baseline configuration. An increase of relative tip clearance ratio from 5 to 7.5 % leads to a reduction in efficiency of 2.1 points and the flow coefficient is shifted by 4.76 % towards smaller mass flow rates compared to the baseline configuration. An increase of relative clearance ratio from 5 % to 10 % results in a deterioration of compressor performance by 3.1 points and a shift of flow coefficient by 7.83 % relative to the baseline. This clearly shows, that increasing the relative tip clearance ratio has a more pronounced effect on the compressor performance than changing the geometrical compressor scale.

In order to analyze the effect of increased relative tip gaps on the compressor performance, Fig. 3.14 a) shows the ratio between tip leakage mass flow rate and compressor mass flow rate and Fig. 3.14 b) shows the tip flow coefficient at trailing edge over the global flow coefficient. Since tip gap area increases, the tip leakage mass flow ratio increases, causing higher losses and reducing the head coefficient as well as the work input coefficient. Fig. 3.14 a) further supports the Reynolds number independence of tip leakage, since the graphs of compressors B and A having a clearance ratio of 5 % show the same tip leakage ratio distribution. Fig. 3.14 b) suggests an increased tip flow coefficient by increasing the relative clearance ratio. Since the tip flow coefficient contains the meridional velocity at trailing edge of the impeller (see Eq. 2.6), it serves as a direct measure to account for flow blockage. The curves therefore suggest increased flow blockage with an increase of relative clearance ratio. As a consequence of higher flow velocities at trailing edge, the slip velocity is more pronounced. Both increase of blockage and slip velocity decrease the work input coefficient as shown in Fig. 3.13 b).

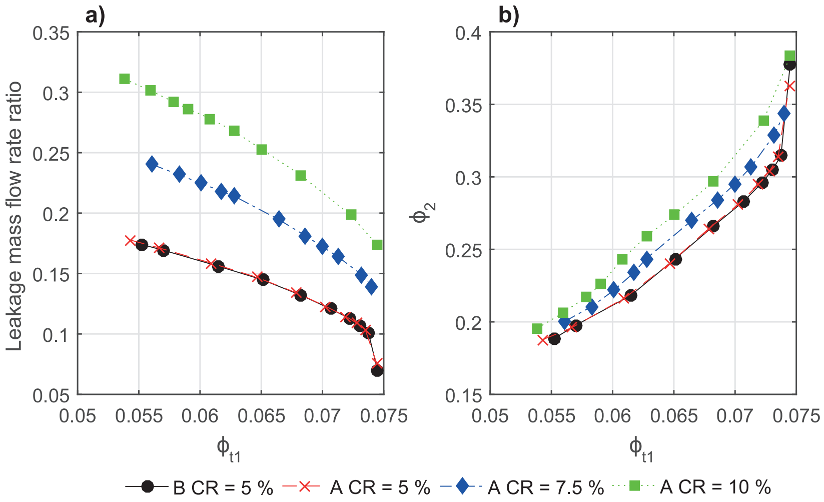

Figure 3.14: Ratio between leakage mass flow rate and overall compressor mass flow rate (a) and tip flow coefficient (b) over the global flow coefficient for down-scaled compressors with different relative clearance ratios. (CFD results)

According to Eq. 1.3, tip leakage mass flow rate consists of three main components, namely the clearance area, the tip jet density and the flow velocity normal to the tip gap. Assuming that increasing the tip gap area is unavoidable by reducing compressor scale, a designer can control tip leakage by controlling tip jets density and flow velocity. Fig. 3.15 shows the mass flux distribution (see Fig. 3.15 a)), the normalized tip jet density (see Fig. 3.15 b)) and the relative Mach number (see Fig. 3.15 c)) as a function of the normalized meridional streamline length along the blade tip of the main blade at peak efficiency points.

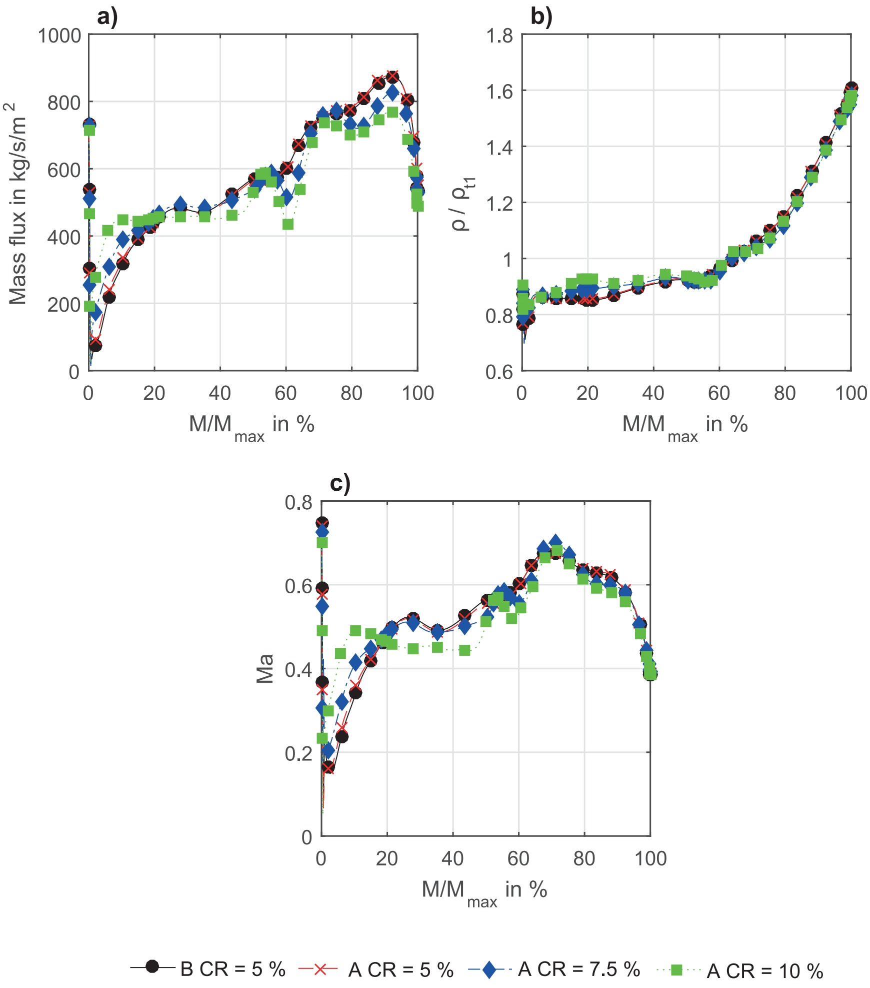

Figure 3.15: Mass flux distribution (a), normalized tip jet density (b) and relative Mach number of tip jet (c) along the main blade suction side of tip gap, showing the design example. (CFD results)

The mass flux distribution along the suction side of the main blade tip suggests, that increasing the relative clearance ratio results in an increase of tip mass flux in the inducer part of the impeller (first 20 % of meridional coordinate). The inducer part is the region where the main blade tip leakage vortex is rolling up, thus increased relative tip leakage increases the intensity of this vortex. Hence, increased relative tip leakage results in more intense tip leakage vortices, which deteriorate the trailing edge flow pattern. The mass flux distribution is almost unaffected by altering the clearance between 20 and 60 % of meridional coordinate. Tip leakage mass flux decreases in the rear part of the impeller by increasing the relative clearance ratio. Nonetheless, reduction of mass fluxes at the rear part remains too small, in order to compensate for the increase of leakage caused by larger tip gap areas.

In the first 20 % of the blade, tip density is less affected by increasing the relative clearance ratio, however, a clear increase of relative Mach number occurs. A clear increase of tip jet density occurs at the mid of the blade with an increase of the relative clearance ratio. At the same time, the relative Mach number is decreased with an increase in clearance, suggesting a reduction of shroud blade loading at this location. A clear reduction in relative Mach number coupled to an unaffected density distribution occurs in the rear part at increased relative clearance ratios.

Fig. 3.15 suggested a strong impact of relative clearance ratio on the tip jet density and velocity. In order to positively influence these parameters, a compressor designer needs to link them to the impeller design, especially near the shroud. Therefore, important flow properties near the impeller blade tip are shown in Fig. 3.16.

The diffusion ratio (see Eq. 2.13) at a blade span of 95 % is shown in Fig. 3.16 a) as a function of the normalized meridional coordinate. Increased relative clearance ratios increase the near-shroud diffusion over the whole blade length, showing local peaks at 50 % of the blade occurring for the highest clearance ratio. The tip leakage vortex increases with an increase of relative clearance ratio, thus the near shroud flow field is disturbed by this vortex. As a consequence, the near shroud velocity is more decelerated.

Fig. 3.16 b) shows the total-static pressure ratio near the shroud, which is increased between 20 and 60 % of the blade with an increase of the relative clearance ratio, leading to an increased tip jet density in this region. This analysis suggests that a compressor designer needs to decrease diffusion around the blade tip, what can be achieved by choosing a narrower end-wall distribution. This could be influenced by redistributing the shroud end-wall contour.

Fig. 3.16 c) shows the blade loading distribution at a blade span of 95 %. The near shroud blade loading is redistributed by increasing the relative clearance ratio, leading to a strong increase of blade loading in the first 20 % of the blade, which corroborates with the increased mass flux in the inducer (see Fig. 3.14 a)). A clear reduction of near shroud loading happens in the rest of the impeller. Especially the increase in near shroud inducer loading, strengthens the tip leakage in this region, thus the tip leakage vortex is more pronounced, resulting in higher trailing edge flow blockage. In order to minimize this disadvantageous effect in the inducer, a compressor designer needs to decrease the inducer loading. As a consequence, a redistribution of shroud blade loading is required to counter against the decreased inducer loading. From that point of view, setting the loading peak at around 50 % of the shroud contour seems desirable. Compared to an aft-loaded design (what is the case for this particular impeller), a mid-loaded distribution has the advantage that the maximum relative velocity of the tip jet

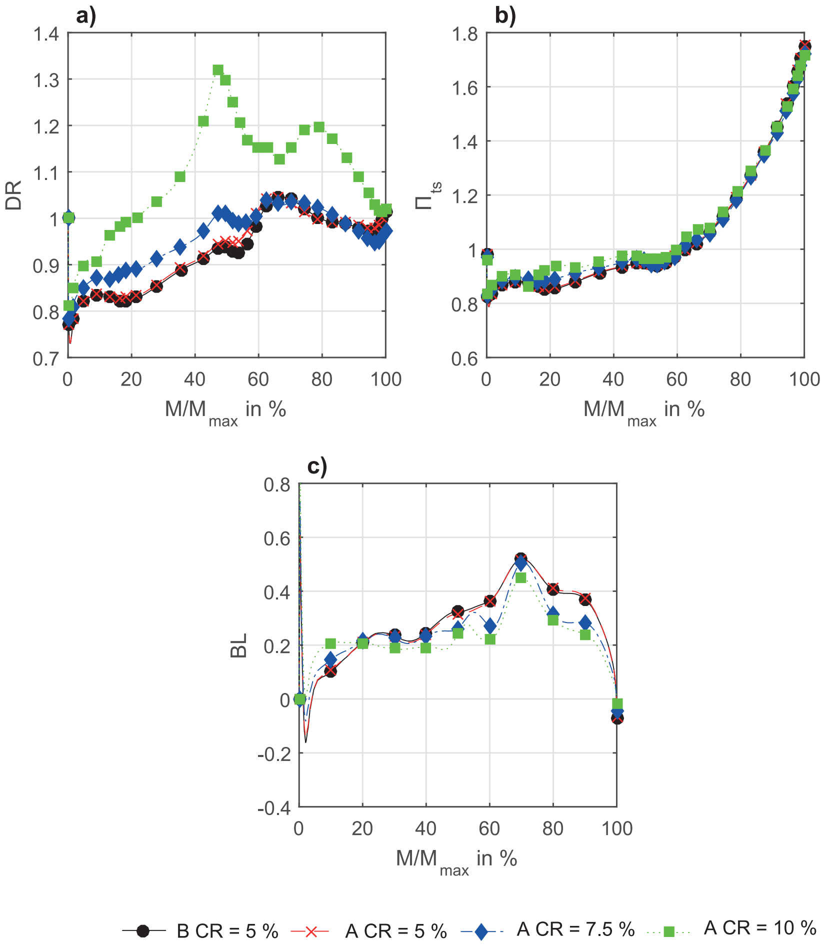

Figure 3.16: Diffusion ratio (a), total-static pressure ratio (b) and blade loading (c) along the 95 % blade span, showing the design example.

occurs in a region where the fluid density is still low. Hence, tip leakage is reduced in the rear part of the impeller, where high flow densities occur.

The flow analysis alone suggests that a compressor designer needs to take care when downscaling a compressor with an additional increase in relative clearance ratio, since it results in significant changes of the governing flow patterns. Due to stronger tip leakage and tip leakage vortices, a deterioration of efficiency and a shift of peak efficiency towards lower flow coefficients is expected. Nonetheless, compressor designers have a few options to control compressor performance by applying geometry adaptions and to avoid a complete new design of compressor geometry:

1. Depending on the relative clearance ratio, the shift of peak efficiency towards smaller mass flow rate can be significant. In order to operate a compressor at is best point, a compressor designer could use a baseline geometry designed for a higher flow coeffi-

cient. Reshaping hub and shroud end-walls in the front part of the impeller to narrower channels might be another option. Especially slimmer inducer passages decrease inducer diffusion and hence the intensity of tip leakage vortex.
In order to counter against the increased trailing edge blockage caused by the tip jet, a compressor designer needs to increase the outlet width, when dealing with large relative clearance ratios.

2. In order to counter the increase in front-loading due to increased relative clearance ratios, a redistribution of the shroud loading distribution is recommended. Therefore, the loading in the inducer needs to be decreased, what minimizes the intensity of tip leakage vortex. Setting the loading peak to the mid of the impeller shroud contour is recommended, to counterbalance the reduced inducer loading. Furthermore, tip jet density in such a loading distribution is less compared to an aft-loaded shroud loading distribution, what is suggested to reduce the tip leakage in the rear part of the impeller.
3. In order to shift the flow coefficient towards higher values, a compressor designer can increase the back-sweep angle of the impeller. As a consequence, the work input coefficient curve is steeper, shifting the peak efficiency towards higher flow rates. Nonetheless, this approach leads to smaller work input and consequently lower head is achieved, thus this strategy might be an option in case the down-scaled compressor has less demanding specifications as the reference geometry.

3.5 Summary and implications for this thesis

A scaling analysis of a centrifugal compressor provided by Schiffmann [12, 13, 14, 15] with alteration of its relative tip clearance ratio leads to following conclusions:

1. Scaling-down a centrifugal compressor is yielding efficiency deterioration and shift of an operating point towards smaller flow rates.
2. The empirical correlation provided by Dietmann and Casey [50, 51] as well as an approach suggested by the author are well suited to capture the mentioned scaling effects.
3. Compressor losses can be split into Reynolds number dependent and independent losses. The model provided by Casey and Robinson [49] to account for these losses is applicable in the whole operating range of the compressor for operating points having the same total-static pressure ratio.
4. Tip leakage losses are independent of the compressors Reynolds number. Furthermore, Reynolds number independent losses can be split into losses which depend on the relative clearance ratio and losses which are independent.
5. The one-dimensional model (see section 2.5) captures the Reynolds number effect well and Reynolds number dependent and independent losses are in the same order of magnitude as suggested by CFD.

6. Increasing the relative clearance ratio leads to an increase of trailing edge blockage. In addition, the inducer loading as well as inducer diffusion increase with an increase in relative clearance ratio, leading to increased tip leakage in the inducer and hence a more intense main blade tip leakage vortex.
7. Design guidelines for minimizing the deteriorating effect of tip leakage induced phenomena are suggested.

As a consequence, investigation of tip leakage losses and also design optimizations with respect to tip leakage flows can be done at any scale. Hence, findings of altering the tip gap as done in chapter 4 and postulation of design guidelines as done in chapter 5 can be performed on the scaled up test rig, which has been presented in section 2.4. The obtained results with respect to tip leakage induced phenomena can be transferred to the original-size compressor, considering the drop in efficiency and shift of global flow coefficient caused by the Reynolds number effect.

4 Impact of tip clearance alteration on the compressor performance

Both the performance deterioration and the shift of the best efficiency point towards lower mass flow rates due to increased relative tip clearance ratios has been identified as a major challenge of reduced-scale compressors in the previous chapter. This chapter presents a thorough investigation of the tip leakage phenomena, which are present in a centrifugal compressor.

In a first step, the impact of changing the relative clearance on the performance and flow pattern is analyzed for the compressor provided by Schiffmann [12, 13, 14, 15] and the scaled up version by Javed et al. [27]. Both compressor units are investigated numerically as well as experimentally. CFD simulations are validated using experimental data and are used to gain a detailed insight into the flow physics. In a next step, the driving mechanisms, namely impeller diffusion and shroud blade loading distribution, are examined, in order to study design possibilities to decrease tip leakage losses. Besides tip leakage, the impact of relative clearance alteration on the trajectories of main and splitter blade tip leakage vortices is discussed.

The validity of various empirical correlations used to predict the efficiency loss associated to a change in relative clearance ratio is assessed at design and off-design. A sensitivity parameter is introduced, which characterizes the sensitivity of a compressor by altering its relative clearance ratio. This sensitivity parameter serves as correlation for a novel more comprehensive tip leakage loss correlation.

In addition, the prediction quality of the one-dimensional model presented in section 2.5 is assessed in terms of tip leakage and plausibility checks are performed for this model. Furthermore, a reduced-order technique for preliminary tip leakage estimation is closer investigated.

The contents of section 4.1, section 4.2 and section 4.3 have been presented by Diehl and Schiffmann [89] for the compressor unit provided by Schiffmann [12, 13, 14, 15].

4.1 Performance deterioration due to alteration of tip clearance

In general, two tip clearance adjustment approaches exist. The first one uses shimming plates between the compressor housing, thus the shroud end-wall is moved axially away from the impeller. As a consequence, only the axial clearance near the trailing edge is varied, whereas the radial clearance, especially in the inducer part is unaffected. In addition, the areas of diffuser and volute are geometrically modified by that approach, thus matching between the components is not necessarily guaranteed. The advantage of this method, however, is the low costs to adjust tip clearance. The relative tip gap of the experimental results provided by Schiffmann [12, 13, 14, 15], which are presented in subsection 4.1.2, is adapted in such way. In the second approach, the relative clearance ratio is altered by adapting the blade height of the impeller. The shroud end-wall remains constant, thus diffuser and volute areas are unaffected by a change in tip clearance. The drawbacks of this approach lie in the high costs, since for each relative clearance ratio an impeller having a specific blade height is required. Nonetheless, the latter approach corresponds to a situation, which a compressor designer encounters, since compressor design starts from 0mm-clearance impeller. The relative tip clearance is altered by that approach for the numerical study of the compressor by Schiffmann [12, 13, 14, 15] (see subsection 4.1.1) as well as the numerical and experimental investigation of the scaled up compressor by Javed et al. [27] (see subsection 4.1.3 and 4.1.4).

4.1.1 Numerical results (CFD) of compressor by Schiffmann

The relative tip clearance ratio at impeller trailing edge of the numerically validated (see subsection 2.6.4) baseline compressor by Schiffmann [12, 13, 14, 15] having a relative clearance ratio of 5 %, was altered in the range of 3 % up to 15 %. The study has been performed numerically for the design speed line of 180 000 rpm. Important parameters for the CFD solver setup are presented in appendix C.

The impact of changing the relative clearance ratio on the compressor performance is shown in Fig. 4.1 for the design speed line of the compressor by Schiffmann [12, 13, 14, 15], using CFD data. Tip clearance was adjusted by adapting the impeller blade height in this subsection. Fig. 4.1 a) shows the total-total polytropic head coefficient, Fig. 4.1 b) the work input coefficient and Fig. 4.1 c) the total-total polytropic efficiency as a function of the global flow coefficient between inlet of the compressor and outlet of the vaneless diffuser. A relative clearance ratio of 3 % is presented as red solid line with diamonds, a relative clearance ratio of 5 % as black solid line having circles, a relative clearance ratio of 7.5 % as blue solid line with squares, a relative clearance ratio of 10 % as green solid line showing upper triangles and a relative clearance ratio of 15 % as magenta solid line with diagonal triangles. This color code is used for the entire tip gap study of the compressor unit by Schiffmann [12, 13, 14, 15].

Fig. 4.1 a) suggests, that the total-total polytropic head coefficient decreases with increasing relative clearance ratio, indicating that tip leakage is an internal loss mechanism with a direct impact on the achievable diffusion and hence a total pressure loss. The drop in total-total polytropic head coefficient is mostly related to an increase of the tip gap area, thus more tip leakage mass flow is passing through the tip gap. Fig. 4.1 b) indicates that the work input coefficient is decreasing when the relative tip gap is increased, thus less work is transferred

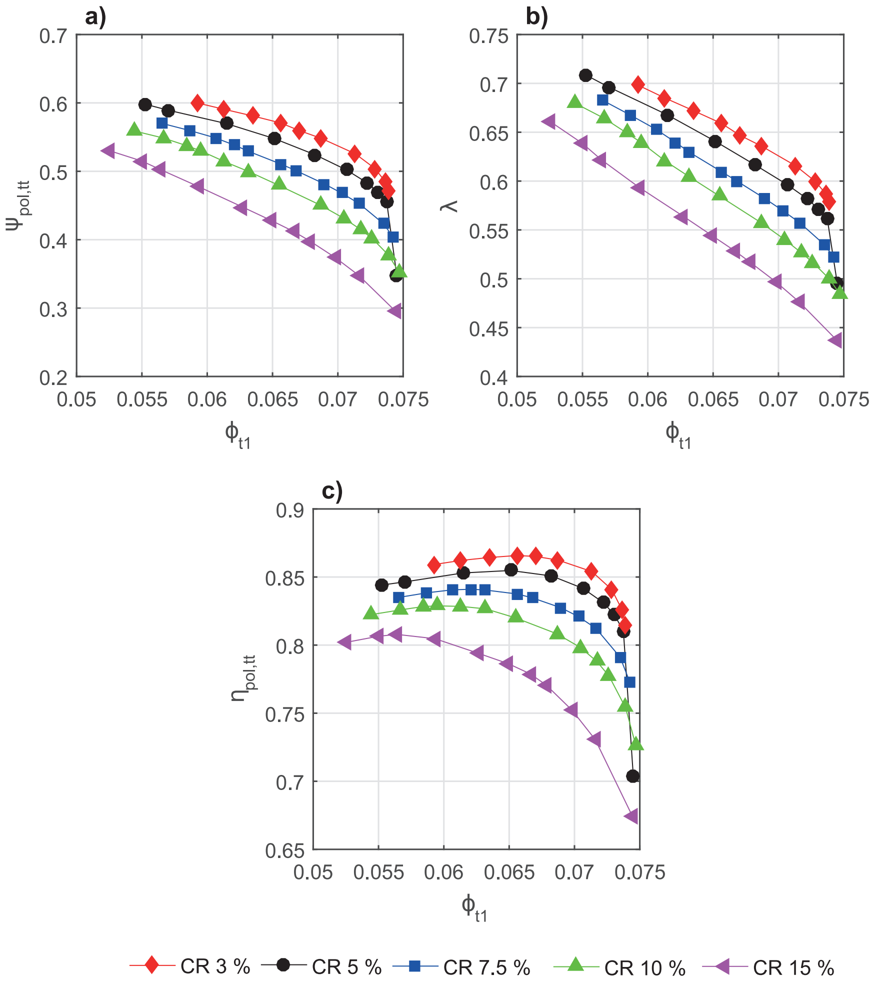

Figure 4.1: Numerically obtained total-total polytropic head coefficient (a), work input coefficient (b) and total-total polytropic efficiency (c) from impeller inlet to vaneless diffuser outlet for various clearance ratios of the compressor unit provided by Schiffmann [12, 13, 14, 15]. Tip clearance is adjusted by impellers having different blade height.

to the fluid and more input power is required to achieve the same pressure ratio compared to lower relative clearances. Fig. 4.1 c) shows that the total-total polytropic efficiency drops with an increase of relative clearance ratio and that a given operating point is shifted towards smaller flow rates.

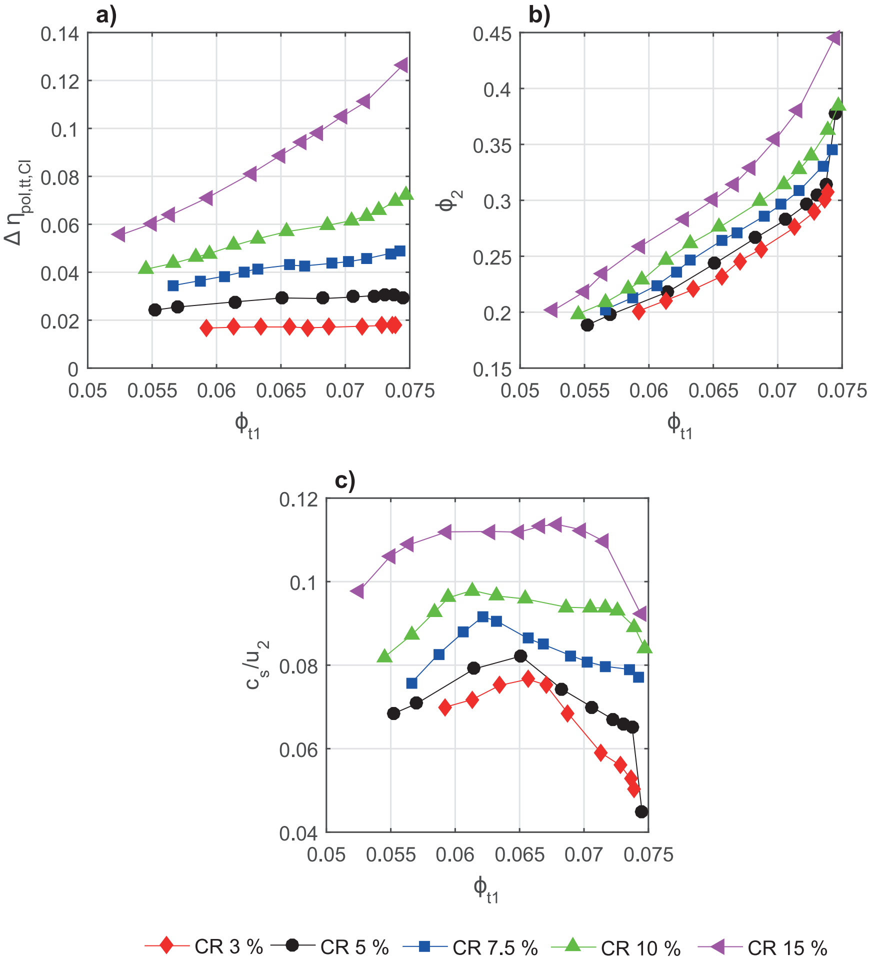

Figure 4.2: Numerically determined efficiency loss due to kinetic energy of the tip jet (a), tip flow coefficient (b) and normalized slip velocity (c) as a function of the global flow coefficient, showing various relative clearance ratios of the compressor unit by Schiffmann [12, 13, 14, 15].

Fig. 4.2 a) shows the drop in efficiency due to tip leakage evaluated with Eq. 1.4. Hereby, it is assumed that the complete kinetic energy of the tip jet normal to the tip gap is lost, what is supported by Senoo and Ishida [34, 35]. Since the tip gap area available for through flow increases with increasing relative clearance ratio, more mass flow passes through the tip gap. As a consequence, a higher loss occurs due to tip leakage.

Fig. 4.2 b) shows the tip flow coefficient evaluated according to Eq. 2.6. The tip flow coefficient is a direct measure for flow blockage at trailing edge, thus an increasing tip flow coefficient indicates increased blockage. The curve clearly suggest, that the tip flow coefficient and blockage increase for an increase of relative tip clearance ratio. This behavior serves as an

explanation for the shift of best efficiency point towards lower mass flow rates (see Fig. 4.1 c)) with increasing tip clearance.
As a consequence of the the increased blockage at the impeller trailing edge, the slip velocity (see section 2.2) increases with an increase of relative clearance ratio (see Fig. 4.2 c)), which further lowers the work input coefficient. Hence, more input power is required for increased clearances, in order to achieve the same head as operating at lower relative clearance ratios.

The impact of the tip jet on the trailing edge blockage and slip velocity is further illustrated in Fig. 4.3, where the plots show the relative Mach number distribution at trailing edge of the impeller for relative clearance ratios ranging from 3 % up to 15 % at their best efficiency points. Firstly, Fig. 4.3 suggests, that both blade passages show a distribution in relative Mach number, that changes with the relative clearance. The splitter blade passage shows a more non-homogenized relative velocity distribution as the main blade passage. The tip leakage vortices (see subsection 1.1.1), which evolve from the main and splitter blade leading edge, cause the different velocity distributions in both blade passages. As discussed in subsection 1.1.1, the trajectory of main blade tip leakage vortex penetrates in the splitter blade channel, where the adverse pressure gradient between the blade pressure side and the blade suction side of the adjacent blade caused by centrifugal and Coriolis forces act on the vortex cores. As a consequence, the tip leakage vortex is pressed against the suction side of the splitter blade. The intensity of the splitter blade tip leakage vortex is increased due to the main blade tip leakage vortex, thus the splitter blade passage is more distorted by the combined vortex.
While increasing the relative tip gap, the blocking effect of tip leakage jet and its vortices increases. This is suggested by the increasing low velocity zone near the pressure side of both blades. By an increase of relative tip gap this low velocity zone migrates to the center of the blade channel and causes an increase of relative velocity near the hub surface. At the same time, the relative velocity field is more deteriorated and higher gradients of relative Mach number occur, suggesting a higher level of secondary flows as discussed in Zangeneh et al. [90].
As a consequence, all findings discussed in Fig. 4.1 and Fig. 4.2 are further supported by Fig. 4.3.

In addition, Fig. 4.4 shows the entropy distribution at impeller trailing edge for various relative clearance ratios at their best efficiency points. For the sake of comparison, the entropy is normalized by the mass flux weighted entropy average on the cross section plane. The entropy distribution is linked to generation of aerodynamic losses and a zone of high entropy indicates high losses. Fig. 4.4 clearly suggests, that most of the losses occur near the shroud suction side of both blades. Due to presence of the combined main and splitter blade tip leakage vortex, the splitter blade passage shows an even more deteriorated entropy pattern. While increasing the relative tip gap, the zone of high entropy migrates towards the center of the blade channel, which is caused by stronger tip leakage jet at the rear part of the impeller, as well as by the decreasing pressure difference between the blade pressure and the suction side of the adjacent blade.
Relative Mach number distribution and entropy distribution are linked to each other, since

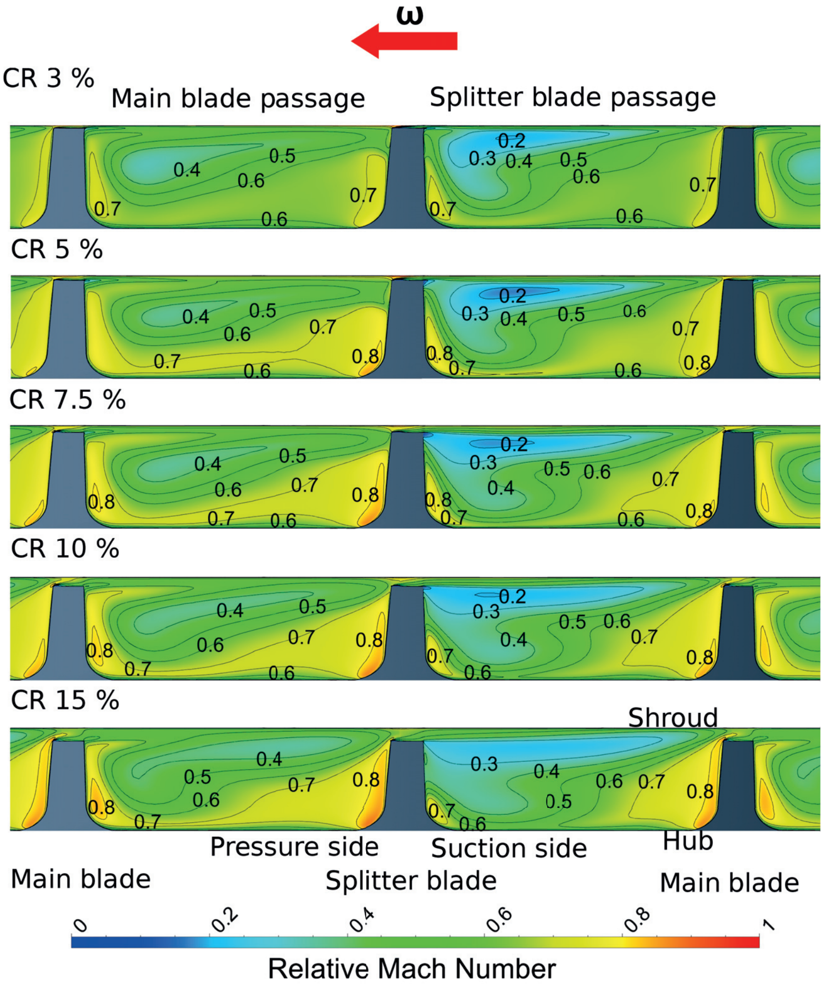

Figure 4.3: Distribution of relative Mach number at impeller trailing edge for various relative clearance ratios (compressor unit by Schiffmann [12, 13, 14, 15]).

zones of high entropy occur, where the relative Mach number gradients are high (see Zangeneh et al. [90]).

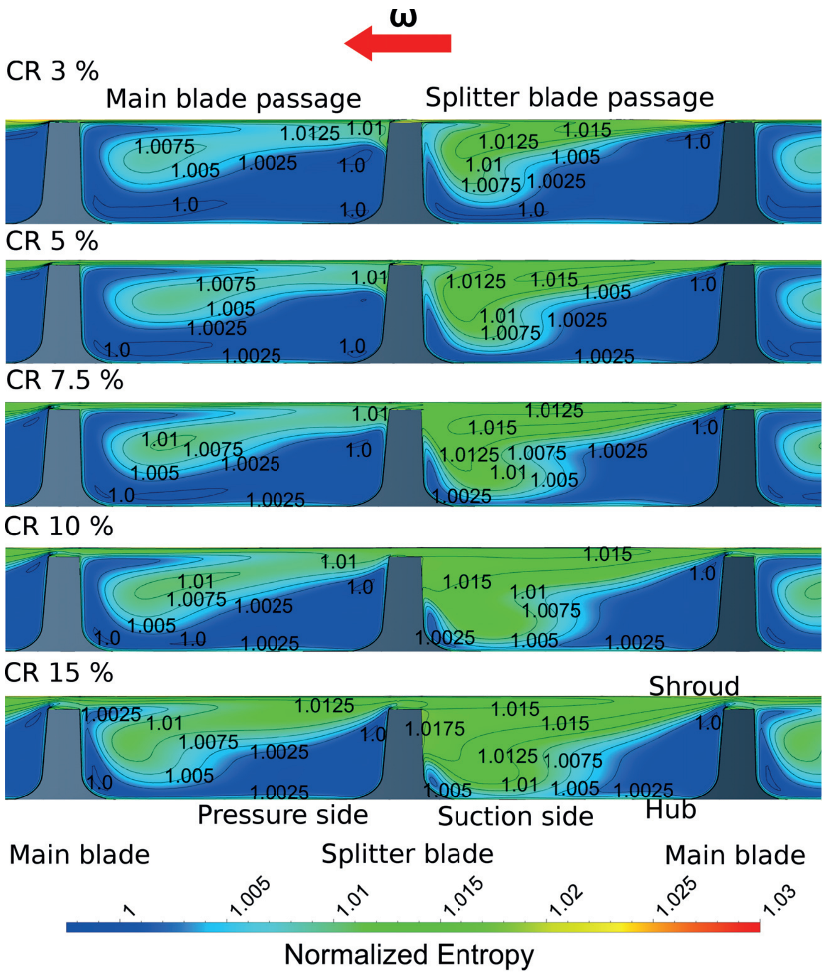

Figure 4.4: Normalized entropy distribution at impeller trailing edge for various relative clearance ratios (compressor unit by Schiffmann [12, 13, 14, 15]).

4.1.2 Experimental results of compressor by Schiffmann

Schiffmann [12, 13, 14, 15] has performed experiments for various relative clearance ratios, where the relative tip gap was adjusted by using shimming plates. The relative clearance ratios were adjusted to 5 %, 6 %, 7 % and 9 % relative clearance ratio at impeller trailing edge. The 5 % relative clearance ratio compressor is the compressor, which served as reference geometry in the numerical tip gap alteration study of the previous subsection. The tip gap in the previous subsection, however, was adjusted by a different approach, thus the results are not comparable to each other.

The experiment was carried out as described in section 2.4 and overall compressor performance was measured by the total temperatures and pressures. Fig. 4.5 shows the total-total polytropic efficiency as a function of the global flow coefficient for different relative clearance ratios at design speed, corresponding to a rotational Mach number of 1.27. The relative clearance ratio of 5 % is presented as black solid line, the relative clearance ratio of 6 % as blue dashed line, the relative clearance ratio of 7 % as red dotted line and the relative clearance ratio of 9 % as green dash-dotted line. In addition, the peak efficiency points are illustrated as magenta line with dots, in order to demonstrate the shift of operating points towards smaller mass flow rates. As suggested by the experimental results provided by Schiffmann [12, 13, 14, 15], the compressor efficiency drops with an increase of relative tip gap at impeller trailing edge and each operating point is shifted towards smaller flow rates. The data set of 6 % and 7 % relative clearance ratio, however, suggest a discrepancy in terms of efficiency deterioration, since there is almost no difference between the data set. One possible reason could be an error in the adjustment approach due to the manufacturing tolerances of the shimming plates.

Although the experimental setup uses a different tip clearance adjustment approach than the numerical setup presented in the previous subsection, experimental results, however, are used to compare numerically and experimentally defined tip leakage sensitivities, which are presented in section 4.2 and 4.3. On the other hand, both adjustment approaches suggest a similar behavior, namely deterioration of compressor efficiency combined with a shift of flow coefficients to lower flow rates with increasing the relative clearance ratio.

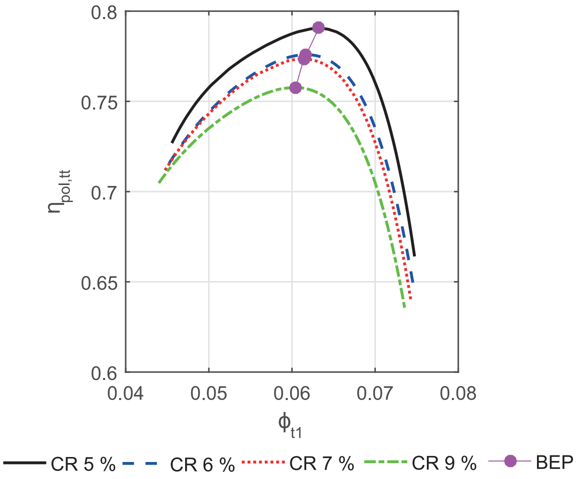

Figure 4.5: Experimental tip gap investigation for Schiffmann [12, 13, 14, 15] compressor using shimming plates. Total-total polytropic efficiency of the compressor as a function of the global flow coefficient. Experimental results are provided by Schiffmann [12, 13, 14, 15].

4.1.3 Numerical results of the up-scaled compressor by Javed et al.

A similar study as described in subsection 4.1.1 has been performed numerically and experimentally for the scaled up centrifugal compressor provided by Javed et al. [27]. Compared to experiments, which have been carried out by Schiffmann [12, 13, 14, 15] in the previous subsection, the relative tip gap of the impeller is adjusted by adapting the blade height of the impeller. For this specific compressor, the relative clearance ratios for investigation has been chosen to be 3 %, 5 %, 10 %, 14.73 % (baseline geometry) and 20 %. The boundary conditions for the CFD solver setup are listed in appendix C. Firstly, the numerical results are presented in this subsection.

Fig. 4.6 shows the impact of changing the relative tip clearance ratio on the main performance values, namely total-total polytropic head coefficient (Fig. 4.6 a)), work input coefficient (Fig. 4.6 b)) and total-total polytropic efficiency (Fig. 4.6 c)) as a function of the global flow coefficient. The simulations have been carried out for the design speed line of 50 000 rpm. The color code in the legend of Fig. 4.6 is kept for the remainder of that chapter.

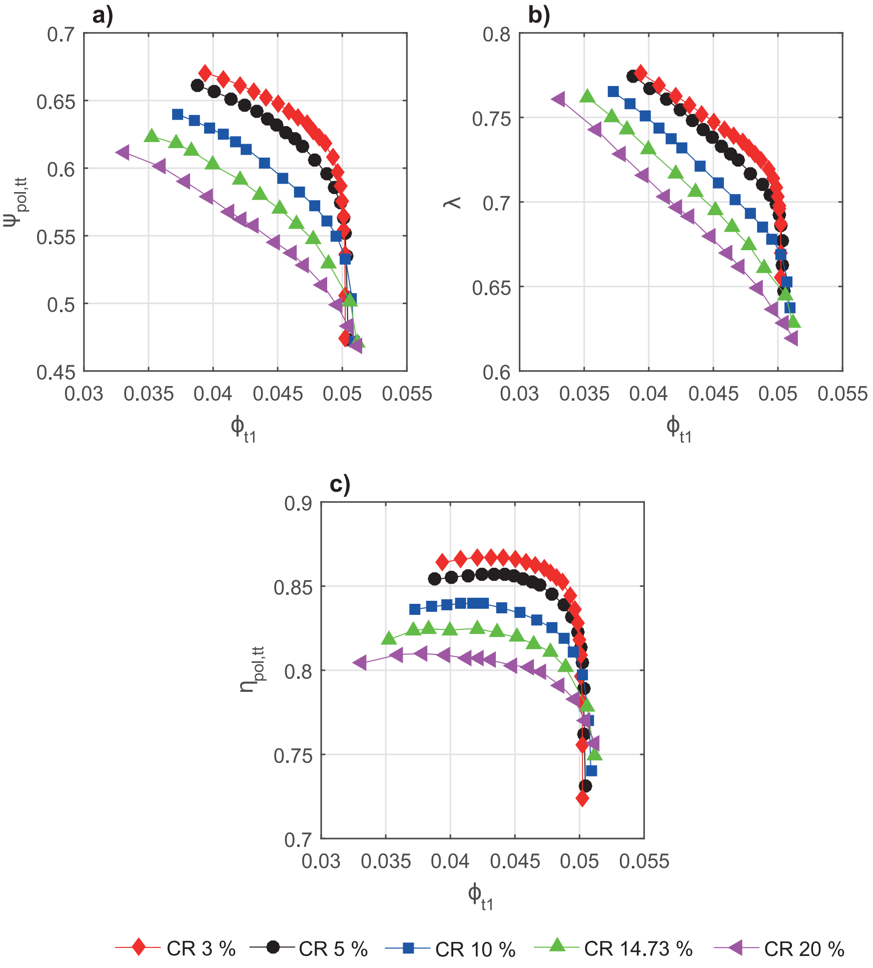

Figure 4.6: Numerically obtained stage characteristics for various relative tip gap ratios as a function of the global flow coefficient for the scaled up compressor by Javed et al. [27].

As suggested by Fig. 4.6 a), the total-total polytropic head coefficient drops with an increasing relative clearance ratio. This is mostly caused by the increased tip gap area available for through flow, thus, according to Eq. 1.4, a higher total pressure loss occurs. The work input coefficient presented in Fig. 4.6 b) decreases due to increased blockage and slip. Nonetheless, due to the adjustment approach, in which the blade surface is removed with increasing tip

clearance, part of the drop in work input coefficient is also slightly attributed to less blade area available for transferring work to the fluid.
The total-total polytropic efficiency (see Fig. 4.6 c)) drops for increased relative clearance ratios, due to the higher total pressure loss of the stronger tip jet, and compressor operating points are shifted towards smaller mass flow rates.

The relative Mach number distribution at impeller trailing edge is shown for the best efficiency points of all numerically tested compressor geometries in Fig. 4.7. First of all, both impeller blade passages show like the compressor by Schiffmann [12, 13, 14, 15] a different flow pattern, what is caused by the tip leakage vortex. Since parts of the main blade tip leakage vortex migrates in the splitter blade passage and accumulates at the splitter blade tip leakage vortex, the splitter blade passage shows a more distorted flow pattern as the one of the main blade passage. By increasing the relative clearance gap, the zone of low momentum fluid increases and is pushed to the center of the blade channel, thus the main core flow gets distorted towards the hub, what is indicated by increased relative Mach number at the hub pressure side corner.

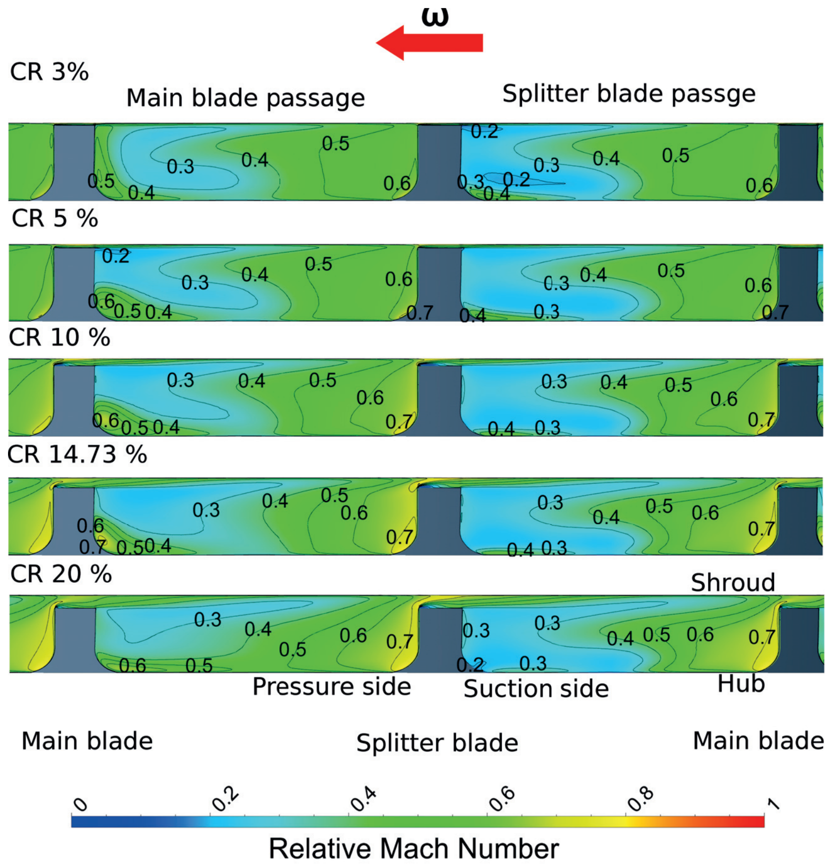

Figure 4.7: Distribution of relative Mach number at impeller trailing edge of scaled up compressor by Javed et al. [27], having different relative clearance ratios.

Since the relative clearance ratio strongly impacts the trailing edge flow pattern, these flow

distortions are transported into the vaneless diffuser where the mixing of low and high momentum fluid occurs. The mixing loss strongly depends on the flow velocities and the velocity difference defines the length of the flow path until the flow is completely mixed out. In order to illustrate the effect of increasing the relative tip gap on the mixing in the vaneless diffuser, Fig. 4.8 - Fig. 4.10 show the entropy distribution at three different radial positions in the vaneless diffuser for relative clearance ratios of 3 %, 10 % and 20 %. The entropy is normalized by the mass flux weighted average of entropy in the corresponding cross section plane, in order to allow comparison between the different clearance cases.
Fig. 4.8 shows the normalized entropy distribution at a radial position of 105 % times the impeller diameter d_2. The entropy distribution becomes less homogenized with increasing the relative tip gap, since zones of high entropy are more pronounced and the low entropy zones show a strong entropy gradient. At this position, the flow in all three cases is not completely mixed out, what is indicated by the high gradients in entropy distribution.

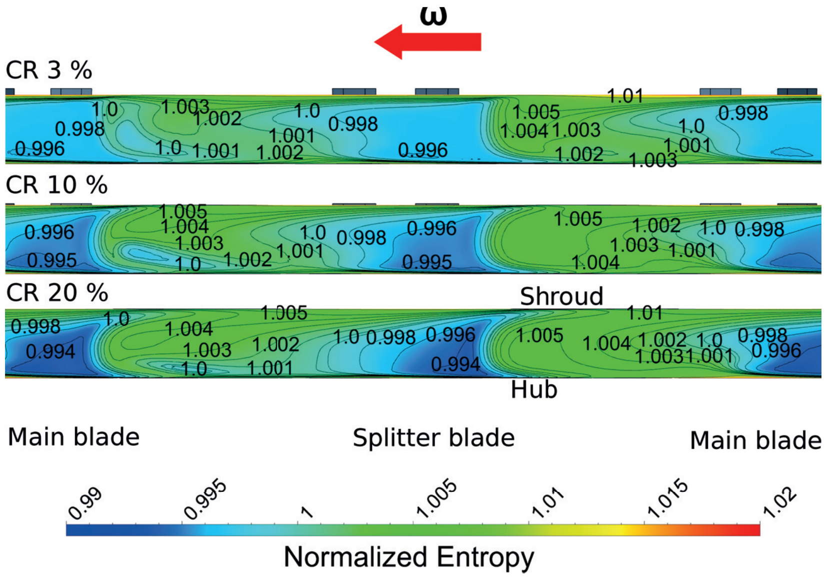

Figure 4.8: Normalized entropy distribution at 105 % times the impeller diameter for the scaled up compressor by Javed et al. [27].

Fig. 4.9 shows the entropy distribution for a cross section of 110 % d_2. At this position, the flow has been already mixed out more and the flow patterns of different clearance ratios become more similar. Nonetheless, the highest clearance ratio of 20 % shows still strong entropy gradients, indicating a less mixed-out state than the other relative clearance ratios.

Eventually, Fig. 4.10 shows the diffuser flow pattern at a radial position of 125 % times the impeller diameter. The flow patterns of all three different relative clearance ratios look nearly similar, what indicates that the mixing of jet and wake is almost finished at this position. The lowest relative clearance ratio shows compared to the other relative clearance the most homogenized entropy distribution. This suggests, that the relative tip clearance ratio not only impacts the impeller flow, but has also a strong impact on the flow in the diffuser. Nonetheless,

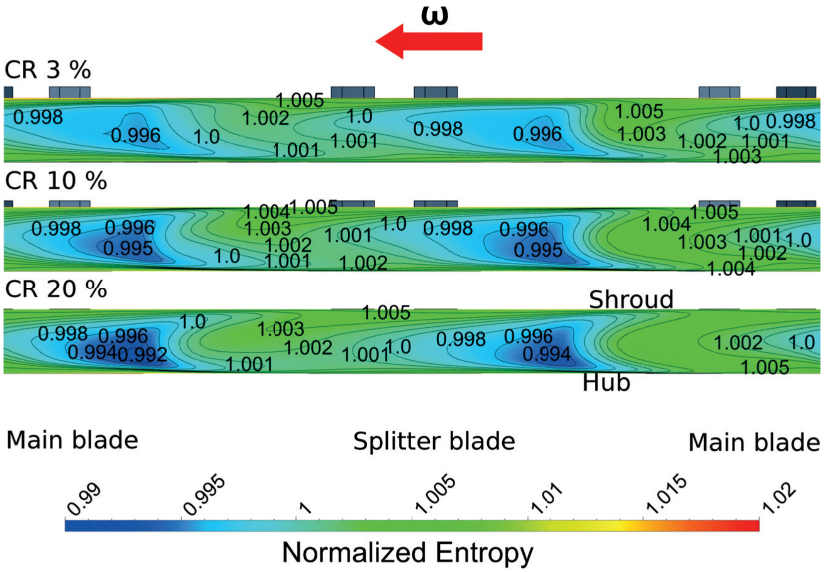

Figure 4.9: Normalized entropy distribution at 110 % times the impeller diameter for the scaled up compressor by Javed et al. [27].

the mixing loss is attributed to the impeller performance in one-dimensional compressor modeling techniques, which can be found in literature.

The numerical investigation of the reduced-scale compressor by Schiffmann [12, 13, 14, 15] as well as the up-scaled compressor geometry by Javed et al. [27] showed a similar impact of increasing the relative tip gap on the compressor performance as well as on the flow patterns. Since the two compressors are different in design, it can be stated, that increasing the relative clearance ratio results in a deteriorating effect on the compressor performance. On the one hand, increased relative clearance ratios yield increased total pressure losses, mainly caused by the increase of tip gap area available for through flow. On the other hand, an increased relative clearance ratio results in a strong distorting effect on the main flow, thus the work input coefficient drops. Both effects lead to a deterioration of compressor efficiency with a shift of flow coefficients towards smaller flow rates.

As indicated by the flow patterns at impeller trailing edge, increasing the relative clearance ratio has the following impact: (1) The relative Mach number distribution becomes less homogenized and higher gradients occur, what serves as indicator for higher secondary flows. (2) The relative velocity close to the hub increases, since the low momentum fluid is pushed by the tip jet towards the center of the blade channel. This change of flow pattern further impacts the mixing of low and high momentum fluid in the vaneless diffuser and the mixing of both flows requires more mixing length for increased relative tip gaps.

From a design point of view, the difference in flow patterns demonstrate the need of having a pinch in the vaneless diffuser, in order to accelerate low momentum fluid into the vaneless diffuser and hence improving the mixing process. In addition, in order to get more homogenized trailing edge flow patterns, the splitter blade needs to be designed individually, since

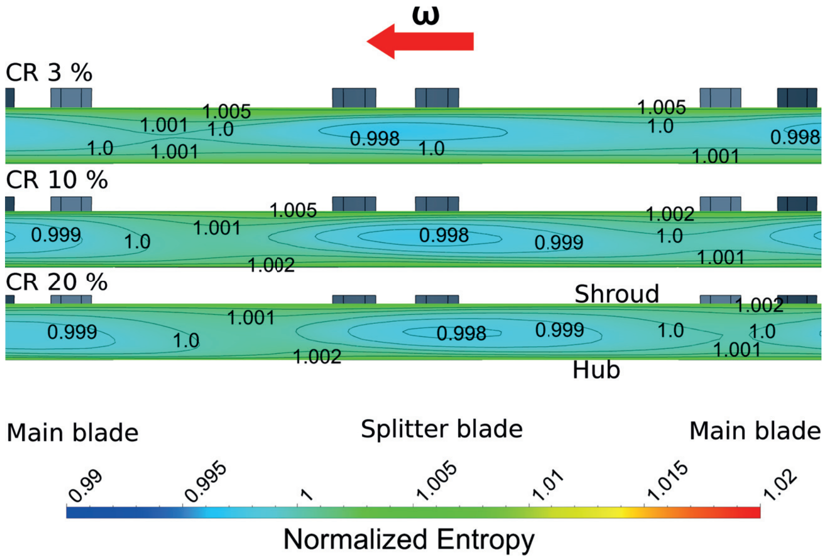

Figure 4.10: Normalized entropy distribution at 125 % times the impeller diameter for the scaled up compressor by Javed et al. [27].

both blade passages show different flow patterns caused by the main and splitter blade tip leakage vortex.

4.1.4 Experimental results of scaled up compressor by Javed et al.

The scaled up compressor by Javed et al. [27] was experimentally tested on the test-rig described in subsection 2.4.2. Four relative clearance ratios could be tested, namely 5 %, 10 %, 14.73 % and 20 %. A crash of the impeller occurred while testing the impeller with 5 % relative tip gap, thus the test was stopped. Due to this crash, only half of the design speed line (50 krpm) could be tested. As a result of the crash using the impeller with a relative clearance ratio of 5 %, it was decided to not test the impeller with a relative clearance ratio of 3 %.

The CFD simulations presented in the previous subsection are validated by comparing it to the tracked experimental data as done in subsection 2.6.4. All validation plots including error analysis are appended in appendix C. In addition, time-averaged measurement values are tabulated in appendix C.

Fig. 4.11 shows the measured characteristics of the various tested impeller geometries between compressor inlet and impeller trailing edge. Fig. 4.11 a) shows the total-static isentropic head coefficient, Fig. 4.11 b) the work input coefficient and Fig. 4.11 c) the total-static isentropic efficiency for the design speed line of 50 krpm. The numerical data set obtained by CFD is additionally shown in Fig. 4.11, in order to allow a comparison between experiments and CFD. The aero- and thermodynamic properties in CFD were evaluated at the same positions than the measurement positions. Furthermore, the isentropic change of state has been applied for numerical data, since polytropic efficiency is not accessible in experiments. The color code for experimental data and CFD data is according to the legend of Fig. 4.11.

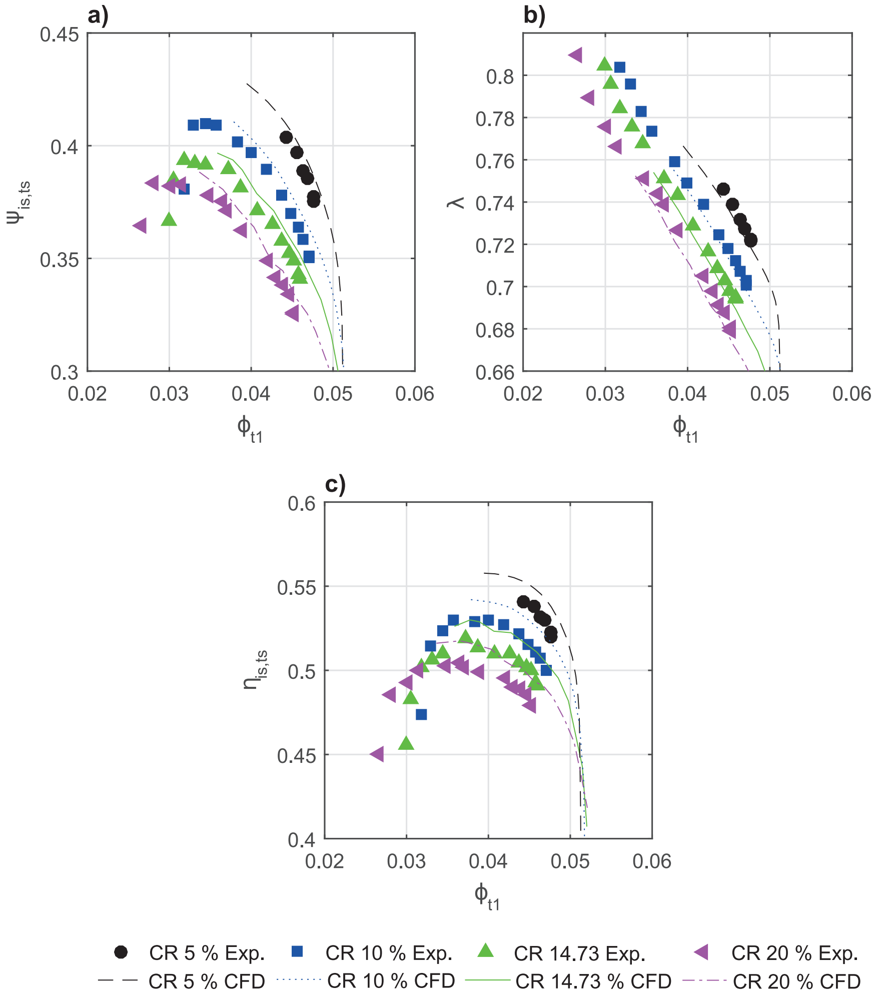

Figure 4.11: Comparison between experimental and numerical dimensionless compressor performance values for various relative tip gap ratios at impeller trailing edge (scaled up compressor by Javed et al. [27]).

The total-static isentropic head coefficient, shown in Fig. 4.11 a), drops with an increase in relative clearance ratio as suggested by the experimental and numerical results. Nonetheless, experimental results are consequently lower than numerical results. This is a result of the assumptions done in CFD setup, what was discussed in subsection 2.6.4. According to the error analysis shown in appendix C, the deviation between experimental data and numerical data is in the same order of magnitude for all relative clearance ratios. Hence, it shows a consistent error between CFD and experiments, what further supports the quality of the numerical setup. The drop in work input coefficient with an increase of relative clearance ratio occurs in experiments in the same manner as suggested by numerical data. CFD captures the work input within the measurement error as shown in appendix C. The deterioration in total-static efficiency and the shift of the compressor map towards smaller mass flow rates is captured by the experiment as well. Nonetheless, an over-estimation of around 1 efficiency points occurs in CFD compared to experimental data.

Fig. 4.12 a) shows the total-static isentropic head coefficient and Fig. 4.12 b) the total-static isentropic efficiency at outlet of the vaneless diffuser for numerical data set (CFD) and experimental one. Experimental data follows the same trend as suggested by numerical data. Nonetheless, an over-estimation of around 3 efficiency points is done by CFD. As discussed in subsection 2.6.4, the distorting impact of the collector on the upstream components is not modeled in CFD, what is a reason for the over-estimation in terms of total-static isentropic efficiency at vaneless diffuser outlet.

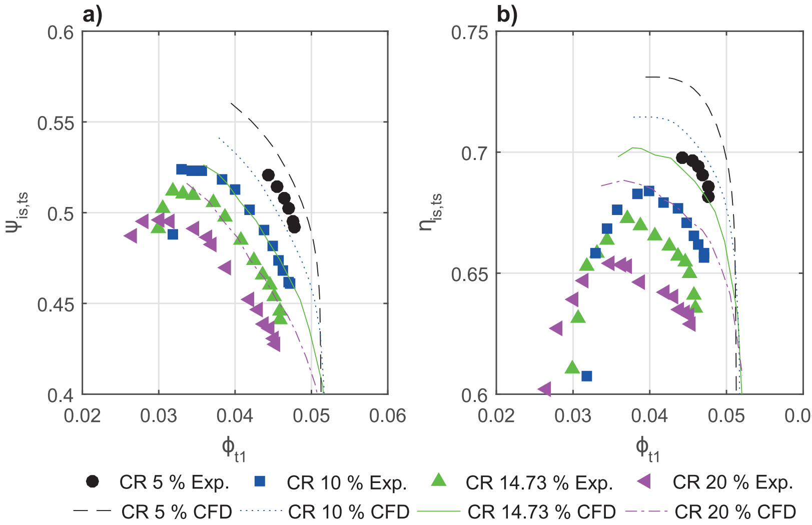

Figure 4.12: Comparison between experimental and numerical total-static isentropic head (a) and efficiency (b) for various relative tip gap ratios at outlet of the vaneless diffuser (compressor by Javed et al. [27]).

Although there is a discrepancy between numerical and experimental data set for the scaled up compressor by Javed et al. [27], numerical results, however, suggest the same trend as experiments, thus the numerical setup can be taken as validated.

4.2 Assessment of empirical tip clearance loss correlations

Various empirical tip leakage loss correlation are available in literature, which model the drop in efficiency as a function of the relative clearance ratio CR at trailing edge. Eq. 1.1 shows the empirical equation suggested by Eckert and Schnell [30] and Pfleiderer and Petermann [29], where Eckert and Schnell [30] recommend using a factor of $a = 0.9$ and Pfleiderer and Petermann [29] a range of $a = 1.5 - 3$. The other empirical tip leakage loss correlations which are investigated are the one by Pampreen [31] (see Eq. 4.1) and Schmidt-Theuner and Mattern [32] (see Eq. 4.2). All of the correlations offer a linear relationship between drop in efficiency and the relative clearance ratio at trailing edge. Merely the correlation of Schmidt-Theuner and Mattern [32] models the drop in efficiency using a quadratic approach, thus the drop in efficiency is less pronounced for large relative clearance ratios. This behavior is also corroborated by Brasz [33]:

$$\begin{aligned} \Delta\eta_{Cl} &= 0 && \text{for } CR \leq 0.03 \\ \Delta\eta_{Cl} &= -0.35CR + 0.01 && \text{for } CR > 0.03 \end{aligned} \tag{4.1}$$

$$\Delta\eta_{Cl} = -0.23CR + 0.46CR^2 \qquad \text{for } 0.035 < CR > 0.14 \tag{4.2}$$

It is not mentioned in literature, however, how the above mentioned correlations (Eq. 4.1 and Eq. 4.2) are evaluated, since two different possibilities exist: On the one hand, the correlations can be applied for operating points at the same mass flow rate. On the other hand, one can evaluate the correlation for a pre-defined operating point (e.g. best efficiency point). Merely the correlations by Eckert and Schnell [30] and Pfleiderer and Petermann [29] need to be evaluated for the best efficiency point, since a correlation for shift in mass flow rate is additionally defined.

In a first step, the empirical correlations are evaluated for the design point of the compressor provided by Schiffmann [12, 13, 14, 15], rotating at 180 000 rpm. Fig. 4.13 show the drop in efficiency as a function of the relative clearance ratio for numerical and Fig. 4.14 for experimental results compared to the empirical correlations.

Numerical results suggest a drop of around 0.6 efficiency points per percent of clearance ratio for operating points with the same flow rate. The drop in efficiency for the same flow coefficient of the baseline compressor design flow coefficient shows a linear trend. The drop in efficiency for the best efficiency points follows a linear trend up to 10 % of relative clearance ratio, but the drop between 10 % and 15 % of relative clearance ratio is less pronounced. The experimental results show a deterioration of around 0.8 efficiency points per percent of relative clearance ratio for operating points with same mass flow rate. Overall, the efficiency drop for points with the same global flow coefficient is suggested to be more pronounced compared to drop in efficiency of peak efficiency points, what is corroborated by both data set. As mentioned in subsection 4.1.2, the experimentally investigated compressors having a

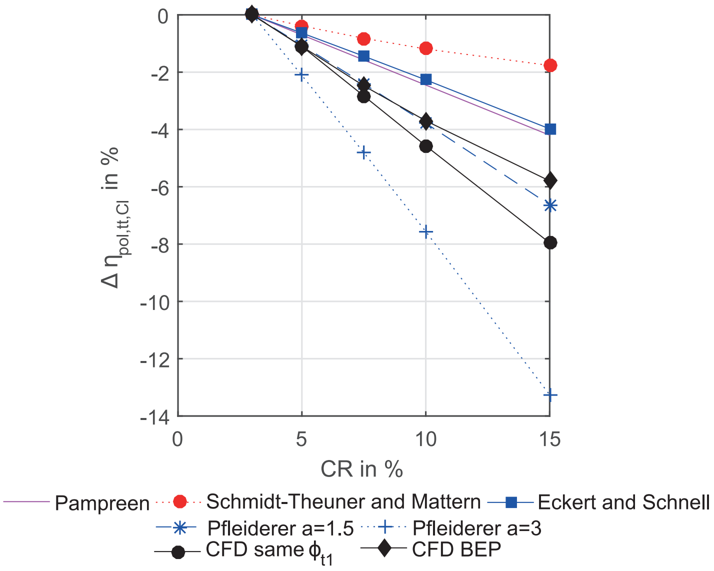

Figure 4.13: Numerical (CFD) drop in compressor efficiency due to alteration of relative clearance ratio compared to commonly-used empirical correlations (compressor by Schiffmann [12, 13, 14, 15]).

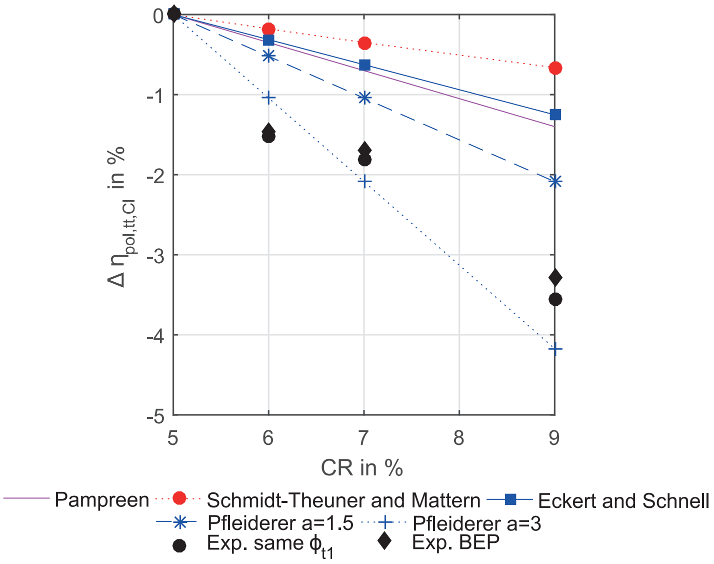

Figure 4.14: Experimental drop in compressor efficiency due to alteration of relative clearance ratio compared to commonly-used empirical correlations (compressor by Schiffmann [12, 13, 14, 15]).

relative clearance ratio of 6 % and 7 % suggest a very low change in efficiency, which is most likely caused by errors occurring in the clearance adjustment approach.
The empirical correlation of Schmidt-Theuner and Mattern [32] strongly under-estimates the expected efficiency drop. A drop in efficiency of around 0.15 % per percent of clearance ratio is suggested by this correlation.
The commonly used correlations of Eckert and Schnell [30] as well as the one of Pampreen [31] are almost in line with each other and a drop in efficiency of around 0.3 efficiency points per percent of clearance ratio is predicted. Nonetheless, both correlations under-estimate the impact of increasing tip clearance on the efficiency drop as shown for this particular impeller. The more pessimistic correlation by Pfleiderer and Petermann [29] (a=1.5) shows a good agreement for the expected efficiency drop of this compressor.

In a next step, numerical and experimental results of the scaled up compressor by Javed et al. [27] are evaluated against the mentioned empirical correlations for the design point, the global flow coefficient of 0.042 and the best efficiency points, respectively. Fig. 4.15 shows drop in efficiency for numerical and Fig. 4.16 for experimental results, where the compressor operates at design speed (50 krpm).

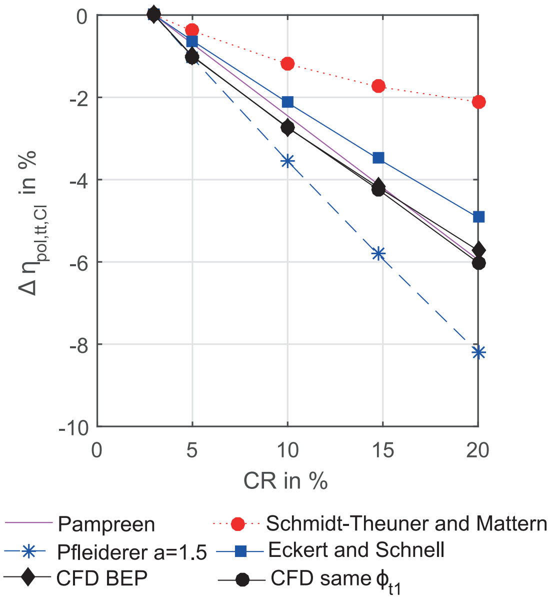

Figure 4.15: Numerical (CFD) drop in compressor efficiency due to alteration of relative clearance ratio compared to commonly-used empirical correlations (compressor by Javed et al. [27]).

Numerical results suggest no difference between operating points with the same global flow coefficient and peak efficiency points, whereas experimental results suggest a more pronounced efficiency drop for points having the same global flow coefficient. The numerical results (Fig. 4.15) suggest a drop of around 0.35 efficiency points and experimental results (Fig. 4.16) a drop of around 0.4 effiency points per percent of relative clearance ratio for operating points with

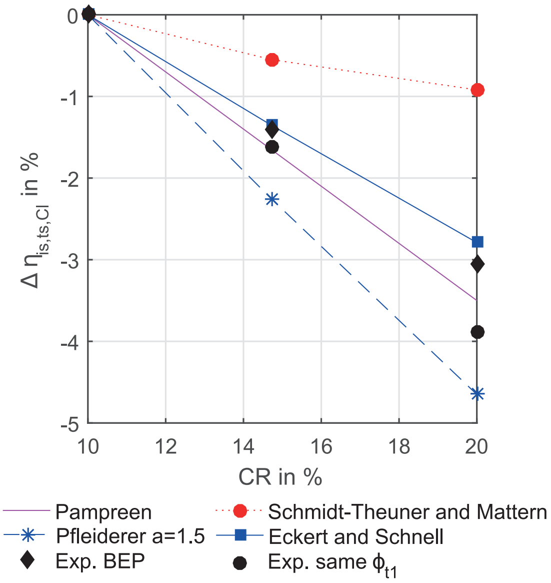

Figure 4.16: Experimental drop in compressor efficiency due to alteration of relative clearance ratio compared to commonly-used empirical correlations (compressor by Javed et al. [27]).

the same global flow coefficient. In this case, the commonly used empirical correlations by Eckert and Schnell [30] as well as by Pampreen [31] predict the drop in efficiency in line with numerical and experimental results. The pessimistic correlation of Pfleiderer and Petermann [29] strongly over-estimates the drop in efficiency for this particular impeller. Compared to the compressor by Schiffmann [12, 13, 14, 15], the scaled up compressor provided by Javed et al. [27] is less sensitive to a change in relative clearance ratio.

This analysis suggests, that two different compressors show a different sensitivity with regards to a change of relative tip clearance ratio. No conclusion can be drawn about the quality of empirical correlations, since they seem to depend on compressor design. The compressor by Javed et al. [27] shows a sensitivity, which is half the value of the one by Schiffmann [12, 13, 14, 15]. Hence, the sensitivity parameter might be dependent on compressor design parameters and/or operating conditions. Overall, most of the empirical correlations underestimate the drop in efficiency, thus it seems plausible to evaluate the empirical correlations for peak efficiency points, since the drop in efficiency of peak efficiency points is less pronounced compared to efficiency drop of operating points with the same global flow coefficient.

4.3 Tip clearance sensitivity parameter

4.3.1 Sensitivity of compressor by changing its tip gap

As seen in the previous section, most of the commonly-used empirical tip leakage loss correlations model the expected drop in efficiency as a linear relationship of the relative clearance ratio. In addition, the compressor by Schiffmann [12, 13, 14, 15] and the one by Javed et al. [27] show a linear dependency between the drop in efficiency and the relative clearance ratio for operating points with the same mass flow rate at design conditions. This motivates the author to model tip leakage loss as a function of the relative clearance ratio at trailing edge according to Eq. 4.3 for a specific flow coefficient

$$\Delta\eta_{Cl} = m_{Cl} CR \tag{4.3}$$

, where m_{Cl} is the proportionality constant and the tip clearance sensitivity parameter.
In order to obtain a relationship for clearance loss as a function of the operating range, Eq. 4.3 is applied in the entire operating range of the compressor for operating points having the same global flow coefficient. Numerical data suggests that all operating points having the same global flow coefficient can be correlated with a linear relationship as a function of the relative clearance ratio for both investigated compressor geometries. Fig. 4.17 shows the numerically defined drop in efficiency as a function of the relative clearance ratio for three different operating points (near surge (see Fig. 4.17 a); BEP (see Fig. 4.17 b); near choke (see Fig. 4.17 c)) having the same flow coefficient (compressor by Schiffmann [12, 13, 14, 15]). All points are fitted by a line and the slope of this line represents the tip clearance sensitivity for a specific flow coefficient. Nonetheless, the compressor by Javed et al. [27] shows discrepancies by modeling the efficiency drop linearly near choke, what is shown by Fig. 4.18.

The resulting sensitivity parameter m_{Cl} as a function of the global flow coefficient is presented in Fig. 4.19 for the compressor by Schiffmann [12, 13, 14, 15], based on numerical results (black solid line with circles) and on experimental results (red dashed line with cross).

The sensitivity parameter m_{Cl} based on experimental data is around 0.2 efficiency points higher compared to numerical results. This most likely sources from the tip gap adjustment using shimming plates, thus diffuser and volute areas are affected. Hence, the components do not necessarily match anymore and an additional loss occurs, what is depicted in the experiment. The numerical results, however, were obtained by using a different tip clearance adjustment approach. Nonetheless, both curves feature the same slope, thus suggesting a good qualitative agreement between numerical and experimental results. Overall, the tip gap sensitivity increases from surge towards choke. This is a result of the efficiency curve shift towards smaller mass flow rates (see Fig. 4.1 c)), thus the curves diverge towards choke by having almost the same choking mass flow rate.

Fig. 4.20 shows the sensitivity parameter m_{Cl} as a function of the global flow coefficient for the scaled up compressor by Javed et al. [27]. Numerical results are presented as red line with diamonds and experimental results are presented as black line with circles.

As demonstrated in the previous section, this compressor features a lower sensitivity to relative tip clearance changes compared to the compressor by Schiffmann [12, 13, 14, 15] at the peak efficiency point. As for the compressor by Schiffmann [12, 13, 14, 15], the experimental

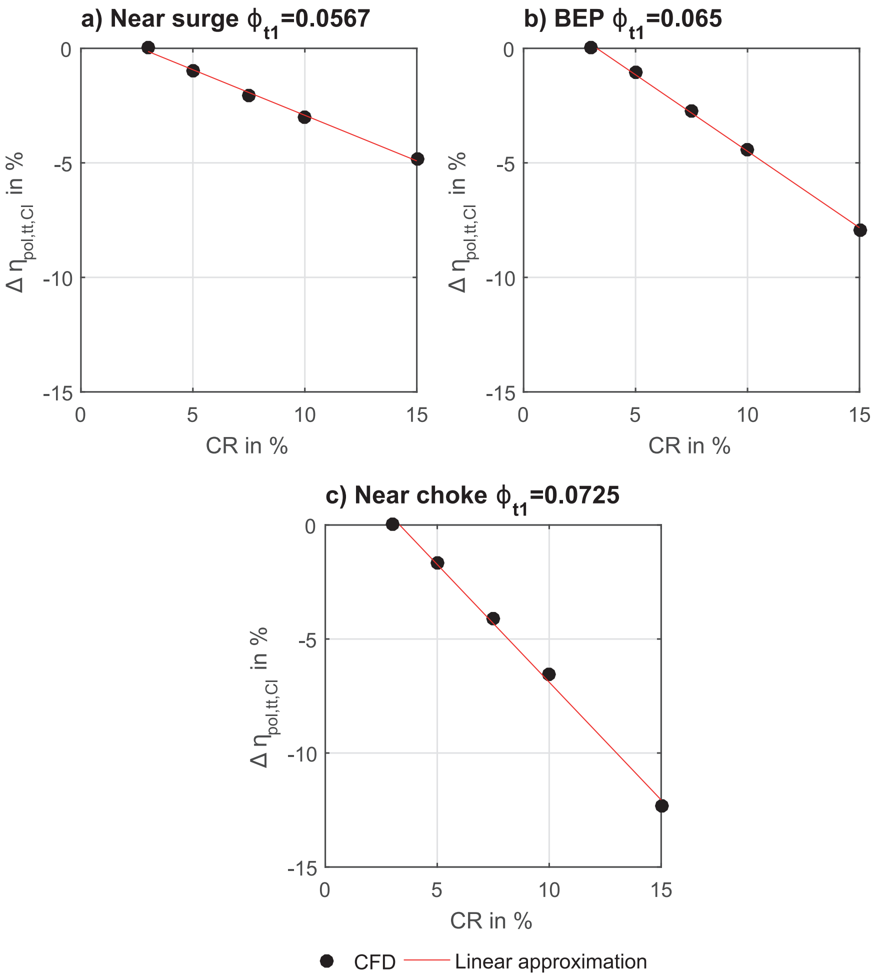

Figure 4.17: Linear fitting of numerical efficiency drop caused by relative clearance alteration for the compressor unit provided by Schiffmann [12, 13, 14, 15] at different operating points.

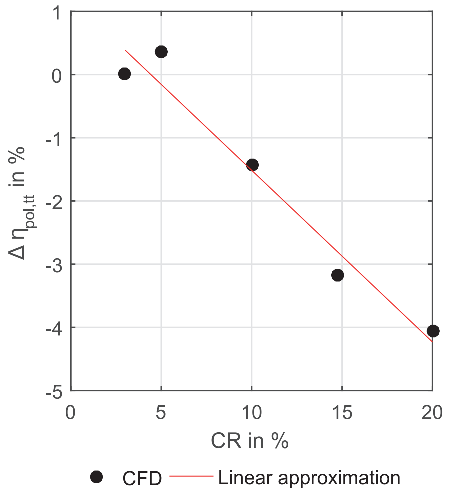

Figure 4.18: Problem of using a linear fit at high mass flow rates (ϕ_{t1}=0.05) for the compressor by Javed et al. [27].

results yield marginally higher as the numerical data set. The sensitivity parameter first increases from surge towards higher mass flow rates, what is similar to the compressor of Schiffmann [12, 13, 14, 15] caused by the shift of efficiency curves towards smaller mass flow rates, thus diverging towards choke. At high mass flow rates, the sensitivity parameter starts to stagnate, which might be caused by the intersection of different clearance ratio efficiency lines, since the largest clearance ratio features a higher choking mass flow rate than the lowest one. Nonetheless, experimental data and numerical data suggest a similar distribution of the sensitivity parameter in the investigated operating range, thus further supporting a good qualitative agreement between numerical and experimental data.

Both investigated compressor geometries show a different sensitivity to the relative clearance ratio at trailing edge, thus suggesting a strong dependence of the tip clearance sensitivity parameter m_{Cl} on design parameters and/or operating conditions.

4.3.2 Scaling tip clearance sensitivity

The evaluation of tip clearance sensitivity parameter according to Eq. 4.3 is performed for the scaling analysis presented in chapter 3 as a function of the global flow coefficient. Following the same procedure as in the previous subsection, the tip clearance sensitivity parameter m_{Cl} is obtained for different geometric scales for relative clearance ratios ranging from 3 % up to 15 %. The tip clearance sensitivity for differently geometrically scaled geometries is presented in Fig. 4.21 a) and b) as a function of the global flow coefficient. The used color code is in accordance with the one used in chapter 3.

Due to the shift of global flow coefficient caused by the Reynolds number effect (see chapter 3), the efficiency curves are shifted towards higher mass flow rates with an increase of geometrical scale (see Fig. 4.21 a)). One can clearly see that all curves feature the same slope, but are

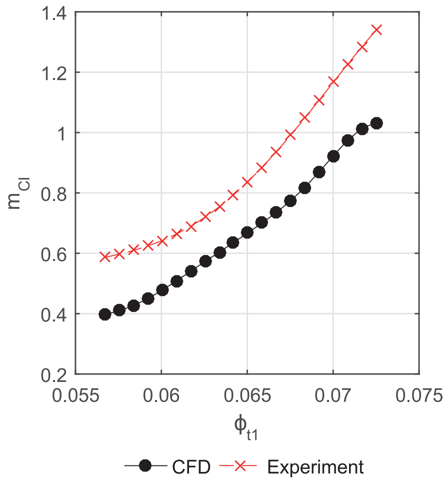

Figure 4.19: Experimentally and numerically obtained tip clearance sensitivity parameter over the global flow coefficient for compressor provided by Schiffmann [12, 13, 14, 15].

shifted horizontally. Applying the correction of global flow coefficient (see Eq. 3.3) for the baseline compressor with a relative clearance ratio of 5 %, all curves collapse to a single one (see Fig. 4.21 b)). Hence, these findings further underline the Reynolds number independence of tip leakage related phenomena and prove that findings of the up-scaled compressor by Javed et al. [27] can be transferred to the original size compressor.

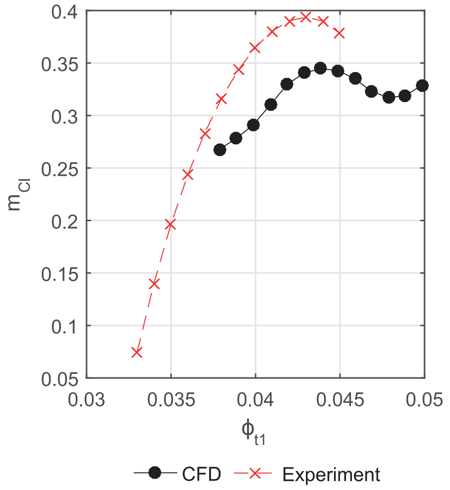

Figure 4.20: Experimentally and numerically obtained tip clearance sensitivity parameter over the global flow coefficient for compressor provided by Javed et al. [27].

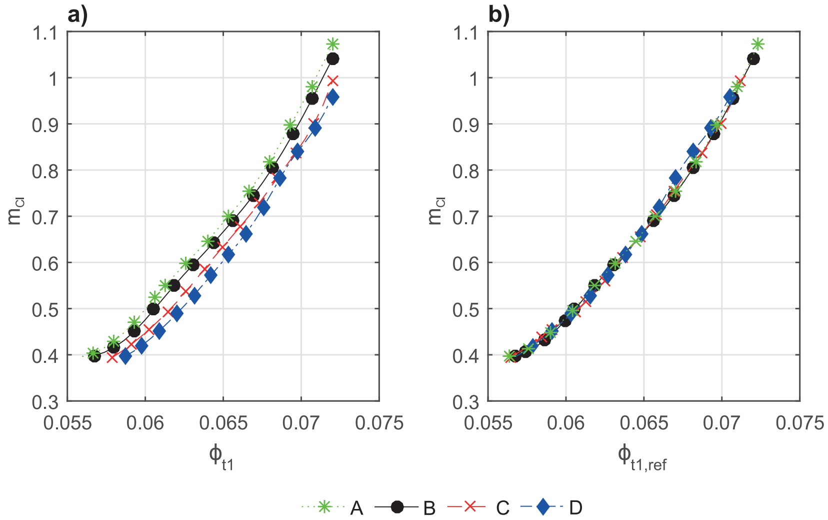

Figure 4.21: Evaluation of tip clearance sensitivity parameter for geometrical compressor scaling of the unit by Schiffmann [12, 13, 14, 15]. (a) Non-corrected results; (b) Corrected results considering Reynolds number effect.

4.4 Interaction of tip leakage with blade loading and diffusion

As demonstrated in the previous sections, the compressor units by Schiffmann [12, 13, 14, 15] and Javed et al. [27] feature different behavior in terms of tip clearance sensitivity. Hence, design features like blade angle and end-wall distribution most likely impact tip leakage, the corresponding exhaust flow patterns and losses. In order to identify design strategies to suppress tip leakage, a more thorough insight on how relative clearance impacts the impeller flow is required. CFD data is therefore used.
In a first step, the ratio between leakage mass flow rate and overall compressor mass flow rate as a function of the global flow coefficient is presented in Fig. 4.22 a) for the compressor unit by Schiffmann [12, 13, 14, 15] and in Fig. 4.22 b) for the one by Javed et al. [27], for various relative clearance ratios.

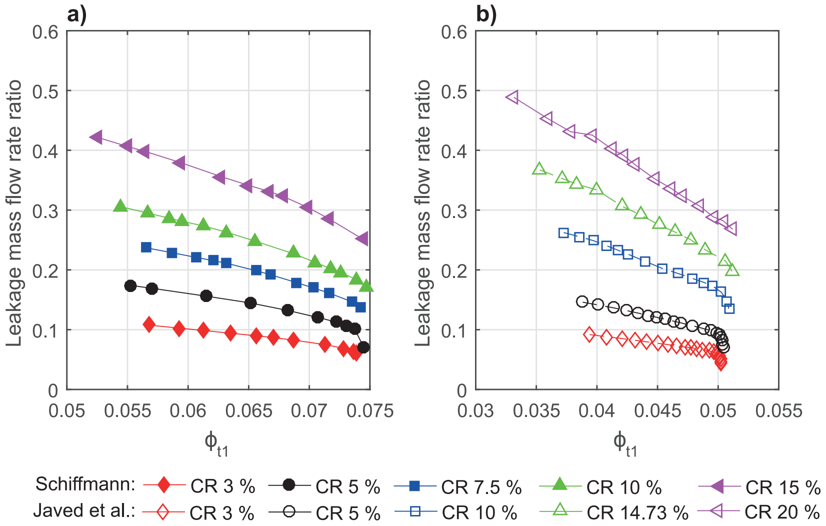

Figure 4.22: Leakage mass flow rate ratio as a function of the global flow coefficient for Schiffmann [12, 13, 14, 15] compressor (a) and the scaled up compressor unit provided by Javed et al. [27] (b).

Fig. 4.22 suggests that the relative leakage mass flow rate increases with the relative clearance ratio. In addition, tip leakage mass flow rate ratio increases from choke region towards the unstable surge region, what is caused by the higher pressurization and hence higher density towards smaller mass flow rates. At the same time, the loading difference between the blade tip increases with a decrease of the compressor mass flow rate, what leads to an increase of tip jet velocity. The compressor by Schiffmann [12, 13, 14, 15] shows slightly higher leakage mass flow rates for a given relative clearance ratio compared to the one provided by Javed et al. [27], what proves that impeller design has an impact on tip leakage.

In a next step, aerothermal properties along the suction side of the tip gap for main and splitter blade are shown in Fig. 4.23 for the compressor by Schiffmann [12, 13, 14, 15] having various relative clearance ratios at peak efficiency point. Fig. 4.23 a) and d) show the distribution of mass flux for main and splitter blade as a function of the meridional length. Fig. 4.23 b) and e) show the density distribution along the suction side of the tip gap for main and splitter blade. In this case, the density is normalized by the total inlet density. Furthermore, Fig. 4.23 c) and f) show the relative Mach number of the tip jet as a function of the meridional streamline length for main and splitter blade.

Mass flux (see Fig. 4.23 a) and d)) increases independently of the tip gap size from leading towards trailing edge, where it reaches a maximum at around 90 % of the meridional coordinate. At this position, the highest mass flux occurs for the lowest clearance ratio and vice versa, thus suggesting that tip leakage mass flow rate not only depends on the tip gap area, but also on other aerothermal properties like density and velocity. By increasing the relative tip gap, the mass flux increases in the inducer part of the impeller (first 20 % of meridional coordinate).
The tip jet density (see Fig. 4.23 b) and e)) increases from leading to trailing edge of the impeller, what is in line with the pressurization in the impeller passage (see Fig. 4.25). At the rear part of the impeller, the tip jet density decreases with an increase of relative clearance ratio, what is caused by the higher pressure losses due to stronger tip jets. In the inducer part, the tip jet density increases with relative clearance ratio, thus increased mass fluxes occur at this position. This is also the position where the tip leakage vortex detaches from the main blade. Hence, intensity of tip vortices increase as highlighted by the increasing zone of low relative Mach numbers shown in Fig. 4.3 and Fig. 4.4.
The relative Mach number of the tip jet reaches a maximum between 70 and 80 % of meridional coordinate for all relative clearance ratios. This maximum reduces for increased clearance ratios. At the inducer part of the impeller, the relative Mach number of the tip jet increases with an increase of relative clearance ratio. Similar as the increase of tip jet density in the inducer, the increase in relative Mach number further strengthens the tip leakage vortex. Overall, the relative Mach number distribution follows the blade loading distribution at shroud (see Fig. 4.27), what indicates that the shroud blade loading being a further driving mechanism of tip leakage.

Fig. 4.24 shows similar characteristics as Fig. 4.23 for the compressor unit by Javed et al. [27]. Mass flux distribution looks different compared to the one by Schiffmann [12, 13, 14, 15]. In this case, the mass flux starts to increase from leading edge up to 40 % of meridional coordinate. At this position up to 50 %, the mass flux drops almost to zero. This effect is more pronounced for larger relative clearance ratios. From 50 % up to around 90 %, a maximum in mass flux is reached and this maximum is increased for smaller relative clearance ratios. The decrease in tip flux in the mid part of the impeller is caused by the wide opening of the blade channel at this position, what leads to a strong diffusion and thus a strong deceleration of relative velocity.
The density distribution follows the pressurization of the impeller (Fig. 4.26). An increase in tip leakage density with an increase of relative clearance ratio is spotted in the inducer region as occurring in Schiffmann's [12, 13, 14, 15] compressor.
In terms of relative Mach number distribution, a maximum is reached at around 70 % of the meridional coordinate, what is in accordance with the loading distribution at shroud (see Fig.

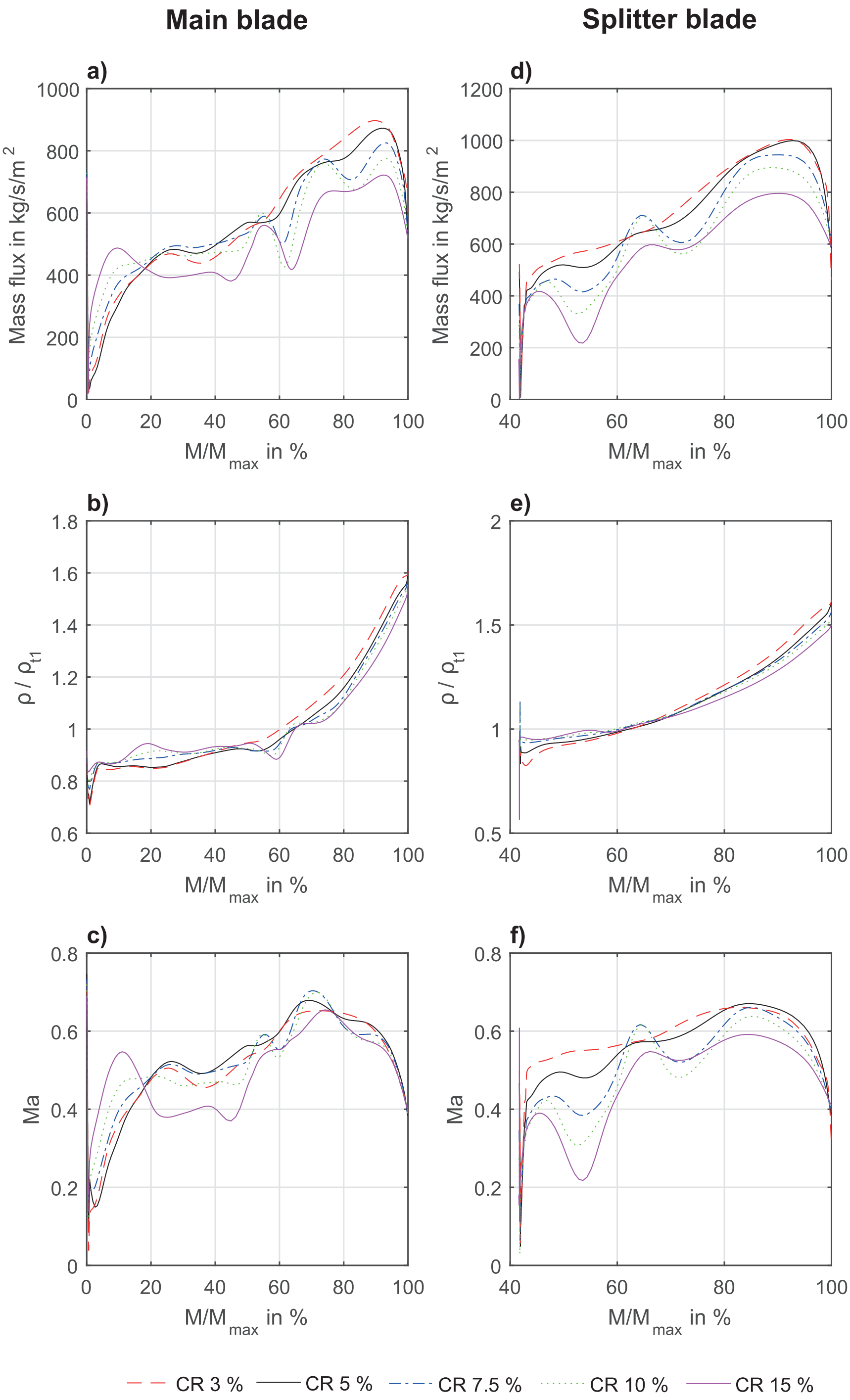

Figure 4.23: Aerothermal properties along the suction side of main and splitter blade tip gap as a function of the meridional tip gap length, showing the compressor unit provided by Schiffmann [12, 13, 14, 15] for various clearance ratios at their peak efficiency point.

4.28 a) and b)). The relative Mach number of the tip jet decreases at around 50 % of meridional coordinate to almost zero, what explains the low tip mass flux at this location. Due to wide opening of the blade passage at this position, the relative flow gets strongly decelerated, thus the shroud becomes unloaded, what is shown in the shroud loading distribution in Fig. 4.28 a) and b). This further demonstrates that shroud blade angle distribution and in this case the end-wall shape of hub and shroud can have a strong impact on tip leakage. Hence, these design variables can be used as control mechanism for tip leakage.

Fig. 4.25 shows the total-static pressure ratio for the compressor by Schiffmann [12, 13, 14, 15] as a function of the normalized meridional coordinate at 90 % blade span. Fig. 4.25 suggests that the pressurization and hence the diffusion in the inducer region increases with an increase of relative tip gap ratio. The increased pressurization is observed up to 40 % of meridional coordinate. The increase in tip jet density in the inducer region (see Fig. 4.23 b) and e)) is caused by this stronger pressurization. Hence, the flow density as well as the density of tip jet increases and stronger tip mass fluxes occur in the inducer. Due to the increased total pressure loss caused by an increase of the relative clearance ratio, the pressurization decreases in the rear part of the impeller, what lowers the tip jet density.

Fig. 4.26 shows the total-static pressure ratio along 90 % blade span for the scaled up compressor by Javed et al. [27]. The pressurization in the inducer increases in a similar manner as in Schiffmann's [12, 13, 14, 15] compressor, thus suggesting a stronger diffusion and hence stronger tip leakage flows, leading to a more intense main blade tip leakage vortex with an increase in relative clearance ratio.
Compared to the compressor by Schiffmann [12, 13, 14, 15], the compressor by Javed et al. [27] shows a strong diffusion, which occurs at 50 % of the normalized impeller coordinate. This large diffusion occurring in the mid of the impeller was desired by Javed et al. [27], in order to strongly decrease the shroud blade loading at this position. This was achieved by a wide opening of the impeller passage, resulting in a clear reduction of shroud blade loading. As a consequence, Javed et al. [27] achieved to guide the tip leakage vortices near the blade suction sides, what reduces blockage in the rear part of the impeller. More specific details about their design is provided in chapter 5.
The large diffusion ratios, however, might be critical in terms of compressor stability thus the end-wall shape has to be re-designed (see chapter 5). Nonetheless, it also proves the strong impact of end-wall shape on the diffusion ratio, the blade loading and hence the positive impact on tip leakage mass flow. Compared to Schiffmann's [12, 13, 14, 15] compressor, the lower sensitivity to tip clearance of this compressor is caused by the stronger diffusion through the wide blade channel, leading to an unloading of the shroud at this position. This effect is amplified by an increase in relative clearance ratio, thus the tip leakage mass flux decreases with an increase in relative clearance ratio.

Fig. 4.27 shows the blade loading parameter of main (see Fig. 4.27 a)) and splitter blade (see Fig. 4.27 b) and section 2.2) at 90 % blade span and as a function of the meridional coordinate for the compressor provided by Schiffmann [12, 13, 14, 15].

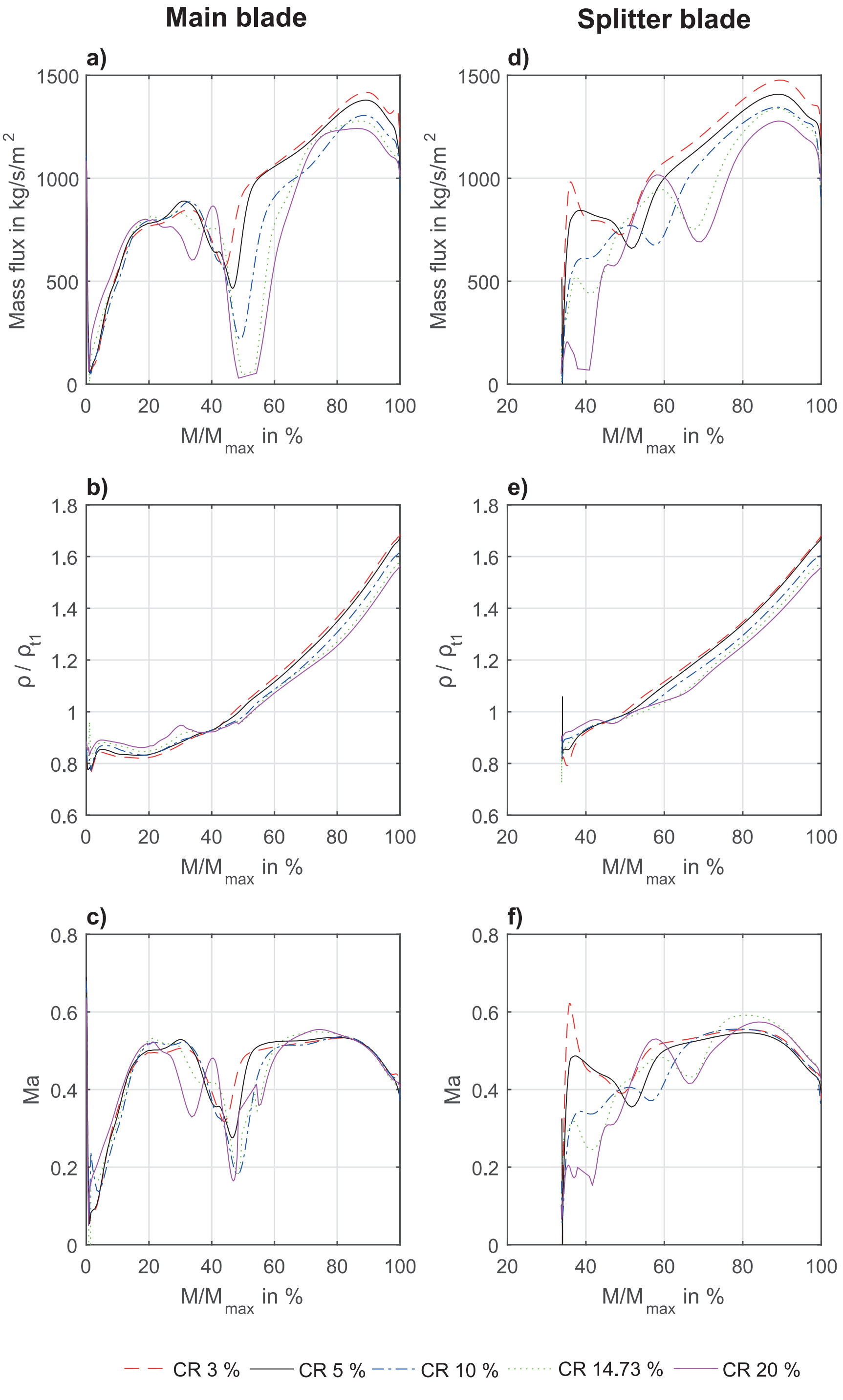

Figure 4.24: Aerothermal properties along the suction side of main and splitter blade tip gap as a function of the meridional tip gap length, showing the compressor unit provided by Javed et al. [27] for various clearance ratios at their peak efficiency point.

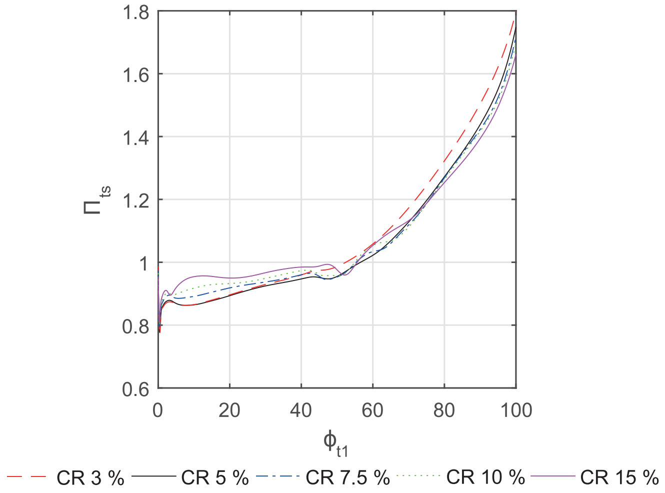

Figure 4.25: Total-static pressure ratio along the normalized meridional length at a blade span of 90 % for various clearances at their peak efficiency point (Schiffmann [12, 13, 14, 15]).

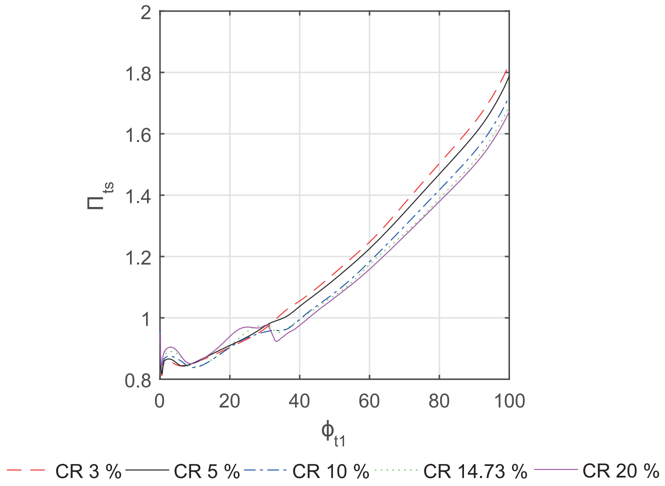

Figure 4.26: Total-static pressure ratio along the normalized meridional length at a blade span of 90 % for various clearances at their peak efficiency point (Javed et al. [27]).

The loading at a blade span of 90 % is in accordance with the relative Mach number distribution of the tip jet shown in Fig. 4.23, suggesting that the tip leakage is directly linked to the blade loading distribution. The loading distribution in the inducer region shows that the impeller main blade becomes more and more loaded in this region with an increase in relative clearance ratio, driving both the tip jet velocity and the tip leakage mass flux.

The shroud blade loading decreases at the rear part of the impeller with an increase in relative clearance ratio, yielding smaller pressure difference between the blade pressure and the suction side of the adjacent blade. Hence, the low relative velocity zone shown in Fig. 4.3 gets shifted towards the center of the blade passage by increasing the relative clearance ratio, since the stronger tip leakage jet in the rear part of the impeller pushes this low momentum fluid against a decreasing pressure gradient.

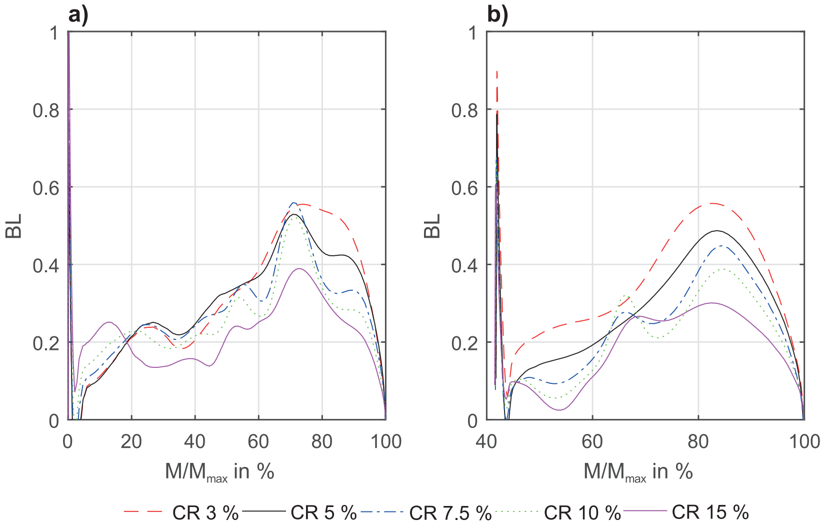

Figure 4.27: Blade loading as a function of the normalized meridional length at 90 % blade span for various relative clearance ratios at their peak efficiency point (Schiffmann [12, 13, 14, 15]).

In addition, Fig. 4.28 a) and b) show the loading distributions at 90 % of blade span of the up-scaled compressor by Javed et al. [27] for main and splitter blade. Similar conclusions can be drawn as for the compressor by Schiffmann [12, 13, 14, 15]. The loading distribution shows the strong unloading of the impeller main blade shroud with an increase in relative tip gap. Due to the increase in passage area of the blade channel (see Fig. 5.1), the relative flow gets decelerated such, that the shroud unloads at this position. This effect is amplified with an increase in relative clearance ratio, yielding a lower tip leakage mass flow rate. Hence, this compressor is less sensitive to variations of the relative clearance ratio, what has already been shown in the previous sections. On the one hand, this has a positive effect on the tip mass flux distribution, since less tip leakage mass flow rates occur, thus the compressor is less sensitive to tip leakage losses. On the other hand, a very strong diffusion of the flow occurs in the mid of the impeller passage, leading to a complete unloading of the shroud thus no work is transferred to the fluid.

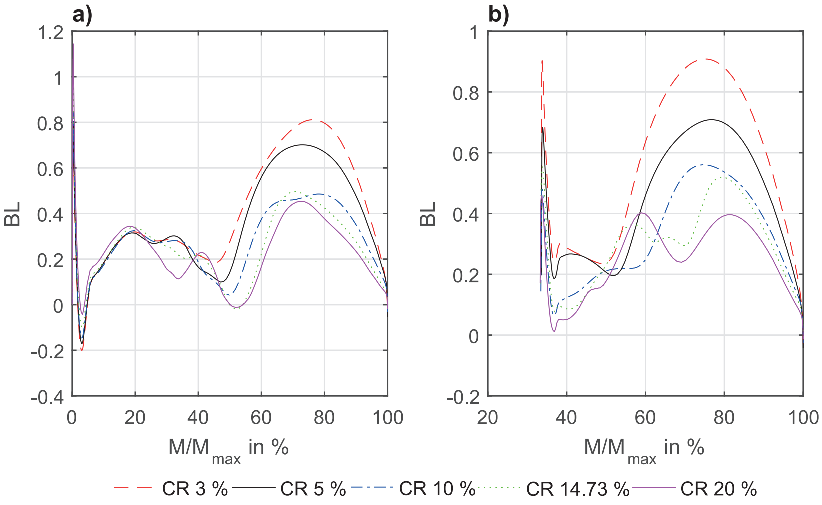

Figure 4.28: Blade loading as a function of the normalized meridional length at 90 % blade span for various relative clearance ratios at their peak efficiency point (Javed et al. [27]).

Fig. 4.23 to Fig. 4.28 suggest, that tip leakage mass flows not only depend on the geometrical tip gap area but also on aerothermal flow properties like density and tip jet velocity. Altering the tip gap size has a significant impact on the diffusion in the blade passage and relative Mach number distribution of the tip jet. By increasing the relative clearance ratio, the mass flux in the inducer region increases due to an increase in tip jet density and relative Mach number. Hence, the tip leakage vortex of the main blade becomes stronger with increasing the relative clearance ratio. Both tip leakage and tip leakage vortices are influenceable by the end-wall distribution of hub and shroud as well as the shroud blade angle distribution. In addition, distribution of aerothermal properties along main and splitter blade looks different, thus causing an unequal flow pattern at trailing edge exhaust (see Fig. 4.3 and Fig. 4.7). The need of an individual splitter blade design is therefore demonstrated by this analysis. The comparison of both impellers further suggest, that the impeller design by Javed et al. [27] shows an improved behavior in terms of tip leakage, since the impeller shroud is partially unloaded and almost no tip leakage occurs at this position.

Furthermore, the impact of increasing the relative tip gap size on the trajectory of main and splitter blade tip leakage vortex is analyzed for the compressor provided by Javed et al. [27]. Streamlines of the main blade tip leakage vortex are illustrated in red and the streamlines of the splitter blade tip leakage vortex are shown in blue.
Fig. 4.29 shows the trajectories of main and splitter blade for a relative tip gap size of 3 %. The main blade tip leakage vortex migrates to the splitter blade passage where part of it attaches to the pressure side of the splitter blade and the other part to the suction side of the splitter blade. The accumulated fluid on the pressure side of the splitter blade is transported via tip leakage to the suction side of the splitter blade, where it combines with the splitter blade tip leakage vortex. The splitter blade tip leakage vortex rolls up at the suction side and combines with the main blade tip leakage vortex, accumulating at the splitter blade suction side. Only a

small part of the main blade vortex remains in the main blade passage.

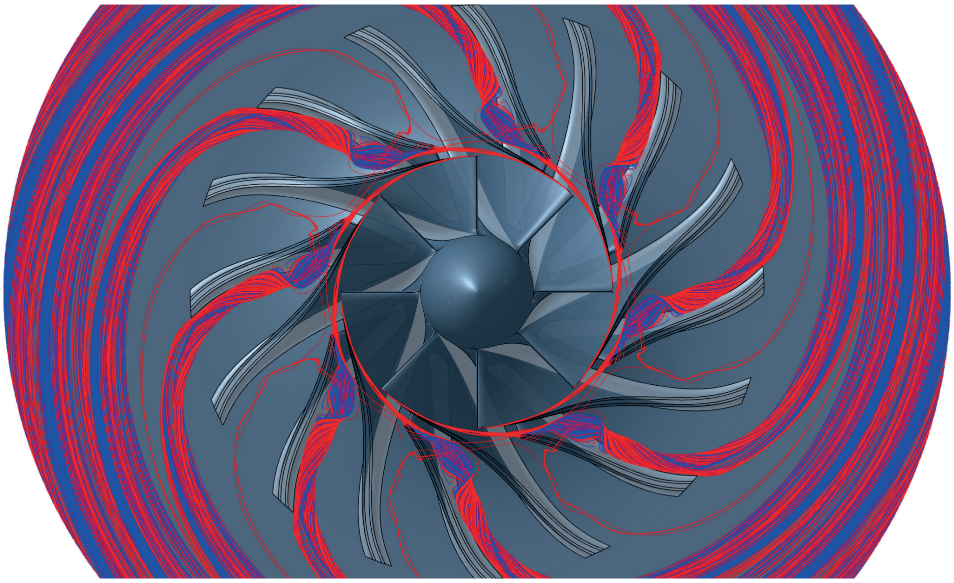

Figure 4.29: Trajectories of main (red streamlines) and splitter blade (blue streamlines) tip leakage vortices for the scaled up compressor by Javed et al. [27], having a relative clearance ratio of 3 %.

The trajectories of main and splitter blade vortices of a relative clearance ratio of 5 % show a difference compared to a relative clearance ratio of 3 %. The main blade vortex migrates to the splitter blade passage and most of it accumulates directly at the suction side of the splitter blade, mixing with the splitter blade tip leakage vortex. Here, the combined leakage vortex is pushed to the pressure side of the main blade, where a small part of it is transported to the main blade suction side by tip leakage. The other part of the combined vortex attaches to the suctions side of the splitter blade. A small leakage vortex attaches additionally at the suction side of the main blade, what explains the accumulation of low momentum fluid near the shroud suction side of the main blade shown in Fig. 4.30.

At a relative clearance ratio of 10 %, the streamlines show clear differences of the tip leakage vortex trajectories compared to the low clearance cases (see Fig. 4.31). The main blade tip leakage vortex migrates to the splitter blade, where one part accumulates to the splitter blade tip leakage vortex, following the suction side of the splitter blade. The other part of the main blade tip leakage vortex follows the suction side of the main blade, thus further increasing flow blockage in the main blade channel.

The situation becomes more amplified by increasing the relative clearance ratio, presented by Fig. 4.32 and Fig. 4.33 for a relative clearance ratio of 14.73 % and 20 %, respectively. As for a relative clearance ratio of 10 %, the main blade tip leakage vortex splits up into two parts, where one part accumulates at the pressure side of the splitter blade and is then transported by tip leakage to the suction side of the splitter blade. Nonetheless, the main blade tip leakage

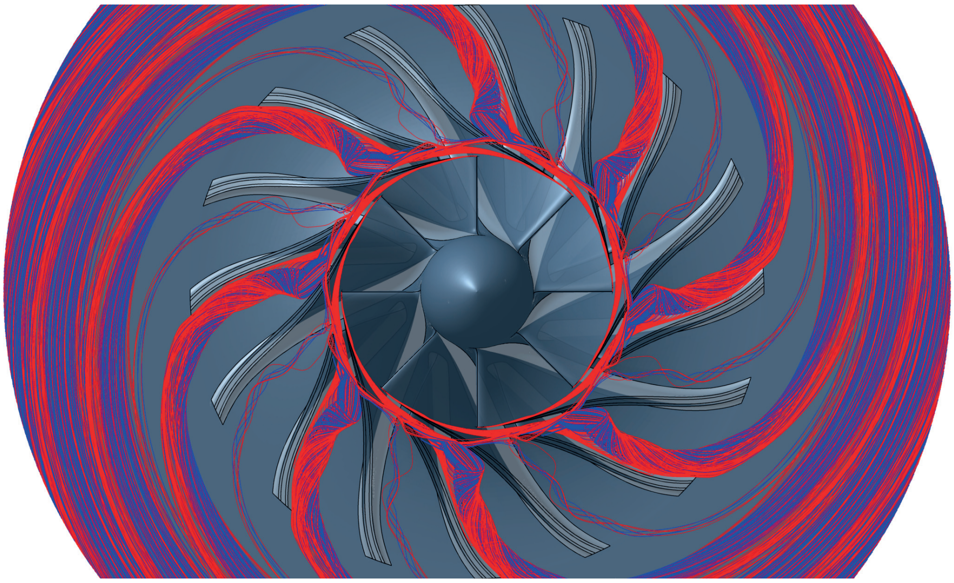

Figure 4.30: Trajectories of main (red streamlines) and splitter blade (blue streamlines) tip leakage vortices for the scaled up compressor by Javed et al. [27], having a relative clearance ratio of 5 %.

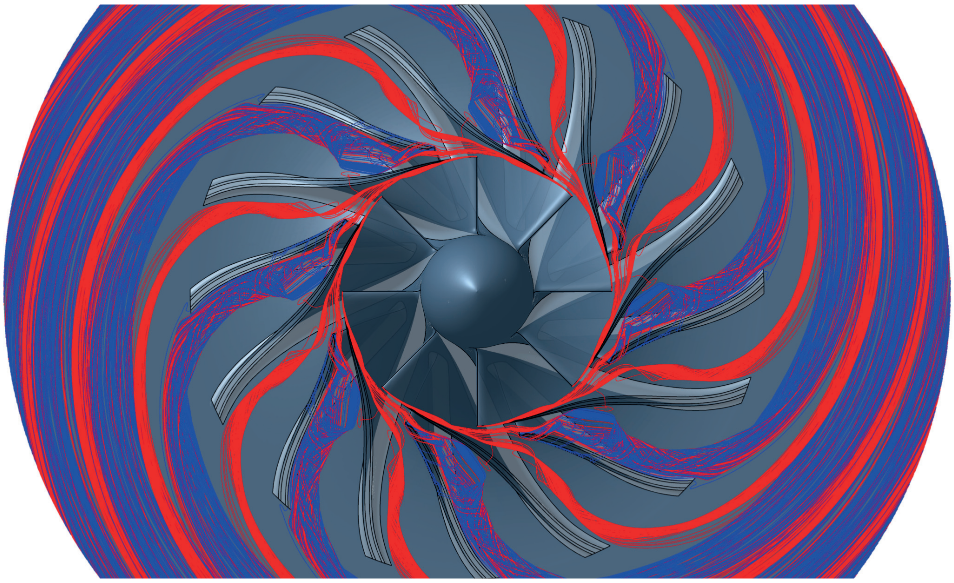

Figure 4.31: Trajectories of main (red streamlines) and splitter blade (blue streamlines) tip leakage vortices for the scaled up compressor by Javed et al. [27], having a relative clearance ratio of 10 %.

vortex interacts with the pressure side of the splitter blade and impacts the shroud loading, thus increased secondary flows occur. The other part of the main blade vortex attaches to the suction side of the main blade. By increasing the relative clearance ratio, the vortex core of both tip leakage vortices is more located in the center of the blade passage. This originates from two phenomena: (1) Tip leakage jet is more intense at the rear part of the impeller due to an increase in tip gap area, thus the low momentum fluid is pushed to the center of the blade passage, (2) at the same time, the pressure gradient between the blade pressure and suction side decreases with an increase in relative clearance ratio, thus the vortex cores are less pressed against the suction side by this pressure difference.

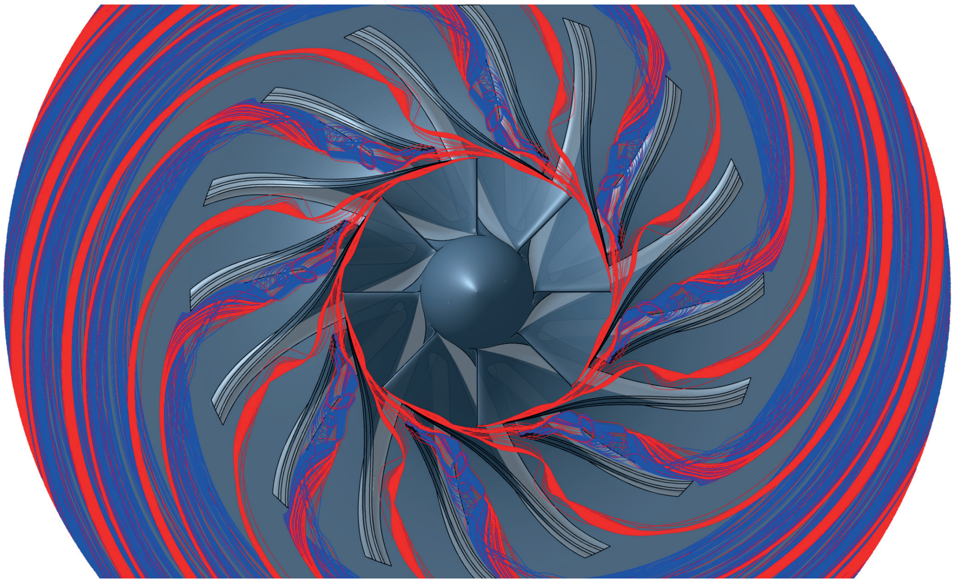

Figure 4.32: Trajectories of main (red streamlines) and splitter blade (blue streamlines) tip leakage vortices for the scaled up compressor by Javed et al. [27], having a relative clearance ratio of 14.73 %.

This streamline analysis suggest that the relative clearance ratio has a strong impact on the trajectory of tip leakage vortices. Especially the main blade tip leakage vortex is strongly affected by the tip gap size. At small relative clearance ratios, the tip leakage vortex directly migrates to the suction side of the splitter blade, where it combines with the tip leakage vortex, evolving from splitter blade leading edge. An increase in relative clearance ratio, however, results in a split of main blade tip leakage vortex into two parts, where one part accumulates at the suction side of the splitter blade and the other part follows the suction side of the main blade, creating additional blockage.

The following design implications when dealing with large relative clearance ratios can be drawn. It is assumed that the designer starts the design from a 0 mm clearance case as done in most of the preliminary design tools for centrifugal compressors.

1. A large shift of the best efficiency point towards lower mass flow rates occurs by increas-

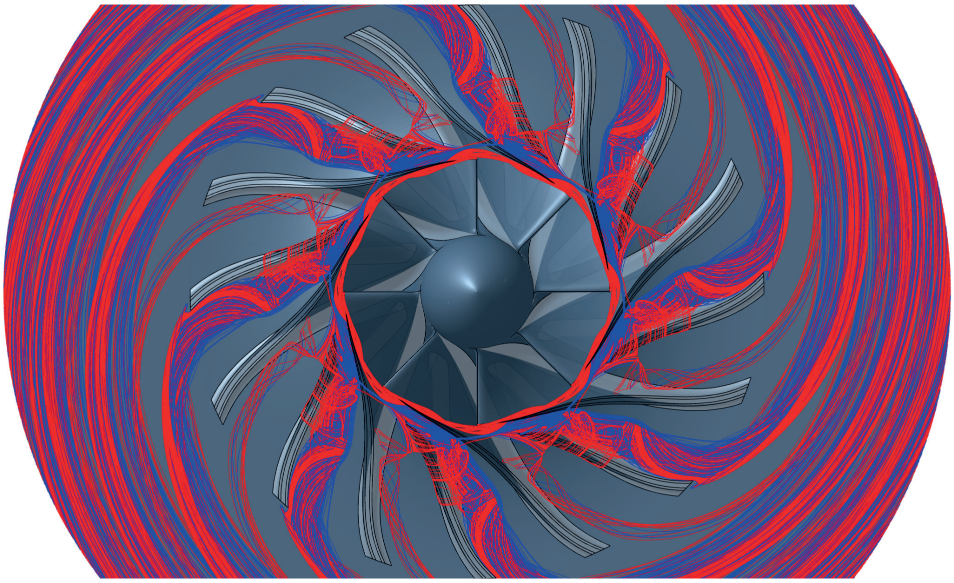

Figure 4.33: Trajectories of main (red streamlines) and splitter blade (blue streamlines) tip leakage vortices for the scaled up compressor by Javed et al. [27], having a relative clearance ratio of 20 %.

ing the relative clearance ratio. One possibility to overcome the shift of operating points towards lower mass flow rates is to design the compressor geometry having a higher global flow coefficient as the desired one. In addition, the tip flow coefficient ϕ_2 needs to be under-estimated, in order to counteract against the increased trailing edge blockage, leading to wider blade channels.

Another possibility to counteract this shift is lowering the trailing edge blade angle (increase the back-sweep angle), thus the work input coefficient curves becomes more steep. As a consequence, the best efficiency operating point is shifted towards higher mass flow rates, but also more input power is required to achieve the desired pressure ratio.

2. The inducer becomes increasingly loaded with higher tip clearance, what increases the relative Mach number of the tip jet. In addition, the diffusion in the inducer region increases, what leads to higher tip jet density and hence more tip leakage mass flow. A compressor designer therefore needs to unload the inducer region by adapting the shroud blade loading. The inducer passage width needs to be reduced by adapting shroud and hub end-walls as well as the blade angle distributions, in order to achieve less diffusion in the inducer.

3. The maximum blade loading decreases by increasing the relative clearance ratio. In case the inducer is unloaded as stated in the previous point, a compressor designer can increase the maximum loading in the mid and/or rear part of the impeller.

4. Tip leakage depends on the tip gap area, the diffusion in the impeller and the shroud

blade loading. From this point of view, it is desirable to set the maximum turning point of the shroud blade angle distribution closer to the leading edge, what leads to a front-loaded loading distribution. On the other hand, the tip leakage vortex becomes more pronounced for front-loaded shroud loading distribution. From that perspective, it seems desirable to set the maximum turning point of the shroud blade angle distribution to the mid of the impeller, in order to minimize the intensity of main blade tip leakage vortex and reduce tip leakage in the exducer.

5. Besides increased tip leakage due to an increase of the relative clearance ratio, the trajectory of the main blade tip leakage vortex is strongly affected by relative clearance ratio. A compressor designer needs to take care about guiding tip leakage vortices through the compressor. It seems desirable to guide the vortex cores near the blade suction sides. The position of these vortex cores at trailing edge depend on the pressure difference between the blade pressure side and the suction side of the adjacent blade. These vortex cores are shifted closer to the suction side with an increase of the pressure difference, hence justifies an aft-loaded shroud loading distribution. Such a loading distribution, however, is yielding strong tip leakage losses in the rear part of the impeller, thus a mid-loaded shroud loading configuration seems to offer a trade-off between losses associated to tip leakage and the position and intensity of tip leakage vortices.

4.5 Prediction of performance and leakage by reduced-order models

4.5.1 Tip clearance sensitivity by one-dimensional model (section 2.5)

The one-dimensional compressor model, presented in section 2.5, is used to investigate the prediction behavior in terms of altering the relative clearance ratio at impeller trailing edge. Therefore, the compressor geometry provided by Schiffmann [12, 13, 14, 15] is used and a similar tip gap study as presented in subsection 4.1.1 is performed. Five different relative clearance ratios at trailing edge are investigated, ranging from 3 up to 15 %.
Fig. 4.34 shows the stage characteristics in terms of polytropic head coefficient (Fig. 4.34 a)), work input coefficient (Fig. 4.34 b)) and total-total polytropic efficiency (Fig. 4.34 c)) as a function of the global flow coefficient.

The polytropic head coefficient decreases by increasing the relative clearance ratio, what is in accordance with CFD data. The tip leakage loss correlation of Jansen [72] is proportional to the relative clearance, thus it has direct impact on the internal loss mechanisms. Hence, total-total polytropic head coefficient is deteriorated.
Drop in work input coefficient due to increased blockage is captured by the one-dimensional compressor model, as suggested by Fig. 4.34 b). Hence, the drop in total-total efficiency as well as shift of the compressor map towards lower mass flow rates seems plausible.

The sensitivity parameter analysis, as presented in section 4.3, is performed based on the data

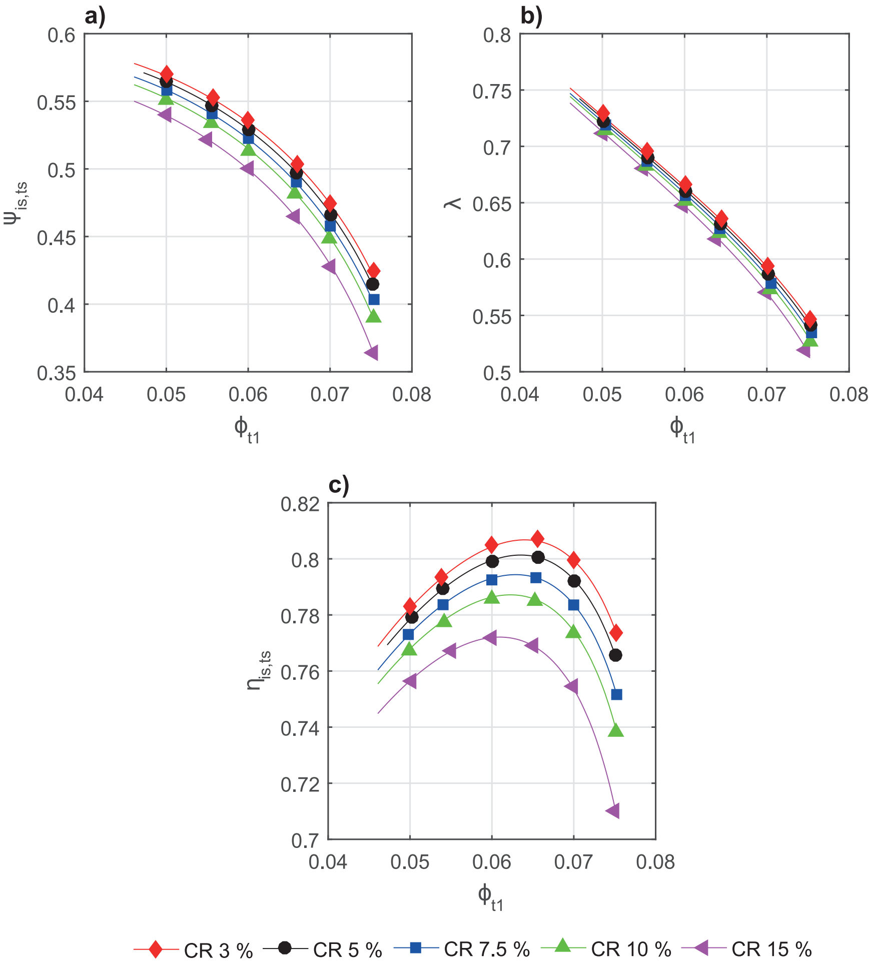

Figure 4.34: Stage characteristic for various relative tip gap ratios obtained by the one-dimensional model (compressor by Schiffmann [12, 13, 14, 15]).

set of the one-dimensional model for the compressor by Schiffmann [12, 13, 14, 15]. Fig. 4.35 shows the tip clearance sensitivity parameter m_{Cl} as a function of the global flow coefficient for data obtained from the one-dimensional model (black line with circles) and from CFD data (red cross line).

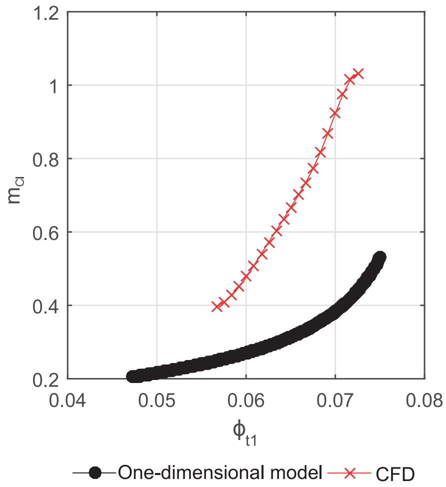

Figure 4.35: Tip clearance sensitivity parameter as a function of the global flow coefficient. Comparison between data set of CFD and one-dimensional model.

Fig. 4.35 clearly suggests, that the CFD data set and the one of the one-dimensional model are not in accordance with each other. At the design point (global flow coefficient of 0.065), the one-dimensional model predicts a drop of around 0.3 efficiency points per percentage of clearance ratio, whereas CFD predicts 0.6 efficiency points. In addition, the distribution of the sensitivity parameter m_{Cl} is not in accordance with CFD data, since sensitivity increases much faster as suggested by the one-dimensional model. The slope of the tip clearance sensitivity parameter is a measure for the shift in flow coefficient caused by an increase of relative clearance ratio. Hence, this further suggests that the shift in operating points due to a change in clearance ratio provided by the one-dimensional model is less pronounced compared to CFD.

This analysis suggests, that the one-dimensional model, although it predicts the performance characteristics of the compressor well (see Fig. 2.13), does not fully capture the sensitivity of the tip clearance effect. This discrepancy is most likely a result of two main sources. (1) A fixed blockage coefficient at trailing edge is used in the recent implementation of the one-dimensional model, thus the increased trailing edge blockage due to an increase of the tip gap is not captured. This suggests the need of a blockage correlation considering increased blockage at trailing edge induced by tip leakage, (2) the correlation by Jansen [72] seems predicting the efficiency drop caused by tip leakage too weak, thus a calibration of the one-dimensional model is required.

4.5.2 Preliminary estimation of tip leakage mass flow

Aungier [45] suggests a method for preliminary tip leakage estimation based on aerodynamic properties available at leading and trailing edge of the impeller. The resulting tip jet velocity is calculated based on a Bernoulli approach according to Eq. 1.2. The average pressure difference between the blade pressure and the suction side is calculated from the work transferred to the fluid as suggested by Eq. 4.4.

$$\Delta p_{Cl} = \frac{\dot{m}\,(r_2 c_{u2} - r_1 c_{u1})}{z \bar{r} \bar{b} L} \tag{4.4}$$

Eventually, tip leakage mass flow rate is calculated as suggested by Eq. 1.3, where ρ_2 is used as average tip jet density.
Fig. 4.36 shows the ratio between tip leakage mass flow rate and compressor mass flow rate over the global flow coefficient for the compressor by Schiffmann [12, 13, 14, 15] (Fig. 4.36 a)) and the up-scaled compressor by Javed et al. [27] (Fig. 4.36 b)). The results of the reduced-order model are computed by properties from CFD data and are compared to them, where the CFD data is marked as bold line with filled symbols and data of the reduced-order model as dashed lines with non-filled symbols.

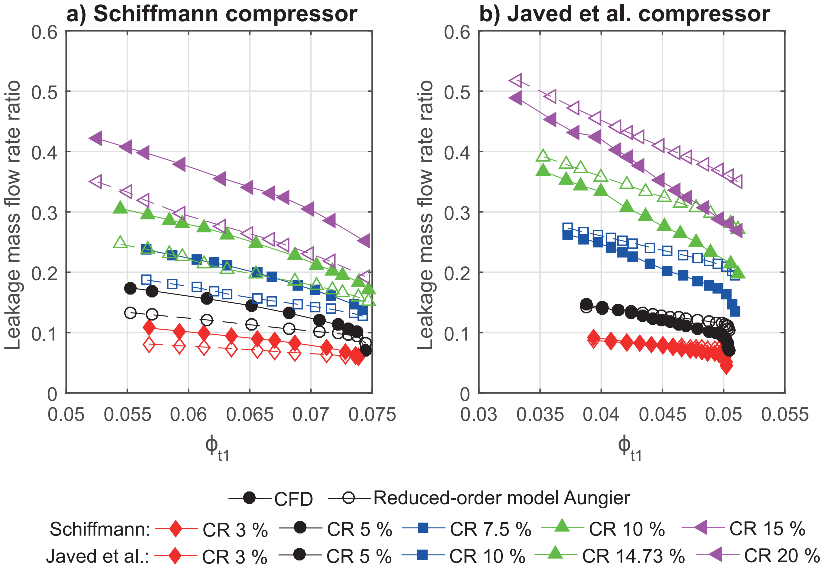

Figure 4.36: Comparison between predicted tip leakage ratio by a reduced-order model provided by Aungier [45] and CFD data.

The reduced-order model by Aungier [45] under-estimates tip leakage mass flow rates compared to CFD data in the whole operating range independently of the clearance ratio for the compressor geometry provided by Schiffmann [12, 13, 14, 15]. The deviation between two data set is more pronounced towards small mass flow rates. A maximum deviation of around 25 % occurs between data of reduced-order model and CFD.

The reduced-order model by Aungier [45] behaves in an opposite manner for the scaled compressor by Javed et al. [27]. In this case, the model matches well towards lower mass flow rates, but over-estimates the tip leakage mass flows towards high mass flow rates and a maximum deviation of around 45 % occurs.
Nonetheless, the reduced-order model by Aungier [45] does not take parameters like end-wall shape and blade angle distribution at shroud into account, which have been demonstrated to be important in the previous section. Therefore, the reduced-order model predicts tip leakage mass flow rates in the right order of magnitude. Hence, the model might be suitable for preliminary one-dimensional performance calculations.

4.6 Chapter summary and implications

A thorough experimental and numerical flow analysis of two compressors with different design variables (compressor by Schiffmann [12, 13, 14, 15] and compressor by Javed et al. [27]) in terms of tip leakage induced phenomena has been conducted and lead to the following conclusions:

1. The compressor efficiency is more deteriorated and an operating point is shifted towards smaller flow rates with an increase of relative clearance ratio. On the one hand, this originates from higher total pressure losses, thus the head coefficient is decreased. On the other hand, flow blockage caused by tip leakage increases, thus the work input decreases and an operating point is shifted towards smaller flow rates.
2. The flow blockage at the impeller trailing edge increases with increasing relative clearance ratio and the flow field becomes more distorted. This distortion is transported into the vaneless diffuser, where the mixing of flow for large relative clearance ratios requires more length.
3. No clear recommendation about application of empirical tip leakage correlations in terms of efficiency drop caused by an increase of relative clearance ratio can be given, since both investigated compressor geometries have suggested having a different sensitivity to a change in relative clearance ratio. The correlation of Pfleiderer and Petermann [29] (a=1.5) matched well for Schiffmann's [12, 13, 14, 15] compressor, whereas the correlations of Eckert and Schnell [30] and Pampreen [31] predict well for the compressor by Javed et al. [27].
4. Operating points of different relative clearance ratios with the same flow coefficient depend linearly on the relative clearance ratio in the entire operating range for both investigated compressors. A tip clearance sensitivity parameter m_{Cl} has been introduced, in order to model the efficiency drop associated to altering the relative clearance ratio, depending on the flow coefficient. This tip clearance sensitivity parameter, however, strongly depends on the compressor geometry, thus leading to different values for both compressor geometries.

5. Tip leakage strongly interacts with the passage diffusion and the shroud blade loading. The shroud blade loading in the rear part of the impeller decreases with an increase of relative clearance ratio, what has an impact on the position of the tip leakage vortex cores. Nonetheless, the inducer loading as well as the diffusion in the inducer region increases with increasing relative clearance ratio, leading to stronger tip leakage mass flows in the inducer.

6. A compressor designer has two options to control tip leakage and the trajectories of the tip leakage vortices: (1) Adaption of the shroud blade loading, in order to guide tip leakage vortices and control the tip leakage mass flux distribution. (2) Adaption of the hub and shroud end-wall shape, in order to control diffusion in the blade passage, what can be used to decrease the tip jet density and thus the tip leakage mass flux.

7. The one-dimensional model, which has been presented in section 2.5, does not capture properly the compressor sensitivity to a change of relative clearance ratio, thus a calibration of the one-dimensional model is required.

8. A reduced-order model to evaluate tip leakage mass flows from overall flow properties provided by Aungier [45] is suitable for preliminary tip leakage estimation.

5 End wall and blade loading investigation

It has been shown in chapter 3 and 4, that an increase in relative clearance ratio leads to a strong shift of the flow rate. Thus a compressor designer has to take special care when dealing with large relative tip clearance ratios, in order to maintain the required design specifications and to provide a sufficient compressor efficiency.

The impact of the shroud blade angle distribution as well as the end-wall shape on phenomena related to tip leakage is investigated in this chapter, where the scaled up compressor provided by Javed et al. [27] with a relative clearance ratio of 14.73 % serves as baseline geometry. In a first step, the hub end-wall shape is modified to relax the strong diffusion rate in the mid section of the impeller. Afterward, the shroud blade angle distribution is varied, in order to obtain an aft-loaded, a mid-loaded and a front-loaded shroud loading distribution.

The study has been performed experimentally as well as numerically by using CFD. The experimental data are used to compare with CFD data, thus allowing a more thorough insight into compressor aerodynamics by using a validated CFD setup. The objective of this study is to show how the hub- and shroud end-wall shape as well as the shroud blade angle distribution impact tip leakage induced phenomena. Based on these findings, design strategies are postulated about designing centrifugal compressors, which operate on relatively large clearance ratios.

5.1 Modifications of impeller geometry

5.1.1 New end-wall distribution

The hub end-wall distribution of the reference impeller provided by Javed et al. [27] with a relative clearance ratio of 14.73 % is modified in this subsection, in order to study the impact of end-wall distribution and hence altered diffusion on tip leakage induced phenomena.

The reference impeller geometry by Javed et al. [27] yields a high diffusion rate at 50 % of the meridional impeller coordinate. Due to this strong diffusion, the impeller shroud starts to get unloaded, what has a positive effect on the tip leakage at this position. Nonetheless, this is not common in centrifugal compressor design, since no work is transferred to the fluid at this position.

From that point of view, the end-wall distribution was adapted to obtain slimmer channels in the mid section of the impeller, leading to a higher shroud loading. Hence, slightly higher tip leakage is expected by using this modified end-wall distribution.

The newly designed impeller geometry has to be investigated in the same test rig as the baseline compressor by Javed et al. [27], what leads to the same shroud end-wall distribution. Hence, only the hub end-wall distribution is modified.

It is common practice in centrifugal compressor design to adapt the cross section area distribution by modifying hub and shroud end-walls, in order to obtain a cross section area distribution, which decreases from leading to trailing edge without local extrema (see e.g. Japikse [80] or Aungier [45]). The cross section area distribution of the original Impeller by Javed et al. [27] increases up to 50 % of the meridional coordinate and then decreases towards the trailing edge, causing a high flow diffusion at around 50 % of meridional coordinate. From that point of view, it was tried to adapt the hub end-wall shape such, that the cross section area distribution decreases continuously from leading towards trailing edge. Fig. 5.1 shows a comparison between the baseline compressor by Javed et al. [27] and the newly designed hub end-wall distribution. In addition, Fig. 5.2 shows the cross section area distributions of the baseline compressor and the one of the modified hub end-wall shape as a function of the meridional coordinate.

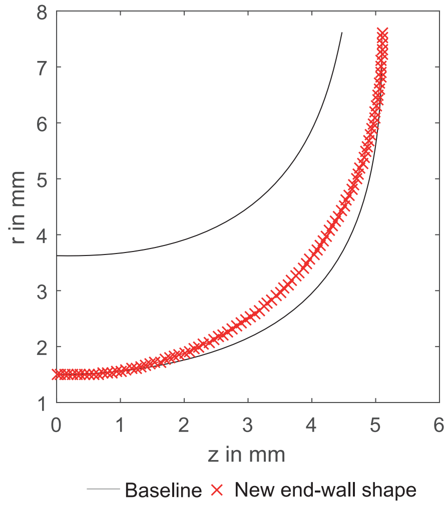

Figure 5.1: Comparison between the hub and shroud end-walls of the baseline compressor and the modified hub-end-wall shape in a z-r-coordinate system.

5.1.2 Different loading distributions

The impact of shroud loading distribution on tip leakage induced phenomena is investigated by modifying the shroud blade angle distribution, in order to obtain an aft-, a mid- and a front-loaded shroud loading distribution. Therefore, the maximum loading point of the shroud blade angle distribution is shifted accordingly.

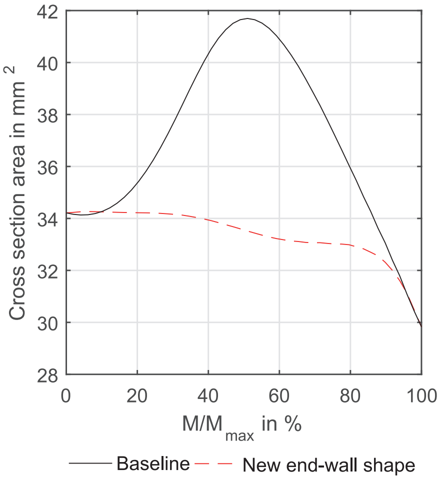

Figure 5.2: Cross section areas of the baseline compressor and the modified hub-end wall shape as a function of the meridional impeller length.

The reference impeller by Javed et al. [27] is designed having an aft-loaded shroud. The blade angle distribution at hub and shroud as a function of the relative meridional impeller coordinate is shown in Fig. 5.3.

A similar loading distribution as the reference impeller was chosen to study the aft-loaded shroud blade loading distribution. This loading distribution was combined with the new end-wall distribution, shown in Fig. 5.1. A stronger diffusion and hence a higher pressurization is achieved with the original end-wall distribution by Javed et al. [27]. As a consequence, the new end-wall distribution having a narrower blade passage diffuses less and less pressurization is achieved. However, a constraint of this design study is to have impellers, which allow having the same design specifications in terms of mass flow rate and total-total pressure ratio as the baseline compressor. In order to overcome this drawback in terms of less diffusion of the new end-wall distribution, flow diffusion needs to be gained through the blading, what was achieved by adapting the blade wrap angle. Therefore, the blade wrap angle was decreased from 70° to 60°. As a consequence of the lower wrap angle, the blade is shorter resulting in less frictional losses. On the other hand, the loading of the blade is increased, since a stronger curvature of the blading occurs, likely leading to higher secondary flows on the blade.

In a next step, the turning point of shroud blade angle distribution is shifted towards 50 % of the meridional impeller coordinate, in order to study the mid-loaded shroud configuration. The hub blade angle distribution was slightly adapted for matching the operating point with the desired design specifications.

A further shift of the shroud blade angle turning point towards impeller leading edge yields a front-loaded shroud configuration. In this case, a redistribution of hub blade angle was required to match with design specifications. Fig. 5.3 shows the hub and shroud blade angle distribution of the three newly designed impellers.

In addition, the three different loading distributions are shown in appendix D for a blade span of 90 % in a conformal map.

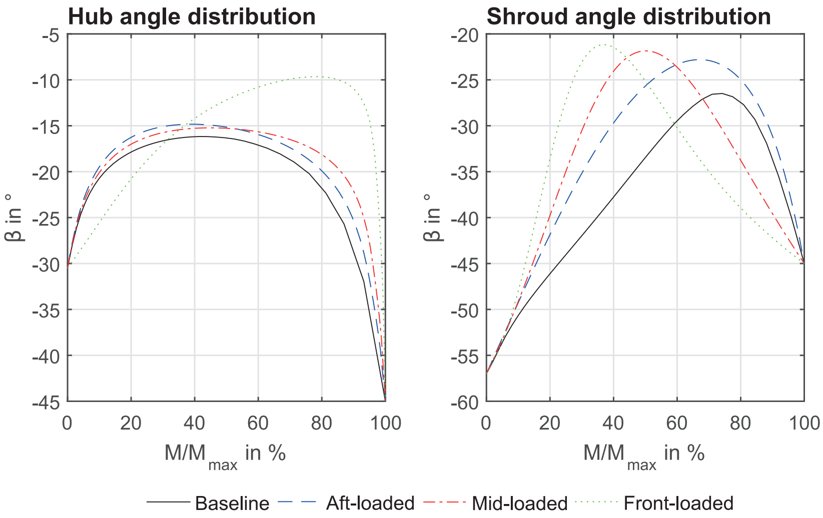

Figure 5.3: Blade angle distributions of the baseline compressor and the different shroud blade loading distributions as a function of the normalized meridional coordinate.

5.1.3 Common impeller blade design

Literature provides limited guidelines (refer to Javed et al. [27]) about the optimal shroud blade loading distribution of a centrifugal compressor impeller. Dallenbach [91] suggested shroud velocity distributions, in order to gain high compressor efficiency. His findings are summarized in Lüdtke [47]:

1. The most critical streamline in terms of flow deceleration and hence stability is the impeller shroud. Here, the flow velocity should be more rapidly decelerated in the inducer, leveled out in the middle of the impeller and stayed constant in the exducer. As a consequence, boundary layer growth is mitigated, what positively impacts the compressor stability and flow pattern.
2. A maximum blade loading value of $BL = 0.7 - 1.0$ (see Eq. 2.12) should not be exceeded, in order to suppress secondary flows between the blades as well as tip leakage.
3. The point of maximum blade loading should be located at around 60 up to 70 % of the normalized meridional coordinate. The maximum blade loading should neither be set near the leading edge nor near the trailing edge.

In addition, Mishina and Nishida [92] have conducted an experimental study with impellers having different blade loading distributions, diffusion ratios and flow coefficients. The findings of their experimental study can be concluded as following:

1. The diffusion along the shroud streamline is considered to to be most important in terms of impeller performance.

2. When the shroud deceleration is too strong, the impeller exit velocity profile becomes strongly distorted and compressor efficiency is deteriorated.
3. The point of maximum blade loading as well as the blade loading magnitude have only a minor impact on the compressor efficiency.

These two sets of empirical guidelines clearly demonstrate, that literature is not coherent about providing guidelines to obtain an optimal blade loading distribution. Dallenbach [91] suggests setting the maximum shroud blade loading in the rear part of the impeller for obtaining high compressor efficiencies, whereas Mishina and Nishida [92] claim that shroud blade loading distribution has only a minor impact on compressor performance. However, the empirical guidelines from Dallenbach [91] and Mishina and Nishida [92] were derived from impellers, which operate on low relative clearance ratios, thus compressor efficiency is less governed by tip leakage induced phenomena. In addition, implications by Dallenbach [91] are obtained from inviscid quasi-three-dimensional calculations without considering tip leakage.
From this point of view, it seems reasonable to investigate the impact of the shroud blade angle distribution on the performance of compressors operating on large relative clearance ratios, since previous chapters have been suggested a strong impact of the shroud loading distribution on tip leakage as well as on the trajectory of tip leakage vortices.

5.2 Effect of changing the blade loading and end-wall distribution on compressor performance

5.2.1 Impact on compressor performance (numerical and experimental approach)

In a first step, all modified impeller geometries have been tested numerically by using CFD. The numerical solver setup is described in appendix D.
Fig. 5.4 shows the stage characteristics in terms of total-total polytropic head coefficient (Fig. 5.4 a)), work input coefficient (Fig. 5.4 b)) and total-total polytropic effciciency (Fig. 5.4 c)) as a function of the global flow coefficient between inlet of the compressor and outlet of the vaneless diffuser. The scaled baseline compressor by Javed et al. [27] is marked as black lines with circles, the aft-loaded shroud distribution as blue line with squares, the mid-loaded shroud distribution as red line with diamonds and the front-loaded design as green line with triangles. In addition, Fig. 5.5 shows the total-total pressure ratio as a function of the global flow coefficient, suggesting that all compressor geometries provide the same pressure rise (total-total) in the design region.

As can be seen by Fig. 5.4 a) and Fig. 5.5 , all compressor units achieve the same total-total polytropic head and total-total pressure ratio in the design range. In addition, the operating range towards high mass flow rates is slightly increased by the aft- and mid-loaded shroud configuration. Furthermore, CFD data suggests a higher slope of head coefficient curves at low mass rates occurring for the modified geometries compared to the baseline compressor by

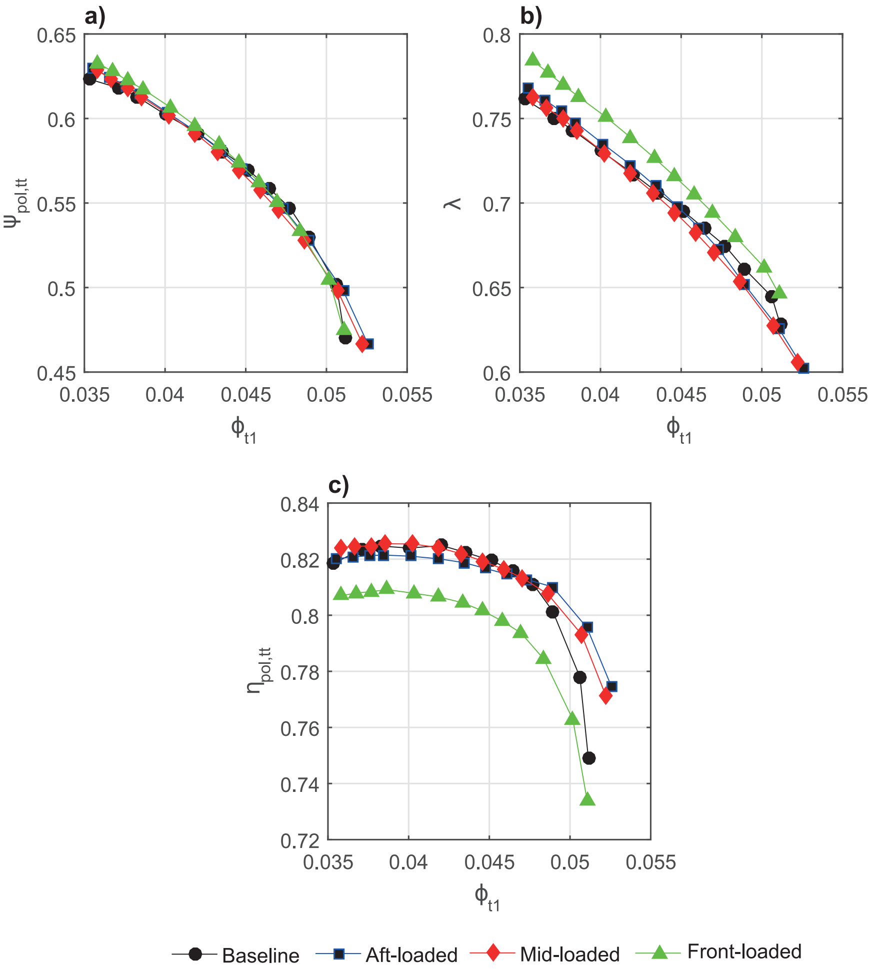

Figure 5.4: Numerically (CFD) obtained stage characteristics as a function of the global flow coefficient for differently designed impellers with a relative clearance ratio of 14.73 %.

Javed et al. [27], suggesting a more stable compressor behavior towards low mass flow rates. Fig. 5.4 b) shows that all compressors except for the front-loaded design feature the same trend in terms of work input coefficient. The work input slightly decreases for the aft- and mid-loaded configurations towards higher mass flow rates compared to the baseline geometry. The front-loaded design yields an increased work input coefficient over the entire operating range. One main reason for the increased work input coefficient of the front-loaded design is the large trailing edge blockage caused by large zones of relative velocity, leading to increased Euler-work to achieve similar pressure ratios than the other loading configurations. A more detailed explanation is given further below.
Fig. 5.4 c) illustrates that the total-total polytropic efficiency of the baseline configuration and the mid-loaded design show a similar efficiency distribution around the peak efficiency point. In addition, the efficiency distribution of the mid-loaded configuration is improved compared to the baseline design towards lower and higher mass flow rates, thus the efficiency curves become more flat. The aft-loaded design shows slightly inferior total-total polytropic efficiency distribution in the design range and towards off-design compared to the baseline compressor. Nonetheless, efficiency is gained towards higher mass flow rates compared to baseline geometry and mid-loaded configuration. The front-loaded design shows the lowest efficiency in its entire operating range compared to the other configurations, what is caused by the higher work input.

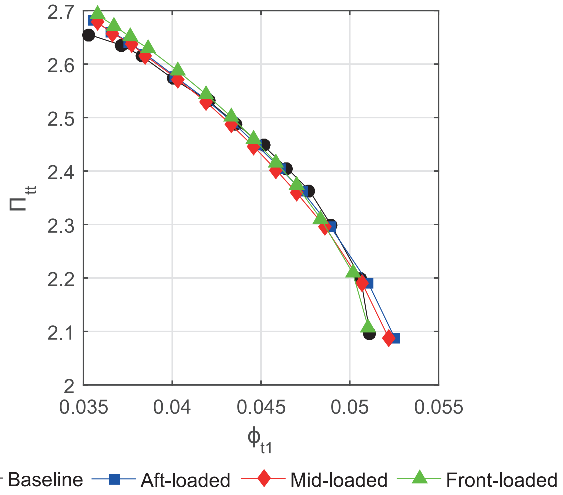

Figure 5.5: Total-total pressure ratio as a function of the global flow coefficient for differently designed impellers with a relative clearance ratio of 14.73 % (CFD).

Furthermore, all impeller geometries were tested experimentally at their design speed line. Fig. 5.6 shows the stage characteristics evaluated at 105 % times the impeller diameter in terms of isentropic total-static head coefficient, work input coefficient and total-static isentropic efficiency. Fig. 5.7 shows total-static isentropic head coefficient at vaneless diffuser outlet as well as the corresponding total-static isentropic efficiency at this location. CFD data evaluated at the corresponding measurement positions is additionally shown in Fig. 5.6 and Fig. 5.7, in order to allow a comparison between both data set. The color code for experimental and CFD results is defined in the legend of Fig. 5.6 and Fig. 5.7.

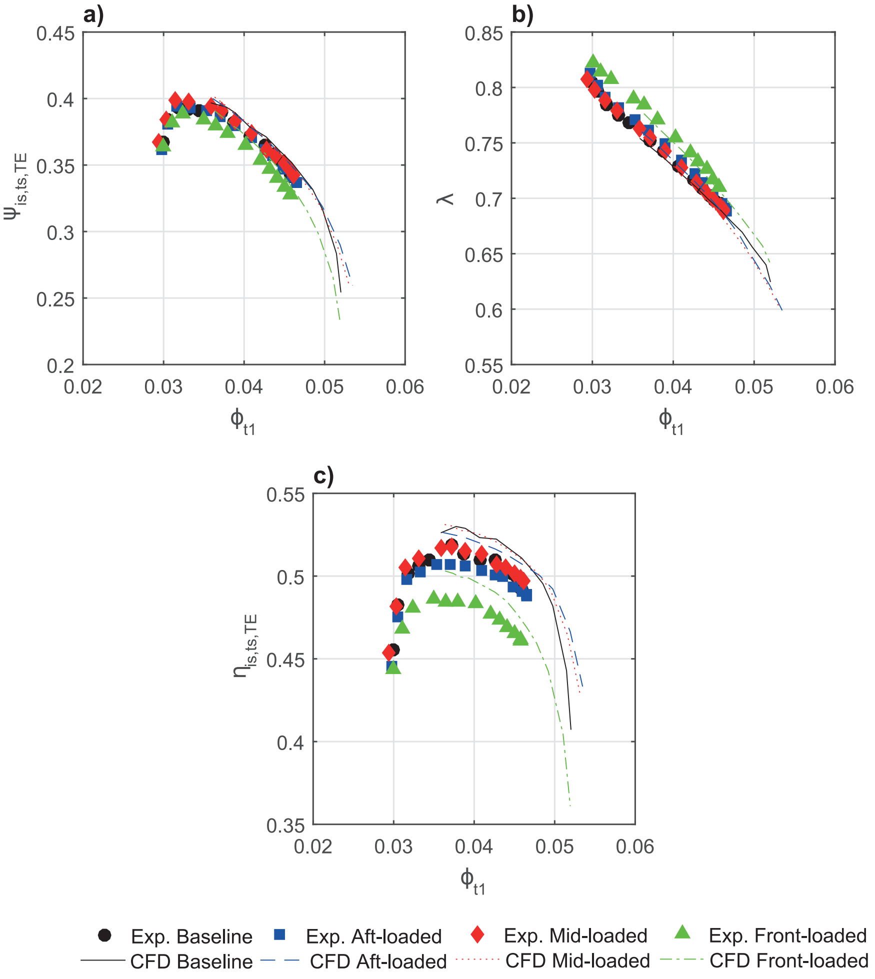

Figure 5.6: Comparison between numerical and experimental stage characteristics at 105 % times the impeller diameter over the global flow coefficient for various designs (CR=14.73 %).

Fig. 5.7 a) suggests a similar distribution in terms of isentropic total-static head coefficient for all investigated compressor geometries, thus suggesting a similar pressure rise, what is a necessary constraint for this design study. Due to limitations of the test-rig in terms of reaching the choking mass flow rate caused by the pressure loss of the refrigeration loop, the extension of compressor operating range towards higher flow rates by aft- and mid-loaded shroud configuration could not be verified. Fig. 5.6 b) suggests an increased work input coefficient occurring at the front-loaded design, what results in the lowest efficiency (Fig. 5.6 c) and Fig. 5.7 b)) compared to the other impeller geometries. The total-static isentropic efficiencies (see Fig. 5.6 c) and Fig. 5.7 b)) for the mid-loaded design are in line with the one of the baseline compressor and higher compressor efficiency was measured towards higher mass flow rates. The aft-loaded design suggests a lower efficiency compared to the baseline configuration and the mid-loaded shroud blade design. Although CFD over-estimates

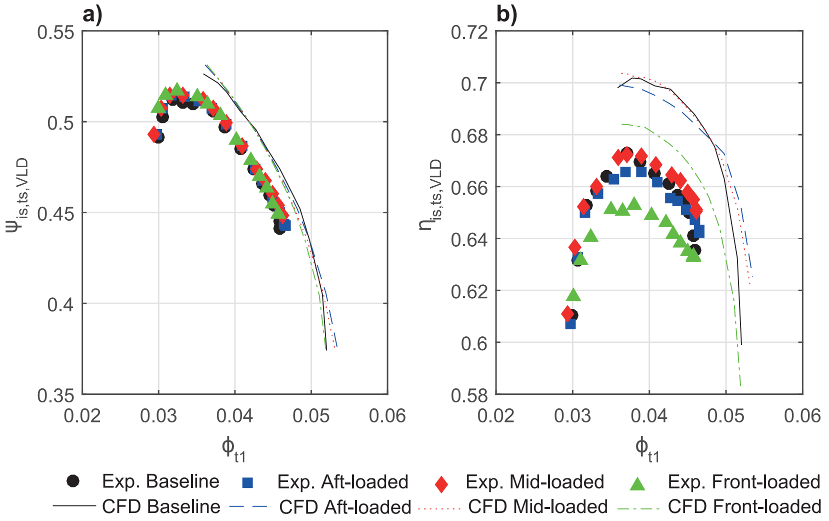

Figure 5.7: Comparison between experimental and numerical total-static isentropic head coefficient (a) and total-static isentropic efficiency (b) at outlet of the vaneless diffuser over the global flow coefficient for various designs (CR=14.73 %).

compressor efficiencies compared to experimental results (see subsection 2.6.4), the trend suggested by CFD data could be verified with the experimental setup. Hence, the numerical setup can be taken as validated and CFD data is used to investigate the compressor flow. The time-averaged measurement data as well as the validation plots of CFD and experiment are appended in appendix D.

A further insight into the compressor flow by using CFD data is given in Fig. 5.8 showing the distribution of tip flow coefficient (Fig. 5.8 a)), normalized absolute tangential velocity (Fig. 5.8 b)) and diffusion rate (Fig. 5.8 c)) as a function of the global flow coefficient.

Fig. 5.8 a) suggests that all compressor designs feature the same distribution in terms of tip flow coefficient except for the front-loaded design, which shows an increased tip flow coefficient. Hence, suggesting an increased trailing edge blockage compared to the other designs, what serves as one possible explanation for the inferior efficiency of this compressor. The normalized tangential velocity shown in Fig. 5.8 b) serves as indicator for zones of low relative velocity. According to Casey [65], values between 0.6 and 0.7 are desirable for normalized absolute tangential velocity at the design point. The mid- and aft-loaded shroud configurations suggest a similar distribution of normalized absolute tangential velocity, whereas the mid-loaded configuration yields slightly higher values. Hence, a larger zone of low relative velocity occurs in the mid-loaded design compared to the aft-loaded design (see Fig. 5.9). The baseline configuration shows a slightly smaller normalized absolute tangential velocity at design conditions and towards smaller mass flow rates than the other impeller geometries. The mid- and aft-loaded configurations achieve lower values towards higher mass flow rates compared to the baseline configuration, what explains the higher efficiencies of these designs towards choke (see Fig. 5.4 c)). The front-loaded design shows the highest absolute tangential

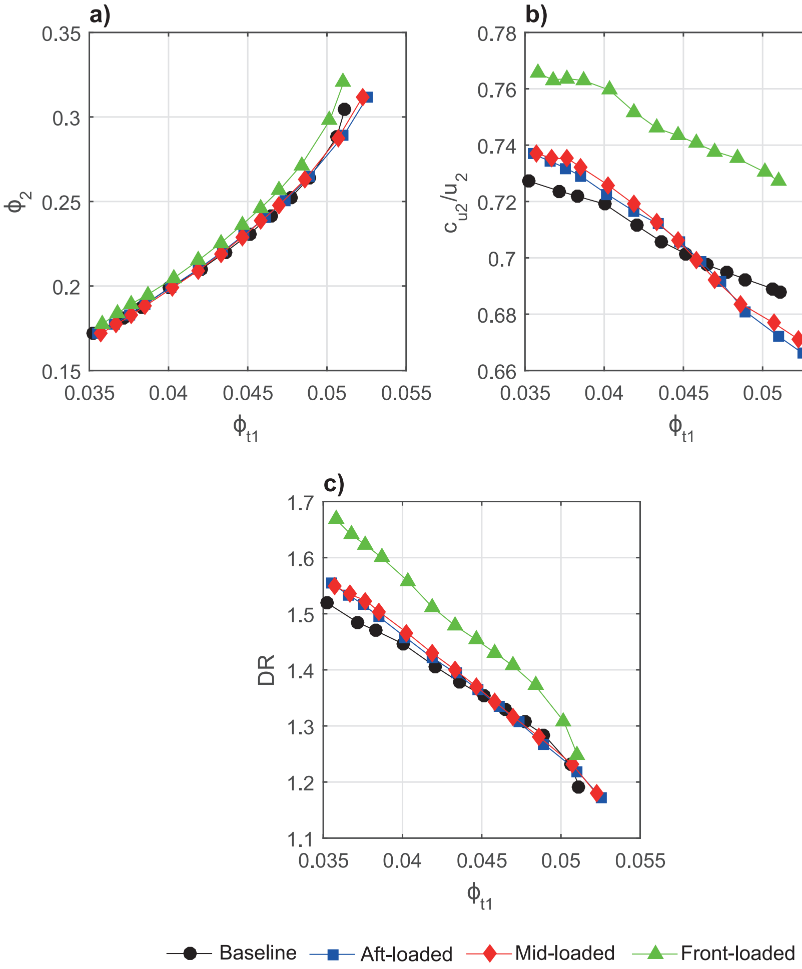

Figure 5.8: Numerically defined flow characteristics as a function of the global flow coefficient. Tip flow coefficient (a), normalized absolute tangential velocity (b) and diffusion ratio (c) over the global flow coefficient.

velocities in its entire operating range, thus leading to a deteriorated efficiency distribution. The high values indicate the existance of a large zone of low relative velocity, what increases trailing edge flow blockage and lowers efficiency.

The diffusion ratio presented in Fig. 5.8 c) is similar for the baseline and the aft- and mid-loaded configurations around the design point, but increased flow diffusion occurs in the modified geometries towards small mass flow rates. The highest diffusion occurs for the front-loaded configuration, what is caused by the larger zone of high absolute tangential velocity as indicated by Fig. 5.8 b).

Fig. 5.8 clearly suggests that the shroud blade angle distribution strongly affects the impeller flow patterns. The front-loaded configuration shows a higher trailing edge blockage due to a large zone of low relative velocity, having a high absolute tangential velocity. Such zones are called wake in the jet-wake theory (see Dean and Senoo [41]) and most of the impeller losses occur in that zone. Further insight into the origin of the different flow patterns is given in the next subsection.

Fig. 5.9 shows the relative Mach number distribution at trailing edge for the four designs at design conditions. The flow pattern is more disturbed for the front-loaded configuration, since higher gradients in relative Mach number occur. As demonstrated in Fig. 4.3 and Fig. 4.4, entropy generation and relative Mach number distribution are linked to each other. According to Zangeneh et al. [90], gradients in relative Mach number account for intensity of secondary flows, thus the front-loaded shroud loading distribution suggests to have the strongest secondary flows.

In addition, the front-loaded design yields the lowest relative velocities. It shows a larger wake in both blade passages compared to the other impeller geometries, leading to increased flow blockage.

Furthermore, these low relative velocity zones are located in the mid of the blade passages for the front-loaded design and they migrate towards the blade suction sides by setting the maximum loading point towards the trailing edge of the impeller. This indicates for an interaction of these low relative velocity zones with the pressure gradient between pressure side of one blade and the suction side of the adjacent blade at the rear part of the impeller. As a consequence, the aft-loaded design has the strongest pressure gradients between the blade surfaces in the rear part of the impeller (see shroud blade loading distribution in Fig. 5.12), thus zones of low velocity zones are located closer to the blade suction sides.

5.2.2 Impact on tip leakage, trajectory of tip leakage vortices and blade secondary flows

This subsection summarizes the results of the investigation on the impact of end-wall and shroud blade angle distribution on tip leakage, the trajectory of tip leakage vortices as well as secondary flows on blade surfaces.

Fig. 5.10 shows the ratio between tip leakage mass flow rate and compressor mass flow rate as

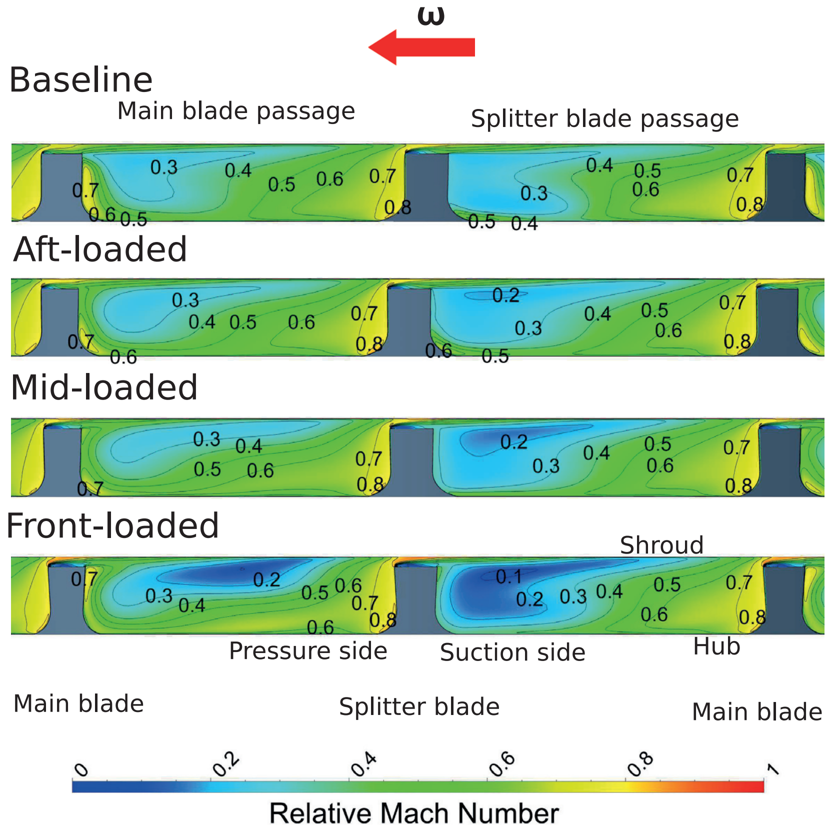

Figure 5.9: Relative Mach number distribution at impeller trailing edge for differently designed impeller geometries with a relative clearance ratio of 14.73 %.

a function of the global flow coefficient for the different impeller designs. The scaled baseline compressor shows the lowest overall tip mass flow rates compared to the other designs, which is caused by the strong diffusion in the mid region of this impeller, thus no tip leakage occurs at this position. By comparing the other blade designs with different shroud blade angle distributions, the following can be stated: The aft-loaded design shows the highest tip leakage mass flow rate followed by the mid-loaded design. The front-loaded designs shows the lowest tip leakage, even more towards higher mass flow rates. The tip leakage mass flow rate decreases over the whole operating range by shifting the maximum blade loading closer to the leading edge. This proves, that tip leakage itself mainly depends on flow density as well as the position where most of fluid is transported from the blade pressure to the blade suction side by tip leakage. An explanation for that behavior is given below, by having a closer look into the tip gap flow properties. As suggested by Fig. 5.4, Fig. 5.6 and Fig. 5.7, the front-loaded design has shown the lowest efficiency over the entire operating range, although having the smallest overall tip leakage. Hence, tip leakage mass flow rate itself is not a good metric to identify the most promising design.

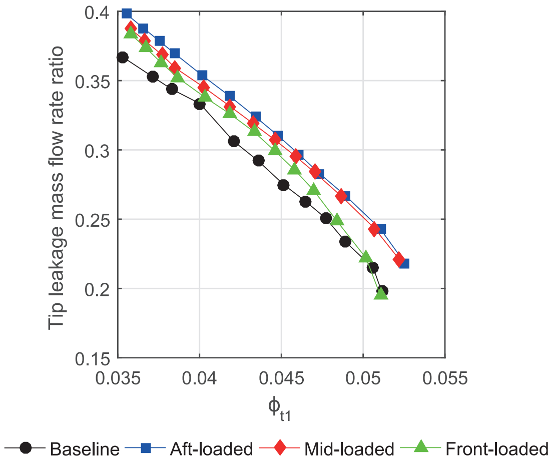

Figure 5.10: Numerically obtained ratio between tip leakage mass flow rate and total compressor mass flow rate as a function of the global flow coefficient for the four different designs.

Fig. 5.11 shows the aerothermal properties along the suction side of the tip gap (main and splitter blade) for the four designs at design conditions. Fig. 5.11 a) and d) show the mass flux distribution as a function of the meridional coordinate. A maximum in mass flux distribution along the main blade tip gap is achieved between 80 and 90 % of meridional coordinate for all designs. At this position, the aft-loaded design shows the highest mass fluxes and the front-loaded design the lowest. An additional peak of tip leakage mass flux occurs at around 20 % of meridional coordinate, where the front-loaded design shows the highest tip leakage flux.

A peak in tip leakage mass flux is reached between 80 and 90 % at the blade tip of the splitter blade for the baseline, aft-loaded and mid-loaded blade loading distributions. The front-loaded configuration shows consequently lower tip mass fluxes over the rear part of the splitter blade. In addition, mid- and aft-loaded design show an additional loading peak near the

leading edge of the splitter blade.
The density distribution shown in Fig. 5.11 b) and e) increases due to the increasing pressurization from main and splitter blade leading to trailing edge, where the front-loaded design shows the lowest tip density over the whole compressor length. Lower density is achieved in the aft- and mid-loaded design compared to the baseline impeller, what is caused by the slimmer blade channels. Hence, these curves suggest that the end-wall shape has a strong impact on the tip jet density and is a design variable to control tip leakage flows. Although tip density is reduced in the rear part of the impeller by the new end-wall shape, the baseline compressor achieves, however, lower mass fluxes as compared to mid- and aft-loaded shroud loading distributions.
The relative Mach number distribution shown in Fig. 5.11 c) and f) shows a peak for the front-loaded design at around 20 % of main blade meridional coordinate, which counteracts with the tip leakage mass flux distribution. The aft-loaded design reaches its peak in relative Mach number at around 80 % of main blades meridional coordinate and the mid-loaded shroud configuration shows the most uniform distribution in relative Mach number distribution on the main blade. In addition, the mid- and aft-loaded shroud configurations show an additional peak in relative Mach number near the leading edge of the splitter blade what is in accordance with the increased mass flux at this position. The relative Mach number distributions of main and splitter blade suggest, that the velocity of the tip jet strongly depends on the shroud blade angle distribution. Nonetheless, the baseline compressor by Javed et al. [27] shows the lowest overall tip mass flow rates, what is caused by the decrease in loading at 50 % of the meridional coordinate. Hence, the relative Mach number at 50 % of meridional coordinate drops due to the wide opening of the blade passage at this location.

The evolution of aerothermal properties along the tip gap suggest a strong impact of the loading distribution on the relative velocity of tip jet. However, tip jet mass flows also depend on the flow density, which increase from leading to trailing edge in the same manner as the pressurization in the impeller. Hence, the front-loaded design shows the lowest overall tip leakage, since the highest velocity of tip jet occur in the inducer, where the fluid is less dense. The aft-loaded configuration has a higher tip leakage mass flow as well as a higher tip jet velocity in the rear part, thus stronger tip leakage losses are expected.

Fig. 5.12 shows the loading distributions of main and splitter blade at a blade span of 90 % as a function of the meridional coordinate for all investigated geometries at their design point. The shroud loading distribution directly corresponds to the relative Mach number distribution of the tip jet (see Fig. 5.11 c) and f)), thus demonstrating the shroud blade loading as the driving mechanism of tip leakage jet.
Furthermore, the shroud blade loading in the rear part of the impeller decreases by setting the maximum turning point of the shroud blade angle distribution towards the main blade leading edge. Fig. 5.9 suggests that the location of low relative velocity zones at the exhaust flow pattern of the impeller depends on the shroud blade angle distribution. Hence, there is an interaction between shroud loading, tip leakage and tip leakage vortices. A reduction of the exducer shroud loading leads to zones of low relative velocities, which are located in

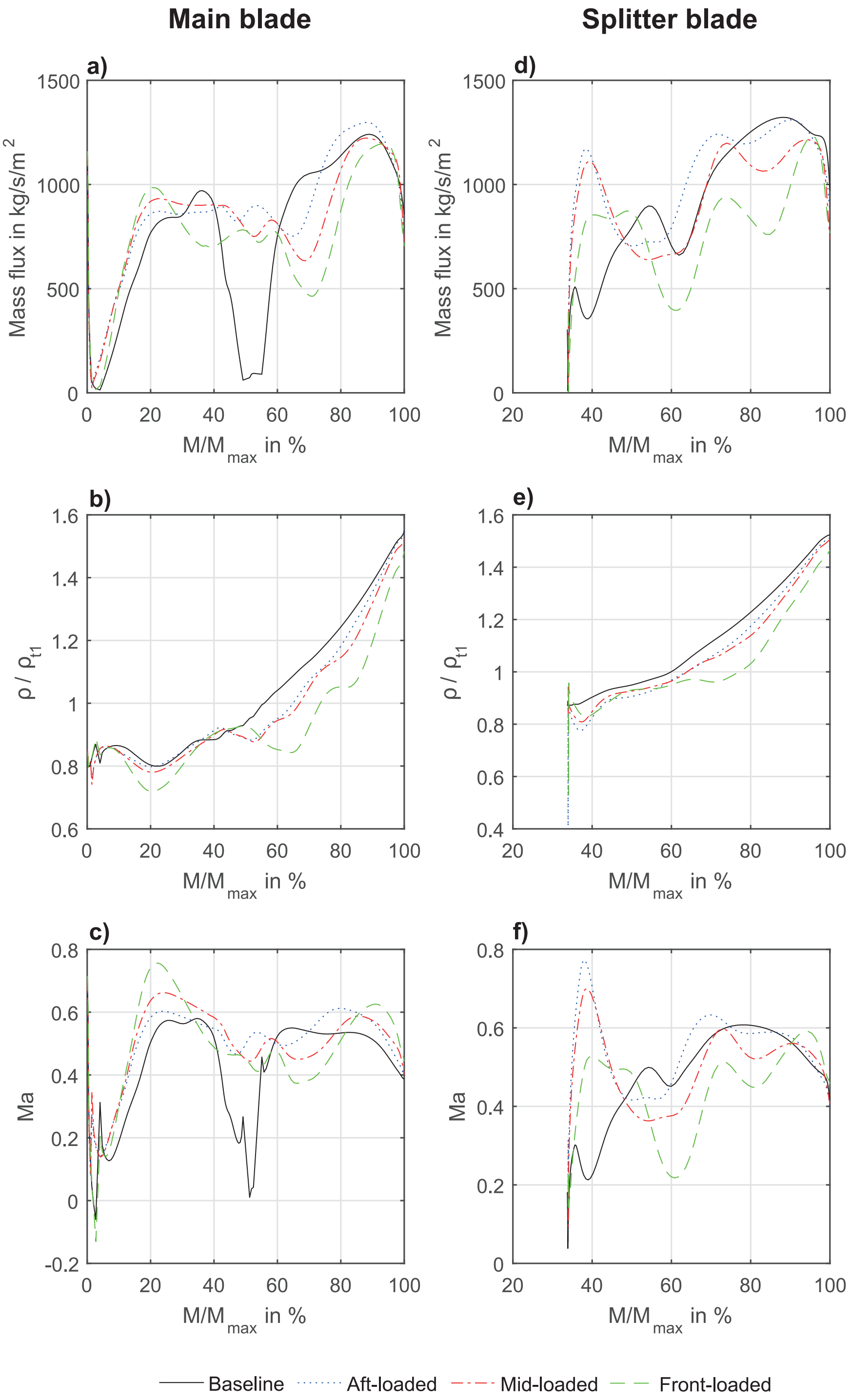

Figure 5.11: Tip mass flux, normalized density of tip jet as well as relative tip jet Mach number as a function of the normalized meridional coordinate for the four different designs.

the middle of the blade passage. Therefore, besides a control mechanism for tip leakage the shroud blade loading distribution is also a control mechanism for guiding tip leakage vortices through the impeller.

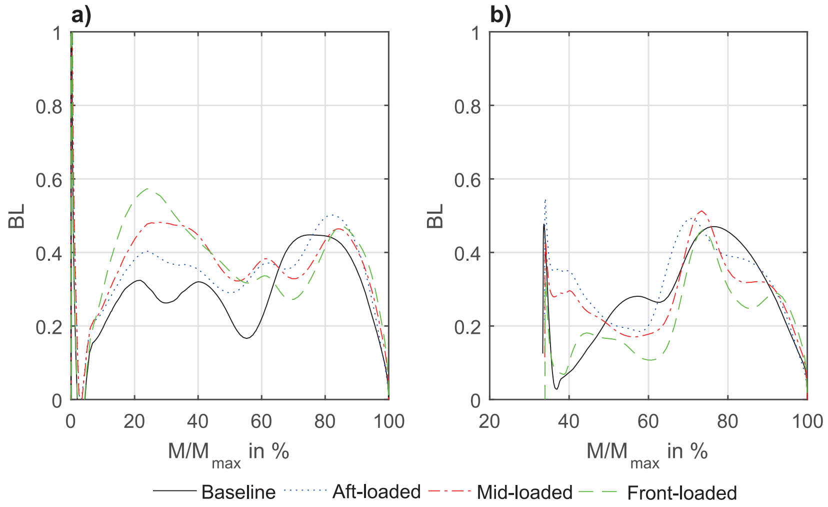

Figure 5.12: Blade loading parameter along the 90 % blade span for differently designed impellers.

On the one hand, the front-loaded shroud loading suggests to have the lowest overall tip leakage mass flow rates compared to mid- and aft-loaded shroud loading distributions in the entire operating range of the design speed line. On the other hand, the front-loaded design yields the lowest efficiency compared to other loading distributions. Hence, another contributor causes the strong deterioration of efficiency, occurring in the front-loaded design. Fig. 5.9 suggests the occurrence of a large zone of low relative velocity at the trailing edge of the front-loaded impeller. Compared to the other loading distributions, this zone of low relative velocity is located in the middle of the blade passage. In addition, investigation of the impact of relative clearance ratio on the trajectories of main and splitter blade tip leakage vortex (see chapter 4) suggests a strong impact on the tip leakage vortex trajectories, especially on the one of the main blade tip leakage vortex. It has been shown (see Fig. 1.2), that the tip leakage vortex intersects zones of low relative velocities, occurring at impeller trailing edge. These low relative velocity zones are linked to zones of high entropy. Hence, the shroud blade angle distribution has an impact on the location of the wake at the impeller exhaust.

In order to investigate the impact of shroud blade loading on the location of these low relative velocity zones, trajectory plots of main and splitter blade tip leakage vortex are shown. The trajectory of main blade tip leakage vortex is illustrated in red and the one of the splitter blade tip leakage vortex in blue.

Fig. 5.13 shows the trajectory of main and splitter blade vortices for the up-scaled compressor by Javed et al. [27]. The tip vortex, which evolves from main blade leading edge, follows the suction side of the main blade and is then split into two parts. One part follows the main blade suction side and the other part migrates towards the leading edge of the splitter blade, where it accumulates at the pressure and the suction side of the splitter blade. Another tip leakage vortex evolves from the splitter blade leading edge and follows the suction side of the splitter blade. Due to the tip leakage over the splitter blade, part of the main blade vortex, which has attached to the pressure side of the splitter blade, is transported to the suction side of the splitter blade, mixing with the splitter blade tip leakage vortex. Additional leakage going from the suction to the pressure side of the main blade is observed in the mid part of the main blade, what is caused by the wide opening of the blade passage in this region. This leakage attaches to the tip leakage vortex of the splitter blade and follows the splitter blade suction side. Javed et al. [27] tried to unload the main blade at the mid part, thus the tip leakage vortex of the main blade is located closer to the suction side of the main blade. This was achieved by adapting the end-wall shape at this position, what lead to a wide opening of the impeller blade passage. On the one hand, this shows how important it is to guide tip leakage vortices near the blade suction sides, since a high efficiency is obtained by that design. On the other hand, results of this investigation suggest that this approach is not the most promising one, since no work is transferred to the fluid, where the shroud loses its loading due to the wide opening of the blade passage.

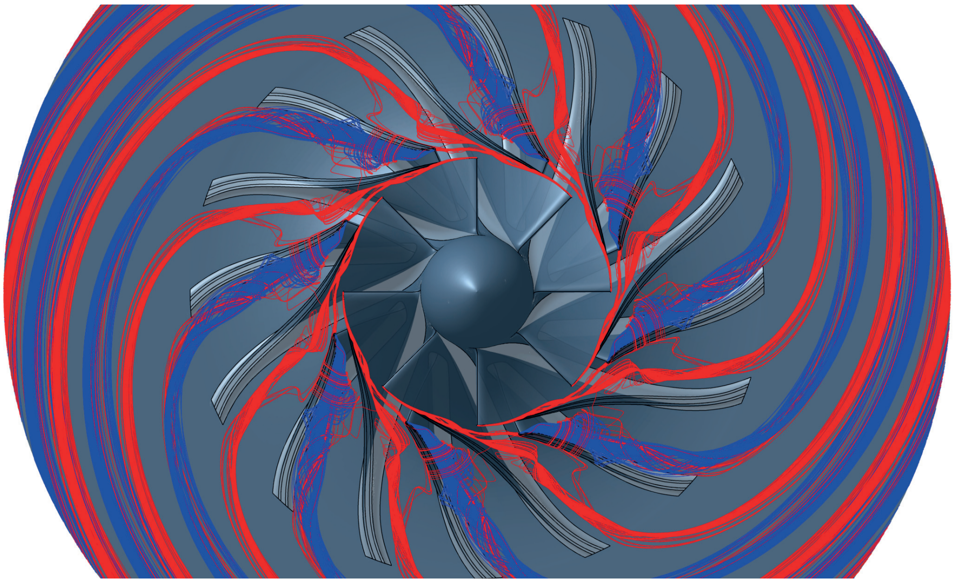

Figure 5.13: Trajectories of main (red streamlines) and splitter blade (blue streamlines) tip leakage vortices for the scaled up compressor by Javed et al. [27] at its design point.

Fig. 5.14 shows the tip leakage vortex trajectories of the aft-loaded shroud loading configuration. The main blade tip leakage vortex rolls up along the main blade suction side and follows it, before splitting into two parts. One part continues following the main blade suction side. The other part accumulates at the pressure side of the splitter blade where it is transported by tip leakage to the suction side of the splitter blade. Here, it mixes with the tip leakage vortex of the splitter blade and accumulates at the splitter blade suction side. Tip leakage vortices are located close to the blade suction side in the exducer, since a high pressure gradient between the blade pressure and the suction side of the adjacent blade occurs. Compared to the compressor by Javed et al. [27], the tip leakage vortices create less blockage in the main blade passage, what is further supported by the relative Mach number distribution shown in Fig. 5.9.

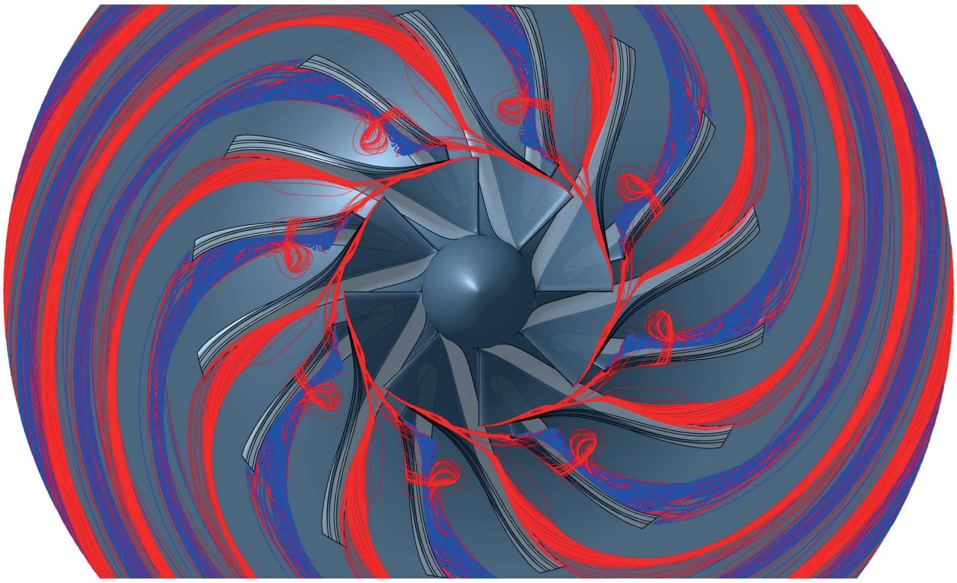

Figure 5.14: Trajectories of main (red streamlines) and splitter blade (blue streamlines) tip leakage vortices for the aft-loaded compressor at its design point.

The trajectory of tip leakage vortex occurring in the mid-loaded shroud loading configuration is shown in Fig. 5.15. The trajectories of the mid-loaded design suggest a similar behavior as the aft-loaded shroud configuration. However, part of the main blade tip leakage vortex stick to the pressure side of the splitter blade, creating additional losses. This is most likely caused by the pressure gradient, which is in the case of a mid-loaded shroud configurations strongest in the mid of the impeller. Nonetheless, the pressure gradient in the rear part of the impeller is still able to push the zones of low relative velocity near the blade suction sides.

Fig. 5.16 shows the tip leakage vortex trajectories of the front-loaded design. One can clearly see a difference in trajectories compared to the aft-and mid-loaded configurations. A significant amount of the main blade tip leakage vortex attaches to the pressure side of the splitter blade and is not transported to the suction side. On the other hand, part of the main blade tip leakage vortex, which migrates to the splitter blade, is stronger compared to the other loading configurations, thus leading to increased blockage. Both tip leakage vortices, however, do not follow the suction side of the blades and are located near the mid of the blade passage. It is therefore suggested that due to reduction of loading in the rear part, the pressure gradient between pressure and suction side is not strong enough to transport tip leakage vortices to the suction sides.

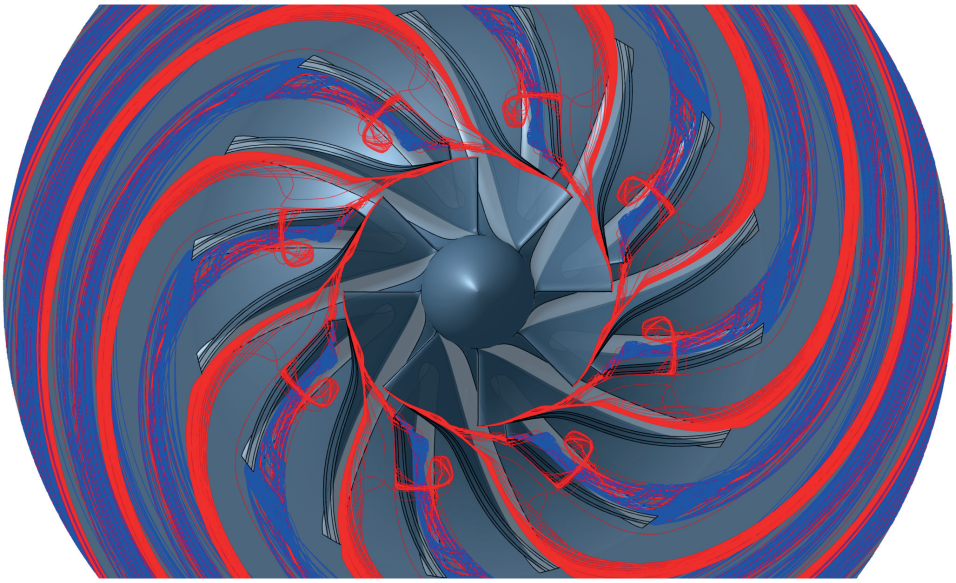

Figure 5.15: Trajectories of main (red streamlines) and splitter blade (blue streamlines) tip leakage vortices for the mid-loaded compressor at its design point.

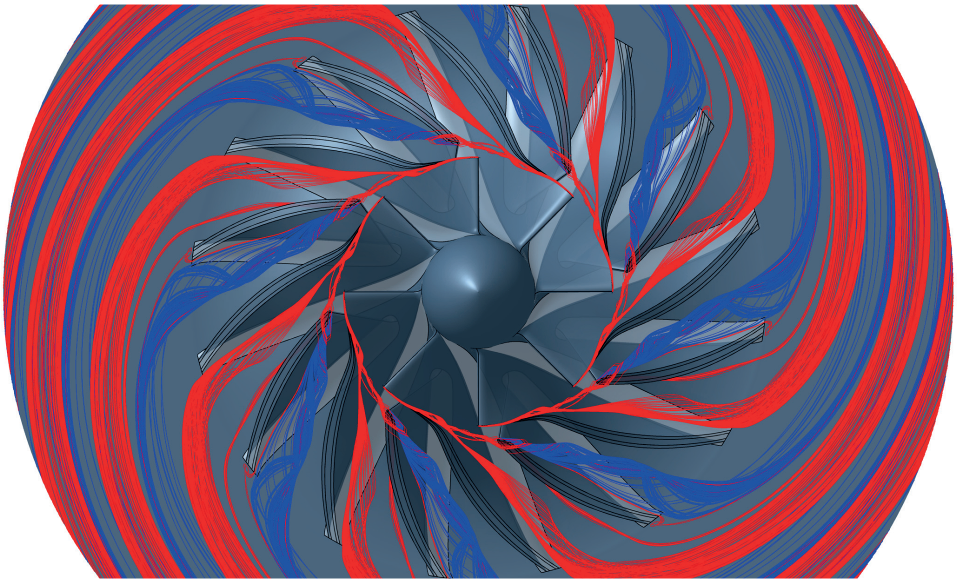

Figure 5.16: Trajectories of main (red streamlines) and splitter blade (blue streamlines) tip leakage vortices for the front-loaded compressor at its design point.

The trajectory plots have shown that the loading distribution not only impacts tip leakage, but also the trajectory of the tip leakage vortices. These vortices and their trajectory have a significant impact on blockage at the impeller exhaust and hence on the achievable efficiency. Therefore, the shroud loading distribution needs to be tailored such, that both tip leakage vortices (main and splitter blade) attach to the suction side of the corresponding blade. Javed et al. [27] tried to achieve this by reducing the shroud blade loading of the main blade in the mid part of the impeller, thus more fluid accumulated at the suction side of the splitter blade. Nonetheless, additional flow blockage in both blade passages occurs, thus this approach needs to be questioned. It seems to be beneficial to set the maximum shroud loading more towards the trailing edge in terms of location of the wake at impeller exhaust, since the aft-loaded design suggested to have lowest trailing edge flow blockage compared to other loading configurations. Furthermore, tip leakage vortices impact other secondary flows, since they have a strong impact on hub and shroud loading distributions, what is suggested by the relative Mach number distribution (see Fig. 5.9) and is discussed below.

According to Zangeneh et al. [90], gradients in isentropic Mach number distribution serve as direct measure to account for the generation and accumulation of secondary flows on blade surfaces. Generally, a pressure difference between hub and shroud on the blade surface occurs, which is caused by the different radii of hub and shroud, thus a secondary flow from hub to shroud is generated. Fig. 5.17 shows the difference between isentropic Mach number of hub (10 % blade span) and shroud (90 % blade span) as a function of the normalized meridional coordinate. In addition, in appendix D, the isentropic Mach number distribution on the blade surfaces is illustrated for all different impeller geometries (see Fig. D.13, Fig. D.14, Fig. D.15 and Fig. D.16).

By comparing the gradients of isentropic Mach number on the main blade pressure side (see Fig. 5.17 a)) of the three different loading distributions one can clearly state, that the front-loaded impeller geometry shows the highest gradient between hub and shroud isentropic Mach number. Hence, stronger secondary flows occur compared to other geometries. By comparing the baseline compressor of Javed et al. [27] with the aft-loaded design, there are higher gradients of isentropic Mach number between hub and shroud at the mid part of the baseline impeller, thus leading to stronger secondary flows at this location of the impeller. This is, again, a consequence of the wide opening of the blade passage. At the rear part of the impeller, the baseline and aft-loaded designs show the lowest gradient in isentropic Mach number, thus generation and accumulation of secondary flows on this blade surface are minimized. The Mach number gradients increase by shifting the maximum turning point of the blade angle distribution towards the leading edge of the main blade. Hence, the highest gradients in isentropic Mach number occur in the rear part of the impeller for the front-loaded design. A different situation occurs in the inducer part, where the front-loaded design shows the lowest difference in isentropic Mach number, suggesting lower blade secondary flows compared to the mid- and aft-loaded geometry.

At the pressure side of the splitter blade (see Fig. 5.17 c)), the reference geometry by Javed et al. [27] suggests to have the strongest secondary flows on the blade surface near the leading

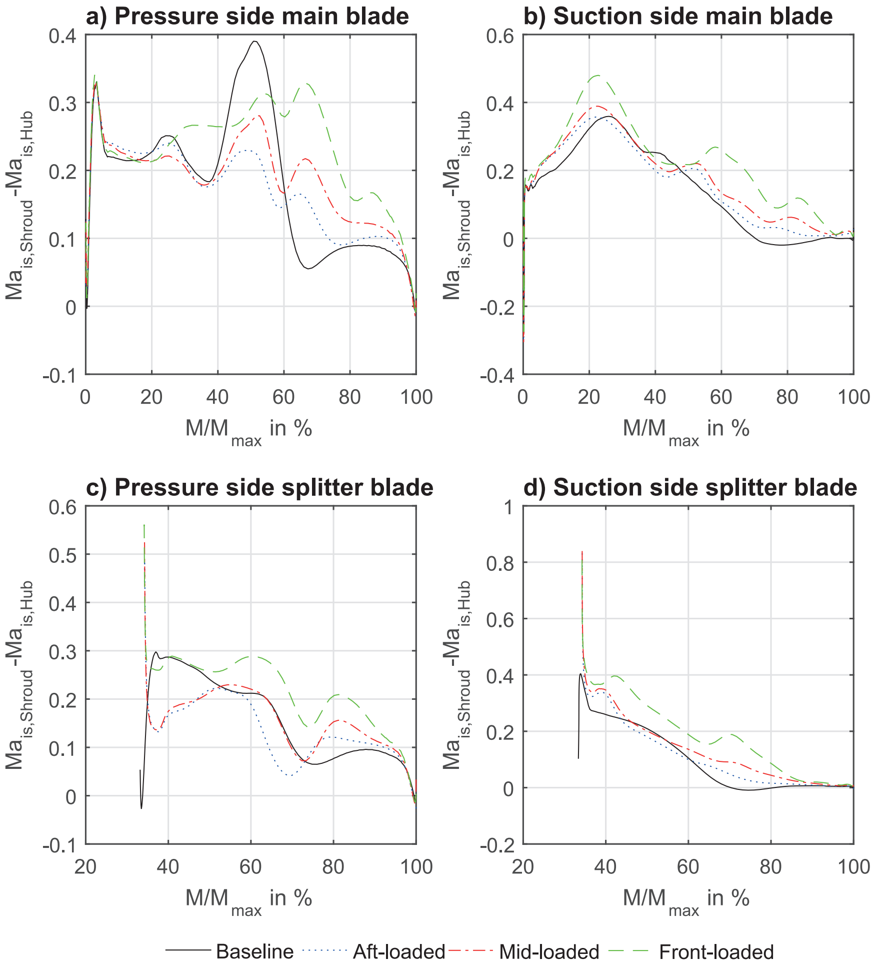

Figure 5.17: Difference between isentropic Mach number at hub and shroud for the different impeller designs as a function of the normalized meridional coordinate.

edge, since the highest gradients in isentropic Mach number between hub and shroud occur. In addition, by shifting the maximum turning point of the shroud blade angle distribution towards the leading edge of the main blade, secondary flows on the rear part of the blade are amplified. As shown by the trajectory plot of tip leakage vortices, part of main blade tip leakage vortex attaches to the pressure side of the splitter blade and is not transported to the suction side, what disturbs the near shroud loading at the pressure side of the splitter blade with an increase in loading difference between hub and shroud.

The secondary flows on the suction side of the main blade (see Fig. 5.17 b)) are lowest for the reference geometry by Javed et al. [27], however, stronger secondary flows occur at around 50 % of meridional impeller coordinate. This behavior is caused by the wide opening of the blade passage at the mid part of the impeller, thus flow velocities near the shroud of the suction surface are lower. Especially in the mid part of the impeller, the reference geometry suggests almost the same isentropic shroud Mach number distribution at the pressure and suction side, leading to a decrease in blade loading. Hence, less tip leakage flows occur for the baseline compressor.

Aft - and mid-loaded shroud loading configurations show a similar distribution of isentropic Mach number on the main blade suction side, thus yielding a similar degree of hub to shroud secondary flows. The front-loaded design shows near-shroud isentropic Mach numbers highest compared to the other compressor geometries, thus stronger secondary flows occur. A peak of isentropic Mach number difference is observed in the inducer region.

Eventually, the splitter blade suction side (see Fig. 5.17 d)) shows the highest gradients in isentropic Mach number occurring for the front-loaded design, especially in the rear part of the impeller. The aft-loaded as well as the reference geometry show the lowest secondary flows occurring in the rear part of the impeller.

Overall, the front-loaded design is suggested to have the highest intensity of secondary flows at the rear part of the impeller on each blade surface, whereas the aft-loaded design has the lowest secondary flows in the rear part. Although the front-loaded design shows reduced tip leakage compared to the mid- and aft-loaded design, strong secondary flows occur in the rear part of the impeller. This serves as an additional explanation for the less homogenized flow pattern shown in Fig. 5.9 and the lowest overall efficiency.

A more thorough investigation of the interaction between shroud blade loading and tip leakage induced phenomena suggested that the correct guidance of main and splitter blade tip leakage vortices is essential for having a high compressor efficiency. These trajectories are influenced by the shroud blade angle/loading distribution. The position of the wake and hence the blockage at the impeller trailing edge depend on the trajectory of these vortices. The higher the pressure gradient in the exducer between the blade pressure side and the suction side of the adjacent blade is, the closer is the wake located near the suction side and the lower is the flow blockage. In case of wrong guidance (see front-loaded configuration), high secondary flows on the blade are induced by these vortices, what lowers the achievable efficiency.

Compared to observations of Mishina and Nishida [92] (see subsection 5.1.3), the shroud blade loading distribution is suggested to have a significant impact on tip leakage and even more on trajectories of main and splitter blade tip leakage vortex for compressors, which are operated at large relative clearance ratios.

5.2.3 Tip clearance sensitivity parameter

The tip clearance sensitivity parameter m_{Cl}, which was introduced in section 4.3, is evaluated for the different blade loading designs. As shown in the previous chapter, the efficiency drop in terms of altering the relative clearance ratio for a certain flow rate can be modeled by a linear approach. Therefore, one additional compressor setup having a relative clearance ratio of 10 % was simulated for each compressor.
Fig. 5.18 shows the tip clearance sensitivity parameter as a function of the global flow coefficient for the different compressor designs.

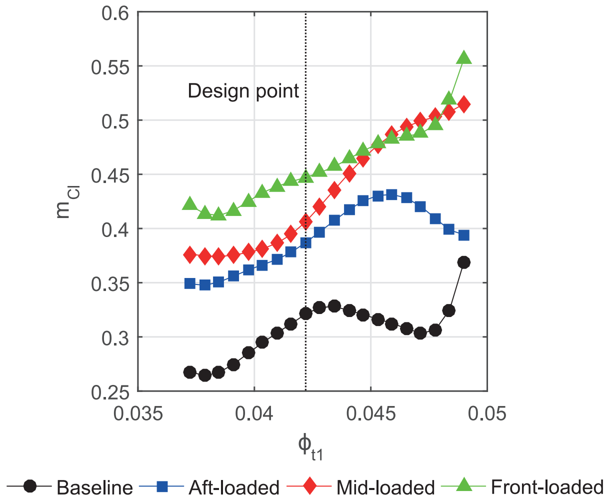

Figure 5.18: Tip clearance sensitivity parameter over global flow coefficient for impellers with different shroud loading distributions and the baseline geometry by Javed et al. [27].

The baseline configuration shows the lowest tip clearance sensitivity over the whole operating range. The aft- and mid-loaded configuration show almost the same tip clearance sensitivity at design range and off-design where the mid-loaded one yields consequently higher values. Towards high mass flow rates the mid-loaded compressor unit becomes more sensitive to a change in relative clearance ratio. The front-loaded compressor design suggests to have the highest sensitivity against changing the relative clearance ratio. At the design point a drop of 0.32 efficiency points is observed for the baseline configuration, a drop of 0.38 points for the aft-loaded shroud blade angle configuration, a drop of 0.39 efficiency points for the mid-loaded design and a drop of 0.45 efficiency points for the front-loaded design per percentage of relative clearance ratio.
Although the front-loaded design is suggested to have the lowest overall tip leakage, it shows the highest tip clearance sensitivity, thus the tip clearance sensitivity parameter is mostly influenced by the trajectory of tip leakage vortices.

This example has shown that the tip clearance sensitivity parameter depends on end-wall distribution as well as blade loading distribution. Therefore, it can be used as a design parameter, in order to achieve a compressor which is less sensitive to a change in relative tip clearance ratio.

Since operating points of different relative clearance ratios, which have the same flow coefficient, can be approximated by a linear relationship (see section 4.3), the tip clearance sensitivity parameters for each design at design conditions (ϕ_{t1}=0.042), which were derived from Fig. 5.18, are used to extrapolate efficiency data towards small relative clearance ratios according to Eq. 4.3.
Fig. 5.19 shows the polytropic total-total efficiency as a function of the relative clearance ratio for the three different blade loading designs (aft-, mid- and front-loaded) at their design point. In addition, the total-total polytropic efficiency obtained from CFD data for relative clearance ratios of 1 %, 5 %, 10 % and 14.73 % are plotted in Fig. 5.19 at design conditions (ϕ_{t1}=0.042).

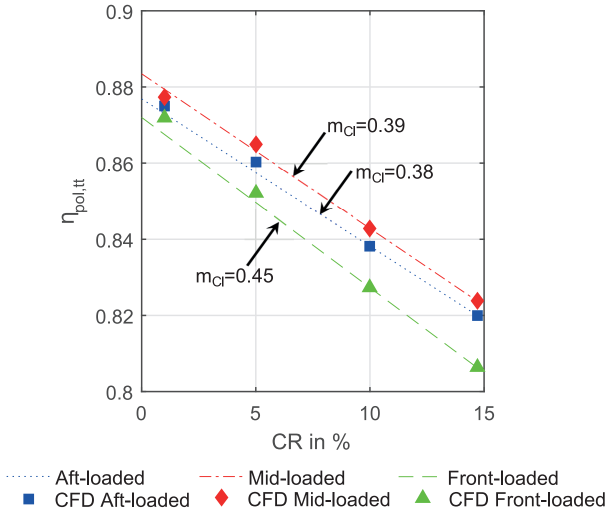

Figure 5.19: Total-total polytropic efficiency over the relative clearance ratio for different loading distributions obtained from Eq. 4.3 and CFD.

Fig. 5.19 suggests that the difference between efficiency values of the aft-, mid- and front-loaded configurations becomes smaller towards smaller relative clearance ratios. Hence, the shroud blade loading distributions seems to have a minor impact on the compressor efficiency for relative clearance ratios smaller than 5 %. Especially the efficiency difference between the different loading cases at a relative clearance ratio of 1 % is not remarkable. Here, an efficiency value of 87.51 % is achieved for the aft-loaded, an efficiency value of 87.72 % for the mid-loaded and an efficiency value of 87.18 % for the front-loaded design. This corroborates with results provided by Mishina and Nishida [92] and demonstrates that the shroud blade loading distribution has a significant impact on the compressor efficiency at large relative clearance ratios. Here, the mid- and aft-loaded loading configurations are the most promising shroud loading distributions, what is in accordance with suggestions by Dallenbach [91] concerning the location of the maximum loading point.

5.3 Summary and design implications

The impact of shroud blade loading distribution as well as hub and shroud end-wall shape on tip leakage induced phenomena is presented in this chapter.
The end-wall shape of the baseline compressor provided by Javed et al. [27] was adapted and starting from the new end-wall distribution an aft-loaded, a mid-loaded and a front-loaded shroud blade loading configuration was realized. The mid-loaded shroud blade loading distribution suggested a similar efficiency at design point and superior efficiency at off-design than the baseline configuration. The aft-loaded shroud loading distribution is suggested to yield slightly inferior efficiency at the design point compared to the baseline and mid-loaded design. The front-loaded design showed the lowest efficiencies over the entire operating range. The following observations in terms of flow field analysis can be stated:

1. The front-loaded design yields an increased tip flow coefficient compared to the other blade loading distributions, indicating for stronger flow blockage at impeller exhaust.
2. The front-loaded design shows the most heterogeneous trailing edge flow pattern, indicating a high level of secondary flows. In addition, the position of the wake is located in the center of the blade passage, leading to increased flow blockage and deteriorating overall compressor efficiency.
3. The aft-loaded design yields the highest tip leakage mass flows, followed by the mid-loaded and front-loaded shroud blade loading configuration. It shows that losses associated to the kinetic energy of the tip jet are strongest for the aft-loaded design, since most of the tip leakage occurs at the rear part of the impeller, where a high flow density combined with high tip jet velocities is leading to increased losses compared to the other loading distributions.
4. The trajectory of tip leakage vortices depends on the shroud loading distribution. Tip leakage vortices are guided close to the suction side in the aft-and mid-loaded configuration, indicating that the pressure difference between blade pressure side and the suction side of the adjacent blade has a strong effect on the vortex trajectories. In case of the front-loaded design, the blade pressure difference in the rear part of the impeller is reduced, thus the trajectories of the tip leakage vortices are located in the mid of the blade passage, creating a higher blockage.
5. Tip leakage vortices have a strong impact on secondary flows along the blade surfaces, thus the front-loaded shroud loading configuration is suggested to have the highest blade secondary flows in the rear part of the impeller.
6. The front-loaded design is suggested to have the highest tip clearance sensitivity parameter m_{Cl}, followed by the mid-loaded and the aft-loaded loading configuration. Hence, tip clearance sensitivity is mostly determined by the trajectory of tip leakage vortices. Furthermore, this also implies that the shroud blade loading configuration has a minor

impact on compressor performance for compressors running on low relative clearance ratios.

The overall efficiency is strongly affected by tip leakage induced phenomena such as tip leakage and main and splitter blade tip leakage vortices. Adapting the shroud blade loading distribution, however, has been identified as a way to efficiently mitigate this phenomena. The following design strategies can be given:

1. The flow analysis suggested that it is beneficial to guide the trajectories of main and splitter blade tip leakage vortices close to the blade suction sides, in order to minimize flow blockage at impeller exhaust while mitigating the blade secondary flows between hub and shroud surfaces. The front-loaded design showed inferior efficiency, since parts of the tip leakage vortices were attached to the blade pressure sides, creating increased blockage and higher secondary flows on the blade pressure side.
2. The aft-loaded design is suggested to have the highest overall tip leakage, since most of the tip leakage occurs in the rear part of the impeller, where the flow density is high and - due to the higher blade loading towards the rear part of the impeller - also the pressure difference and hence the velocity across the blade, leading to increased tip leakage mass flows. Nonetheless, the optimal guidance of tip leakage vortices seems more important for reaching a high compressor efficiency, since the difference in efficiency between mid-loaded and aft-loaded design is small compared to the one between mid-loaded and front-loaded design.
3. The most promising shroud blade loading configuration in this study is the mid-loaded one, which represents a tradeoff between reduced tip leakage and optimal guidance of tip leakage vortices. Hence, highest efficiency was reached by that configuration. Nonetheless, it has been demonstrated that the difference in efficiency between the different loading distributions gets absolutely smaller towards smaller relative clearance ratios, thus suggesting a minor impact of the blade loading distribution on the efficiency at small relative clearance ratios. This corroborates with experimental findings of Mishina and Nishida [92].

In addition, the end-wall distribution is another possibility to reduce tip leakage and to allow well guided tip leakage vortex trajectories as shown by the baseline configuration provided by Javed et al. [27]. Javed et al. [27] tried to tailor the tip leakage vortex trajectories by adapting the end-wall shape, what resulted in widely opened blade passages in the mid of the impeller. On the one hand, this approach is beneficial in terms of overall tip leakage and tip leakage vortex guidance. On the other hand, their design showed an increased level of blade secondary flows and strong flow diffusion, what might be critical in terms of compressor stability. From that point of view, the author advices designers to first adapt the shroud blade loading distribution, before changing the end-wall shape.

In general, this analysis has shown that tip leakage and position of tip leakage vortices is crucial in terms of compressor efficiency for reduced-scale compressors running at large relative clearance ratios. The appropriate guidance of tip leakage vortices proves the importance of analyzing the three-dimensional compressor flow field, in order to achieve highest compressor efficiencies.

6 Conclusion and further steps

6.1 Summary and Conclusion

Techniques for performance prediction as well as design strategies to mitigate the key aerodynamic loss mechanisms occurring at reduced-scale centrifugal compressors are investigated in this PhD-thesis. Literature suggests that the main loss contributors of reduced-scale turbomachinery are related to the small feature size and to manufacturing tolerances. For instance, due to the small feature size, a reduced-scale compressor has a low Reynolds number and as a consequence higher frictional losses occur. The main loss contributor related to manufacturing tolerances is the large relative tip gap, occurring at such reduced feature sizes. Caused by manufacturing tolerances of a part as well as by form and positioning tolerances, which play an important role while assembly, the relative tip clearance of a reduced-scale compressor is larger compared to a large-scale industrial compressor.
The main goal of this PhD-thesis is to clarify three main research objectives:

1. How is the impact of low Reynolds number flow and large relative tip gaps on the performance and flow pattern of a reduced-scale compressor compared to a large-scale compressor?
2. Are empirical correlations available in the literature applicable, in order to predict the deterioration in performance of reduced-scale compressors caused by the main loss contributors?
3. Formulation of design guidelines to mitigate the negative aspects of the two main loss contributors, i.e. low Re-numbers and large relative tip clearances.

Two different compressor designs have been experimentally and numerically investigated. The first one is the compressor by Schiffmann [12, 13, 14, 15] with an impeller tip diameter of 20 mm. This compressor is numerically investigated using CFD and the the CFD setup is validated using experimental data provided by Schiffmann [12]. The second compressor geometry is the one by Javed et al. [27], which has an impeller tip diameter of 15.24 mm and a large relative clearance ratio of around 15 %. This compressor was up-scaled applying a scaling factor of 4.6, in order to allow for a more detailed flow measurement at impeller trailing edge and at outlet of the vaneless diffuser. This up-scaled compressor geometry was numerically investigated (CFD) and the results were validated using experimental data, which were obtained on a test rig described in subsection 2.4.2. In addition, a one-dimensional model to allow performance calculations of a centrifugal compressor has been developed and validated.

In a first step, the compressor provided by Schiffmann [12, 13, 14, 15] was numerically up- and down-scaled and the impact of the varying Reynolds number on the compressor performance was analyzed. The main findings are that the compressor efficiency gets deteriorated and a given operating point gets shifted towards smaller mass flow rates when down-scaling a given geometry.
Various empirical correlations predicting the efficiency change due to a change in geometrical feature size have been assessed. For this particular compressor, the correlation provided by Dietmann and Casey [50, 51] as well as an own correlation showed a good agreement in terms of efficiency prediction.
Besides the change of geometrical size, the compressor performance of five different relative tip clearance ratios ranging from 3 to 15 % have been analyzed for each geometrical size. A method provided by Casey and Robinson [49] for dividing compressor losses into Reynolds number dependent and Reynolds number independent losses has been applied over the whole operating range of this particular compressor. It has been figured out, that the Reynolds number dependent losses are independent of the relative tip gap size. The relative tip gap size merely impacts the Reynolds number independent losses. Furthermore, the Reynolds number independent losses could be further split into losses independent of the clearance ratio and losses which are entirely associated to relative clearance ratio.
In a last step, a design example is given, where the centrifugal compressor by Schiffmann [12, 13, 14, 15] is down-scaled with a simultaneous increase in relative clearance ratio. This example clearly demonstrates, that increasing the relative tip clearance ratio has a similar effect on the compressor map as decreasing compressors Reynolds number, but this effect is more pronounced. Eventually, design suggestions are given, in order to counterbalance the negative aspects of increased clearance ratios by compressor design.
Furthermore, the scaling analysis has been performed using the one-dimensional compressor model, in order to investigate the performance prediction of the model. The model captures both effects occurring while scaling a compressor, namely change in efficiency with a shift of an operating point. Furthermore, the model predicts Reynolds number dependent and independent losses for various relative tip clearance ratios in the same order of magnitude as CFD.

In a next step, the impact of altering the relative tip clearance ratio on the compressor performance has been numerically and experimentally investigated for the reduced-scale compressor provided by Schiffmann [12, 13, 14, 15] and the scaled up compressor provided by Javed et al. [27]. Overall, an increase in relative tip clearance ratio leads to a lower efficiency and a shift of peak efficiency points towards smaller flow rates. On the one hand, this is related to higher total pressure losses, what lowers the head coefficient. On the other hand, the work input coefficient drops due to increased flow blockage caused by the tip leakage and tip leakage vortices.

Empirical correlations have been compared to experimental and numerical results. The compressor provided by Schiffmann [12, 13, 14, 15] has shown a larger drop in efficiency by changing its clearance than the one provided by Javed et al. [27], thus suggesting a clear dependence on design features. Hence, no clear recommendation about a preferred correlation can be given, since the more pessimistic correlation suggested by Pfleiderer and Petermann [29] matched well for the compressor by Schiffmann [12, 13, 14, 15] and the commonly used correlations provided by Eckert and Schnell [30] and by Pampreen [31] matched well for the compressor by Javed et al. [27].

In addition, the drop in efficiency in terms of altering the relative clearance ratio ratio has been analyzed in the operating range of the compressor. Operating points having the same mass flow rate could be correlated with a linear relationship in the entire operating range and the slope of this linear relationship represents the tip clearance sensitivity of a compressor. The analysis suggest that this tip clearance sensitivity increases from surge towards choke caused by the map shift due to increased tip leakage flow blockage. The compressor by Schiffmann [12, 13, 14, 15] has shown a larger tip clearance sensitivity parameter as the one by Javed et al. [27], indicating for a design dependence.

A more detailed analysis of the tip gap properties suggested that the intensity of tip leakage jet is linked to diffusion and pressurization in the impeller passage as well as the shroud blade loading. By increasing the relative clearance ratio, a compressor achieves a higher diffusion in the inducer part, what results in larger tip jet densities. On the other hand, the inducer gets loaded additionally by increasing the relative clearance ratio, thus higher tip jet velocities in the inducer occur. Both effects strengthen the tip leakage vortex, evolving from main blade leading edge. From that point of view, a compressor designer needs to minimize the inducer shroud blade loading as well as the diffusion in the inducer, in order to reduce inducer tip leakage.

In addition, the tip clearance sensitivity of Schiffmann's [12, 13, 14, 15] compressor was analyzed using a one-dimensional compressor model. Although the one-dimensional model capture the governing effects of increasing relative tip clearance ratio, the tip clearance sensitivity is not in line with CFD data, thus suggesting a required calibration of the reduced-order model.

In a last step, the impact of hub- and shroud end-wall distribution as well as the shroud blade loading distribution on the compressor performance with special regards to tip leakage is analyzed. The compressor provided by Javed et al. [27] was used as reference geometry for this study.

In a first design step, the hub end-wall was modified such that the diffusion in the mid-part of the impeller was lowered. Hence, the shroud loading increases, what leads to increased tip leakage compared to the reference geometry, suggesting that end-wall shape and the passage diffusion has a strong impact on tip leakage.

Three different shroud loading distributions have been investigated using the modified end-wall shape, namely an aft-, a mid- and a front-loaded one. The front-loaded design suggested the lowest overall tip leakage compared to a mid-loaded and an aft-loaded shroud loading distribution. Nonetheless, it also provided the lowest efficiency, what is caused by a more intense main blade tip leakage vortex as well as stronger secondary flow losses on the blades. In addition, the position of main and splitter blade tip leakage vortices at impeller trailing edge depends on the shroud loading distribution. The intensity of pressure difference in the rear part of the impeller defines the location of the vortex cores, thus tip leakage vortices in the aft-loaded shroud loading distribution are located closer to the blade suction sides than in the front-loaded configuration.

The best shroud blade loading configuration in terms of efficiency is a tradeoff between losses associated to tip leakage and the guidance of tip leakage vortices. On the one hand, the front-loaded configuration yields the lowest overall tip leakage and hence the lowest tip leakage losses. On the other hand, tip leakage vortices are located closer to the blade suction side by using an aft-loaded shroud loading configuration, what is beneficial in terms of flow blockage and blade secondary flows. From that point of view, using a mid-loaded shroud loading configuration seems desirable, since it achieves lower tip leakage losses than an aft-loaded shroud loading and the tip leakage vortices are located closer to the blade suction sides than in the front-loaded configuration. Experimental as well as numerical investigations of different shroud loading distributions suggested a superior efficiency of such a mid-loaded configuration compared to an aft- and a front-loaded one. However, the analysis also suggested that the shroud loading distribution becomes important for compressors running on large relative tip clearance ratios (CR > 5 %). The shroud loading distribution has only a minor impact on the compressor efficiency for compressors running on low relative clearance ratios (CR < 5 %), what is in accordance with experimental findings suggested by Mishina and Nishida [92].

6.2 Recommendations about empirical correlations

The following section provides the reader with a short overview of recommended empirical correlations in terms of centrifugal compressor performance prediction for (1) scaling and (2) altering the relative clearance ratio of centrifugal compressors .

Scaling:

The correlation by Dietmann and Casey [50, 51] has been suggested to offer increased performance prediction for a numerically conducted scaling analysis of a reduced-scale centrifugal compressor provided by Schiffmann [12, 13, 14, 15]. Both the change in efficiency as well as shift of an operating point is captured by using their correlation. In addition, their correlation

has been applied at design and off-design conditions. Their correlation is based on Eq. 1.11 and Eq. 1.12, where the friction factors are evaluated according to appendix B.
Furthermore, the author developed an own scaling correlation based on the method suggested by Casey and Robinson [49]. The correlation, however, was derived from only one particular compressor geometry, thus a general validity of this correlation could not be tested.

Altering the relative clearance ratio:

No clear recommendation about a correlation offering a relationship for the efficiency deterioration caused by altering the relative clearance ratio of a centrifugal compressor can be given. Two reduced-scale centrifugal compressors have been investigated for relative clearance ratios ranging from 3 % up to 20 %. Both compressors suggested having a different sensitivity to a change of relative clearance ratio. Hence, tip clearance sensitivity seems to be more a design feature than being modeled by a simple empirical correlation. Nonetheless, both investigated compressor geometries showed an efficiency behavior through changing the relative clearance ratio, which could be approximated by a linear approach for operating points having the same flow rate at design and off-design.

6.3 Design implications for compressors operating at relative clearance ratios exceeding 5 %

Both reducing the feature size and increasing the relative clearance ratio of a centrifugal compressor have a similar effect on the compressor performance, namely a drop in efficiency and a shift of operating points towards smaller flow rates. The latter, however, has a stronger impact on the compressor performance thus this section offers design implications, in order to counterbalance the negative aspects of large relative clearance ratios. It is assumed that the compressor designer starts from a 0mm-clearance case as commonly done in compressor design:

1. Due to the shift of global flow coefficient caused by large relative clearance ratios, a compressor designer needs to select a 0mm-clearance design, which is designed for a higher global flow coefficient as the desired one.
2. The trailing edge blockage increases with an increase of relative clearance ratio. A designer needs to increase the trailing edge width, when applicable, in order to mitigate trailing edge blockage.
3. The inducer starts to get more loaded and the diffusion/pressurization increases with increasing relative clearance ratio. A designer needs to unload the inducer by end-wall contours and/or blade angle distribution.
4. A shroud blade angle distribution, where the maximum turning point is located at around 50 up to 70 % of the meridional coordinate, seems desirable in terms of tip

leakage, guidance of tip leakage vortices, homogeneity of the exit flow field as well as blade secondary flows.

5. It seems desirable to guide the tip leakage vortices of main and splitter blade near the blade suction sides, since a more homogenous exit flow field has been observed.

6.4 Further steps

In order to confirm the suggested design strategies, more compressor geometries running with large relative clearance ratios, but having different design specifications, need to be tested numerically as well as experimentally. The results of this PhD work suggest that design of reduced-scale compressors running at a large relative clearance ratio require three-dimensional flow field optimizations, such as tailoring the trajectories of the tip leakage vortices along the blade suction sides. From that point of view, it might be interesting to use generic optimisation algorithms for compressor design, in order to identify further beneficial trends of designing compressors running on large clearances.

A 4.6 times scaled-up version of the compressor unit provided by Javed et al. [27] has been investigated in this thesis. The original size compressor, however, was not ready to operate during this PhD thesis. Nonetheless, an experimental and numerical comparison between the original size compressor and the scaled-up one might be worthwhile in terms of testing the suggested scaling correlation of chapter 3.

The one-dimensional model for predicting compressor performance needs to be further validated and calibrated. A generic optimization algorithm could be used for that purpose, by minimizing deviations to experimental data in terms of head coefficient and work input coefficient. By doing this for various compressors trends could be identified, what potentially results in an improved set of calibration coefficients used for the empirical correlations of the one-dimensional compressor model.

In addition, the recent implementation of the one-dimensional model is still based on a pipe flow friction model. The scaling analysis in chapter 3, however, has demonstrated the good quality of the modified flat plate friction model by Casey and Robinson [49], thus an implementation into the one-dimensional model seems reasonable.

The experimental test rig requires improvements in terms of measurement equipment. For instance, the total pressure could not be measured due to the lack of a sufficiently small traversing probe, thus the total pressure was estimated by using a reduced-order model. As a further consequence, merely total-static isentropic efficiencies could be measured at impeller trailing edge and outlet of the vaneless diffuser.

In addition to the total pressure measurement, a traverse probe would further allow to define the absolute flow angle, in order to split up the velocities into a tangential and radial/meridional component. Hence, more detailed flow measurements could be performed for the impeller, the diffuser and the volute, what allows full performance characterization of each

individual compressor component.
Furthermore, a hot-wire anemometer for measuring velocity fluctuations at the inlet of the compressor might be useful for determination of turbulent properties. These properties could then be directly used in CFD, in order to improve the quality of inlet boundary conditions.

In addition, diabatic compressor operation has not been investigated in this thesis. Nonetheless, the high surface-to-volume ratio of reduced-scale centrifugal compressors makes the compressor more sensitive for heat addition, thus a deterioration in terms of compressor efficiency is expected. A numerical and experimental investigation of diabatic effects is therefore worthwhile for further improving the compressor efficiency by mitigating heat effects.

Furthermore, a more thorough investigation of tip leakage vortex trajectories is required, in order to obtain a simple model of these trajectories and to define characteristic numbers, which could be further used as a design variable in the preliminary compressor design phase. Such design variables would minimize the numerical effort for investigating the three-dimensional flow field.

The option of shrouding an impeller was discussed, but was not further investigated, since literature claims that an unshrouded impeller shows superior efficiency than a similar shrouded one. Sirakov [16], however, suggests that using an individually designed shrouded impeller could further improve the efficiency of reduced-scale compressors. From this point of view, it might be beneficial to study the option of shrouding impellers at such reduced-scale. Shrouding an impeller, however, strongly depends on the mechanical stress, which is caused by the cover, thus besides the aerodynamic analysis a stress analysis is required.

A Appendix A

A.1 Geometrical details about investigated centrifugal compressor geometries

A.1.1 Centrifugal compressor by Schiffmann

Impeller			
Leading Edge		Trailing Edge	
Hub diameter $d_{1,h}$	0.004 m	Tip diameter d_2	0.02 m
Shroud diameter $d_{1,s}$	0.0113 m	Blade angle β_2	-48.9 °
Hub blade angle $\beta_{1,h}$	-22.44 °	Outlet width b_2	0.00105 m
Shroud blade angle $\beta_{1,s}$	-59.8 °	Tip clearance t_2	0.05 mm
Tip clearance t_1	0.05 mm	Blade thickness e_2	0.25 mm
Blade thickness e_1	0.25 mm	Back face clearance t_{Back}	0.2 mm
Full/Splitter blades	9/9	(between impeller back face and housing)	
Throat			
Throat area A_{th}	60.252 mm^2		
Vaneless diffuser			
Outlet diameter d_3	0.033 m		
Outlet width b_3	0.905 mm		
Volute			
Throat area $A_{th,Vol}$	48.8 mm^2		
Outlet area $A_{Out,Vol}$	88.8 mm^2		

Table A.1: Main dimensions of compressor unit provided by Schiffmann [12, 13, 14, 15].

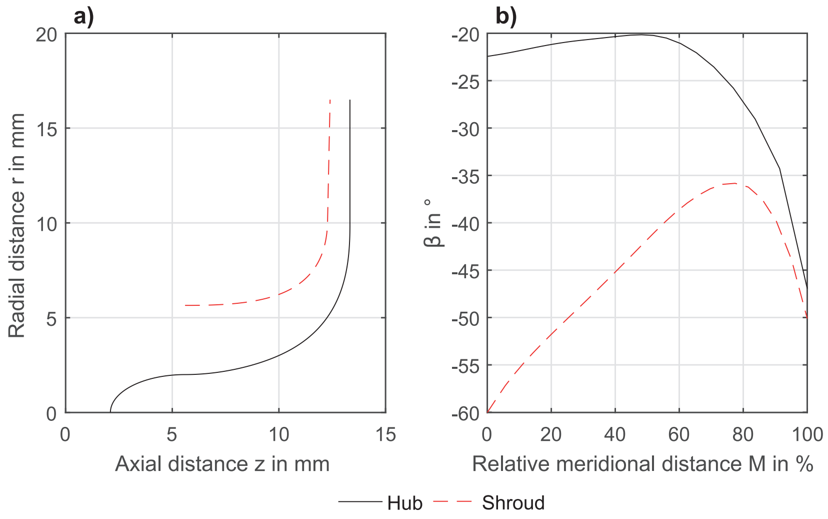

Figure A.1: End wall distribution (a) and blade angle distribution (b) at hub and shroud of compressor unit by Schiffmann [12, 13, 14, 15].

A.1.2 Centrifugal compressor by Javed et al.

Impeller			
Leading Edge		Trailing Edge	
Hub diameter $d_{1,h}$	0.003 m	Tip diameter d_2	0.01524 m
Shroud diameter $d_{1,s}$	0.0725 m	Blade angle β_2	-45.0 °
Hub blade angle $\beta_{1,h}$	-30.5 °	Outlet width b_2	0.000623 m
Shroud blade angle $\beta_{1,s}$	-57.0 °	Tip clearance t_2	0.08 mm
Tip clearance t_1	0.08 mm	Blade thickness e_2	0.25 mm
Blade thickness e_1	0.25 mm	Back face clearance t_{Back}	0.2 mm
Full/Splitter blades	8/8	(between impeller back face and housing)	
Throat			
Throat area A_{th}	22.61 mm^2		
Vaneless diffuser			
Outlet diameter d_3	0.025142 m		
Outlet width b_3	0.405 mm		

Table A.2: Main dimensions of original size compressor by Javed et al. [27].

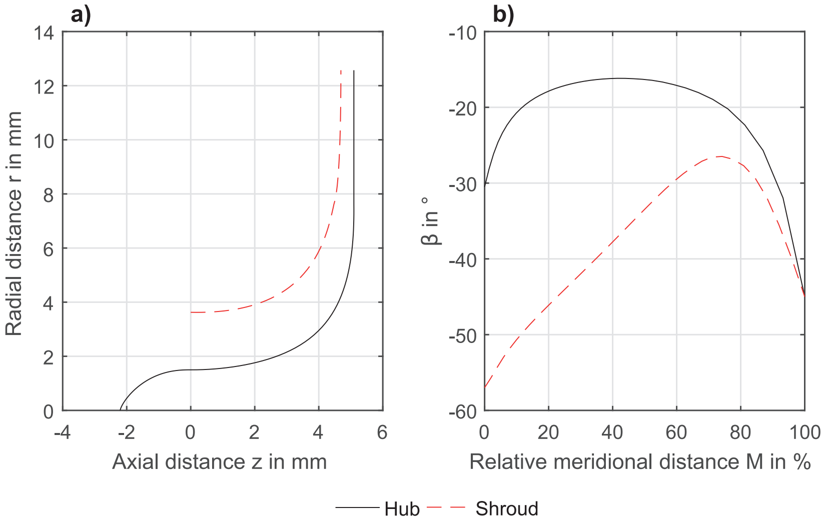

Figure A.2: End wall distribution (a) and blade angle distribution (b) at hub and shroud of original size compressor by Javed et al. [27].

A.2 Details about experimental setup

A.2.1 Compressor unit, drive and magnetic coupling

The main drive of the compressor unit is a spindle used for CNC-applications provided by IBAG [93]. The drive delivers a maximum rotational speed of 60 krpm, having a maximum torque of 4 Nm. The spindle drive is connected with the compressor shaft by a magnetic coupling provided by EagleBurgmann [94], designed for a maximum rotational speed of 60 krpm. The magnets on the motor spindle as well as the one on the compressor shaft are press-fitted. The compressor unit is supported on high-speed ball bearings which are oriented as spring-loaded O-configuration. The ball bearings are provided by SKF [95]. The assembly drawing of the compressor shaft is illustrated in Fig. A.3.
The whole compressor unit is mounted on a heavy machine table as shown in Fig. A.4.

A.2.2 Refrigeration loop

The following subsection offers a summary of the used components in the refrigeration loop as shown in Fig. 2.8.

Heat exchanger

The heat exchanger (SWEP BH56N-Wx130) is provided by SWEP [96] and is of the type plate heat exchanger. The heat exchanger is designed for 40 kW, what is realized with 64 channels on the refrigerant side and 65 channels on the water-glycol side.

Electrical expansion valve

The electrical expansion valve is a E7V provided by CAREL [97]. The expansion valve is operated in the mode "‘analog positioner"’, meaning that an input voltage between 0 and 10 Volt defines the nozzle position. This input voltage is controlled by a LabView-VI [98]. A 24 VDC connection serves as power supply for the electrical expansion valve.

Heated suction side accumulator

In order to allow a liquid droplet-free inlet flow, which is conveyed to the impeller, a suction side accumulator is used. The suction side accumulator is based on the injector principle and the component is provided by ESK-Schultze [99] (type number FA54-9).
In order to provide heat for super heating the fluid upstream the compressor, a heating collar with a maximum power of 4 kW is used and is mounted around the suction side accumulator. The power of this heating collar is controlled by a solid state relay for adapting the degree of superheat.

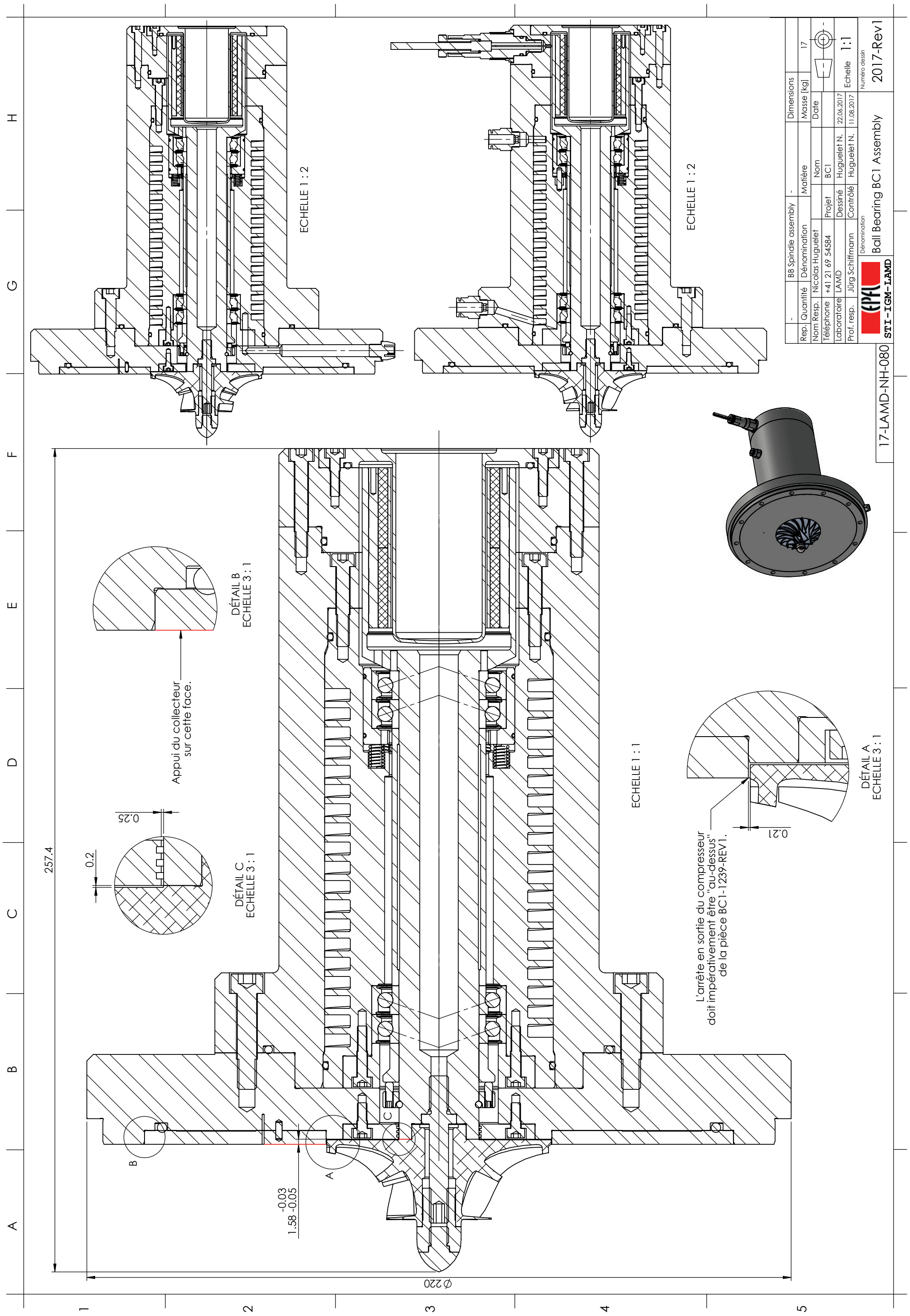
A
B
C
D
E
F
G
H
1
2
3
4
5
ECHELLE 1 : 2
ECHELLE 1 : 2
ECHELLE 1 : 1
DÉTAIL B
ECHELLE 3 : 1
Appui du collecteur
sur cette face.
DÉTAIL C
ECHELLE 3 : 1
0.25
0.2
DÉTAIL A
ECHELLE 3 : 1
0.21
L'arrête en sortie du compresseur
doit impérativement être "au-dessus"
de la pièce BC1-1239-REV1.
257.4
∅220
1.58 -0.03 -0.05
A
B
C
- | BB Spindle assembly | -
Rep. | Quantité | Dénomination | Matière | Dimensions
Masse [kg] | 17
Nom Resp. | Nicolas Huguelet | Nom | Date
Téléphone | +41 21 69 54584 | Projet | BC1
Laboratoire | LAMD | Dessiné | Huguelet N. | 22.06.2017
Prof. resp. | Jürg Schiffmann | Contrôlé | Huguelet N. | 11.08.2017
Echelle 1:1
EPFL
STI-IGM-LAMD
Dénomination
Ball Bearing BC1 Assembly
Numéro dessin
2017-Rev1
17-LAMD-NH-080

Figure A.3: Cut of the compressor shaft used in the experimental setup.

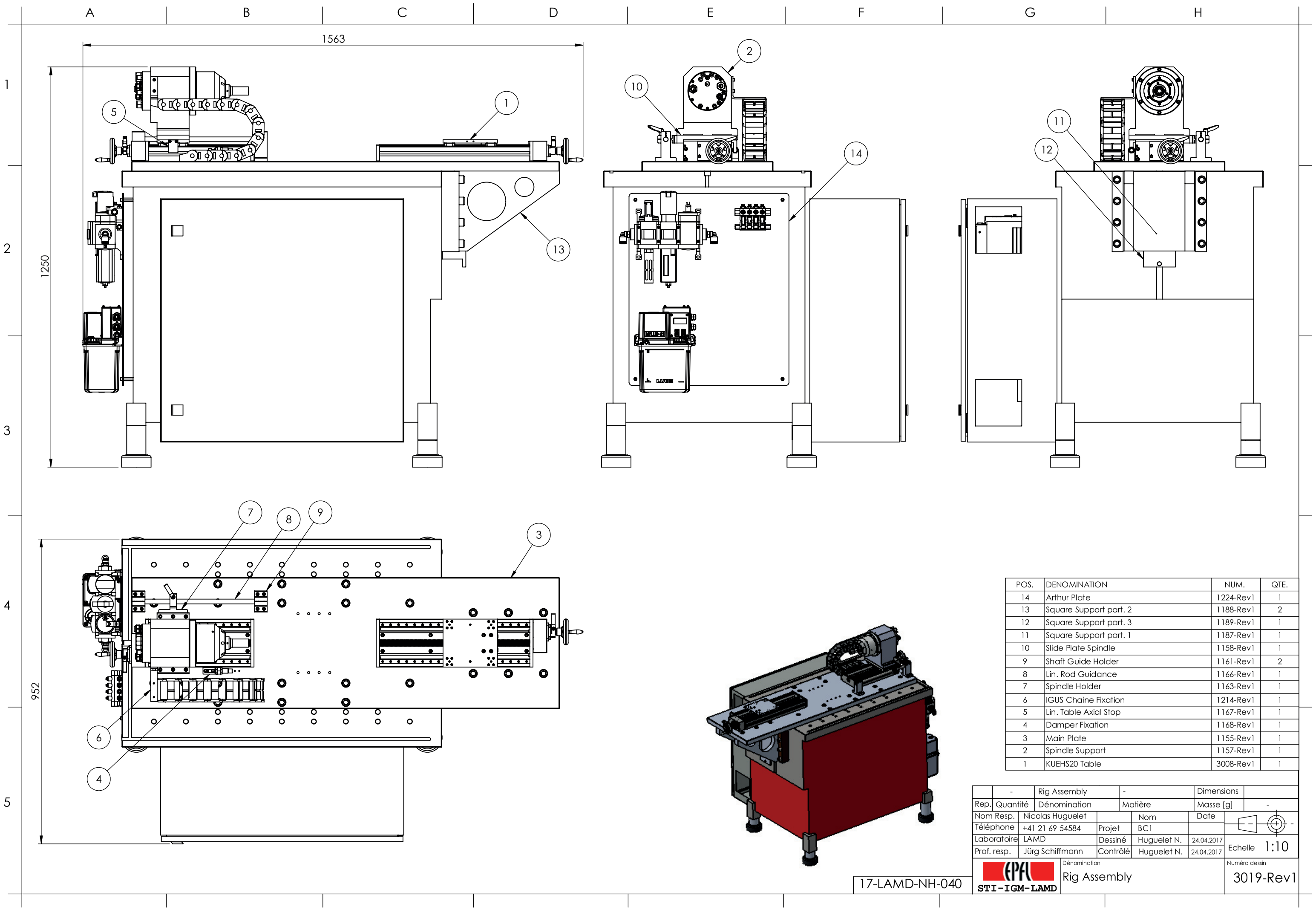

POS.	DENOMINATION	NUM.	QTE.
14	Arthur Plate	1224-Rev1	1
13	Square Support part. 2	1188-Rev1	2
12	Square Support part. 3	1189-Rev1	1
11	Square Support part. 1	1187-Rev1	1
10	Slide Plate Spindle	1158-Rev1	1
9	Shaft Guide Holder	1161-Rev1	2
8	Lin. Rod Guidance	1166-Rev1	1
7	Spindle Holder	1163-Rev1	1
6	IGUS Chaine Fixation	1214-Rev1	1
5	Lin. Table Axial Stop	1167-Rev1	1
4	Damper Fixation	1168-Rev1	1
3	Main Plate	1155-Rev1	1
2	Spindle Support	1157-Rev1	1
1	KUEHS20 Table	3008-Rev1	1

	-	Rig Assembly	-	Dimensions	
Rep.	Quantité	Dénomination	Matière	Masse [g]	-

			Nom	Date
Nom Resp.	Nicolas Huguelet			
Téléphone	+41 21 69 54584	Projet	BC1	
Laboratoire	LAMD	Dessiné	Huguelet N.	24.04.2017
Prof. resp.	Jürg Schiffmann	Contrôlé	Huguelet N.	24.04.2017

Echelle 1:10

STI-IGM-LAMD

Dénomination Rig Assembly

Numéro dessin 3019-Rev1

17-LAMD-NH-040

Figure A.4: Assembly drawing of the whole compressor unit.

Filter Drier

During brazing of the refrigeration loop, the test-rig is contaminated by various particles which may destroy the compressor wheel. In order to filter-out particles and dust, a filter drier provided by ESK-Schultze [99] is used. The used filter drier has the type number FT-42-CDM. According to Fig. 2.8, the filter drier can be by-passed, thus the refrigerant only passes through the heated separator. Nonetheless, it is advised to run the compressor test rig with filter drier after maintenance has been done.

A.2.3 Used measurement devices

Total temperatures, static pressures as well as the compressor mass flow rate are measured in the compressor test rig, which has been described in subsection 2.4.2. A summary of the used measurement devices is given:

Coriolis mass flow meter

In order to measure the compressor mass flow rate, a Coriolis mass flow meter has been used downstream the compressor exhaust. This mass flow meter is provided by Emerson [100] (type number CMFS100M179N2FNEKZZ) and was pre-calibrated by the manufacturer, in order to allow mass flow measurement for a refrigerant. The measured mass flow rate was always located in the range, where the mass flow meter provides an accuracy of ± 0.25 % of the actual reading.

K-type thermocouples

K-type thermocouples provided by Transmetra GmbH [101] have been used to track inlet (3 thermocouples) and outlet temperature (3 thermocouples) of the compressor unit as well as inlet and outlet temperature of the heat exchanger refrigerant side (3 thermocouples each) and water-glykol side (1 thermocouple each), respectively. In addition, one thermocouple was used to measure the room temperature, thus a total number of 15 thermocouples have been used. The thermocouples were calibrated in a thermal bath using a Pt100-reference thermometer. The temperature of the thermal bath was adapted ranging from -20 °C up to 100 °C in 10K temperature steps.

The measurement error of one thermocouple strongly depends on many parameters concerning the installation of the thermocouple. For instance, thermocouple diameter, thermocouple length and the immersion depth have a strong impact on the quality of the temperature measurement. No obligatory recommendations about the absolute error of a thermocouple exist in literature and from that point of view an absolute error of ± 0.5K is assumed for each thermocouple. This absolute error is used for the Gaussian error propagation.

Differential pressure scanner

A ScaniValve [102] DSA3218 differential pressure scanner is used to track the static pressure in the compressor unit, which has a special heating device, in order to measure condensable gases like refrigerants. The maximum differential pressure acting on the membrane of the pressure scanner is 250 psi, what corresponds to around 17.2 bar. Since the sampling rate of the pressure scanner is 4 Hz, the device only allows measurement of time-averaged pressure signals.

A certificate provided with the pressure scanner mentions an accuracy of ± 0.02 % of the full scale value, what corresponds to an absolute error in pressure of around ± 3.4 mbar.

Pressure transducers

Two pressure transducers from Kistler [103] are used to track inlet and outlet static pressure of the heat exchangers refrigeration side. In addition, a pressure transducer from Kistler [103] for measuring the ambient pressure is used, in order to transfer the differential pressures of the pressure scanner (see previous device) into absolute pressure values.

The pressure transducers were calibrated by putting pre-defined high accuracy weights on a pressure balance, in order to pressurize the transducers with a pre-defined pressure.

The error of the ambient pressure transducer is required for the Gaussian error propagation. The used piezo-resistive transducer has a range from 0 up to 5 bar and an error of ± 0.2 % on the full scale value occurs, what corresponds to an absolute error of ± 1 mbar. The sum of this error and the one of the pressure scanner results in a total error of the static pressure measurement of ± 4.4 mbar.

A.3 One-dimensional compressor model

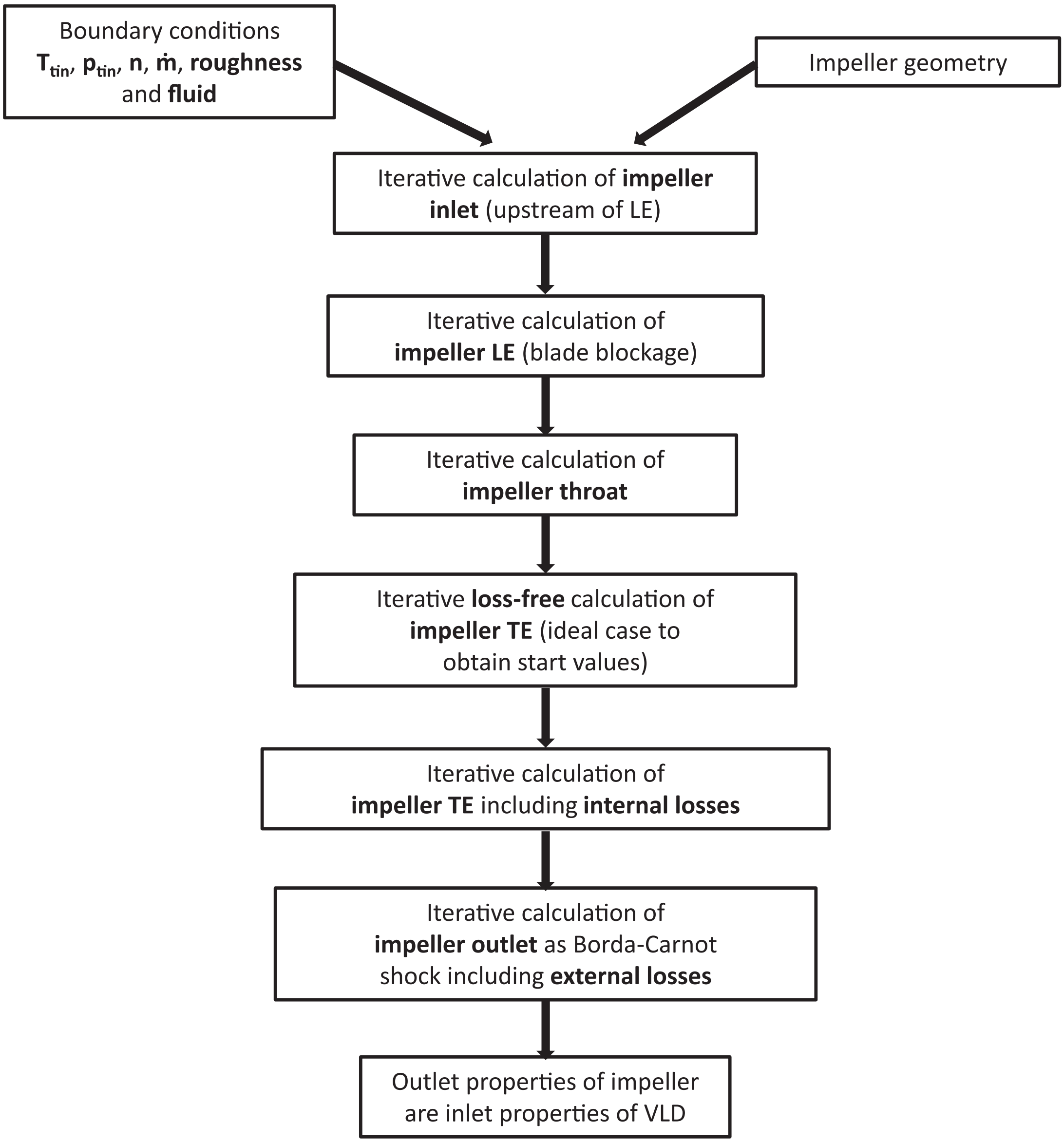
Boundary conditions
T_{tin}, p_{tin}, n, $\dot{m}$, roughness and fluid
Impeller geometry
Iterative calculation of impeller inlet (upstream of LE)
Iterative calculation of impeller LE (blade blockage)
Iterative calculation of impeller throat
Iterative loss-free calculation of impeller TE (ideal case to obtain start values)
Iterative calculation of impeller TE including internal losses
Iterative calculation of impeller outlet as Borda-Carnot shock including external losses
Outlet properties of impeller are inlet properties of VLD

Figure A.5: Iterative solution scheme of the impeller used in the one-dimensional model.

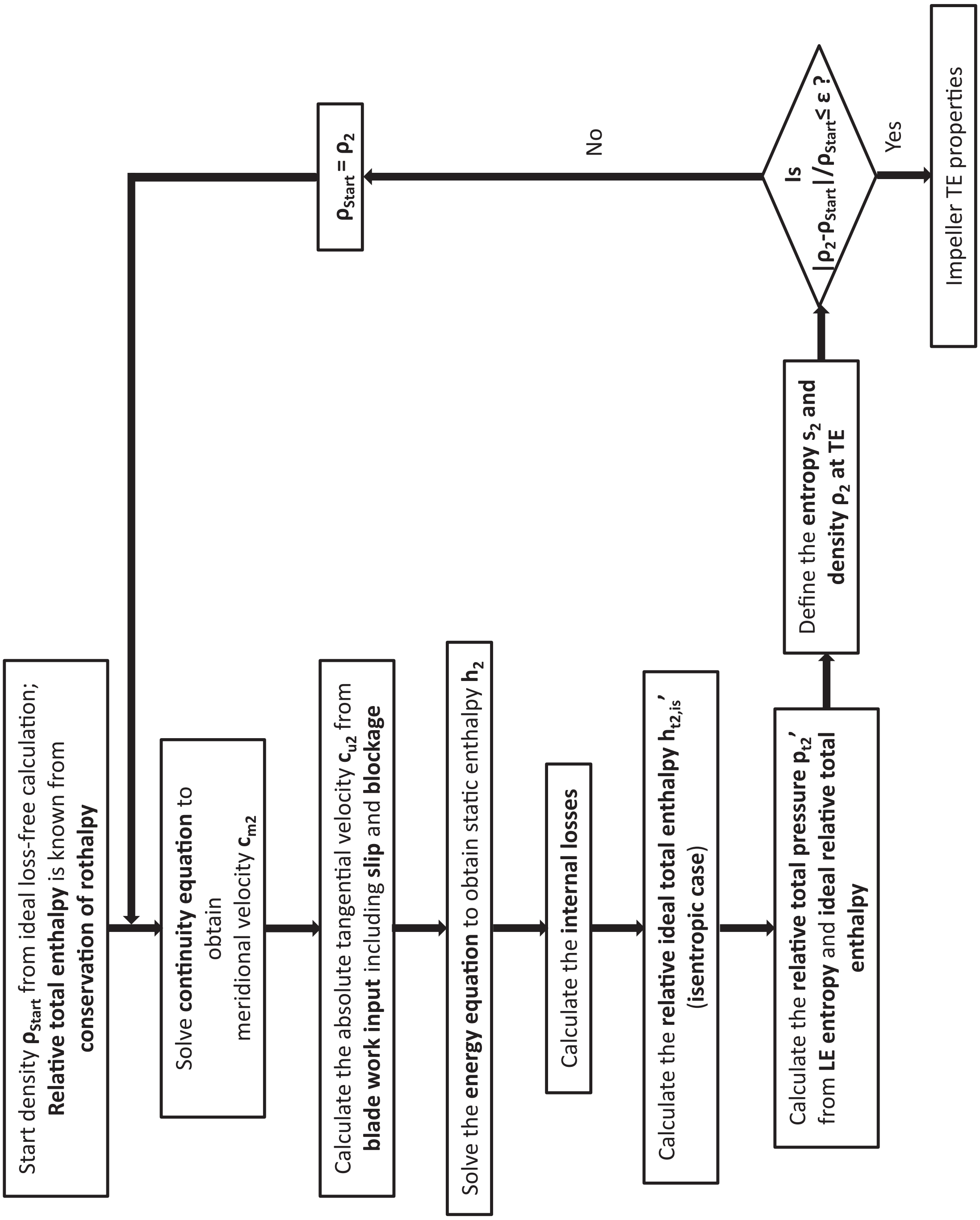
Start density ρ_{Start} from ideal loss-free calculation; Relative total enthalpy is known from conservation of rothalpy
Solve continuity equation to obtain meridional velocity c_{m2}
Calculate the absolute tangential velocity c_{u2} from blade work input including slip and blockage
Solve the energy equation to obtain static enthalpy h_2
Calculate the internal losses
Calculate the relative ideal total enthalpy $h_{t2,is}'$ (isentropic case)
Calculate the relative total pressure p_{t2}' from LE entropy and ideal relative total enthalpy
Define the entropy s_2 and density ρ_2 at TE
Is $|\rho_2 - \rho_{Start}| / \rho_{Start} \leq \varepsilon$?
No
$\rho_{Start} = \rho_2$
Yes
Impeller TE properties

Figure A.6: Iterative solution scheme at impeller trailing edge.

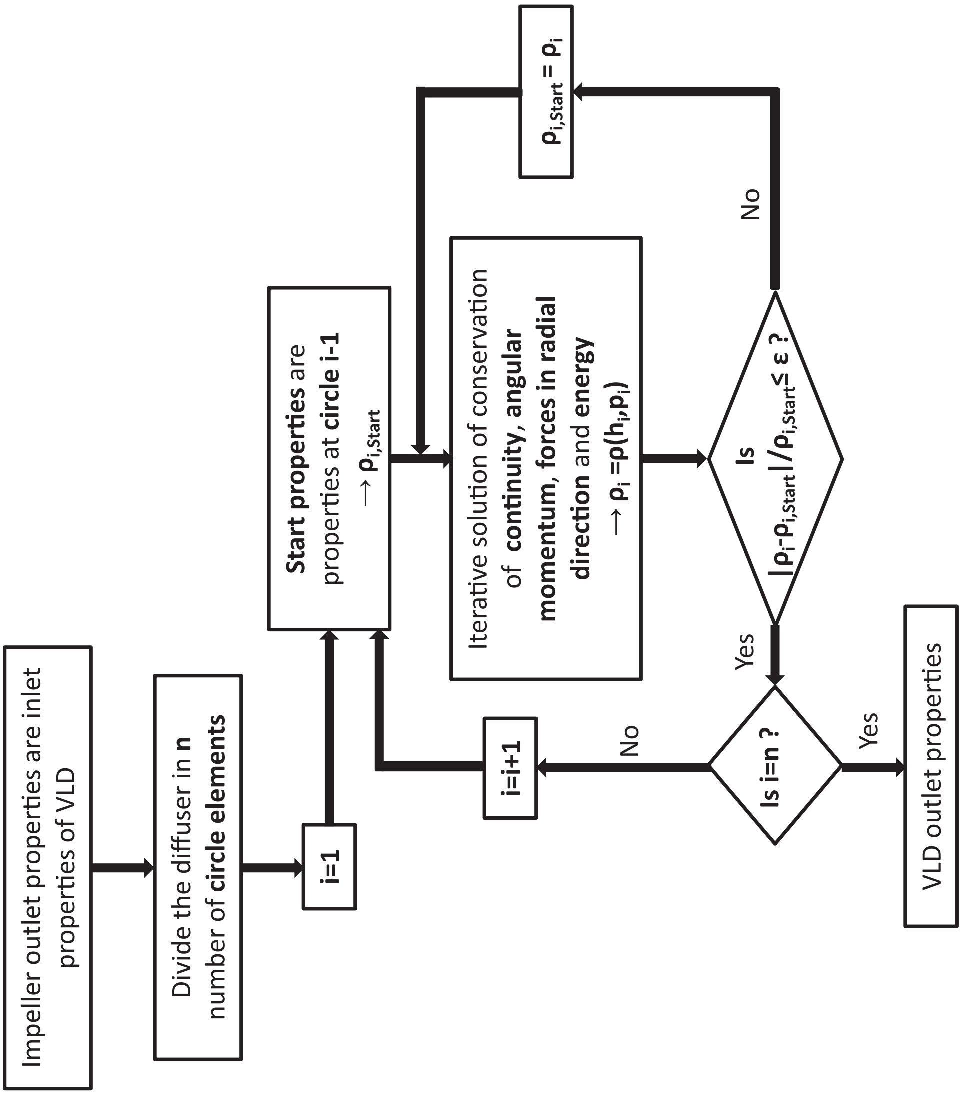
Impeller outlet properties are inlet properties of VLD
Divide the diffuser in **n** number of **circle elements**
i=1
Start properties are properties at **circle i-1** → $\rho_{i,Start}$
Iterative solution of conservation of **continuity**, **angular momentum**, **forces in radial direction** and **energy** → $\rho_i = \rho(h_i, p_i)$
Is $|\rho_i - \rho_{i,Start}| / \rho_{i,Start} \leq \varepsilon$ **?**
No
$\rho_{i,Start} = \rho_i$
Yes
Is i=n ?
No
i=i+1
Yes
VLD outlet properties

Figure A.7: Solution scheme of the partial differential equations in the vaneless diffuser.

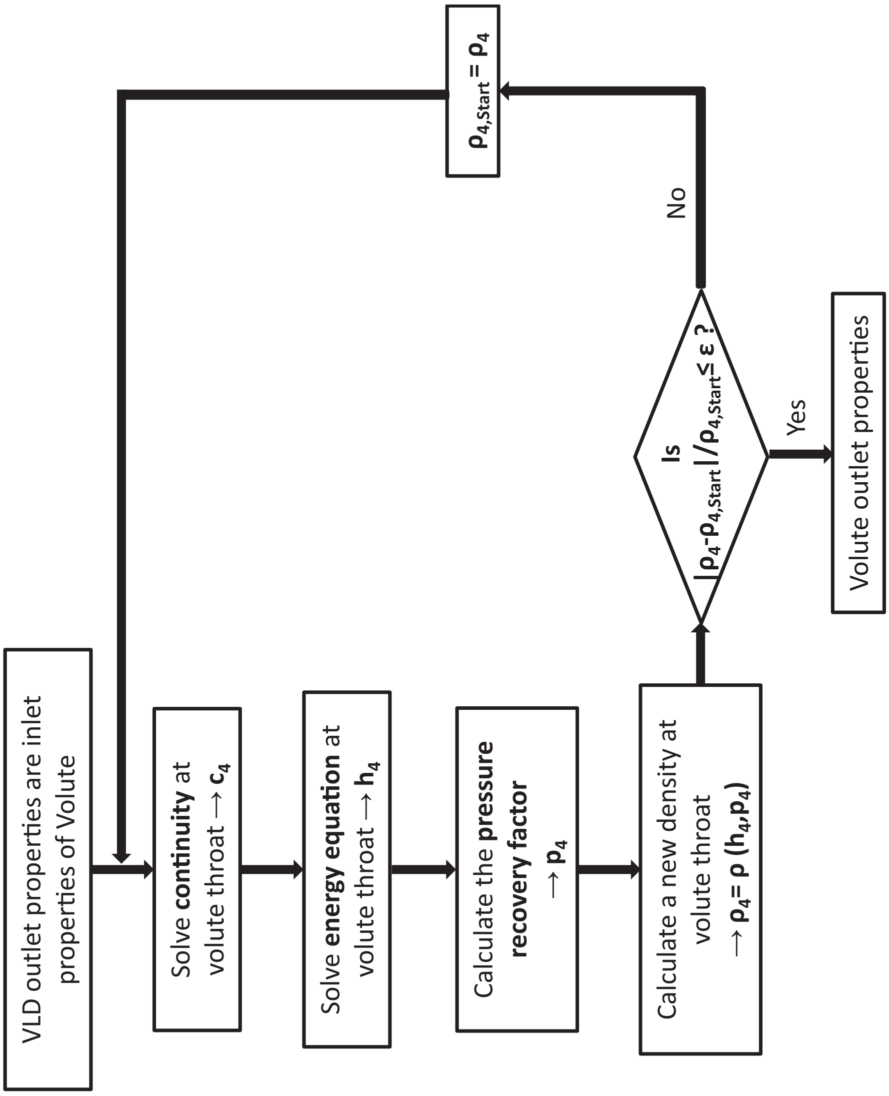
VLD outlet properties are inlet properties of Volute
Solve **continuity** at volute throat → c_4
Solve **energy equation** at volute throat → h_4
Calculate the **pressure recovery factor** → p_4
Calculate a new density at volute throat → $\rho_4 = \rho(h_4, p_4)$
Is $|\rho_4 - \rho_{4,Start}| / \rho_{4,Start} \leq \varepsilon$?
No
$\rho_{4,Start} = \rho_4$
Yes
Volute outlet properties

Figure A.8: Iterative solution scheme of the volute used in the one-dimensional model.

A.4 Computational grid

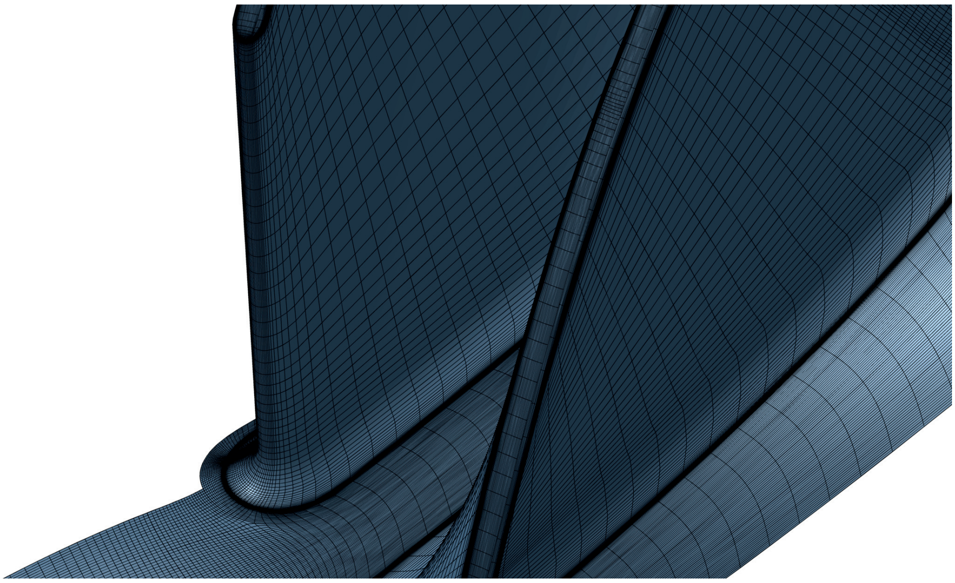

Figure A.9: Computational grid (H-I-topology) around the main blade leading edge of the impeller by Schiffmann [12, 13, 14, 15].

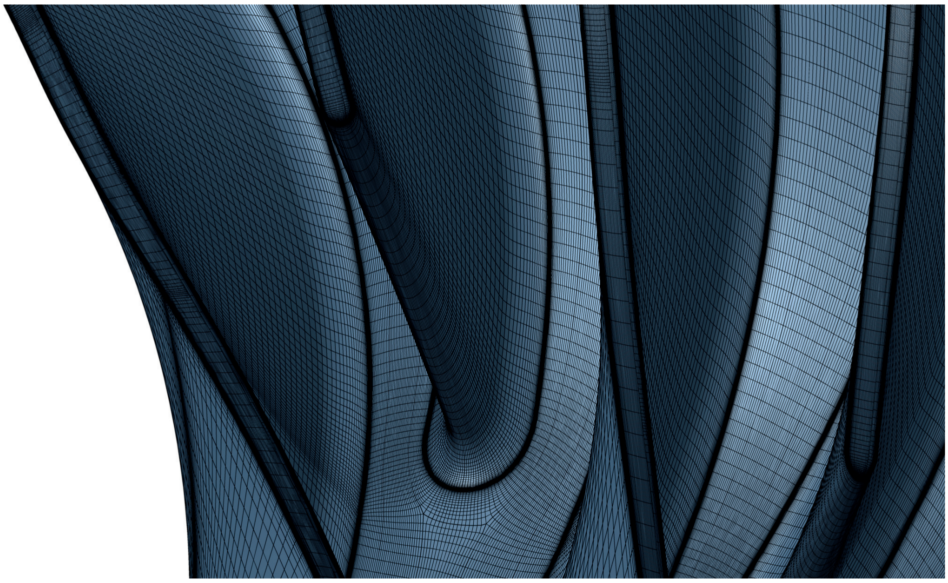

Figure A.10: Computational grid (H-I-topology) around the splitter blade leading edge of the impeller by Schiffmann [12, 13, 14, 15].

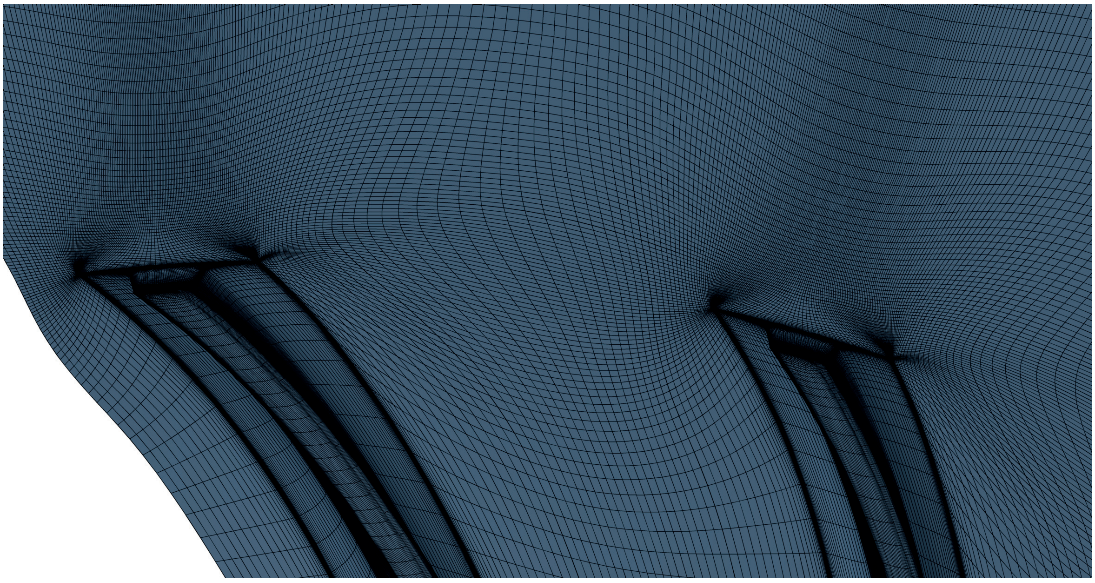

Figure A.11: Computational grid (H-I-topology) around the trailing edge of the impeller by Schiffmann [12, 13, 14, 15].

A.5 Experimental data of up-scaled compressor by Javed et al.

Nozzle Pos. [%]	$\dot{m}$ [kg/s]	T_{In} [K]	p_{In} [bar]	p_{TE} [bar]	p_{VLD} [bar]	T_{Out} [K]	p_{Out}[bar]
52.5	0.2242	270.65	1.696	3.102	3.757	306.42	3.635
55	0.2298	269.91	1.689	3.187	3.823	305.79	3.798
57.5	0.2396	269.33	1.686	3.239	3.887	304.87	3.827
60	0.2509	268.48	1.679	3.238	3.887	303.77	3.818
62.5	0.2601	267.89	1.667	3.222	3.872	302.91	3.781
65	0.2793	267.55	1.650	3.203	3.835	301.78	3.670
67.5	0.2909	267.17	1.638	3.155	3.780	300.91	3.563
70	0.3077	266.55	1.636	3.125	3.731	299.62	3.485
75	0.3221	266.08	1.626	3.097	3.670	298.52	3.379
80	0.3330	265.61	1.626	3.076	3.646	297.62	3.300
85	0.3380	265.49	1.613	3.034	3.594	297.09	3.206
90	0.3439	265.25	1.616	3.030	3.576	296.56	3.161
95	0.3499	265.15	1.613	3.004	3.535	296.27	3.119
100	0.3501	265.22	1.612	2.995	3.508	296.32	3.116

Table A.3: Time averaged experimental data for up-scaled compressor by Javed et al. [27] having a relative clearance ratio of 14.73 %

B Appendix B

B.1 Solver setup for scaling analysis

All important CFD solver parameters of the scaling analysis, which has been presented in chapter 3, are summarized in Table B.1.

General	
Components	Inlet duct, impeller and vaneless diffuser
Scaling factor	0.75, 1, 2 and 4
Relative clearance ratio in %	3, 5, 7.5, 10 and 15
Numerical model	Steady-state passage model (periodicity 9)
Grid	
Configuration	H-I-mesh (splitter configuration)
Number of grid points	CR 3 %: 7512237
	CR 5 %: 7605869
	CR 7.5 %, 10 % and 15 %: 7699501
Near wall cell size in m	10^{-7}
Number of spanwise tip cells	CR 3 %: 21
	CR 5 %: 25
	CR 7.5 %, 10 % and 15 %: 29
Inlet boundary conditions	
Total temperature in K	261.71
Total pressure in Pa	155850
Inflow angle in °	0
Turbulent intensity in %	5
Outlet boundary conditions	
Averaged static pressure in Pa	CR 3 %: 250000 - 375000
	CR 5 %: 250000 - 370000
	CR 7.5 %: 250000 - 355000
	CR 10 %: 250000 - 350000
	CR 15 %: 225000 - 336500
Solver parameters	
Fluid	R134a
Mathematical model	Turbulent Navier-Stokes
Turbulence model	Low Reynolds number shear-stress-transport
Rotating parts	Impeller and part of hub surface with 180 000 rpm
Solid boundary conditions	No-slip and adiabatic
CFL number	3
Coarse grid initialization	100 iterations on 2 coarser grids
Number of iterations	1000-1300 iterations on finest grid

Table B.1: Solver setup for scaling analysis of Schiffmanns [12, 13, 14, 15] compressor.

B.2 Modified friction model for turbomachinery provided by Casey and Robinson

The modified friction model suggested by Casey and Robinson [49] and Dietmann and Casey [50, 51] is based on the flat plate friction model provided by Gülich [48]. The Fanning friction factor c_f consists of a laminar part $c_{f,lam}$ and a turbulent part $c_{f,turb}$, which is calculated according Eq. B.1 and Eq. B.2, respectively.

$$c_{f,lam} = 2\frac{1.328}{\sqrt{Re}} \tag{B.1}$$

$$c_{f,turb} = \frac{0.136}{\left(log_{10}(0.2\epsilon + 12.5Re)\right)^{2.15}} \tag{B.2}$$

A factor p and an exponent t is calculated by Eq. B.3 and Eq. B.4.

$$p = \frac{1}{1+e^{-t}} \tag{B.3}$$

$$t = 5\left(\frac{c_{f,lam}}{c_{f,turb}} - 1\right) \tag{B.4}$$

Eventually, the Fanning friction factor is calculated according Eq. B.5. The Darcy-Weissbach friction factor f is calculated from the Fanning friction factor by applying $f = 4c_f$.

$$c_f = pc_{f,turb} + (1-p)c_{f,turb} \tag{B.5}$$

B.3 Shift of flow coefficient due to scaling

A physical explanation of the shift in flow coefficient based on the flat plate theory is given by Casey and Robinson [49]. It is assumed that the relative boundary layer thickness along the blade is modeled by Eq. B.6. The constant k_{const} is a factor which contains geometrical features.

$$\frac{\delta}{M} = k_{const}f \tag{B.6}$$

Hence, a change in boundary layer thickness is related to a change in friction factor what is shown in Eq. B.7.

$$\Delta\delta = Mk_{const}\Delta f \tag{B.7}$$

By considering the blockage as $k = \frac{\delta}{b_2}$, a change in blockage is given by Eq. B.8:

$$\Delta k = k_{const}\frac{M}{b_2}\Delta f \tag{B.8}$$

The change in flow coefficient is related to the change of blockage, what is given by Eq. B.9.

$$\frac{\Delta\phi_{t1}}{\phi_{t1}} = -\Delta k = -k_{const}\frac{M}{b_2}\Delta f = -C_{ref}\frac{\Delta f}{f_{ref}} \tag{B.9}$$

This in accordance with Eq. 1.12 presented in subsection 1.1.2.

C Appendix C

C.1 Solver setup for tip gap analysis

All important CFD solver parameters of the tip gap alteration analysis, which have been presented in chapter 4, are summarized in Table C.1 for the up-scaled compressor provided by Javed et al. [27]. The solver setup for the tip gap study of the compressor by Schiffmann [12, 13, 14, 15] is in accordance with Table B.1 and a scaling factor of 1.

General	
Components	Inlet duct, impeller and vaneless diffuser
Scaling factor	1
Relative clearance ratio in %	3, 5, 10, 14.73 and 20
Numerical model	Steady-state passage model (periodicity 8)
Grid	
Configuration	H-I-mesh (splitter configuration)
Number of grid points	CR 3 % and CR 5 %: 7970165 CR 10 %, 14.73 % and 20 %: 8157429
Near wall cell size in m	$5 \cdot 10^{-7}$
Number of spanwise tip cells	CR 3 % and CR 5 %: 17 CR 10 %, 14.73 % and 20 %: 25
Inlet boundary conditions	
Total temperature in K	276.15
Total pressure in Pa	272000
Inflow angle in °	0
Turbulent intensity in %	5
Outlet boundary conditions	
Averaged static pressure in Pa	CR 3 %: 500000 - 680000 CR 5 %: 500000 - 670000 CR 10 %: 500000 - 650000 CR 14.73 %: 500000 - 635000 CR 20 %: 500000 - 625000
Solver parameters	
Fluid	R134a
Mathematical model	Turbulent Navier-Stokes
Turbulence model	Low Reynolds number shear-stress-transport
Rotating parts	Impeller and part of hub surface with 50 000 rpm
Solid boundary conditions	No-slip and adiabatic
CFL number	3
Coarse grid initialization	100 iterations on 2 coarser grids
Number of iterations	1000-1300 iterations on finest grid

Table C.1: Solver setup for tip gap analysis of the up-scaled compressor provided by Javed et al. [27].

C.2 Experimental data of tip gap study

The time-averaged experimental data of each relative clearance ratio for the up-scaled compressor geometry by Javed et al. [27] are summarized in Table C.2 for a relative clearance ratio of 5 %, in Table C.3 for a relative clearance ratio of 10 % and in Table C.4 for a relative clearance ratio of 20 %. The experimental data of the baseline configuration having a relative clearance ratio of 14.73 % are summarized in Table A.3.

Nozzle Pos. [%]	$\dot{m}$ [kg/s]	T_{In} [K]	p_{In} [bar]	p_{TE} [bar]	p_{VLD} [bar]	T_{Out} [K]	p_{Out}[bar]
75	0.3367	265.76	1.619	3.298	3.959	300.11	3.724
80	0.3460	265.33	1.611	3.265	3.927	299.24	3.625
85	0.3521	265.11	1.602	3.216	3.877	298.64	3.554
90	0.3574	264.76	1.601	3.208	3.856	298.08	3.517
95	0.3641	264.29	1.598	3.173	3.825	297.27	3.434
100	0.3653	264.36	1.601	3.170	3.810	297.30	3.439

Table C.2: Time averaged experimental data for up-scaled compressor by Javed et al. [27] having a relative clearance ratio of 5 %.

Nozzle Pos. [%]	$\dot{m}$ [kg/s]	T_{In} [K]	p_{In} [bar]	p_{TE} [bar]	p_{VLD} [bar]	T_{Out} [K]	p_{Out}[bar]
55	0.2377	270.15	1.680	3.154	3.724	306.11	3.705
57.5	0.2478	269.00	1.674	3.307	3.946	305.24	3.919
60	0.2604	268.14	1.674	3.329	3.970	304.00	3.928
62.5	0.2704	267.56	1.667	3.327	3.970	303.04	3.895
65	0.2916	267.26	1.660	3.298	3.956	302.14	3.840
67.5	0.3050	266.95	1.657	3.284	3.933	301.28	3.752
70	0.3210	266.33	1.649	3.256	3.881	300.08	3.634
75	0.3352	265.98	1.638	3.198	3.815	299.00	3.512
80	0.3435	265.75	1.627	3.148	3.753	298.37	3.426
85	0.3501	265.14	1.617	3.115	3.703	297.41	3.332
90	0.3549	264.90	1.614	3.092	3.676	296.93	3.301
95	0.3627	264.75	1.619	3.073	3.660	296.51	3.262
100	0.3620	265.02	1.615	3.059	3.646	296.67	3.252

Table C.3: Time averaged experimental data for up-scaled compressor by Javed et al. [27] having a relative clearance ratio of 10 %.

Nozzle Pos. [%]	$\dot{m}$ [kg/s]	T_{In} [K]	p_{In} [bar]	p_{TE} [bar]	p_{VLD} [bar]	T_{Out} [K]	p_{Out}[bar]
52.5	0.1985	270.90	1.700	3.079	3.719	306.88	3.654
55	0.2095	270.33	1.690	3.165	3.759	305.76	3.713
57.5	0.2272	269.53	1.694	3.186	3.796	304.55	3.729
60	0.2385	268.46	1.690	3.200	3.811	303.20	3.726
62.5	0.2622	267.95	1.667	3.157	3.766	302.14	3.684
65	0.2752	267.84	1.662	3.150	3.741	301.55	3.579
67.5	0.2832	266.15	1.665	3.153	3.755	299.63	3.505
70	0.3009	264.34	1.665	3.144	3.726	297.34	3.442
75	0.3223	265.13	1.642	3.055	3.596	297.01	3.309
80	0.3302	264.75	1.632	3.011	3.556	296.13	3.178
85	0.3356	264.98	1.625	2.988	3.504	295.91	3.092
90	0.3401	265.60	1.623	2.966	3.483	296.27	3.057
95	0.3463	265.54	1.625	2.940	3.467	295.93	3.051
100	0.3465	265.62	1.623	2.932	3.444	295.96	3.046

Table C.4: Time averaged experimental data for up-scaled compressor by Javed et al. [27] having a relative clearance ratio of 20 %.

C.3 Performance and error analysis of tip gap study

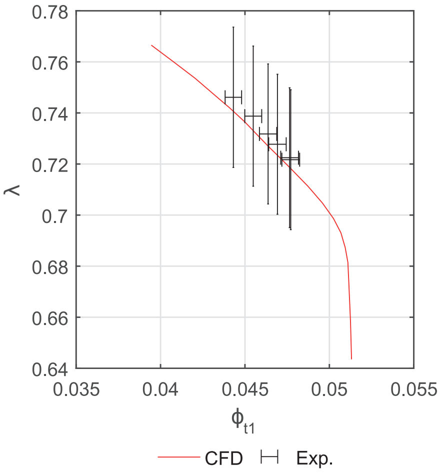

Figure C.1: Comparison of experimentally and numerically determined work input coefficient for scaled up compressor by Javed et al. [27] with CR = 5%.

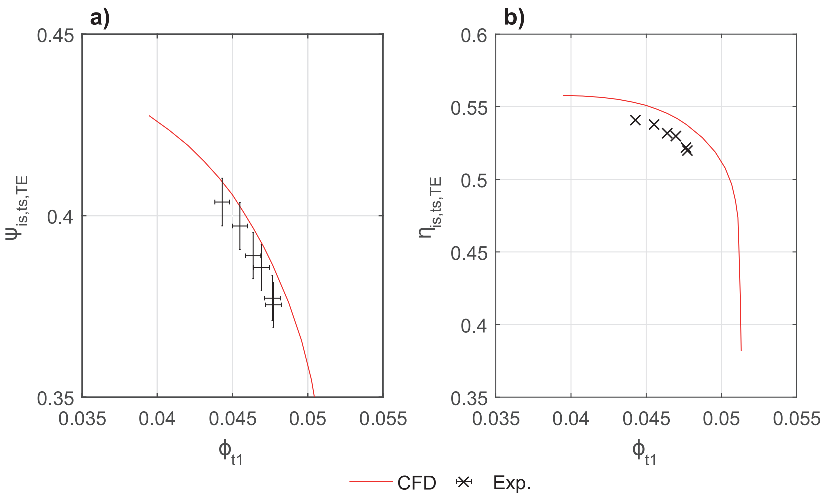

Figure C.2: Comparison of numerically and experimentally determined total-static isentropic head coefficient (a) and efficiency (b) for scaled up compressor by Javed et al. [27] with CR = 5% at 105 % of d_2.

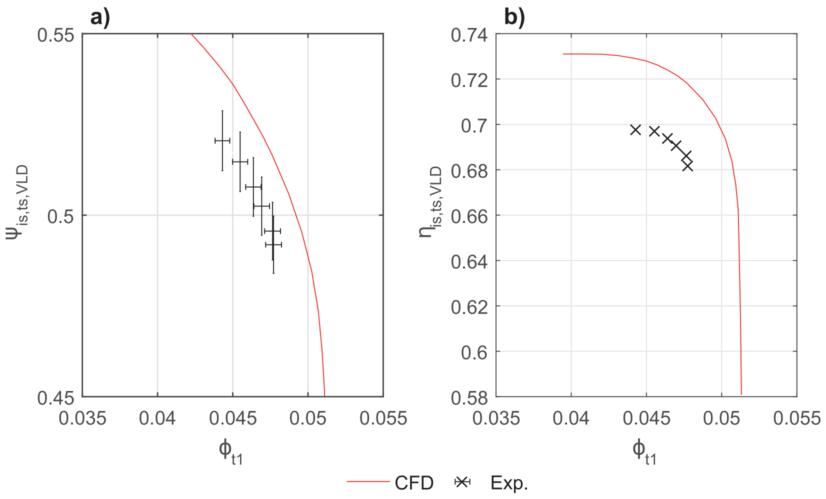

Figure C.3: Comparison of numerically and experimentally determined total-static isentropic head coefficient (a) and efficiency (b) for scaled up compressor by Javed et al. [27] with CR = 5% at outlet of vaneless diffuser.

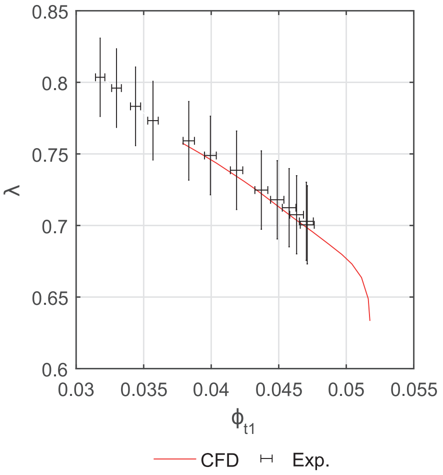

Figure C.4: Comparison of experimentally and numerically determined work input coefficient for scaled up compressor by Javed et al. [27] with CR = 10%.

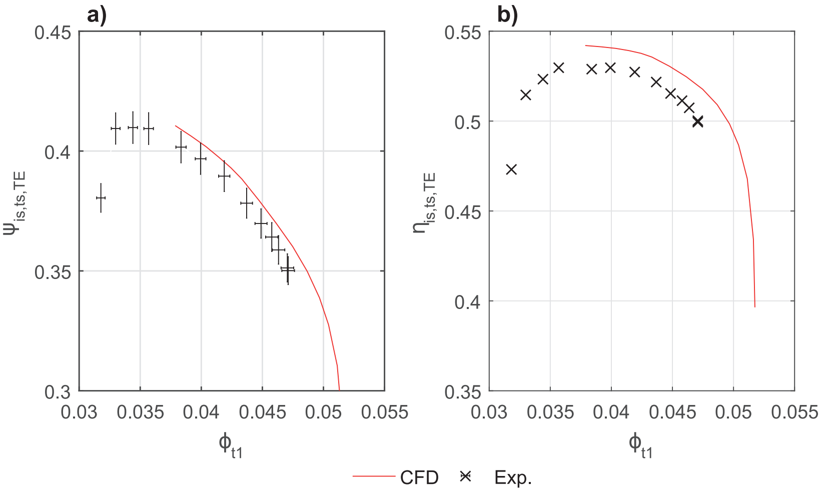

Figure C.5: Comparison of numerically and experimentally determined total-static isentropic head coefficient (a) and efficiency (b) for scaled up compressor by Javed et al. [27] with CR = 10% at 105 % of d_2.

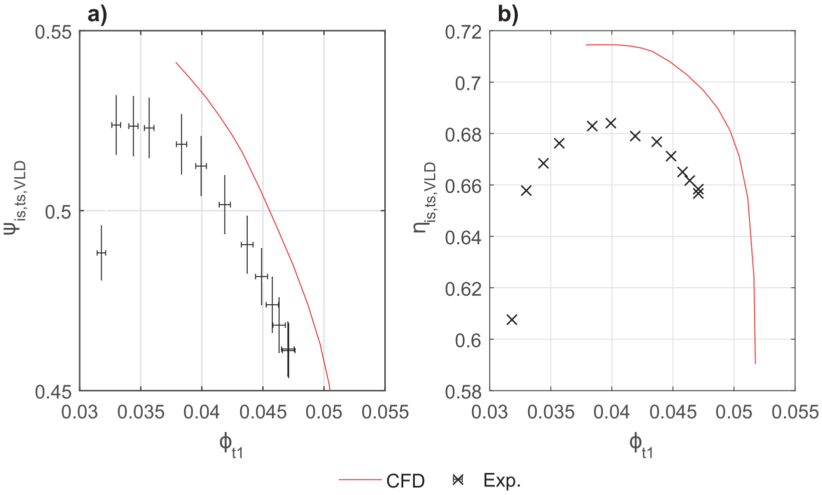

Figure C.6: Comparison of numerically and experimentally determined total-static isentropic head coefficient (a) and efficiency (b) for scaled up compressor by Javed et al. [27] with CR = 10% at outlet of vaneless diffuser.

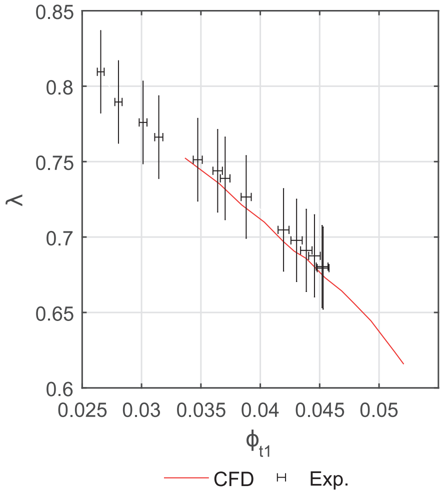

Figure C.7: Comparison of experimentally and numerically determined work input coefficient for scaled up compressor by Javed et al. [27] with CR = 20%.

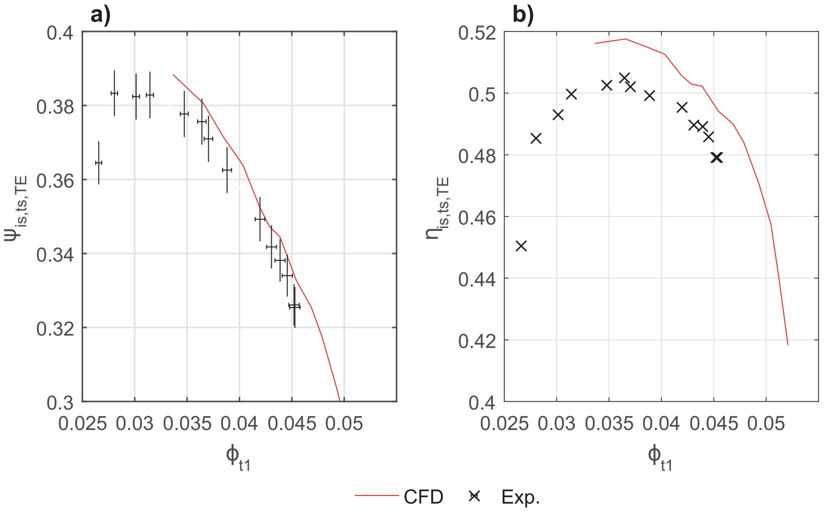

Figure C.8: Comparison of numerically and experimentally determined total-static isentropic head coefficient (a) and efficiency (b) for scaled up compressor by Javed et al. [27] with CR = 20% at 105 % of d_2.

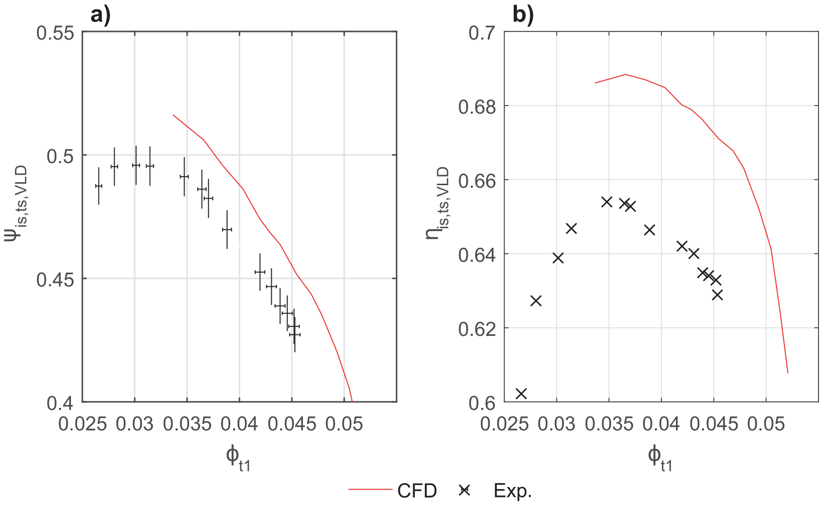

Figure C.9: Comparison of numerically and experimentally determined total-static isentropic head coefficient (a) and efficiency (b) for scaled up compressor by Javed et al. [27] with CR = 20% at outlet of vaneless diffuser.

D Appendix D

D.1 Different loading distributions

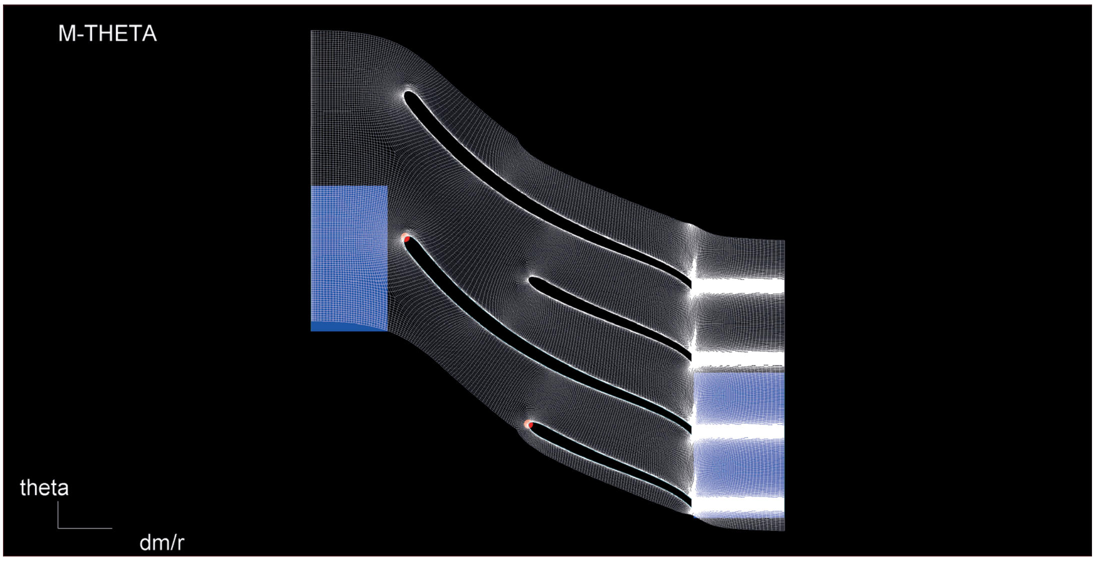

Figure D.1: Aft-loaded shroud configuration at 90 % blade span shown in a conformal plot (viewing direction: from hub).

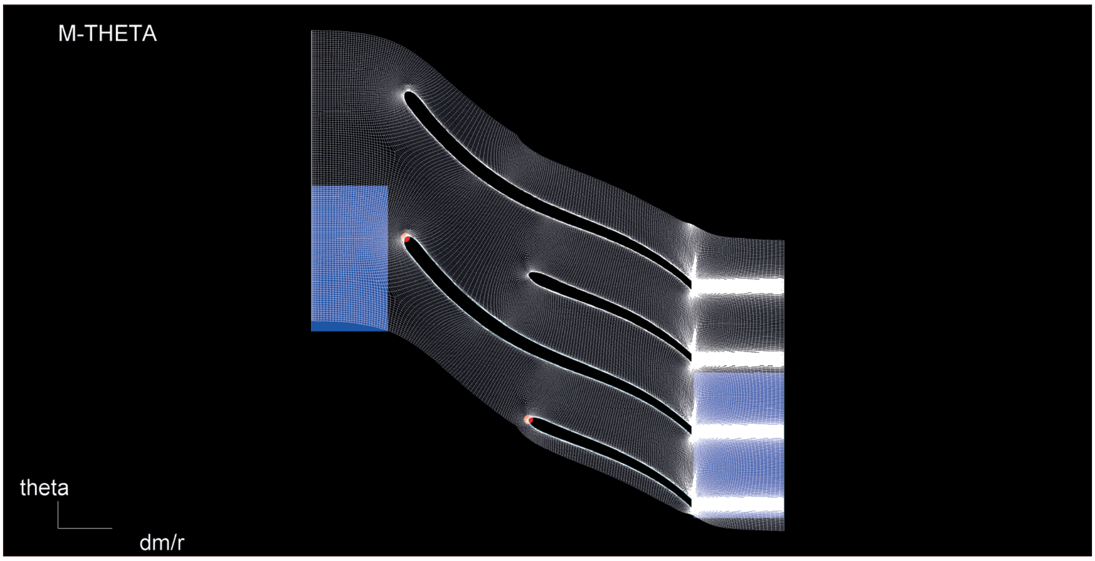

Figure D.2: Mid-loaded shroud configuration at 90 % blade span shown in a conformal plot (viewing direction: from hub).

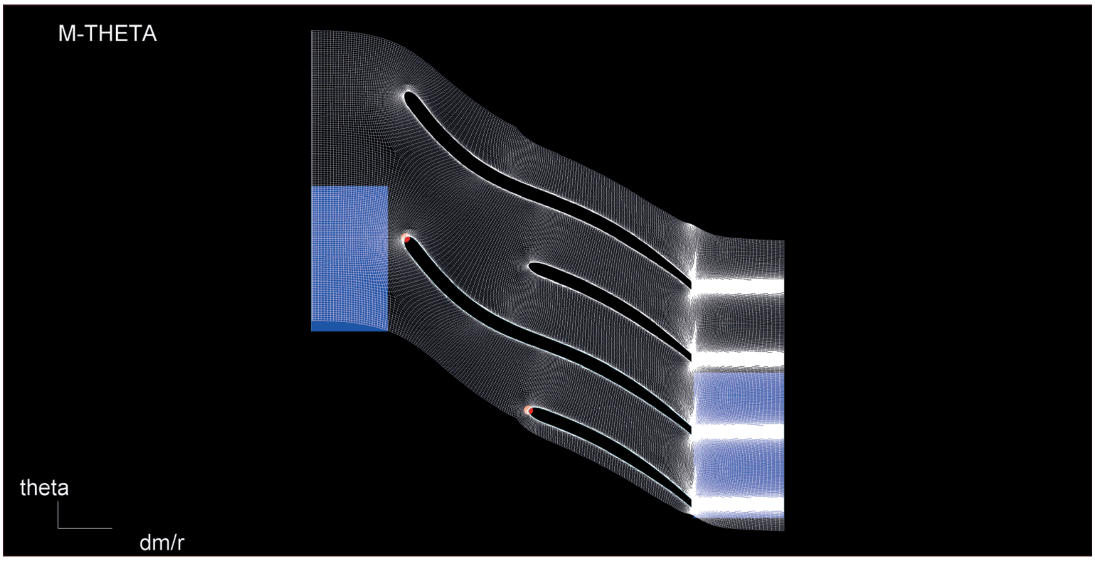

Figure D.3: Front-loaded shroud configuration at 90 % blade span shown in a conformal plot (viewing direction: from hub).

D.2 Solver setup for loading study

The CFD solver setup for the loading study in terms of aft-, mid- and front-loaded shroud loading distribution is summarized in Table D.1.

	General
Components	Inlet duct, impeller and vaneless diffuser
Scaling factor	1
Relative clearance ratio in %	14.73
Numerical model	Steady-state passage model (periodicity 8)
	Grid
Configuration	H-I-mesh (splitter configuration)
Number of grid points	8157429
Near wall cell size in m	$5 \cdot 10^{-7}$
Number of spanwise tip cells	17
	Inlet boundary conditions
Total temperature in K	276.15
Total pressure in Pa	272000
Inflow angle in °	0
Turbulent intensity in %	5
	Outlet boundary conditions
Averaged static pressure in Pa	500000 - 640000
	Solver parameters
Fluid	R134a
Mathematical model	Turbulent Navier-Stokes
Turbulence model	Low Reynolds number shear-stress-transport
Rotating parts	Impeller and part of hub surface with 50 000 rpm
Solid boundary conditions	No-slip and adiabatic
CFL number	3
Coarse grid initialization	100 iterations on 2 coarser grids
Number of iterations	1000-1300 iterations on finest grid

Table D.1: Solver setup for the shroud blade loading investigation applied for the aft-, the mid- and the front-loaded configuration.

D.3 Experimental data of loading study

The time-averaged experimental data for the aft-loaded, mid-loaded and front-loaded shroud loading configurations are summarized in Table D.2, Table D.3 and Table D.4.

Nozzle Pos. [%]	$\dot{m}$ [kg/s]	T_{In} [K]	p_{In} [bar]	p_{TE} [bar]	p_{VLD} [bar]	T_{Out} [K]	p_{Out}[bar]
52.5	0.2235	270.46	1.695	3.078	3.768	306.58	3.655
55	0.2300	269.49	1.688	3.171	3.855	305.66	3.822
57.5	0.2383	268.81	1.681	3.234	3.896	304.72	3.849
60	0.2506	268.00	1.668	3.224	3.889	303.64	3.831
62.5	0.2653	267.78	1.655	3.206	3.861	302.92	3.763
65	0.2771	267.01	1.641	3.173	3.830	301.80	3.706
67.5	0.2919	266.53	1.629	3.136	3.778	300.76	3.637
70	0.3089	265.87	1.623	3.103	3.723	299.40	3.531
75	0.3230	265.53	1.620	3.077	3.669	298.33	3.401
80	0.3312	265.11	1.618	3.060	3.643	297.47	3.327
85	0.3405	264.88	1.607	3.006	3.582	296.63	3.226
90	0.3495	264.35	1.602	2.982	3.544	295.67	3.158
95	0.3532	264.59	1.600	2.965	3.509	295.71	3.146
100	0.3541	264.74	1.601	2.963	3.507	295.78	3.145

Table D.2: Time averaged experimental data for the up-scaled compressor having an aft-loaded shroud loading distribution.

Nozzle Pos. [%]	$\dot{m}$ [kg/s]	T_{In} [K]	p_{In} [bar]	p_{TE} [bar]	p_{VLD} [bar]	T_{Out} [K]	p_{Out}[bar]
52.5	0.2189	270.32	1.687	308.5	3.749	306.26	3.627
55	0.2277	269.56	1.687	3.184	3.850	305.56	3.811
57.5	0.2370	268.93	1.682	3.257	3.898	304.76	3.848
60	0.2497	268.20	1.672	3.255	3.899	303.73	3.833
62.5	0.2697	267.67	1.655	3.226	3.874	302.52	3.760
65	0.2785	267.33	1.644	3.198	3.835	301.82	3.704
67.5	0.2916	266.90	1.631	3.152	3.781	300.85	3.631
70	0.3085	266.39	1.628	3.124	3.727	299.59	3.528
75	0.3239	265.83	1.618	3.071	3.662	298.25	3.392
80	0.3332	265.47	1.614	3.052	3.635	297.46	3.308
85	0.3401	265.09	1.603	3.016	3.583	296.67	3.213
90	0.3462	264.88	1.599	2.991	3.549	296.06	3.149
95	0.3504	264.76	1.599	2.984	3.529	295.82	3.139
100	0.3505	264.86	1.599	2.982	3.527	295.88	3.139

Table D.3: Time averaged experimental data for the up-scaled compressor having a mid-loaded shroud loading distribution.

Nozzle Pos.	$\dot{m}$ [kg/s]	T_{In} [K]	p_{In} [bar]	p_{TE} [bar]	p_{VLD} [bar]	T_{Out} [K]	p_{Out}[bar]
55	0.2261	269.88	1.694	3.095	3.860	306.68	3.788
57.5	0.2326	269.23	1.681	3.167	3.889	305.86	3.788
60	0.2436	268.46	1.676	3.205	3.911	304.89	3.803
62.5	0.2628	268.10	1.657	3.167	3.877	303.88	3.759
65	0.2733	267.69	1.650	3.146	3.853	303.22	3.717
67.5	0.2848	267.13	1.636	3.111	3.806	302.05	3.609
70	0.3023	266.56	1.627	3.072	3.735	300.67	3.492
75	0.3169	266.09	1.618	3.021	3.676	299.54	3.407
80	0.3246	265.77	1.611	2.986	3.625	298.70	3.294
85	0.3323	265.14	1.603	2.956	3.589	297.70	3.217
90	0.3399	264.99	1.601	2.930	3.550	297.09	3.161
95	0.3457	265.09	1.600	2.909	3.526	296.88	3.134
100	0.3454	265.32	1.599	2.904	3.521	297.11	3.128

Table D.4: Time averaged experimental data for the up-scaled compressor having a front-loaded shroud loading distribution.

D.4 Performance and error analyis of loading study

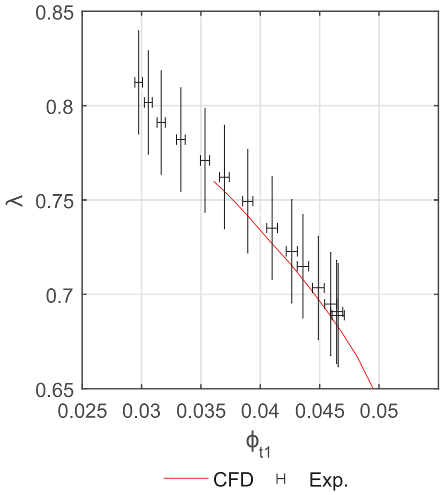

Figure D.4: Comparison of experimentally and numerically determined work input coefficient for aft-loaded shroud loading configuration with CR = 14.73%.

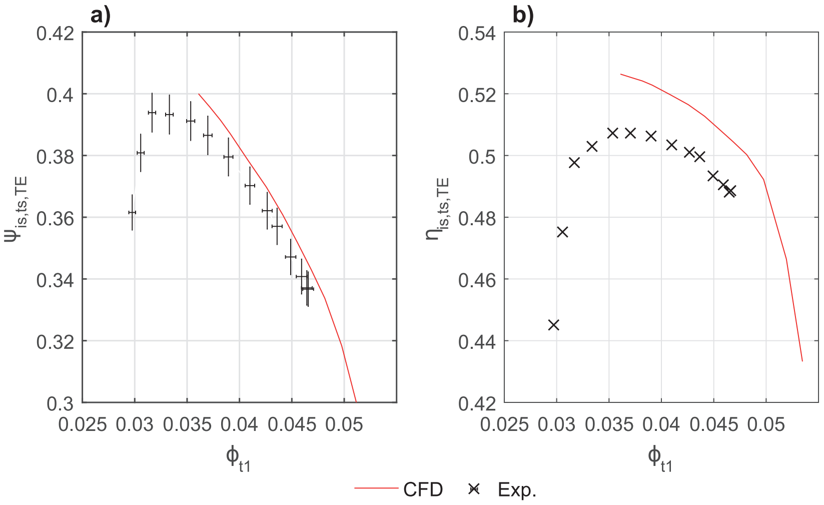

Figure D.5: Comparison of numerically and experimentally determined total-static isentropic head coefficient (a) and efficiency (b) for aft-loaded shroud loading configuration with CR = 14.73% at 105 % of d_2.

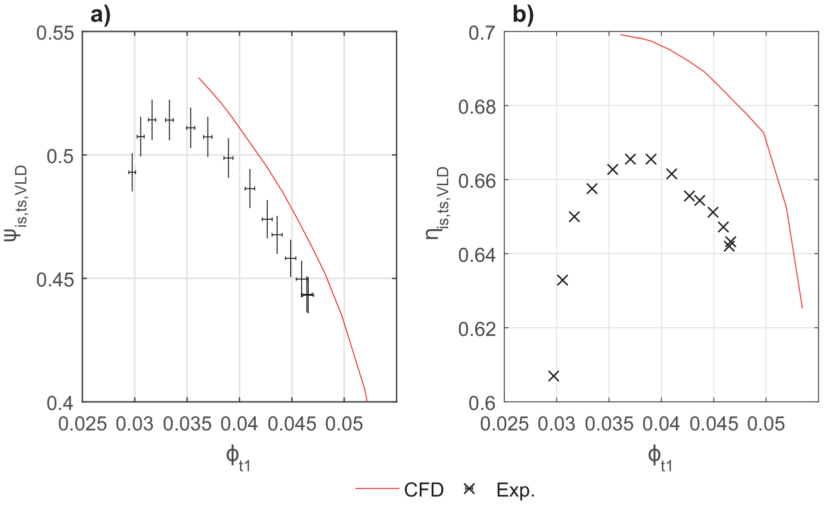

Figure D.6: Comparison of numerically and experimentally determined total-static isentropic head coefficient (a) and efficiency (b) for aft-loaded shroud loading configuration with CR = 14.73% at outlet of vaneless diffuser.

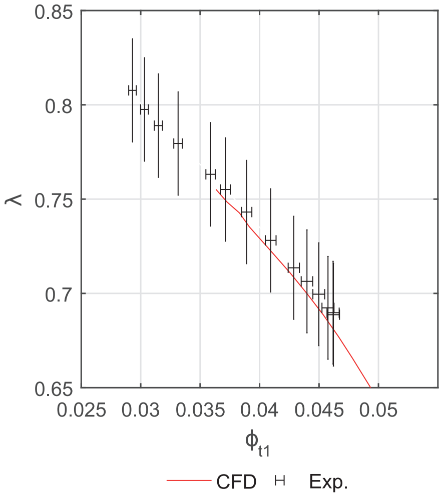

Figure D.7: Comparison of experimentally and numerically determined work input coefficient for mid-loaded shroud loading configuration with CR = 14.73%.

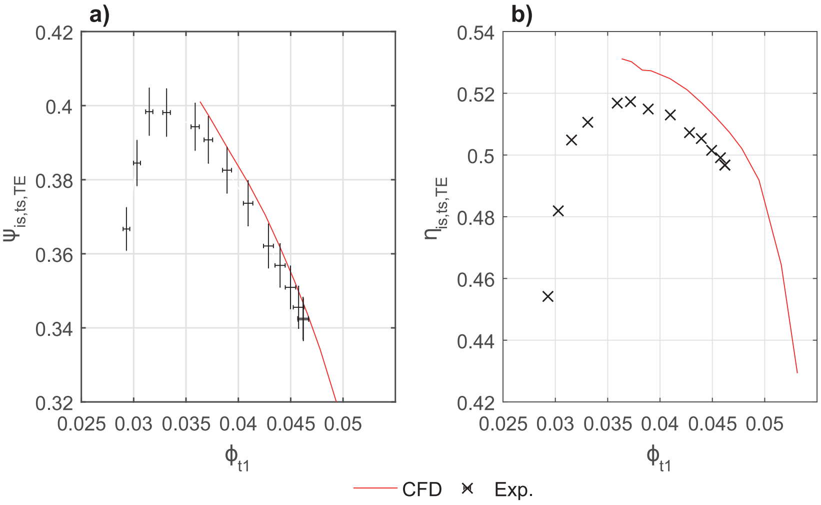

Figure D.8: Comparison of numerically and experimentally determined total-static isentropic head coefficient (a) and efficiency (b) for mid-loaded shroud loading configuration with CR = 14.73% at 105 % of d_2.

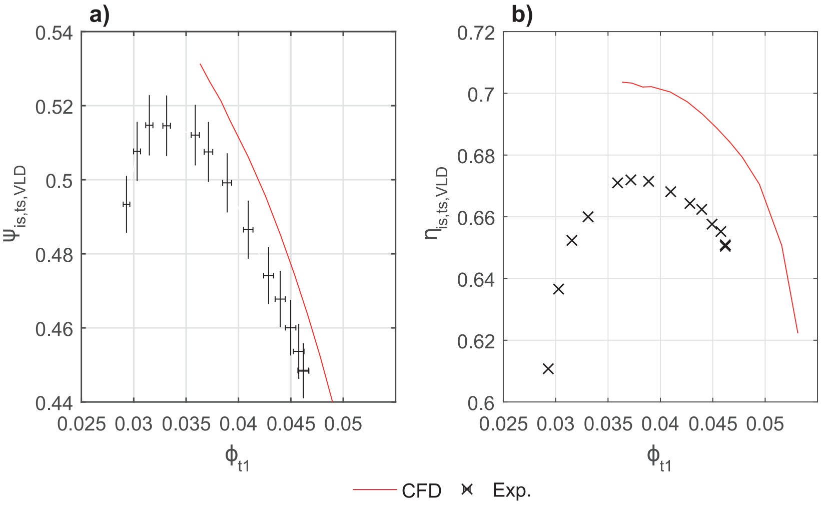

Figure D.9: Comparison of numerically and experimentally determined total-static isentropic head coefficient (a) and efficiency (b) for mid-loaded shroud loading configuration with CR = 14.73% at outlet of vaneless diffuser.

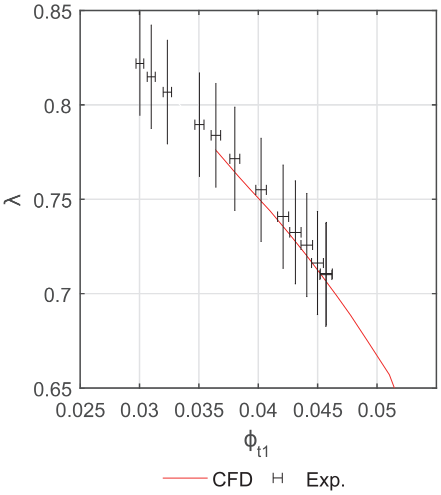

Figure D.10: Comparison of experimentally and numerically determined work input coefficient for front-loaded shroud loading configuration with CR = 14.73%.

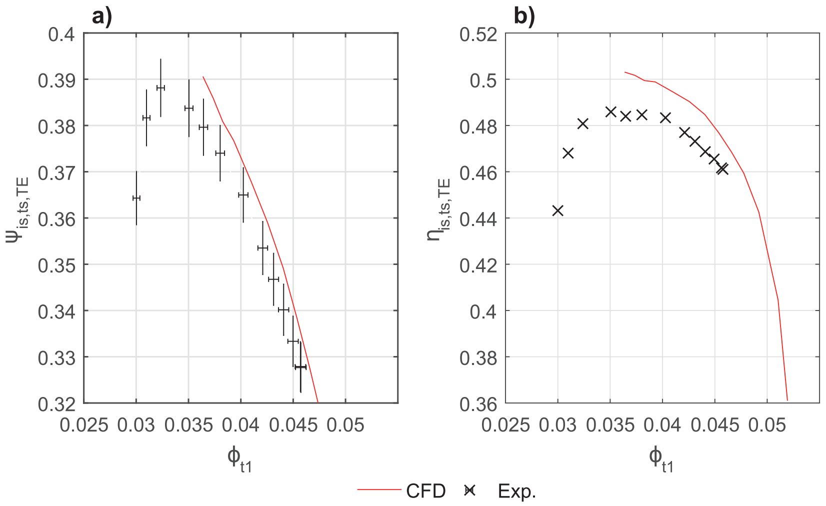

Figure D.11: Comparison of numerically and experimentally determined total-static isentropic head coefficient (a) and efficiency (b) for front-loaded shroud loading configuration with CR = 14.73% at 105 % of d_2.

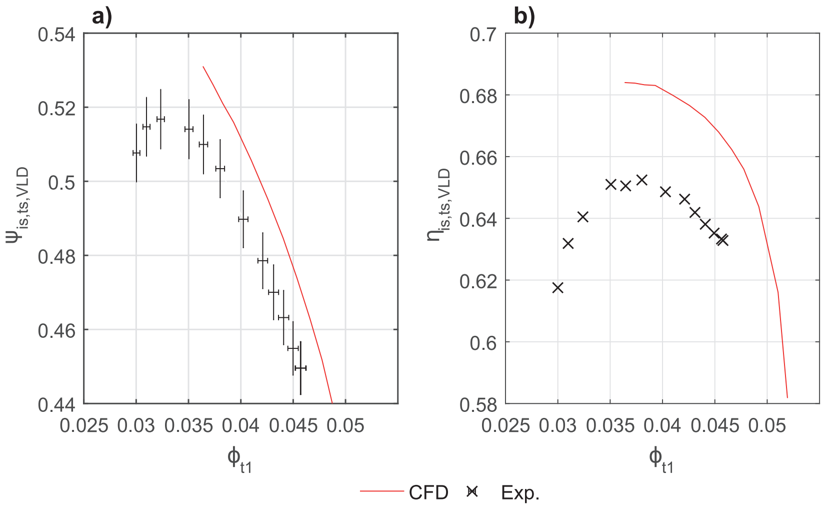

Figure D.12: Comparison of numerically and experimentally determined total-static isentropic head coefficient (a) and efficiency (b) for front-loaded shroud loading configuration with CR = 14.73% at outlet of vaneless diffuser.

D.5 Isentropic Mach number distribution on blade surfaces

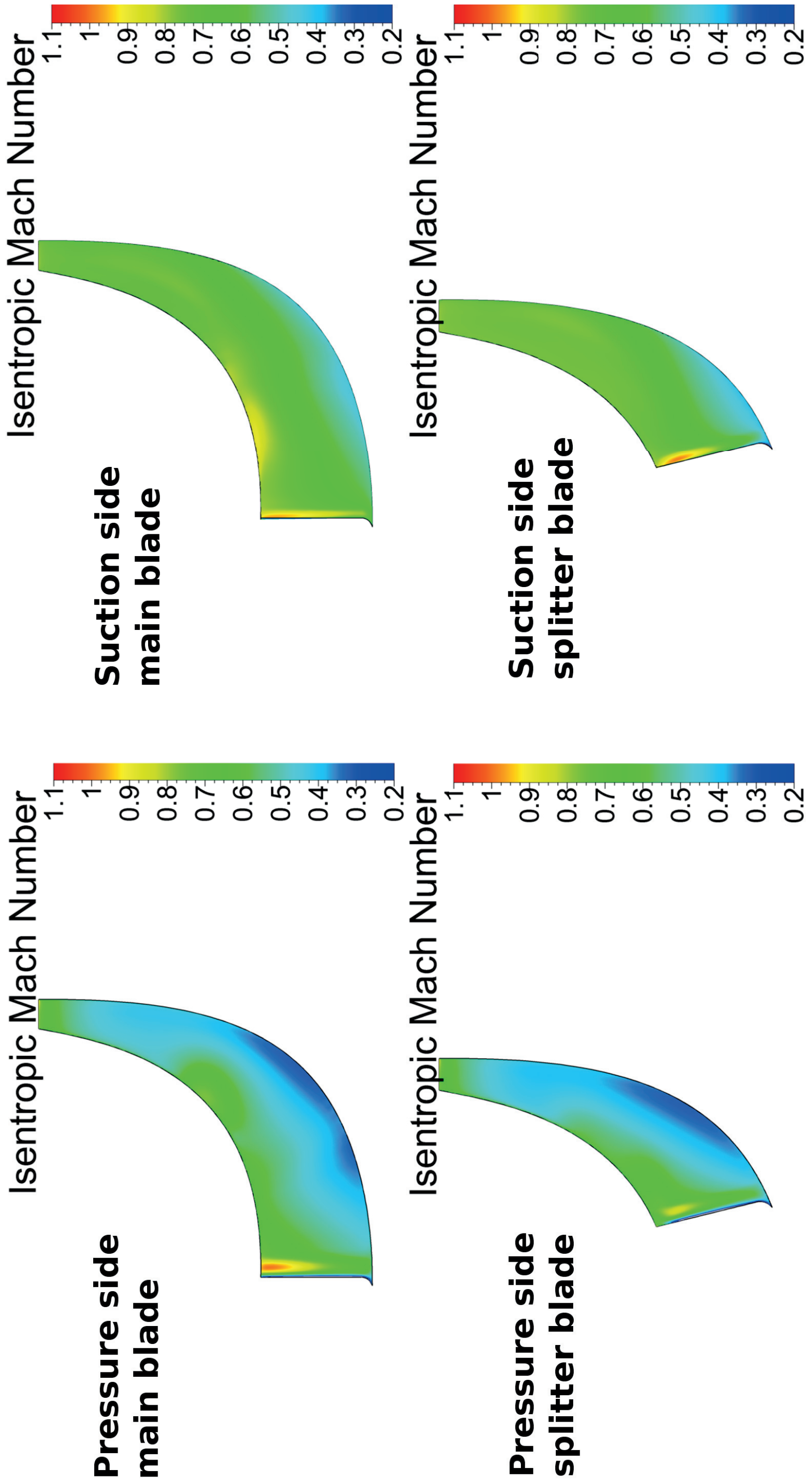

Figure D.13: Isentropic Mach number distribution on the blade surfaces for the scaled up compressor by Javed et al. [27] at its design point.

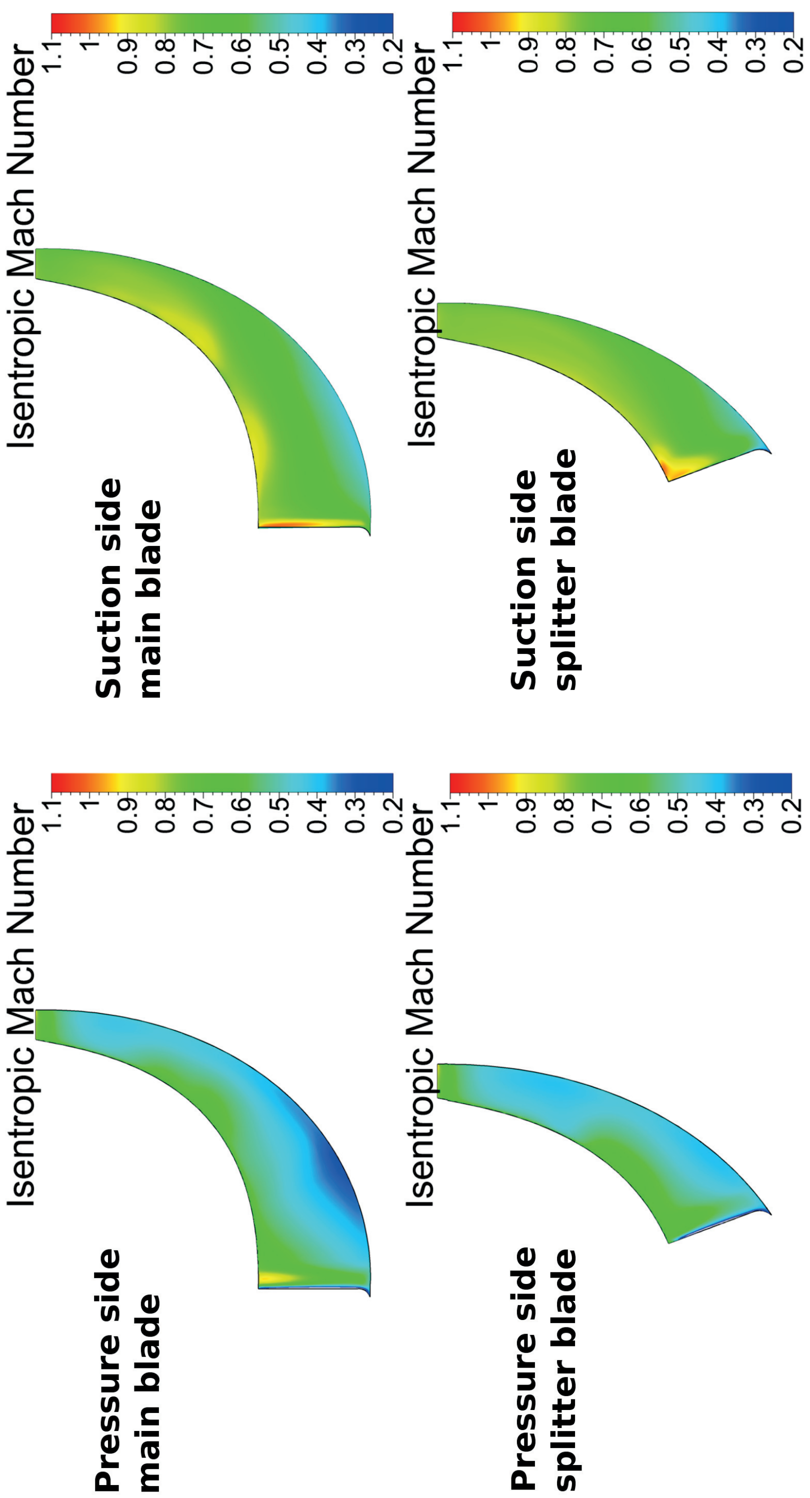

Figure D.14: Isentropic Mach number distribution on the blade surfaces for the aft-loaded shroud loading configuration at its design point.

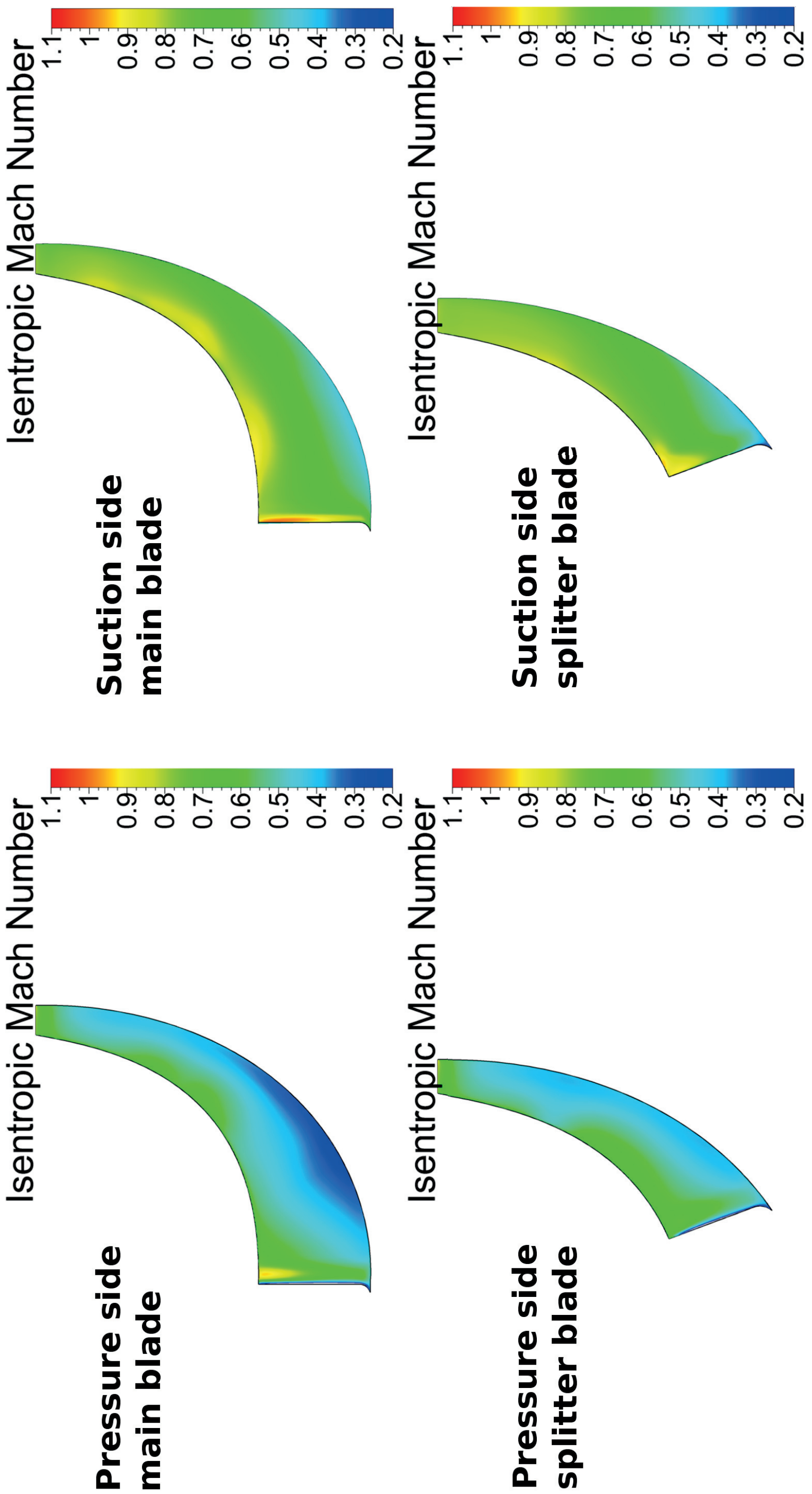

Figure D.15: Isentropic Mach number distribution on the blade surfaces for the mid-loaded shroud loading configuration at its design point.

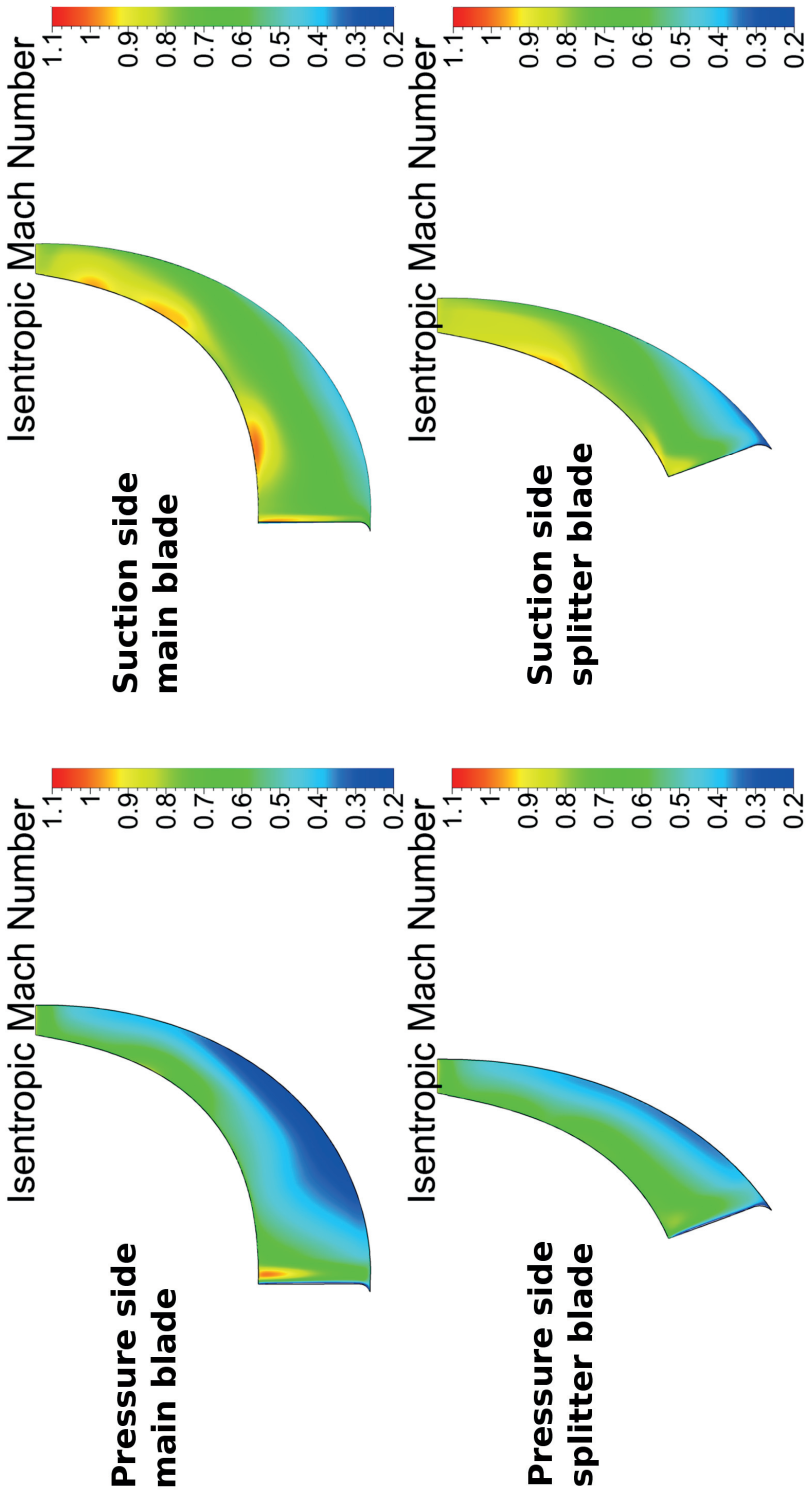

Figure D.16: Isentropic Mach number distribution on the blade surfaces for the front-loaded shroud loading configuration at its design point.

Bibliography

[1] G. C. van Kooten. *Climate Change, Climate Science and Economics: Prospects for an Alternative Energy Future*. Springer, 2012.

[2] M. Herzberg, A. Siddons, and H. Schreuder. Role of greenhouse gases in climate change. *Energy Environment*, 28:530–539, April 2017.

[3] S. K. Ritter and M. Mann. Global warming and climate change: Believers, deniers, and doubters view the scientific forecast from different angles. *Chemical Engineering News*, 87(51):11–21, December 2009.

[4] O. Edenhofer, R. Pichs-Madruga, Y. Sokona, K. Seyboth, P. Matschoss, S. Kadner, T. Zwickel, P. Eickemeier, G. Hansen, S. Schlömer, and C. von Stechow. Special report on renewable energy sources and climate change mitigation. Technical report, Potsdam Institute for Climate Impact Research (PIK), 2012.

[5] J. A. Turner. A realizable renewable energy future. *Science*, 285:687–689, July 1999.

[6] P. Denholm, E. Ela, B. Kirby, and M. Milligan. Role of energy storage with renewable electricity generation. Technical report, National Renewable Energy Lab. (NREL), Golden, CO (United States), January 2010.

[7] M. Beaudin, H. Zareipour, A. Schellenberglabe, and W. Rosehart. Energy storage for mitigating the variability of renewable electricity sources: An updated review. *Energy for Sustainable Development*, 14:302–314, December 2010.

[8] M. Aneke and M. Wang. Energy storage technologies and real life applications – a state of the art review. *Applied Energy*, 179:350–377, October 2016.

[9] L. Hancher, A. de Hauteclocque, and M. Sadowska. *Capacity mechanisms in the EU energy market.* Oxford University Press, 2015.

[10] D. Connolly, H. Lundb, B. V. Mathiesen, E. Picana, and M. Leahya. The technical and economic implications of integrating fluctuating renewable energy using energy storage. *Renewable Energy*, 43:47–60, July 2012.

[11] S. R. Bull. Renewable energy today and tomorrow. *Proceedings of the IEEE*, 89:1216–1226, August 2001.

[12] J. A. Schiffmann. *Integrated design, optimization and experimental investigation of a direct driven turbocompressor for domestic heat pumps.* PhD Thesis, École Polytechique Fédérale de Lausanne, Lausanne, Switzerland, 2008.

[13] J. Schiffmann and D. Favrat. Experimental investigation of a direct driven radial compressor for domestic heat pumps. *International Journal of Refrigeration*, 32(8):1918–1928, 2009.

[14] J. Schiffmann and D. Favrat. Design, experimental investigation and multi-objective optimization of a small-scale radial compressor for heat pump applications. *Energy*, 35(1):436–450, 2010.

[15] J. Schiffmann. Integrated design and multi-objective optimization of a single stage heat-pump turbocompressor. *Journal of Turbomachinery (ASME)*, 137(7):071002–071002–9, 2015.

[16] B. T. Sirakov. *Characterization and Design of Non-Adiabatic Micro-Compressor Impeller and Preliminary Design of Self-Sustained Micro Engine System.* PhD Thesis, Massachusetts Institute of Technology, Boston, USA, 2005.

[17] J. Demierre, A. Rubino, and J. A. Schiffmann. Modeling and experimental investigation of an oil-free microcompressor-turbine unit for an organic Rankine cycle driven heat pump. *ASME Journal of Engineering for Gas Turbines and Power*, 137, October 2014.

[18] V. Mounier and J. A. Schiffmann. ORC driven heat pump running on gas bearings for domestic applications: Proof of concept and thermo-economic improvement potential. In *12th IEA heat Pump Conference 2017*, Rotterdam, May 2017.

[19] V. Mounier. *Potential and Challenges of ORC driven Heat Pumps Based on Gas Bearing Supported Turbomachinery.* PhD Thesis, École Polytechique Fédérale de Lausanne, Lausanne, Switzerland, 2018.

[20] P. H. Wagner. *Integrated Design, Optimization, and Experimental Realization of a Steam-Driven Micro Recirculation Fan for Solid Oxide Fuel Cell Systems.* PhD Thesis, École Polytechique Fédérale de Lausanne, Lausanne, Switzerland, 2019.

[21] P. H. Wagner, Z. Wuillemin, S. Diethelm, J. Van Herle, and J. Schiffmann. Modeling and designing of a radial anode off-gas recirculation fan for solid oxide fuel cell systems. *Journal of Electrochemical Energy Conversion and Storage*, 14, October 2017.

[22] Z. Schabowski and H. Hodson. The reduction of over tip leakage loss in unshrouded axial turbines using winglets and squealers. *Journal of Turbomachinery*, 136, September 2013.

[23] E. M. Greitzer, C. S. Tan, and M. B. Graf. *Internal Flow.* Cambridge University Press, 2004.

[24] J. H. Spurk and N. Aksel. *Strömungslehre.* Springer, 2010. (in German).

[25] S. Kang and C. Hirsch. Numerical simulation and theoretical analysis of the 3D viscous flow in centrifugal impellers. Technical Report 4, Vrije Universireit Brussels, Department of Fluid Mechanics, Pleinlaan 2, 1050 Brussels, Belgium, July 2001.

[26] S. Kang and C. Hirsch. Influence of tip leakage flow in centrifugal compressors. In *3rd ISAIF Beijing*, pages 186–194, 1996.

[27] A. Javed, C. Arpagaus, S Bertsch, and J. Schiffmann. Small-scale turbocompressors for wide-range operation with large tip clearances for a two-stage heat pump concept. *International Journal of Refrigeration*, 69:285–302, September 2016.

[28] G. T. Chen, E. M. Greitzer, C. S. Tan, and F. E. Marble. Similarity analysis of compressor tip clearance flow structure. *Transactions of the ASME: Journal of Turbomachinery*, 113:260–269, April 1991.

[29] C. Pfleiderer and H. Petermann. *Strömungsmaschinen.* Springer, 1991. (in German).

[30] B. Eckert and E. Schnell. *Axial -und Radialkompressoren.* Springer, 1961. (in German).

[31] R. Pampreen. Small turbomachinery compressor and fan aerodynamics. *Transactions of ASME: Journal of Engineering for Power*, 95:251–246, July 1973.

[32] P. Schmidt-Theuner and J. Mattern. The effect of Reynolds number and clearance in the centrifugal compressor of a turbocharger. *The Brown Boveri Review*, 55(8):453–456, 1968.

[33] J. J. Brasz. Investigation into the effect of tip clearance on centrifugal compressor performance. In *ASME - Gas Turbine and Aeroengine Congress*, Amsterdam, June 1988.

[34] Y. Senoo and M. Ishida. Deterioration of compressor performance due to tip clearance of centrifugal impellers. *Transactions of ASME: Journal of Turbomachinery*, 109:55–61, January 1987.

[35] Y. Senoo and M. Ishida. Pressure loss due to the tip clearance of impeller blades in centrifugal and axial blowers. *Transactions of ASME: Journal of Engineering for Gas Turbines and Power*, 108:32–37, January 1986.

[36] J. A. Storer and N. A. Cumpsty. An approximate analysis and prediction method for tip clearance loss in axial compressors. *Transactions of ASME: Journal of Turbomachinery*, 116:648–656, October 1994.

[37] J. D. Denton. Loss mechanisms in turbomachines. *Transactions of the ASME: Journal of Turbomachinery*, 115:621–656, October 1993.

[38] S. Aknouche. *Impact of Tip Clearance Flow on Centrifugal Pump Impeller Performance.* PhD Thesis, Massachusetts Institute of Technology (MIT), Boston, USA, June 2003.

[39] H. Harada. Performance characteristics of shrouded and unshrouded impellers of a centrifugal compressor. *Transactions of the ASME: Journal of Engineering for Gas Turbines and Power*, 107:528–533, April 1985.

[40] P. Dalbert, B. Ribi, T. Kmecl, and M. V. Casey. Radial compressor design for industrial compressors. *Proceedings of the Institution of Mechanical Engineers, Part C: Journal of Mechanical Engineering Science*, January 1999.

[41] R. C. Dean and Y. Senoo. Rotating wakes in vaneless diffusers. *Transactions of the ASME: Journal of Basic Engineering*, 82, September 1960.

[42] C. P. Hamkins and R. D. Flack. Laser velocity measurements in shrouded and unshrouded radial flow pump impellers. *Transactions of the ASME: Journal of Turbomachinery*, 109:70–76, January 1987.

[43] C. Offtinger, C. Henry, R. Morel, and F. Spettel. Experimental comparison of flow fields at the inlet and the outlet of an inducer with shrouded and unshrouded configurations. *Transactions of ASME: Journal of Fluids Engineering*, 119:954–959, December 1997.

[44] L. F. Moody. Friction factors for pipe flow. *ASME Transactions*, 66:671–684, 1944.

[45] R. Aungier. *Centrifugal Compressors - A Strategy for Aerodynamic Design and Analysis*. ASME-Press, 2000.

[46] A. Whitfield and N. C. Baines. *Design of Radial Turbomachines*. Longman Scientific Technical, 1990.

[47] K. H. Lüdtke. *Process Centrifugal Compressors: Basics, Function, Operation, Design, Application*. Springer, 2004.

[48] J. F. Gülich. Effect of Reynolds number and surface roughness on the efficiency of centrifugal pumps. *Transactions of ASME: Journal of Fluids Engineering*, 125:670–679, July 2003.

[49] M. Casey and C. Robinson. A unified correction method for Reynolds number, size and roughness effects on the performance of compressors. In F. Martelli, F. Heitmeir, and M. Manna, editors, *9th Europ. Conf. on Turbomachinery, Fluid Dynamics and Thermodynamics*, March 2011.

[50] F. Dietmann and M. Casey. The effects of reynolds number and roughness on compressor performance. In *10th Europ. Conf. on Turbomachinery, Fluid Dynamics and Thermodynamics-ETC10 Lapeenranta*, 2013.

[51] F. Dietmann. *Zum Einfluss der Reynolds-Zahl und Oberflächenrauigkeit bei thermischen Turbokompressoren*. PhD Thesis, Universität Stuttgart, Stuttgart, Germany, April 2016. (in German).

[52] L. F. Moody. The propeller type turbine. *ASCE Transportation Engineering*, 89:625–647, 1926.

[53] M. Medici. Modellversuche an Francisturbinen. *Wasserkraft und Wasserwirtschaft*, 38:272–275, 1943.

[54] T. Wright. Comments on compressor efficiency scaling with Reynolds number and relative roughness. Technical report, American Soc. of Mech. Eng., 1989.

[55] R. A. Strub, L. Bonciani, C. J. Borer, M. V. Casey, S. L. Cole, B. B. Cook, J. Kotzur, H. Simon, and M. A. Strite. Influence of the Reynolds number on the performance of centrifugal compressors. *Final Report Working Group Process Compressor Sub-Committee International Compressed Air and Allied Machinery Committee (ICAAMC)*, 1987.

[56] W. Traupel. *Thermische Turbomaschinen*. Springer, 1988. (in German).

[57] A. S. Sowayan. Effect of heat losses on the thermodynamics of compression process. *International Journal of Applied Engineering Research*, 6(7):979–987, 2011.

[58] Y. Gong, B. T. Sirakov, A. H. Epstein, and C. S. Tan. Aerothermodynamics of micro-turbomachinery. *Proceedings of ASME TurboExpo 2004: Power for Land, Sea and Air*, June 2004.

[59] S. Shaaban and J. R. Seume. Analysis of turbocharger non-adiabatic performance. Technical report, University of Hannover; Turbomachinery Laboratory, 2006.

[60] M. V. Casey and T. M. Fesich. On the efficiency of turbocharger compressors with diabatic flows. *Transactions of the ASME: Journal of Engineering for Gas Turbines and Power*, 132:072302–1–072302–9, July 2010.

[61] B. T. Sirakov and M. V. Casey. Evaluation of heat transfer effects on turbocharger performance. *Transactions of the ASME: Journal of Turbomachinery*, 135:021011–1–021011–10, March 2013.

[62] A. Yamagata, S. Nagai, K. Nakano, and T. Kawakubo. Prediction and measurement of turbocharger compressor wheel temperature. In *8th International Conference on Turbochargers and Turbocharging*, December 2006.

[63] D. Bohn, T. Heuer, and K. Kusterer. Conjugate flow and heat transfer investigation of a turbocharger. *Transactions of the ASME: Journal of Engineering for Gas Turbines and Power*, 127:663–669, July 2005.

[64] Y. Ma and G. Xi. Effects of Reynolds number and heat transfer on scaling of a centrifugal compressor impeller. In *Proceedings of ASME Turbo Expo 2010: Power for Land, Sea and Air*, Glasgow, June 2010.

[65] M. V. Casey. Lecture notes of Turbokompressoren und Ventilatoren (TKV), 2012/2013.

[66] M. Mallen and G. Saville. Polytropic processes in the prediction of centrifugal compressors. *Institue of Mechanical Engineers*, (C183/77):89–96, 1977.

[67] Numeca International. *Fine^{TM}/Turbo Flow Integrated Environment*. Numeca International, Brussels, Belgium, latest version edition, 2019. See also URL `http://www.numeca.com`.

[68] O. E. Baljé. A contribution to the problem of designing radial turbomachines. *Trans. ASME*, 1952.

[69] C. H. Wu. A general theory of three-dimensional flow in subsonic and supersonic turbomachines af axial-, radial- and mixed-flow types. Technical Report 2604, National Advisory Committee for Aeronautics (NACA), 1952.

[70] M. R. Galvas. Fortran program for predicting off-design performance of centrifugal compressors. Technical report, 1973.

[71] F. Wiesner. A review of slip factors for centrifugal impellers. *Transactions of ASME: Journal of Engineering for Power*, pages 558–572, May 1967.

[72] W. Jansen. A method for calculating the flow in a centrifugal compressor impeller when entropy gradients are present. In *Royal Society conference on internal aerodynamics (turbomachinery)*, 1967.

[73] J. E. Coppage, F. Dallenbach, H. P. Eichenberger, G. E. Hlavaka, , E. M. Knoernschild, and N. Van Lee. Study of supersonic radial compressors for refrigeration and pressurization systems. Technical report, 1956.

[74] S. Lieblein, F. C. Schwenk, and R. L. Broderick. Diffusion factor for estimating losses and limiting blade loading in axial flow compressor blades. Technical Report RME 53, National Advisory Committee for Aeronautics (NACA), 1953.

[75] C. Rodgers. Impeller stalling as influenced by diffusion limits. *Transactions of ASME: Journal of Fluids Engineering*, 99:84–97, 1977.

[76] C. Rodgers. A diffusion factor correlation for centrifugal impeller stalling. *ASME paper 78-GT-61*, 1978.

[77] D. Beinecke. *Methode zur Vorausberechnung der Kennlinien von Radialverdichterstufen mit kleiner Durchflusszahl*. PhD Thesis, Universität der Bundeswehr Hamburg, Hamburg, Germany, June 1988. (in German).

[78] J. Daily and R. Nece. Chamber dimension effects on induced flow and frictional resistance of enclosed rotating disks. *Transactions of ASME, Journal of Basic Engineering*, pages 217–232, March 1960.

[79] J. Daily and R. Nece. Roughness effects on frictional resistance of enclosed rotating disks. *Transactions of ASME, Journal of Basic Engineering*, pages 553–562, September 1960.

[80] D. Japikse. *Centrifugal Compressors Design and Performance.* Concepts ETI, 1996.

[81] J. D. Stanitz. One-dimensional compressible flow in vaneless diffusers of radial- and mixed-flow centrifugal compressors, including effects of friction, heat transfer and area change. Technical Report 2610, National Advisory Committee for Aeronautics (NACA), 1952.

[82] O. Dubitsky and D. Japikse. Vaneless diffuser advanced model. *Transactions of the ASME: Journal of Turbomachinery*, 130:011020–1–011020–10, January 2008.

[83] C. Schreiber. *Inlet recirculation in radial compressors.* PhD Thesis, University of Cambridge, Department of Engineering, Cambridge, United Kingdom, 2017.

[84] C. R. Weber and M. E. Koronowski. Meanline performance prediction of volutes in centrifugal compressors. In *ASME - Gas Turbine and Aeroengine Congress*, number 86-GT-216, New York, 1986.

[85] E. W. Lemmon, I.H. Bell, M. L. Huber, and M. O. McLinden. NIST Standard Reference Database 23: Reference Fluid Thermodynamic and Transport Properties-REFPROP, Version 10.0, National Institute of Standards and Technology, 2018.

[86] F. R. Menter. Two-equation eddy-viscosity turbulence models for engineering applications. *AIAA Journal*, 32(8):1598–1605, 1994.

[87] P. Spalart and S. Allmaras. A one-equation turbulence model for aerodynamic flows. *AIAA*, 439, 01 1992.

[88] H. Schlichting and K. Gersten. *Grenzschicht-Theorie.* Springer, 1997. (in German).

[89] M. Diehl and J. A. Schiffmann. Impact of large tip clearance ratios on the performance of a centrifugal compressor. In *Euro Turbo Conference ETC13 Lausanne*, 2019.

[90] M. Zangeneh, A. Goto, and H. Harada. On the design criteria for suppression of secondary flows in centrifugal and mixed flow impellers. *Transactions of ASME: Journal of Turbomachinery*, 120:723–735, October 1998.

[91] F. Dallenbach. The aerodynamic design and performance of centrifugal and mixed-flow compressors. *SAE Technical Progress Series*, 3:2–30, 1961.

[92] H. Mishina and H. Nishida. Effect of relative velocity distribution on efficiency and exit flow of centrifugal impellers. In *ASME - Gas Turbine Conference*, number 83-GT-74, Phoenix, 1983.

[93] IBAG Switzerland AG. http://www.ibag.ch/en/, 2019.

[94] EagleBurgmann International. http://www.eagleburgmann.ch/de/produkte/magnetkupplungen, 2019.

[95] SKF. https://www.skf.com/ch/de/products/bearings-units-housings/ball-bearings/index.html, 2019.

[96] Swep. https://www.swep.de/produkte/b56/, 2019.

[97] CAREL INDUSTRIES S.p.A. https://www.carel.de/electronic-expansion-valve/-/journal_content/56_INSTANCE_i4q5KIMLInKK/10191/95255, 2019.

[98] E. Chance, V. Vipin, Z. Wesley, and H. Richard. *National Instruments LabVIEW: A Programming Environment for Laboratory Automation and Measurement*. National Instruments, latest version edition, 2018. See also URL `http://www.ni.com/en-us.html`.

[99] ESK-Schultze. https://www.esk-schultze.de/, 2019.

[100] Emerson Electric Co. https://www.emerson.com/de-de/catalog/micro-motion-elite-coriolis-de-de?fetchFacets=true#facet:&facetLimit:&productBeginIndex:0&orderBy:&pageView:list&minPrice:&maxPrice:&pageSize:&, 2019.

[101] Transmetra GmbH. https://www.transmetra.ch/, 2019.

[102] Scanivalve. http://scanivalve.com/, 2019.

[103] Kistler Group. https://www.kistler.com/de/?gclid=EAIaIQobChMI8srUhJ_N4gIVD9-yCh1_QwYPEAAYASAAEgJKmfD_BwE, 2019.

Markus Diehl

Curriculum vitae

Moosgasse 22
CH-3232 Ins
☎ *+41 (0) 76 3176961*
✉ *markdiehl87@googlemail.com*

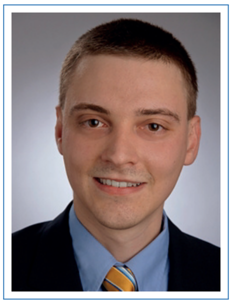

Personal details

Date of birth: 17.12.1987
Place of birth: Sindelfingen/Germany

Education

2015–2019	**Doctoral student**, *École polytechnique fédéral de Lausanne (EPFL), Laboratory for applied mechanical design (LAMD)*, Lausanne/Switzerland.
2011–2014	**Master of Science**, *University of Stuttgart*, Stuttgart/Germany, Energy.
2008–2011	**Bachelor of Science**, *University of Stuttgart*, Stuttgart/Germany, Mechanical engineering.
1998–2007	**Gymnasium**, *Eduard-Spranger Gymnasium*, Filderstadt/Germany.

Practical experience

2013–2014	**Masterthesis**, *Robert Bosch GmbH*, Stuttgart/Germany, Title: Entwicklung einer Methodik zur Auslegung und Nachrechnung von Radialverdichterstufen.
2014–2014	**Internship**, *Modine Europe GmbH*, Filderstadt/Germany, Code development for plate heat exchangers.

Language Skills

German	**First language / mother tongue**	
English	**Fluent**	*School as well as official working language*
Latin		*School from 7th to 13th grade*
Frensh	**Basic**	*Self-educated*

Hobbies and interests

- Mountainbiking
- Hiking
- Astronomy

Markus Diehl
Neuchâtel, June 11, 2019

Ce document a été imprimé au Centre d’impression EPFL,
imprimerie climatiquement neutre, certifiée myClimate.